UNIVERSITÀ
DEGLI STUDI
DI PADOVA

Sede Amministrativa: Università degli Studi di Padova

Dipartimento di FISICA TECNICA

SCUOLA DI DOTTORATO DI RICERCA IN INGEGNERIA INDUSTRIALE
INDIRIZZO: FISICA TECNICA
CICLO XXIV

EXPERIMENTAL STUDY OF TWO-PHASE FLOW AND HEAT TRANSFER DURING VAPORIZATION, FILMWISE AND DROPWISE CONDENSATION OF REFRIGERANTS AND STEAM INSIDE SMALL DIAMETER CHANNELS

Direttore della Scuola: Prof. Paolo Bariani
Coordinatore d'indirizzo: Prof. Luisa Rossetto
Supervisore: Prof. Davide Del Col
Correlatore: Prof. Dimos Poulikakos

Dottorando: Daniele Torresin

To my girlfriend Stefania.

ABSTRACT

In this Thesis, film condensation, flow boiling and adiabatic two-phase flow in minichannels are investigated. Also an experimental study on dropwise condensation on plane surfaces in a small diameter channel is presented. Two are the main goals of this work: the investigation of environmentally friendly refrigerants and the enhancement of two phase heat transfer.
Over the past decades, increased attention to environmental problems coupled with the request for compact and efficient heat transfer devices has brought substantial changes and improvements in the technique of refrigeration. The use of new refrigerants with very low values of global warming potentials (GWP) in minichannels, microchannels and nanochannels have gained quite an attention in engineered systems. In particular the fluid R1234yf, which has a GWP equal to 4, has emerged as the global replacement refrigerant of R134a in future mobile air conditioning systems. In the present Thesis R1234yf single phase and two-phase heat transfer and pressure drop are investigated with experiments inside two different minichannels. Tests have been performed inside a circular and a square single minichannel having 0.96 and 1.23 hydraulic diameter respectively. Heat transfer coefficients measured during filmwise condensation, at 40°C saturation temperature, and during vaporization, at 30°C saturation temperature, are compared to the ones previously obtained with R134a. A comparison of two-phase pressure drop during adiabatic flow of these two fluids is also performed.
With the aim of investigating the validity of conventional theory in the micro-scale, two new test sections made of circular minichannels, with 0.96 and 2 mm inner diameter, are designed and realized specifically for single phase and two phase pressure drop measurements. The good agreement found with classical macroscale models is used to validate a technique for determining the hydraulic diameter of ducts from pressure drop measurement in laminar flow.
With the motivation for improved energy efficiency and miniaturization of the heat exchangers a study in the area of enhanced condensation is also performed. Nanoengineered copper surfaces are investigated with the aim of enhancing the heat transfer coefficient during condensation by promoting the dropwise condensation mode (DWC) instead of the film mode. A thermosyphon two-phase test loop is designed to measure the condensation heat transfer coefficients attained during steam condensation at a saturation temperature of 110 °C. A small size rectangular channel (3.6 mm hydraulic diameter) is realized in order to reproduce the effect of the vapour shear, reproducing the real conditions that occur inside a plate heat exchanger. The experimental apparatus allows the measurements of heat transfer coefficient during condensation and the visualization of the droplets movements. A simple wet-chemical fabrication process is used to obtain a superhydrophobic copper surface. The heat transfer performances of the superhydrophobic surface and of some polished copper surfaces are investigated during dropwise condensation.

RIASSUNTO

In questa Tesi sono studiati la condensazione a film, l'ebollizione convettiva e il deflusso adiabatico bifase all'interno di minicanali. Inoltre è presentato uno studio sperimentale riguardante la condensazione a gocce su superfici piane all'interno di un canale di piccole dimensioni. Due sono gli obiettivi principali di questo lavoro: lo studio di fluidi refrigeranti eco-compatibili e il miglioramento dello scambio termico bifase.
Negli ultimi decenni, la sempre maggiore attenzione ai problemi ambientali, abbinata alla richiesta di dispositivi di scambio termico sempre più compatti ed efficienti ha portato notevoli cambiamenti e miglioramenti nella tecnica di refrigerazione. L'uso di nuovi refrigeranti con ridotto effetto serra (GWP) in minicali, microcanali e nanocanali ha assunto particolare attenzione nei sistemi ingegneristici. In particolare il fluido R1234yf, che ha un GWP pari a 4, è emerso come il sostituto del refrigerante R134a nei futuri impianti di climatizzazione nell'industria automobilistica. In questa Tesi sono presentati i coefficienti di scambio termico e le perdite di carico misurati durante deflusso monofase e bifase di R1234yf all'interno di due differenti minicanali. Le prove sperimentali sono state realizzate all'interno di un minicanale a sezione circolare e di un minicanale a sezione quadrata aventi rispettivamente un diametro idraulico pari a 0.96 e 1.23 mm. I coefficienti di scambio termico, misurati durante condensazione a film alla temperatura di saturazione di 40°C e durante vaporizzazione convettiva alla temperatura di saturazione di 30°C, sono stati poi confrontati con quelli ottenuti in precedenza con il fluido R134a. E' stato fatto inoltre un confronto delle perdite di carico bifase misurate con questi due fluidi.
Con l'obiettivo di verificare la validità della teoria convenzionale nella micro-scala, due nuovi minicanali a sezione circolare, aventi 0,96 e 2 mm di diametro interno, sono stati dimensionati e realizzati appositamente per misurare le perdite di carico durante deflusso bifase e monofase. Il buon accordo trovato con i modelli classici validi per i canali convenzionali ha permesso di convalidare una tecnica per determinare il diametro idraulico dei condotti dalle misure di perdita di carico durante deflusso in regime laminare.
Nella presente Tesi è presentato inoltre uno studio riguardante il miglioramento del processo di condensazione con l'obiettivo di aumentare l'efficienza energetica degli scambiatori di calore e di diminuirne le dimensioni. Sono state studiate superfici in rame nano strutturate con lo scopo di promuovere la condensazione a gocce piuttosto che quella a film. Un nuovo impianto sperimentale costituito da un termosifone bifase è stato realizzato per misurare i coefficienti di scambio termico durante condensazione di vapor d'acqua alla temperatura di saturazione di 110 °C. Per investigare l'effetto della velocità del vapore, riproducendo le reali condizioni degli scambiatori a piastre, la sezione sperimentale è stata realizzata mediante un canale rettangolare di piccole dimensioni (3.6 mm di diametro idraulico). L'impianto sperimentale permette di misurare i coefficienti si scambi termico durante la condensazione, ma anche la visualizzazione dei movimenti delle goccioline. Un semplice processo a immersione chimica è stato utilizzato per ottenere una superficie in rame superidrofoba. Le prestazioni di scambio termico di tale superficie e di alcune superfici in rame lucidato sono state studiate durante la condensazione a gocce.

CONTENTS

LIST OF FIGURES

LIST OF TABLES

INTRODUCTION

In the last few decades the International research community has been always more focused in the investigation of the laws governing physical phenomena in the very small scale. The need to transfer high heat fluxes in relatively small surfaces and volumes has brought new challenges also in the heat removal and cooling techniques with the introduction of mini, micro and nanochannels in the engineered systems. The advantages of using very small channels in the heat exchangers are several, from the heat removal enhancement due to the increase of the heat transfer coefficient and the heat exchange surface, to the reduced refrigerant charge and the high pressure that the systems can withstand. In particular, these two last aspects, have gained particular attention over the past decades: the use of small charge reduces direct green house effect of the systems and promotes the use natural refrigerants like hydrocarbon or ammonia, while the resistance to high pressures enables the use of carbon dioxide. Recently, global warming has been one of the most important issues facing mankind; indeed, while HFC refrigerants have no ozone depletion potential (ODP), many of them have relatively large values of global warming potentials (GWP) comprising one of the six so-called "baskets of gases" contained in the Kyoto Protocol (1997). As a result, much effort is being invested in finding alternative refrigerants to conventional HFCs. Specifically, R1234yf ($CF_3CF=CH_2$), which has a 100-year time horizon GWP equal to 4 (Nielsen, 2007), has emerged as the global replacement refrigerant in future mobile air conditioning systems (SAE, 2009); the present refrigerant (R134a) has a 100-years global warming potential equal to 1430 as compared to that of CO_2. Despite recent activity in characterizing its flammability, toxicity, environmental impact, material compatibility, very few data on its heat performance have been published so far in the open literature.

The need for reliable data of the heat transfer performance of this new environmentally friendly refrigerant has been one of the main goals of the present Thesis.

Experimental results during condensation and vaporization of R1234yf in a circular minichannel with 0.96 mm internal diameter and a square minichannel with side length equal to 1.18 mm are presented. The peculiar geometry of the test section (Matkovic (2006)) and the use of a secondary fluid allow to reduce the vapour quality change from the inlet to the outlet of the channel during condensation, and to investigate the vaporization process under a condition of not imposed heat flux.

Mini thermal devices range from air conditioning and refrigeration to cooling elements of electronic devices: despite the variety of their applications, still much work in the understanding of how the transition from the macro to the mini, micro and nanoscale alters the governing physical process has to be done. Generally, the classical thermal and fluid dynamics theory developed for macro system are not always applicable in the miniscale. In the literature, contradictory results and theory have been presented regarding not only the more complicated two-phase flow, but also the single phase regime. In particular the question if the normal relationships between the friction factor and the Reynolds number for flow in macrochannels could be still applied at the miniscale is an opened debate. While in conventional sized tubes laminar flows are of less important, in mini and micro channels the flow if often laminar due to the relative high pressure losses. In these small channels, the roughness height to diameter ratio is not as small as in the conventional tubes, and then, the study of the roughness effect at low Reynolds numbers has become important. With the aim of investigating the validity of conventional theory in the mini-scale, a study of the adiabatic single phase flow of water and refrigerants inside several minichannels with different hydraulic diameter and cross section shape is presented.

Nanotechnology has penetrated in many scientific fields like material science, genetics, biomedicine, fluidics, mechanics, optics and many others. In particular, the recent developments in the material science have opened new frontiers in the enhancement of two phase heat transfer. It is known that nucleate boiling as opposed to film boiling, and dropwise condensation as opposed to filmwise condensation can lead to much higher heat transfer coefficient. Roughness-based superhydrophilic surfaces are believed to provide nucleation sites for vapour bubbles to form but at the same time delay the formation of a vapour film next to the surface. Similarly, superhydrophobic surfaces are believed to promote the dropwise condensation enhancing the heat transfer coefficient by one order of magnitude with respect to the filmwise condensation. Such surfaces could lead to next generation energy efficient equipment in applications like automobiles, electronic devices, heating, ventilating and air conditioning, etc. Attempts have been made, and reported in literature, to use these surfaces to improve nucleate boiling and dropwise condensation. Usually they are obtained with micro-nano fabrication processes which limit their applicability to the research field. Recently, easy and cheap processes have been published in the literature for preparing metallic surfaces with highly specific wettability, which could extend their applicability also in the thermal heat exchange industry. Despite the numerous investigations in the understanding the physical mechanism which dominates during vapour condensation on these surfaces, few data are available for the heat transfer rate. In the preset Thesis, a method for preparing a superhydrophobic copper surface in less than two hours, at ambient conditions and without any special apparatus is proposed. The heat performances of this surface are investigated during dropwise condensation inside a new test apparatus which allows the measurement of the heat transfer coefficient and the visualization of droplets movements. Moreover, in order to reproduce the usual conditions inside the plate heat exchangers, where the dropwise condensation is affected by the steam velocity, tests are done inside a small size channel. The heat transfer performances of the superhydrophobic surface and of some polished copper surfaces during dropwise condensation are compared.

The present work is organized as follows:

-Chapter 1. Heat transfer coefficient during condensation of R1234yf and R134a inside the circular and square minichannel.

-Chapter 2. Heat transfer coefficient during vaporization of R1234yf and R134a inside the circular minichannel and during vaporization of R1234yf inside the square minichannel.

-Chapter 3. Single phase and two phase pressure drop during adiabatic flow of different refrigerants in different cross sectional shapes minichannels.

- Chapter 4. Study of steam dropwise condensation on nanoengineered copper surfaces.

1 CONDENSATION INSIDE MINICHANNELS

1.1 Abstract

The present Chapter reports local heat transfer coefficients measured during condensation of R1234yf within a single circular 0.96 mm diameter and a square 1.28 mm side length minichannel. This experimental work is carried out in a unique test apparatus which allows determining the local heat flux extracted from the condensing fluid from the temperature profile of the coolant. For this purpose, the temperatures of the coolant and of the wall are measured along the test section. The saturation temperature is determined from the saturation pressure which is measured at inlet and outlet of the test channel. Condensation tests are carried out at 40 °C saturation temperature with mass fluxes ranging between 200 and 1000 kg m^{-2} s^{-1} in the circular section and between 100 and 800 kg m^{-2} s^{-1} in the square one. Experimental results are compared to the ones previously measured in the same set up (Matkovic *et al.* (2009) and Del Col *et al.* (2011)) with R134a: at the same conditions, the heat transfer coefficients measured with the new fluid are lower by 15-30%. Since the saturation temperature drop directly affects the heat transfer rate, the pressure drop during adiabatic two-phase flow of R1234yf is also measured and compared to R134a. From this point of view R1234yf performs better than R134a and the results will be presented in Chapter 3.

1.2 Introduction

Over the past decades, increased attention to environmental problems has brought substantial changes and improvements in the technique of refrigeration. In particular, with regards to refrigerants, the transition from CFCs to HCFCs and to HFCs has decreased the environmental impact of common refrigeration. Recently, global warming has been one of the most important issues facing mankind; indeed, while HFC refrigerants have no ozone depletion potential (ODP), many of them have relatively large values of global warming potentials (GWP) comprising one of the six so-called “baskets of gases” contained in the Kyoto Protocol (1997). As a result, much effort is being invested in finding alternative refrigerants to conventional HFCs, with natural refrigerants such as hydrocarbons, ammonia, and carbon dioxide receiving considerable research and development focus. The new refrigerant must have adequate stability to be used in the typical conditions of refrigeration equipment but also have a short atmospheric lifetime so that the contribution to global warming is small.

For certain applications, such as automotive, proactive solutions are being sought that couple scientific, engineering, and business decisions together with legislative efforts. For example, the European Union’s f-gas regulations (Regulation (EC) No 842/2006 and Directive 2006/40/EC) specify beginning on January 1, 2011 new models and on January 1, 2017 new vehicles fitted with air-conditioning cannot be manufactured with fluorinated greenhouse gases having global warming potentials (GWP) greater than 150.

Recently, development efforts have been initiated to investigate halogenated olefins as possible refrigerants for automotive applications, with fluorinated propane isomers, in particular, having emerged as possible solutions. Specifically, R1234yf ($CF_3CF=CH_2$), which has a 100-year time horizon GWP equal to 4 (Nielsen, 2007), has emerged as the global replacement refrigerant in future mobile air conditioning systems (SAE, 2009); the present refrigerant (R134a) has a 100-years global warming potential equal to 1430 as compared to that of CO_2. Zilio *et al.* (2011) conducted

experiments for a typical R134a compact European automotive air conditioning system; a "drop in" R1234yf system was tested, showing that, for a given cooling capacity, R1234yf systems present lower performance than the baseline R134a. Using numerical simulations, the authors demonstrated that enhancing the face area of the condenser by 20%, the one of the evaporator by 10%, and using a overridden compressor, the R1234yf system showed higher COP values then the baseline R134a for equal cooling capacities. R-1234yf, however, certainly could not be used only in automotive air conditioning but it can be employed as working fluid in stationary refrigeration applications and Organic Rankine Cycle (Quoilin *et al.* (2011)).
Up to date, researchers and manufacturers have addressed the research activity regarding R1234yf on characterizing its flammability, toxicity, environmental impact, material compatibility, oil compatibility, air conditioning system performance: for example, the recent research program conducted through SAE (SAE, 2009) was to determine the safety and environmental characteristics of R1234yf. Other studies have been focused on thermodynamic and transport property data, and associated Equation of State (EoS) (Fedele *et al.* (2011), Brown *et al*. (2009)).
On the other side, very few data on heat transfer during vaporization or condensation of R1234yf has been published so far in the open literature: the target of the present work if to give reliable data of heat transfer coefficients measured during condensation of this new fluid inside minichannels.

1.3 Test apparatus

The experimental apparatus will be described in the present chapter. The test rig allows performing heat transfer and pressuring drop measurements during single phase and two phase flow of refrigerants inside minichannels. Two different test sections are installed in the apparatus, in parallel mode: the first section consists of a circular minichannel with 0.96 mm internal diameter; the second section consists of a square minichannel with side length equal to 1.18 mm.
Figure 1.1 reports a scheme of the test rig used for the experimental tests. It consists of the refrigerant loop and of three auxiliary loops: one for the cooling water used in the test section, another one for the cooling water of the post-condenser and the last one for the hot water loop of the evaporator. When the test apparatus is operated for condensation measurements, the subcooled refrigerant coming from the post-condenser passes through the mechanical filter (MF) and the filter dryer (HF) and then is pumped by a variable speed electric motor gear pump through the Coriolis-effect mass flow meter into the evaporator. There, the fluid is heated up, vaporized and superheated. The temperature and pressure measurements at this point (after the evaporator) allow determining the thermodynamic state of the superheated vapour refrigerant. The superheated vapour then enters the test section, which is made of two counter-flow heat exchangers: the first one (desuperheater) is used to achieve saturation conditions, while the second one is the measuring sector where the refrigerant is condensed through the cold water of the auxiliary loop. Finally, the saturated vapour coming out from the test section, at low vapour quality, is sent into the post-condenser where the fluid is totally condensed and subcooled. The same rig can be used for flow boiling measurements. In this case, the liquid refrigerant is directly sent from the pump to the test section where the vaporization process occurs. Two thermal baths are used in the tests: the first one provides the water entering the measuring sector and the desuperheater at a desired temperature, the other one provides the coolant for the post-condenser. When necessary, the cooling water entering the pre-section can be maintained at a higher temperature through an electrical heater installed between the thermal bath and the desuperheater. The cooling water flow rates, in the pre-section and in the measuring section, are measured by means of two Coriolis-effect mass flow meters. For the measurements of the local heat transfer coefficient, three parameters are determined: the local heat flux, the wall temperature and the saturation temperature. The measuring section is realized in such a way that the

local wall temperature and the coolant temperature profile can be measured: in particular, the water temperature profile in the test section is obtained from the thermocouples in the coolant. Afterwards, the local heat flux is determined from the water temperature gradient in each position. The saturation temperature is obtained from the pressure measurements at inlet and outlet of the measuring sector. Indeed, the pressure is gauged through two digital strain gauge pressure (relative and differential) transducers, connected to manometric taps to measure the fluid pressure upstream and downstream of the test tube. The vapour temperature at inlet and outlet of the test section is also measured by means of a T-type thermocouple and a four-junction thermopile, which are soldered to the stainless steel capillary tube in the adiabatic lengths, before and after the measuring sector. The presence of both temperature and pressure sensors at the inlet of the measuring sector allows a double check of the saturation temperature.

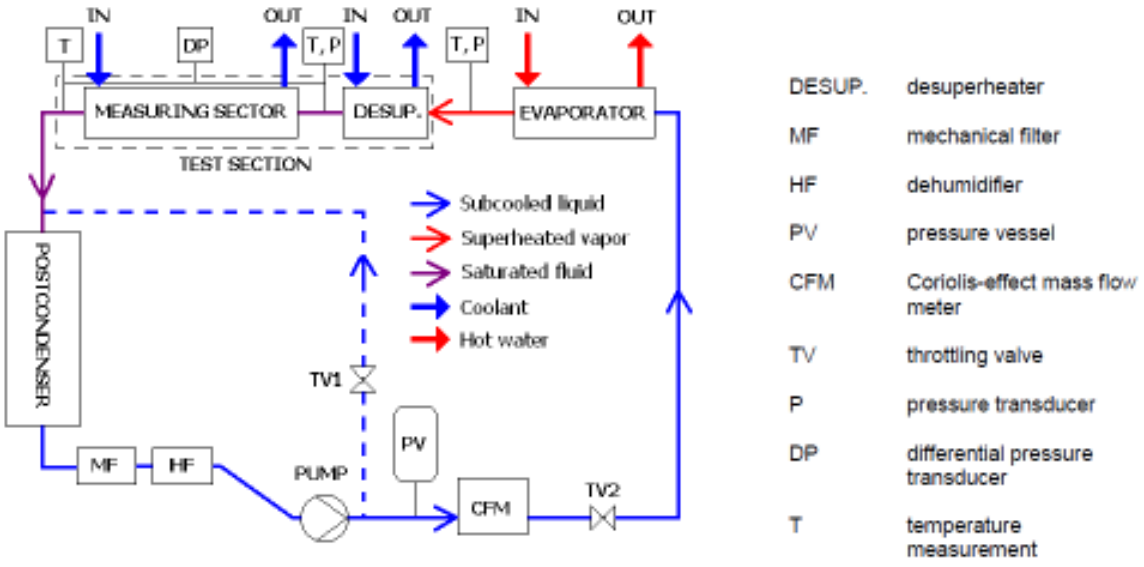

Figure 1.1. Schematic representation of the test rig. The configuration refers to a condensation test.

1.4 Circular minichannel

1.4.1 Description of the experimental section

The most important part of the test rig is the test section, which consists of two sectors. The first one, the pre-sector (PS), is used to obtain the desired inlet vapour quality: in condensation tests the pre-sector works as desuperheater, while in vaporization tests it allows to adjust the desired subcooling. The second one is the measuring sector (MS). Between the two sectors and downstream the MS, adiabatic stainless steel pipes are installed in order to reduce the axial heat conduction through the tube wall, to thermally detach the two sectors from the surrounding and to check the saturation state of the fluid by measuring the adiabatic wall temperature and the fluid pressure. A detailed view with internal geometry of the test section is given in Figure 1.2.

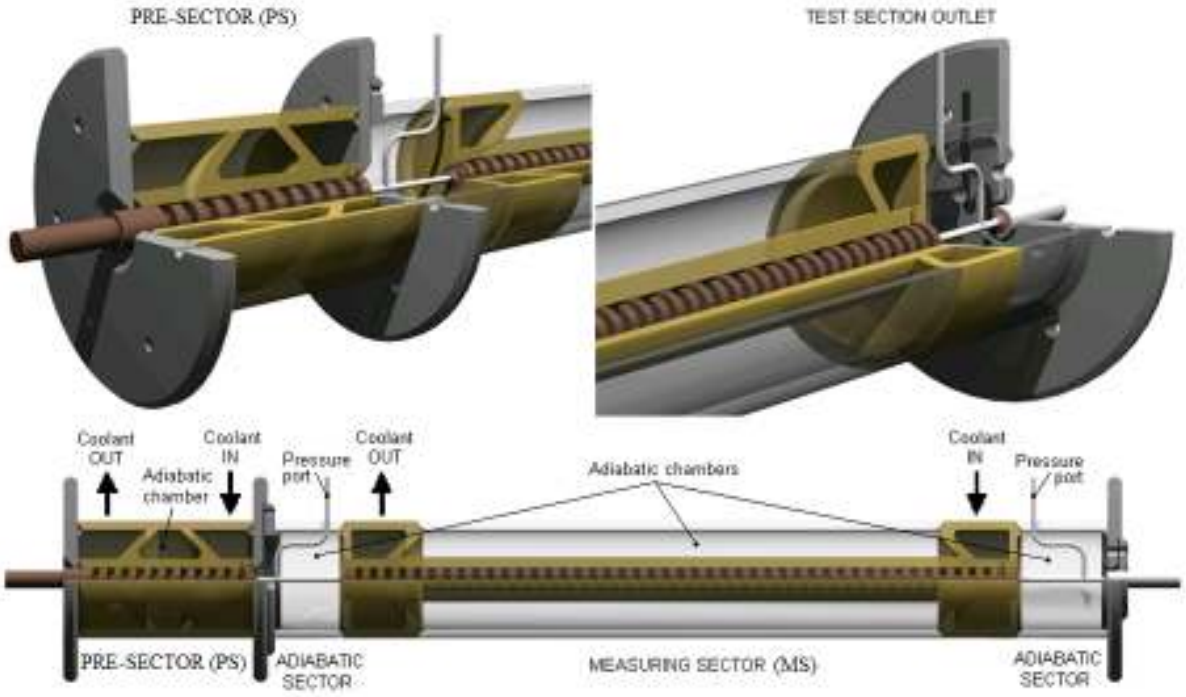

Figure 1.2. View of the circular minichannel test section.

The test section is equipped with 28 thermocouples, 13 in the wall and 15 in the secondary fluid (water) channel along the sector; the test section is made from an 8 mm copper rod with a 0.96 mm internal bore. The thermocouples embedded in the wall are installed in 0.6 mm diameter cylindrical holes, machined 0.5 mm far from the internal tube surface. The refrigerant flows inside the minichannel; condensation and boiling processes are achieved using a secondary fluid (water) that flows in counter-flow outside the minichannel as shown in Figure 1.3. The length of the channel is equal to 228.5 mm.

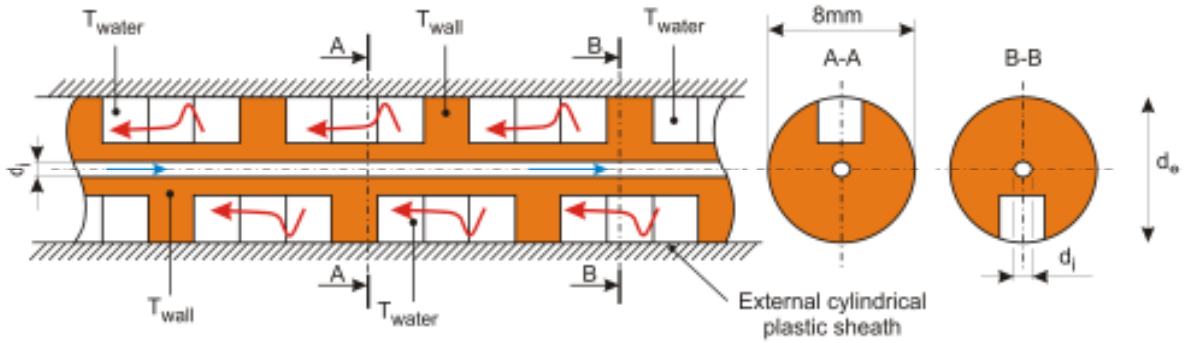

Figure 1.3. Enlarged photo of the round minichannel: water path and cross section.

A rather tortuous path for the secondary fluid is machined in the thick copper wall surrounded by an epoxy resin sheath working as an insulator, armature and support for thermocouple wires. Crucial advantages of such a design reflect in the following characteristics:

-good coolant mixing and thus accurate temperature measurements along the measuring sector is essential to obtain a reliable water temperature profile, which is used for determination of local heat flux;
-both the continuous interrupting of the boundary layer, due to the rather complex coolant flow passage geometry, and the enhanced external wall surface area notably decrease the external heat transfer resistance, which is crucial for precise heat transfer coefficient measurements;
-thermocouple wires embedded in the copper wall are led outside the measuring sites through the epoxy resin without passing through the coolant flow: in this way the error of the temperature measurements due to axial heat conduction along the thermocouple wire and the spurious emf's build up for the presence of high temperature gradients is reduced to a minimum;
-the epoxy resin sheath does not only serve for accommodation of the thermocouple wires and for the insulation purpose; it also plays an important role as the test section's support.

In order to achieve low uncertainty in the measurement of the heat transfer coefficient, the following characteristics of the minichannel test tube are required:

-high external heat transfer coefficient;
-enhanced external surface area;
-homogeneous wall surface temperature distribution along the channel;
-low thermal resistance of the channel wall in radial direction;
-high thermal resistance of the channel wall in axial direction;
-good coolant mixing;
-low pressure drop;

The first two characteristics enhance the external heat transfer, which moves the leading thermal resistance toward the refrigerant side. In this way, the wall to refrigerant temperature difference is increased at given heat flow rate, while the relative error of the corresponding temperature difference measurement is decreased. Enhanced external heat transfer should be achieved so as to avoid systematic errors in wall temperature measurement due to local temperature variations. Furthermore, a high thermal conductivity of the tube wall decreases the associated temperature gradients and thus the wall temperature error due to deviation in temperature sensor positioning. On the other hand, the high thermal conductivity of the test tube also promotes the axial heat conduction. Even though, much smaller in comparison with the radial one, the axial heat conduction is additionally reduced by the multiple groves in the wall thickness of the present design. Additionally, a precise coolant temperature profile measurement is also of paramount importance for high performance heat transfer coefficient measurements. Insufficient coolant mixing is probably one of the most frequent reasons for systematic errors in fluid temperature measurement. On the other hand, a flow passage geometry that enables good fluid mixing and enhanced heat transfer are usually associated with significant pressure drop. In this context, the present coolant flow passage geometry has turned out to offer excellent performance behavior for high precision HTC measurements inside a single minichannel. More details about test section design and building can be found in Matkovic (2006).

1.4.2 Data reduction for condensation tests

The present unique test apparatus allows to determine the local heat flux extracted from the condensing fluid from the temperature profile of the secondary fluid. In particular, the slope of the profile is used to calculate the local heat flux:

$$q'(z) = -\dot{m}_w \cdot c_{pw} \cdot \frac{1}{\pi \cdot d_i} \cdot \frac{\mathrm{d}T_w(z)}{\mathrm{d}z} \tag{1.1}$$

where z is the axial coordinate along the tube, oriented with the refrigerant flow and dT_w/dz is the derivative of the polynomial equation interpolating the water temperature along z. The local heat transfer coefficient inside the minichannel can be obtained as the ratio of heat flux to saturation minus wall temperature difference:

$$\alpha(z) = \frac{q'(z)}{\left[T_{sat}(z) - T_{wall}(z)\right]} \tag{1.2}$$

while the vapour quality x at any axial position is obtained from:

$$x(z) = x_{in} - \frac{q(z)}{\dot{m}_r \cdot h_{LG}} \tag{1.3}$$

The vapour quality at the inlet to the measuring sector x_{in} is obtained from the energy balance on the coolant side of the desuperheater. In fact, the specific enthalpy of the superheated refrigerant at the inlet to the pre-section is known from the local pressure and temperature. The enthalpy variation in the desuperheater is obtained from the heat flow rate transferred in the desuperheater and, in turn, this enthalpy change is used to calculate the vapour quality at the inlet to the measuring sector.
The transferred heat flow rate is obtained by integrating the local heat flux q' from 0 (refrigerant inlet) to z:

$$q(z) = \pi \cdot d_h \cdot \int_0^z q'(z)\,\mathrm{d}z \tag{1.4}$$

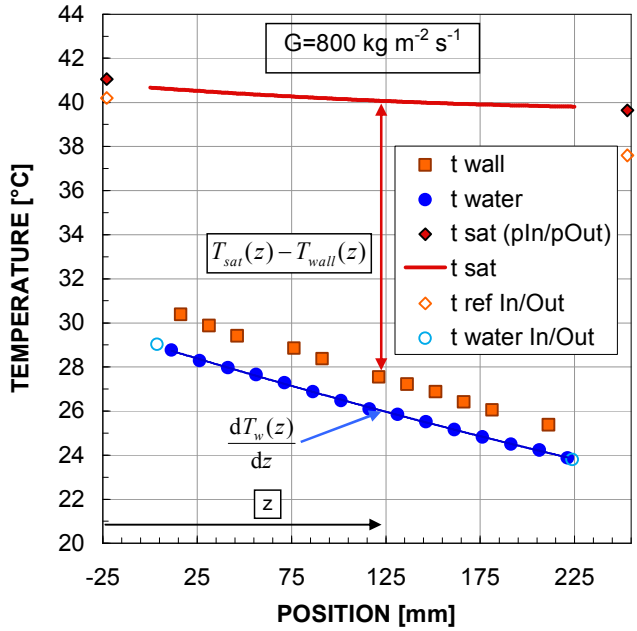

Figure 1.4. Refrigerant, wall and coolant temperature measurements with R1234yf at G = 800 kg m^{-2} s^{-1} along the measuring sector. Symbols refer to local temperature measurements.

Figure 1.4 reports saturation, wall and water temperatures for a test run at 800 kg m^{-2} s^{-1} mass flux with R1234yf. As previously reported the saturation temperature is known only at the inlet and outlet of the measuring sector from the saturation pressure measurements; in particular the outlet pressure is obtained by means of a differential pressure transducer, subtracting the pressure drop from the inlet value. The same graph also reports the temperatures directly measured in the

adiabatic walls upstream and downstream of the condensation length. Since subcooled liquid refrigerant could be present at the outlet, the outlet saturation temperature used in the present data reduction is determined from the pressure.
The saturation temperature in the channel can be taken as a linear variation between inlet and outlet. For a more accurate data reduction, the refrigerant temperature profile along the channel is obtained from the pressure which in turn is determined from the equation of frictional pressure gradient by Friedel (1979) and the momentum component with the Rouhani and Axelsson (1970) void fraction. The pressure profile curve resulting from the application of these models is matched to the measured values at the inlet and at the outlet of the measuring sector by multiplying the pressure gradient by the ratio of calculated to measured pressure drop: this profile is the one used in the data reduction of the present tests.
For most test conditions, there is no appreciable effect on the heat transfer coefficient when using a linear profile for the refrigerant temperature between inlet and outlet. This is due to the fact that, for typical test conditions the saturation temperature drop is small as compared to the difference of saturation minus wall temperature.
Prior to any test measurements, several actions have been undertaken in order to ensure good accuracy of the experimental apparatus. First, an on-site calibration of the thermocouples installed in the wall and in the water channel has been performed: the calibration procedure consists in determining a correction function for each thermocouple determined by the comparison with a calibrated thermistor probe Pt100, during water circulation under adiabatic conditions in the measuring section.
Another important check has been done to verify the thermal balance in the measuring sector. With a three junction copper-constantan thermopile, the overall cooling water temperature gain has been measured. The total heat flow rate calculated from the coolant side has been compared to the one obtained integrating the heat flux between 0 and L, where L is the length of the measuring sector:

$$q_{tot} = \pi \cdot d_h \cdot \int_0^L q'(z)\mathrm{d}z = \dot{m}_w \cdot c_{pw} \cdot \Delta T_w \tag{1.5}$$

In all the tests presented here, the disagreement between the two terms in Eq. (1.5) is below 4%.
The experimental uncertainties of the measured parameters, given by manufacturer's specification, are reported in Table 1.1.

Temperature	±0.05 K
Temperature difference (with thermopile)	±0.03 K
Water flow rate	±0.2%
Refrigerant flow rate	±0.2%
Absolute pressure	±0.05 bar
Pressure difference	±0.001 bar

Table 1.1 Experimental uncertainty for measured parameters

In the case of thermocouples, the reported uncertainty comes from the off-site calibration tests. The range of variation of the water and wall thermocouples readings after the on-site calibration is ±0.02 K. Considering possible additional errors during tests, in later evaluations, the value of thermocouple uncertainty will be taken equal to ±0.03 K.

1.4.3 Error analysis

The present experimental technique allows achieving low experimental uncertainty which is partly due to the particular geometry of the coolant channel: the external enhanced area and the complex

flow passages reduce the thermal resistance on the coolant side. In fact, the ratio of the thermal resistance of the refrigerant side to that of the coolant side is typically around 7, which ensures that the condensation side presents the governing resistance. As a consequence, the uncertainty associated with the calculated heat transfer coefficient is dominated by the uncertainty in the heat flux, which in turn depends on the uncertainty of the cooling water profile.

The experimental uncertainty is made up of two parts: the first component is the "Type A" uncertainty that derives from repeated observations while the second one, "Type B" uncertainty, derives from instruments calibration and manufacturer's specifications. Following general rules reported in ISO Guide to the Expression of Uncertainty in Measurement (1995), the "TypeA" and "TypeB" uncertainties are calculated for each parameter. The resulting uncertainty u of each parameters x is given by Eq. (1.6) were u_a and u_b refer respectively to "TypeA" and "TypeB" components.

$$u(x) = \sqrt{\left(u_a(x)\right)^2 + \left(u_b(x)\right)^2} \tag{1.6}$$

The combined standard uncertainty is obtained by appropriately combining standard uncertainties of the measured quantities (y) as follows:

$$y = f\left(x_1, ..., x_n\right) \tag{1.7}$$

$$u_c(y) = \sqrt{\sum_{i=1}^{n} \left(\frac{\delta f}{\delta x_i}\right)^2 \cdot u^2(x_i)} \tag{1.8}$$

The expanded uncertainty u_M is obtained by multiplying the combined standard uncertainty by a coverage factor k=2 with an interval having a level of confidence of approximately 95%.

$$u_M = k \cdot u_c(y) \tag{1.9}$$

The nominal experimental uncertainty of the local heat transfer coefficient was calculated as follows:

$$u_{\alpha(z)} = \sqrt{\left(\frac{1}{\Delta T_{ref-wall}(z)} \cdot u_{q'(z)}\right)^2 + \left(\frac{q'(z)}{\left(\Delta T_{ref-wall}(z)\right)^2} \cdot u_{\Delta t(z)}\right)^2} \tag{1.10}$$

Figure 1.5 shows the relative percentage uncertainty of the heat transfer coefficient and the uncertainty contributions to the total value during a condensation test at 1000 kg m^{-2} s^{-1}. The overall uncertainty is always below 4%, for the entire range of vapour quality, with the lowest values in the vapour range between 0.4 and 0.6.

Similar trend were found for all the tests with mass velocity varying form 1000 to 200 kg m^{-2} s^{-1}. The lower the mass velocity, the higher the experimental uncertainty. At 600 kg m^{-2} s^{-1}, it is always below 5%, while at 400 kg m^{-2} s^{-1} it ranges between 6% and 4%.

At 200 kg m^{-2} s^{-1} (Figure 1.5) the overall relative uncertainty is always higher than 4%, ranging between 14% and 8%. As it can be seen from Figure 1.5, the uncertainty of the heat flux represents a major contribution to the overall uncertainty, and the procedure for its estimation is reported in the next section.

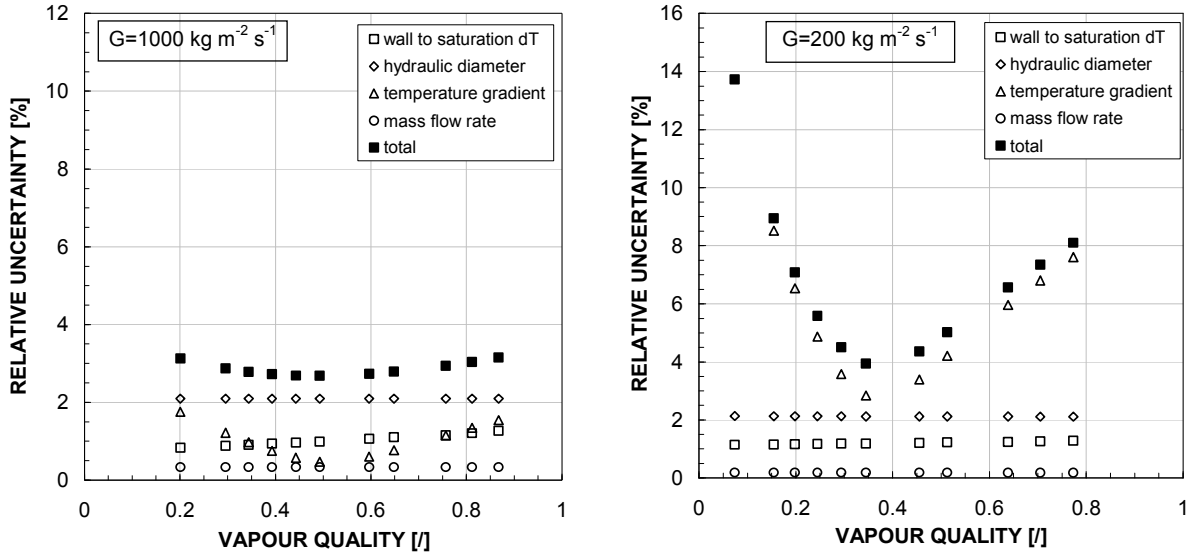

Figure 1.5. Relative uncertainty values for the main contributions of the experimental heat transfer coefficient uncertainty versus vapour quality at 1000 kg m^{-2} s^{-1} and 200 kg m^{-2} s^{-1} mass velocity.

1.4.3.1 Heat flux uncertainty

The three main uncertainties contribute of the heat flux were calculated for all the heat transfer measurements as follow:

$$\delta_{q'(z)} = \sqrt{\left(\frac{c_{pw}\cdot T'_w(z)}{\pi\cdot d_i}\cdot u_{\dot{m}_w}\right)^2 + \left(\frac{c_{pw}\cdot \dot{m}_w\cdot T'_w(z)}{\pi\cdot d_i^{\,2}}\cdot u_{d_i}\right)^2 + \left(\frac{\dot{m}_w\cdot c_{pw}}{\pi\cdot d_i}\cdot u_{T'_w(z)}\right)^2} \tag{1.11}$$

As it can be seen in Figure 1.5, relative contributions to the overall experimental uncertainty due to mass flow rate measurements and hydraulic diameter remain rather constants for the entire span of mass velocities and vapour qualities respectively as 0.3% and 2%. The uncertainty associated with the calculated heat flux is dominated by the uncertainty in the temperature gradient, which mostly depends of the water temperature profile obtained interpolating experimental values with a second order polynomial:

$$t(z) = a_0\cdot z^2 + a_1\cdot z + a_2 \tag{1.12}$$

In particular, temperature values used to obtain, with least square method, the coolant profile of each test run, are the mean $t_{mean(z_i)}$ of 50 readings with a time step of 1 s. Gradient values, used to calculate local heat flux in the position where thermocouples are embed in the wall, are calculated deriving Eq. (1.12). The relative uncertainty in the water gradient has been calculated with two different methods in: the first one (Method a) is based on the statistic theory while the second one (Method b) is the multiple linear regression method.

Method a

With respect to temperature measurements, in accordance to ISO Guide to the Expression of Uncertainty in Measurement (1995), it has been supposed a rectangular probability distribution of a lower bound $t_{mean(z_i)}$-u_t and upper bound $t_{mean(z_i)}$+u_t, where u_t=0.03 °C is the assumed uncertainty in temperature measurements: it is equally probable for $t_{mean(z_i)}$ to be anywhere within this interval.

A specific procedure has been implemented for determining the uncertainty associated with temperature gradient. A temperature variation equal to thermocouple uncertainty has been imposed on each water thermocouple; therefore 2^{15} varied water temperature profiles have been obtained, corresponding to all possible water temperature configurations compatible with experimental uncertainty. For each location z_i along the channel, 2^{15} values of temperature gradient have been calculated obtaining a Gaussian distribution. This procedure has been implemented considering "TypeA" and "TypeB" thermocouple uncertainties. The standard deviation of temperature gradient distribution is the uncertainty associated with temperature gradient.
Such a method requires long computing time for the high number of iteration, so it has been decided to solve the problem with a multiple linear regression method (MLR).

Method b

With the MLR method, based on least square method, it is possible to take into account different uncertainties of each experimental point obtaining the regression parameters but also their uncertainties.
As mentioned before, the water temperatures profile for each test run has been fitted with a second order polynomial (Eq. 1.12). The three coefficients a_0, a_1, a_2 are obtained minimizing the figure of merit χ:

$$\chi^2 = \sum_{i=1}^{15}\left[\frac{t_{w,i} - (a_0 \cdot z_i^{\,2} + a_1 \cdot z_i + a_2)}{u_i(t_w)}\right] \tag{1.13}$$

where z_i is the ith axial location along the channel at which water temperature is measured (i ranges between 1 and 15), $t_{w,i}$ is the water temperature measured at the it location, and $u_i(t_{w,i})$ is the experimental uncertainty associated with the water temperature at the ith location.
Let indicate K a matrix (15x3) whose elements are

$$K_{i,1} = \frac{z_i^{\,2}}{u_{t,z_i}}, K_{i,2} = \frac{z_i}{u_{t,z_i}}, K_{i,3} = \frac{1}{u_{t,z_i}} \quad (i=1,\ldots,15) \tag{1.14}$$

and B a vector, whose elements are the values to be fitted

$$B_i = \frac{\bar{t}_i}{u_{z_i}} \tag{1.15}$$

The condition of minimizing χ yields the following equation

$$\left(K^T \cdot K\right) \cdot A = K^T \cdot B \tag{1.16}$$

in the matrix form, where A is a vector whose components are the parameters to be fitted a_0, a_1, a_2.
The inverse matrix $C=(K^T \cdot K)^{-1}$ is related to the standard uncertainty of the estimated parameters a_i; the diagonal elements of C are the square uncertainties of the fitted parameters:

$$u_{a_i} = C_{jj} \tag{1.17}$$

and the off-diagonal elements C_{jk} are the covariances between the estimated parameters a_j and a_k:

$$\mathrm{cov}(a_j, a_k) = C_{jk} \tag{1.18}$$

Considering negligible the measurements errors in the z_i, it is possible to simple calculate gradient uncertainty according to ISO Guide (1995). The uncertainty related to temperature gradient $u(dtw/dz)$ is obtained from the uncertainty of fitted parameters (Eq. (1.17)) and from the covariances between fitted parameters (Eq. (1.18)) by applying the law of propagation of uncertainty as reported in Eq. (1.19) and Eq. (1.20)

$$grad(z_i) = \frac{dT_{w,i}}{dz} = 2 \cdot a_0 \cdot z_i + a_1 \tag{1.19}$$

$$u(grad_i) = u\left(\frac{dT_{w,i}}{dz}\right) = \sqrt{\left(\frac{\partial grad}{\partial a_0}\right)^2 \cdot u_{a_o}{}^2 + \left(\frac{\partial grad}{\partial a_1}\right)^2 \cdot u_{a_1}{}^2 + 2 \cdot \mathrm{cov}(a_0, a_1) \cdot \left(\frac{\partial grad}{\partial a_0}\right) \cdot \left(\frac{\partial grad}{\partial a_1}\right)} \tag{1.20}$$

Combining the previous two equations:

$$u\left(T'_{w,z_i}\right) = \sqrt{\left(2 \cdot z_i \cdot u_{a_0}\right)^2 + \left(u_{a_1}\right)^2 + 2 \cdot \mathrm{cov}(a_0, a_1) \cdot (2 \cdot z_i)} \tag{1.21}$$

Figure 1.6 shows the heat flux relative uncertainty calculated with the two methods at 1000 kg m^{-2} s^{-1} and 200 kg m^{-2} s^{-1}: the agreement is excellent between the two methods.
Since the MLR method requires a short computing time, it has been decided to use for the calculation of uncertainty in the slope of coolant profile.

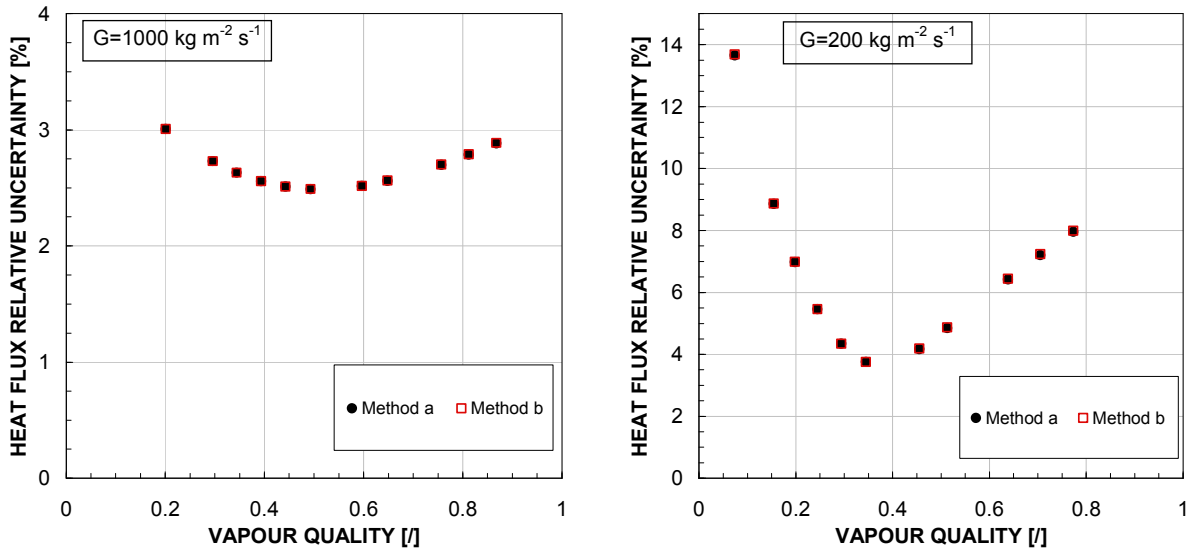

Figure 1.6. Calculated heat flux uncertainty versus vapour quality with method a and method b at 1000 kg m^{-2} s^{-1} and 200 kg m^{-2} s^{-1} mass velocity of R1234yf.

1.4.4 Single phase heat transfer coefficient

Prior to any two-phase measurement, some single phase tests have been carried out with R1234yf.: heat transfer tests have been performed with subcooled liquid, both in heating and cooling mode, at mass fluxes ranging between 400 and 1200 kg m^{-2} s^{-1} and over the temperature range from 15 to 35 °C during heating mode and from 40 to 24 °C during cooling mode. Average values of single phase heat transfer coefficients along the measuring sector were measured: Figure 1.7 reports the average single phase heat transfer coefficient versus Reynolds number, which was varied between 2400 and 7700. The heat transfer coefficients in the cooling mode and in the heating mode are in good agreement.

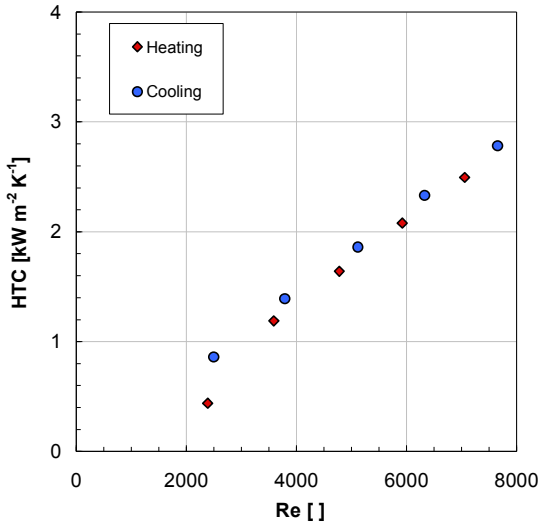

Figure 1.7. Experimental heat transfer coefficients versus Reynolds number measured during single phase heating and cooling of R1234yf.

On the other hand predictions by Gnielinski (2002) and Gnielinski (1993) single phase heat transfer models were calculated and compared against the average experimental values: as it can be seen in Figure 1.8 at high values of HTC, and Reynolds number above 5000, the measured heat transfer coefficient is predicted by the correlations within ±10%, while at lower Reynolds number the two models provide different predictions, but these values correspond to the transition from laminar to turbulent flow and thus predicting models may be less accurate than in the turbulent region. The same trend was reported by Matkovic *et al.* (2009) during single phase flow of R134a in the same test section.

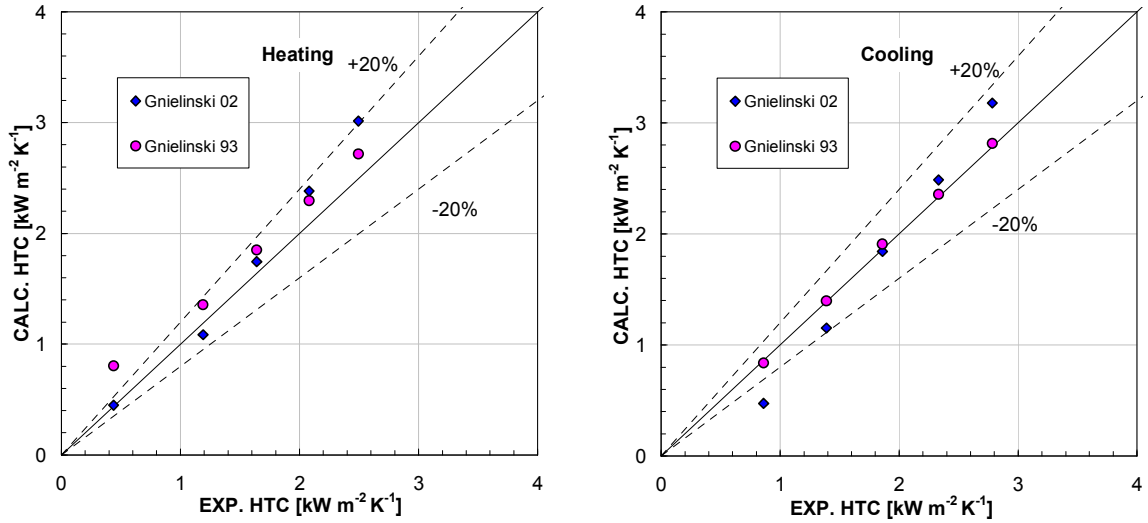

Figure 1.8. Comparison between calculated average single phase HTC according to Gnielinski (2002) and Gnielinski (1993) versus experimental HTCs during heating and cooling mode.

Beside average heat transfer coefficients, local single phase heat transfer coefficient measurements were performed to have qualitative and also quantitative feedback regarding the test apparatus performance.

Figure 1.9 a) reports refrigerant, wall and water temperatures for a test run during cooling mode at 800 kg m^{-2} s^{-1} mass velocity. The coolant and the wall temperature profiles have been obtained from the exponential fitting curve over local temperature measurements,

$$T_w(z) = C_1 + C_2 \cdot e^{-\gamma \cdot z} \tag{1.22}$$

where C_1, C_2 and γ are determined for each test run, while the refrigerant temperature profile was obtained from the thermal balance on the coolant side. Figure 1.9b) reports the local heat transfer coefficient, calculated as a ratio of the local heat flux (referred to the minichannel internal wall surface) and the wall to refrigerant temperature difference: in the same figure, solid line is associated to single phase heat transfer coefficient according to Gnielinski (2002), whereas the dashed lines are referred to Gnielinski (1993) single phase modelling. The local thermodynamic and transport properties are calculated from the refrigerant temperature profile, which is obtained from the thermal balance of the polynomial coolant temperature profile.

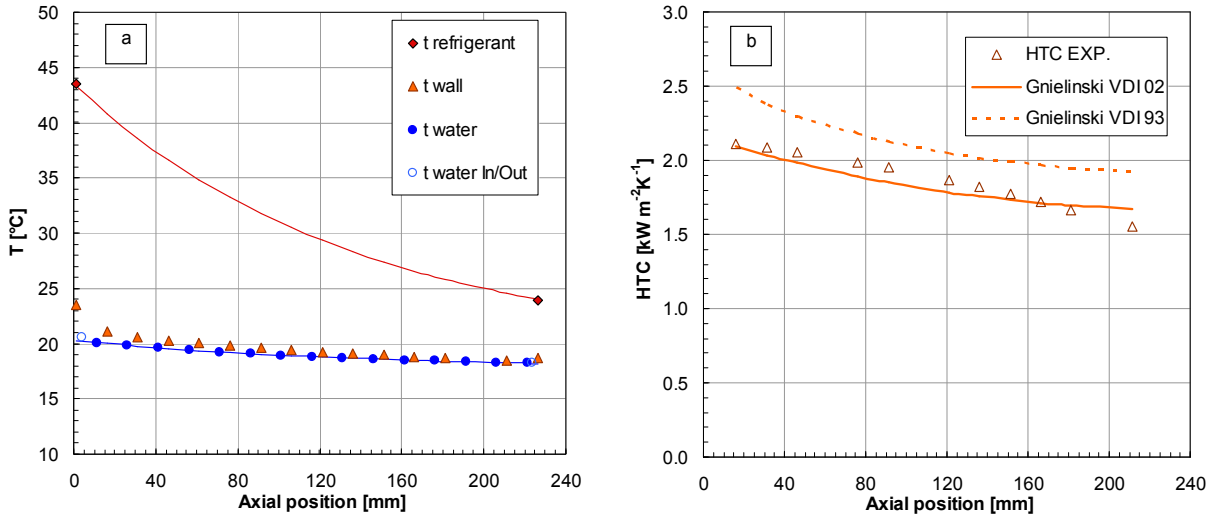

Figure 1.9. a) Local temperature recordings during single phase tests in cooling mode at 800 kg m^{-2} s^{-1} refrigerant mass velocity. b) Local single phase refrigerant heat transfer coefficients at refrigerant mass velocity 800 kg m^{-2} s^{-1} during cooling mode. The full line and the dashed one refer to calculated single phase HTC according to Gnielinski (2002) and Gnielinski (1993) respectively.

In order to obtain the best representation of the actual phenomenon under study, several corrections were applied to the data. These corrections account mainly for:
a) the axial conduction along the tube and its effect on the local heat flux;
b) the radial thermal resistance in the copper between inner surface and thermocouple position and its effect on the wall temperature;
c) the water to ambient heat transfer and its effect on the local heat flux and total heat flow rate.

1.4.5 Condensation of R1234yf in the circular minichannel

Figure 1.10 reports the experimental heat transfer coefficients measured during condensation of R1234yf at 40 °C saturation temperature, correspondent to 1018 kPa saturation pressure, at mass velocities from 200 to 1000 kg m^{-2} s^{-1} over the entire range of vapour quality. Each dot in the diagram corresponds to one experimental value of the wall temperature and is obtained as the ratio of heat flux to saturation minus wall temperature; readings from the first and the last wall

thermocouple are not used since they may be affected by axial boundary effects. Error bars have been introduced for the heat transfer coefficients in Figure 1.10.

The heat transfer coefficients display the usual trend that one would expect for condensation inside plain tubes: it decreases as the condensation proceeds and the vapour quality decreases in the channel. Besides, the heat transfer coefficient increases with mass velocity, implying that condensation must be dominated by shear stress at these operating conditions.

The present database has been compared against predicted heat transfer coefficient calculated from the model by Cavallini *et al*. (2006). This model is a flow regime-based model where all possible operating conditions occurring during condensation in plain tubes are divided in two main regions, depending whether the heat transfer coefficient is ΔT-dependent or ΔT-independent, where ΔT stands for the saturation to wall temperature difference in the channel. Even if the model was not tuned to minichannel heat transfer coefficient, it provides very good prediction of condensation data in minichannel, at least in the ΔT-independent situation (Matkovic *et al.* (2009)). As it can be seen in Figure 1.11, the disagreement between experimental data and predictions is below ±15% for the entire span of mass velocity. It should be pointed out that, regarding to the present database, no data points fall in the ΔT-dependent region, even at 200 kg m^{-2} s^{-1}. Finally, one should consider that such predictions strongly depend on the thermophysical properties, whose determination is still affected by some uncertainty.

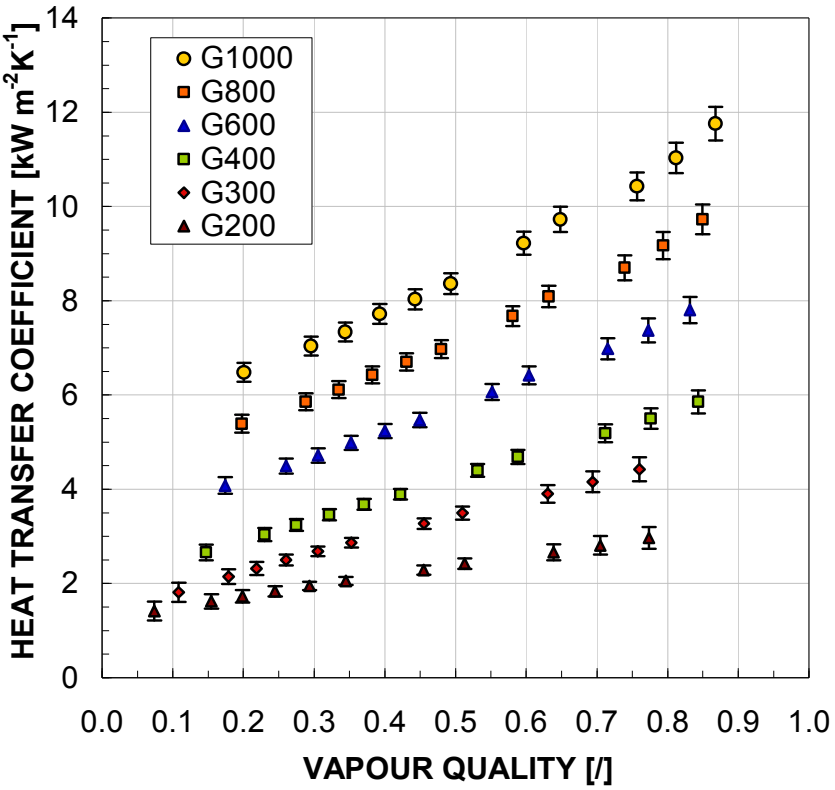

Figure 1.10. Local experimental condensation heat transfer coefficients versus vapour quality for R1234yf at mass velocities ranging from 200 to 1000 kg m^{-2} s^{-1}.

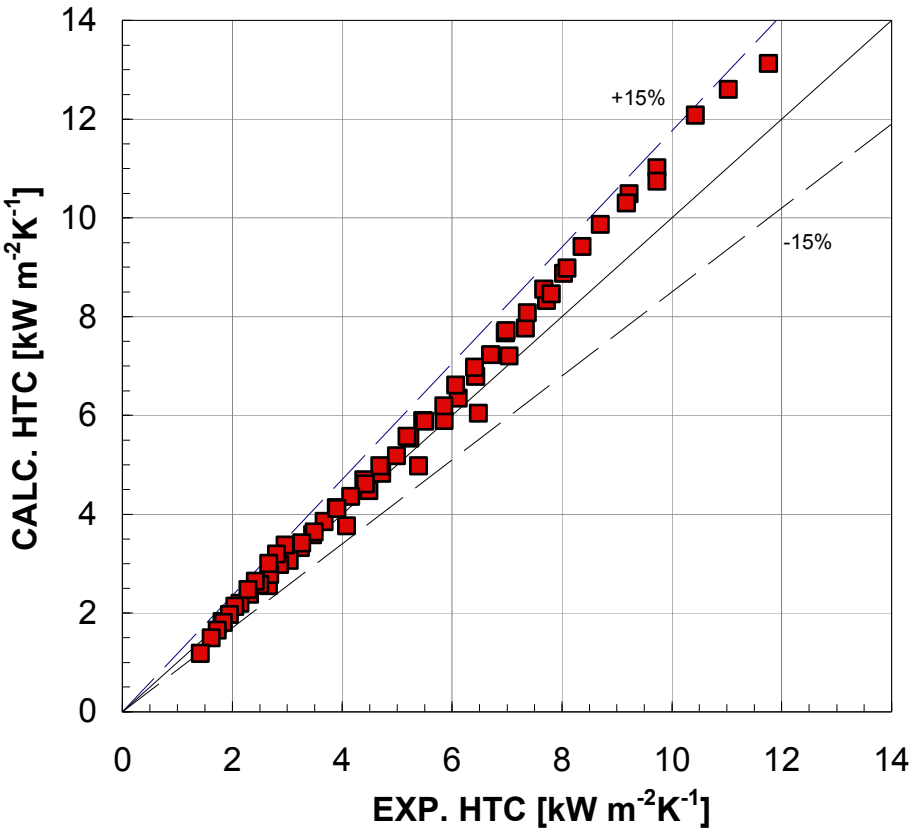

Figure 1.11. Comparison between measurements and calculated (Cavallini et al.(2006)) heat transfer coefficients with R1234yf.

1.4.5.1 Sensitivity to inlet vapour conditions

Since the purpose of the present apparatus is to accurately measure the local heat transfer coefficient, several tests have been run to check repeatability.
Besides, Figure 1.12 shows the experimental heat transfer coefficient measured at 600 kg m^{-2} s^{-1} by imposing different inlet conditions to the refrigerant entering the test section. In the test runs, the refrigerant has been fed at 90% of vapour quality and down to 70% quality: as it can be seen, the local heat transfer coefficient determined in the different test runs perfectly overlaps. That is, the present apparatus provides exactly the same value of the heat transfer coefficient at the same refrigerant conditions, no matter which location this coefficient is measured along the channel.

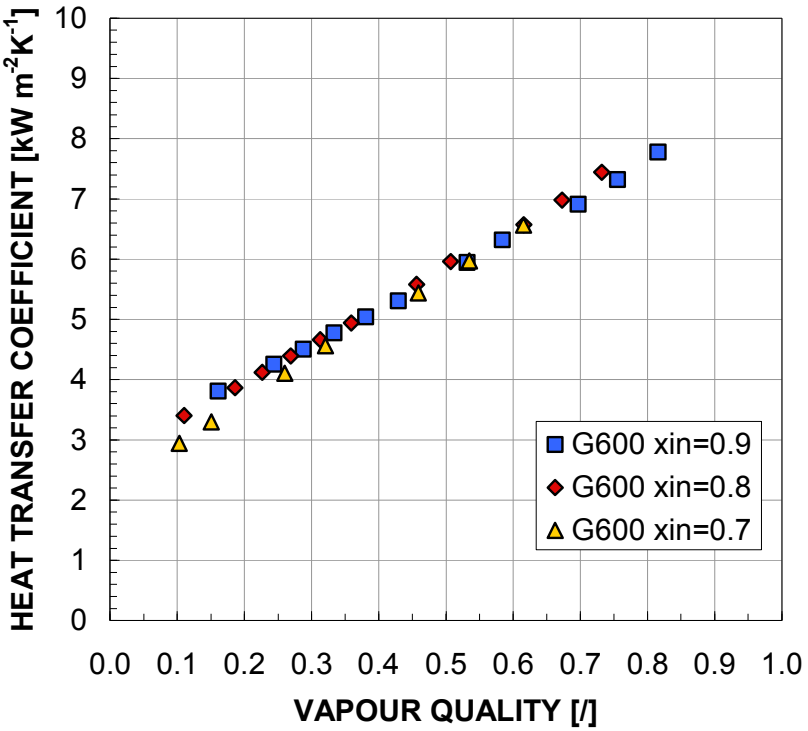

Figure 1.12. Experimental local heat transfer coefficients versus vapour quality for R1234yf at different inlet vapour conditions.

1.4.5.2 Sensitivity to coolant conditions

Some tests have been performed at defined refrigerant conditions varying inlet coolant conditions, to check that the experimental heat transfer coefficients are not sensitive to the coolant situation. Such a study has been conducted at 400 kg m^{-2} s^{-1} mass velocity and 40 °C saturation temperature, varying the inlet coolant temperature from 22 °C up to 29 °C and keeping constant the refrigerant inlet conditions.

Because of the peculiar design of the coolant channel, as previously mentioned, the dominant thermal resistance is on the refrigerant side: therefore, variations of the coolant temperature imply a consequence significant change in the wall temperature and thus in the saturation to wall temperature difference.

From previous investigations by Matkovic *et al.* (2009) with R134a inside the same 0.96 mm diameter channel, it is expect that at 400 kg m^{-2} s^{-1} mass velocity the heat transfer coefficient does not depend on the saturation minus wall temperature difference: the established flow regime is annular for most of the condensation range, and the heat transfer is not significantly affected by gravity while it is shear stress dominated.

The results are plotted in Figure 1.13 showing no effect of the temperature difference in the heat transfer coefficient at 400 kg m^{-2} s^{-1}: this was also expected from previous experiments with HFC refrigerants.

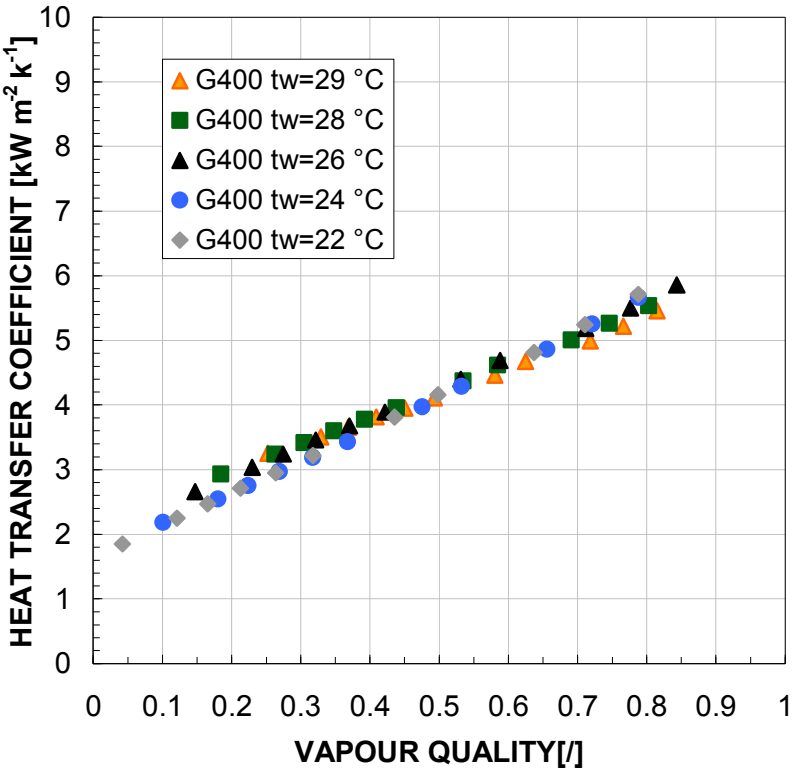

Figure 1.13. Experimental local heat transfer coefficients versus vapour quality for R1234yf at variable inlet water temperatures.

1.4.6 HTC comparison during condensation of R1234yf and R134a

Since R1234yf has emerged as the global replacement refrigerant for R134a in future mobile air conditioning, it is of great interest to compare its heat transfer characteristics with the ones of R134a at the same operating conditions. This is feasible because the heat transfer coefficient during condensation (Matkovic *et al.*, 2009) and pressure drop during adiabatic vapour-liquid flow of R134a (Cavallini *et al.*, 2009) were measured inside the present channel.

In Figure 1.14 the local heat transfer coefficients measured during condensation of R1234yf at 40°C saturation temperature and at three different mass velocities are compared to the ones of R134a at the same operating conditions. Except for the lowest values of vapour quality, R134a displays a heat transfer coefficient higher than R1234yf for all three values of mass velocities.

At 200 kg $m^{-2}s^{-1}$, the heat transfer coefficient of R1234yf is lower than that with R134a by 15% at 0.4 vapour quality and by 30% at 0.8 vapour quality. A similar trend is found at 400 and 800 kg m^{-2} s^{-1} mass velocity.

When comparing the heat transfer coefficient of R1234yf to the one measured for R134a, it can be seen that the latter fluid displays a higher coefficient at the same operating conditions, and this is related to the different properties of the two fluids. Table 1.2 reports saturation properties at 40 °C of R1234yf and R134a: among them, it is particularly interesting to consider the different thermal conductivity of the liquid in the two cases, which affects the thermal resistance in the liquid film. As it can be seen, at 40 °C saturation temperature, the liquid thermal conductivity of R1234yf is lower by 21% as compared to the one of R134a. Properties are calculated using NIST Refprop Version 9.0 (2010).

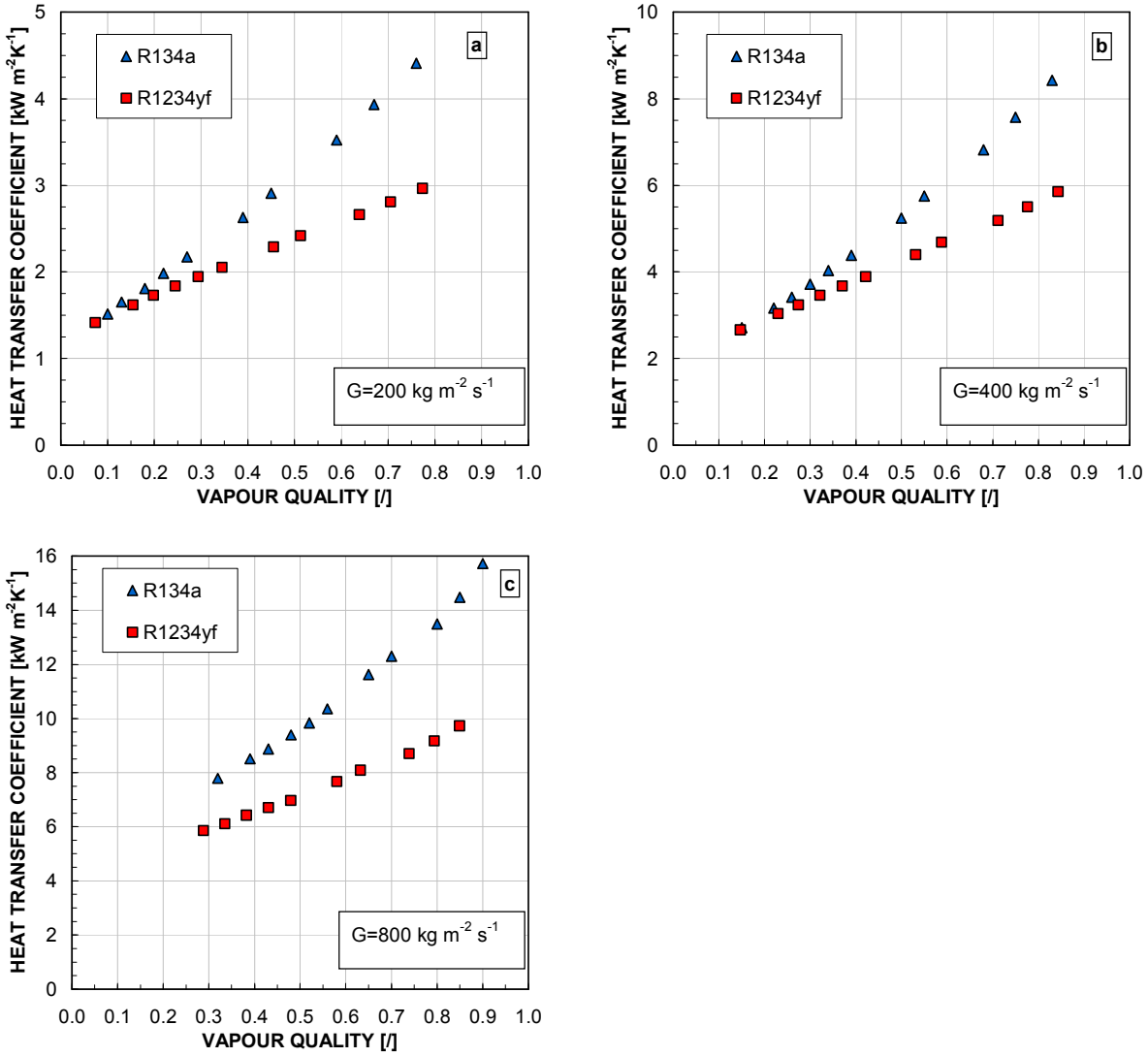

Figure 1.14. Experimental local heat transfer coefficients versus vapour quality for R1234yf and R134a at 200, 400 and 800 kg $m^{-2}s^{-1}$ mass velocity.

Properties	R1234yf	R134a	Difference (%)
Critical pressure [bar]	33.82	40.59	-16.7
Pressure [bar]	10.18	10.17	0.2
Reduced pressure	0.30	0.25	20.2
Liquid Density [kg m^{-3}]	1033.80	1146.70	-9.8
Vapor Density [kg m^{-3}]	57.75	50.09	15.3
Liquid density/Vapour density	17.90	22.90	-21.8
Liquid Enthalpy [kJ kg^{-1}]	254.90	256.41	-0.6
Vapor Enthalpy [kJ kg^{-1}]	387.17	419.43	-7.7
Liquid thermal conductivity [mW m^{-1} K^{-1}]	58.99	74.72	-21.0
Liquid Viscosity [µPa s]	130.00	161.45	-19.5
Vapor Viscosity [µPa s]	13.15	12.37	6.3

Table 1.2. Saturation properties comparison at 40°C between R1234yf and R134a. Properties are calculated using NIST Refprop Version 9.0 (2010).

1.5 Square minichannel

The experimental apparatus reported in Figure 1.1 has been design with the possibility of doing tests in different test section: once they are connected in parallel to each other, it is possible to decide which one to use for the experiments. In the following paragraphs condensation tests which have been done with R1234yf in a square (d_h=1.23 mm) minichannel are presented. This subject is particularly interesting since most of the mini and microchannels used in practical applications do not have circular cross sections.

1.5.1 Description of the experimental section

A new test section has been designed with the aim of investigating the condensation heat transfer inside a square channel (Figure 1.15). The channel is obtained from a copper rod and has a square cross section with 1.18 mm side length. Each corner has a curvature radius equal to 0.15 mm, which leads to a hydraulic diameter equal to 1.23 mm. These dimensions have been checked by means of experimental measurements of the laminar flow friction factor, as detailed in Section 3.3.3.1 The experimental technique adopted here is the same as the one used for the circular channel. In the present test section, the actual measuring sector is made of copper while stainless steel is used for the adiabatic segments before and after the condensing sector. The stainless steel has a much lower thermal conductivity compared to the copper; for this reason, stainless steel rods are used to achieve thermal separation between the desuperheater and the measuring sector and between the measuring sector and the test section outlet. They provide adiabatic sectors where the measurement of the refrigerant temperature can be done with a good accuracy on the outer tube surface. Therefore, copper and stainless steel round rods have been soldered together and then internally holed by electro-erosion to obtain the square channel. The pressure taps at inlet and outlet are also placed in the stainless steel segments. The coolant channel is realized by machining the copper rod to obtain grooves which are the path for the coolant. A sketch of the coolant channel is shown in Figure 1.15. The coolant flows in the grooves and passes from one groove to the following one. The cuts in the copper shown in section A–A and B–B of Figure 1.15 allow allocating thermocouples for the measurement of the water temperature. The thermocouples for the measurement of the wall temperature are placed in the copper fins. The advantages of such a geometry design can be summarized as follows:

– It facilitates accurate measurement of local ‘‘quasi-mixing cup’’ temperatures of the water at low flow rates permitting evaluation of the local heat fluxes.

– It provides improved precision in the evaluation of condensation heat transfer coefficients owing to the large ratio of heat transfer surface areas.

– It allows the insertion of many wall thermocouples without passing through the cooling water, minimizing error due to conduction along the thermocouple wires, and due to spurious emf’s build up for the presence of high temperature gradients in the thermocouples wires.

– During the fabrication process of the test section, the coolant channel in the copper is externally contained by means of a covering made with epoxy resin. This covering film was holed in some places in order to insert the thermocouples for the measurement of the coolant temperature during condensation. Afterwards, other thermocouples have been inserted in the copper fins to measure the wall temperature.

In total more than sixty thermocouples have been placed in the measuring section. The local heat flux can be obtained from the coolant temperature profile while the local heat transfer coefficient is determined from the saturation and wall temperatures.

Furthermore, after the construction, the test section was inserted in a glass cylinder to reduce heat dissipation.

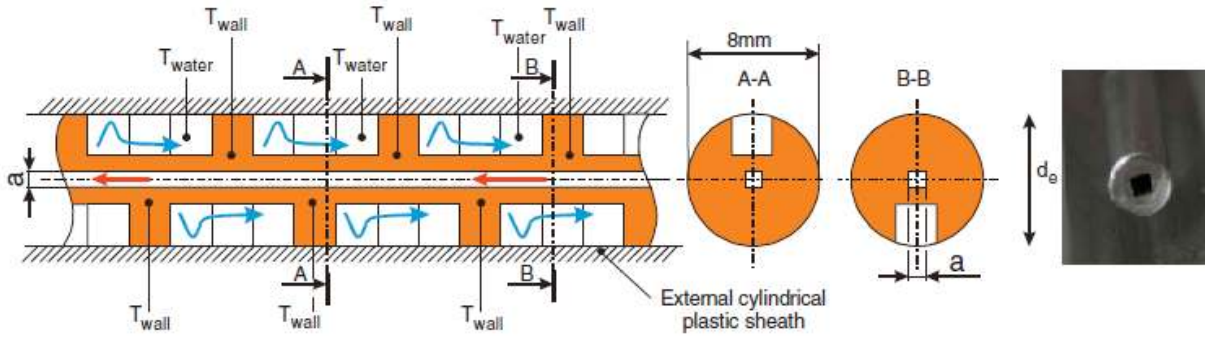

Figure 1.15. Enlarged photo of the square minichannel: water path and cross section detail

1.5.2 Data reduction for condensation tests

Figure 1.16 reports saturation, wall and water temperatures against axial distance from the refrigerant inlet for a test run with R1234yf at 400 kg m^{-2} s^{-1} mass flux. The same graph reports the saturation temperature obtained from the pressure transducers at inlet and outlet and the temperature directly measured in the adiabatic walls upstream and downstream of the condensation length.

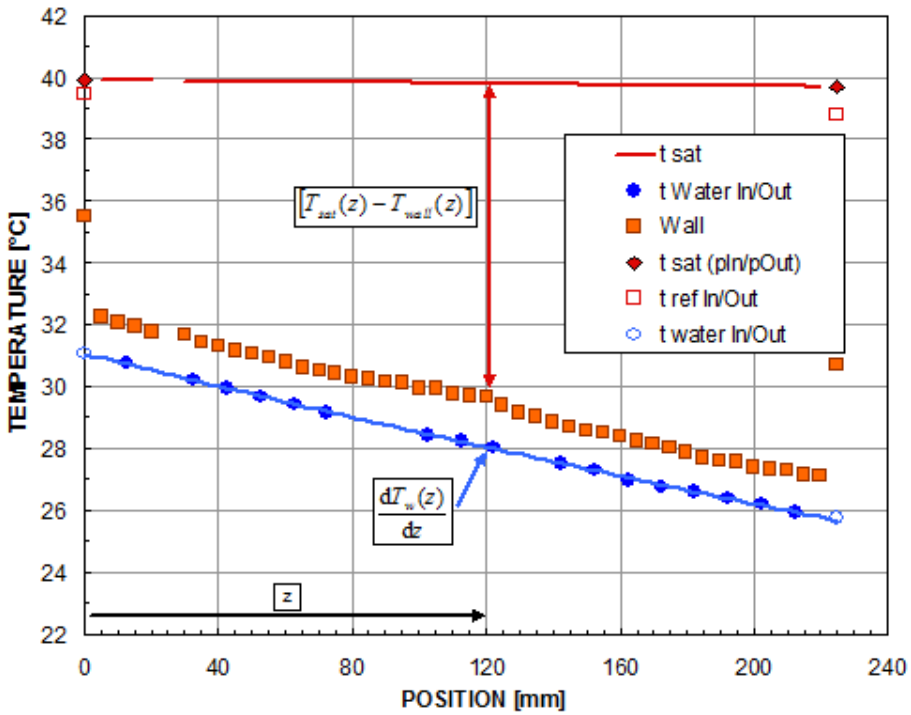

Figure 1.16. Refrigerant, wall and coolant temperature measurements with R1234yf at G = 400 kg m^{-2} s^{-1} along the measuring sector. Symbols refer to local temperature measurements.

The local heat transfer rate per unit length is obtained from the slope of the water temperature profile measured along the channel:

$$q'(z) = -\dot{m}_w \cdot c_{pw} \cdot \frac{1}{p_i} \cdot \frac{\mathrm{d}T_w(z)}{\mathrm{d}z} \tag{1.23}$$

where the internal perimeter of the square minichannel is obtained as

$$p_i = 4 \cdot l - R \cdot (8 - 2 \cdot \pi) \tag{1.24}$$

In the previous equations, z is the axial coordinate along the tube oriented with the refrigerant flow, dTw/dz is the derivative of the polynomial equation interpolating the water temperature along z, l is the side length of the square section and R is the curvature radius. A sensitivity analysis on the fitting equation was performed when the present technique was first implemented (Matkovic *et al.* (2009)) by comparing a polynomial equation to an exponential fitting curve: no significant differences were found and the heat transfer coefficient variation between the two methods was much lower than the experimental uncertainty. Regarding the polynomial degree, it is chosen as the lowest polynomial order which guarantees that all the thermocouples are fitted within the experimental uncertainty of 0.05 K; the polynomial coefficients have been calculated by means of the least square method. It was found that a second order polynomial is able to fit the measured water temperature within the uncertainty band for all the test runs. Using a polynomial order higher than the one used here does not improve the present technique but also leads to higher heat flux uncertainties due to the growing number of coefficients to be determined. It is also possible to calculate the derivative of the equation interpolating the wall temperature, which provides information about the axial conduction along the channel. The local heat transfer coefficient inside the minichannel can be obtained as the ratio of heat flux to saturation minus wall temperature difference:

$$\alpha(z) = \frac{q'(z)}{\left[T_{sat}(z) - T_{wall}(z)\right]} \tag{1.25}$$

It should be pointed out here that the saturation temperature is measured only at the inlet and outlet of the measuring sector and it is obtained from the saturation pressure measurements. Since the difference of saturation minus wall temperature is pretty large for typical test conditions and the saturation temperature drop due to pressure drop is rather small (from 0.05 K at G = 200 kg m^{-2} s^{-1} to 0.8 K at G = 800 kg m^{-2} s^{-1}), for most of the test conditions the saturation temperature along the channel can be derived as a linear trend between inlet and outlet without making a significant error on the heat transfer coefficient. However, because the vapor quality changes during the condensation process, the pressure gradient varies along the channel. Therefore, it would be desirable to plot a saturation temperature curve by implementing a correlation of the two phase pressure gradient and by matching the experimental total pressure drop. The present data are reduced by implementing the correlation of Cavallini *et al.* (2009) for calculating the two-phase pressure gradient along the channel.

The heat flow rate transferred to the secondary fluid up to a certain position z is obtained by integrating the local heat flux q' from 0 (refrigerant inlet) to z

$$q(z) = p_i \cdot \int_0^z q'(z)\,\mathrm{d}z \tag{1.26}$$

The local thermodynamic vapor quality at any location z can be found from the heat flow rate, the mass flow rate, the latent heat and the inlet vapor quality:

$$x(z) = x_{in} - \frac{q(z)}{\dot{m}_r \cdot h_{LG}} \tag{1.27}$$

The vapor quality at the inlet to the measuring sector x_{in} is obtained from the energy balance on the coolant side of the desuperheater (presection). In fact, the specific enthalpy of the superheated refrigerant at the inlet to the pre-section is known from the local pressure and temperature. The

enthalpy variation in the desuperheater is obtained from the heat flow rate transferred in the desuperheater and, in turn, this enthalpy change is used to calculate the vapor quality at the inlet to the measuring sector.
Prior to any test measurements, several actions have been undertaken in order to ensure good accuracy of the experimental apparatus. First, an on-site calibration of the thermocouples installed in the wall and in the water channel has been performed: the calibration procedure consists in determining a correction function for each thermocouple determined by the comparison with a calibrated thermistor probe Pt100, during water circulation under adiabatic conditions in the measuring section.
Another important check has been done to verify the thermal balance in the measuring sector. With a three junction copper-constantan thermopile, the overall cooling water temperature gain has been measured and compared to the one calculated from the integration of the coolant temperature profile.

1.5.3 Calibration procedure and error analysis

Before of any tests, several calibration actions have been undertaken in order to assure the accuracy of the measurements. In particular:

–on site calibration of thermocouples;

–check of agreement between saturation temperature calculated from the pressure and the temperature measured indirectly in the adiabatic sectors under saturated conditions;

–check of thermal balance in the test section and in the measuring sector.

The experimental uncertainties of the measured parameters are reported in Table 1.1. In the case of thermocouples, the reported uncertainty comes from the off-site calibration tests. However, a different successive on-site calibration of the thermocouples installed in the wall and in the water channel has been performed. The thermocouples used in our test section are made with 0.127 mm diameter wire and the junction diameter for front soldering is about the same: the thermocouples are made by means of electrical shortcut with the purpose of reducing the junction diameter. No third material is used for soldering the wires. Those thermocouples are calibrated by circulating water under constant and adiabatic conditions in the channel and using a four wire Thermistor (Standard AS115) with a Hart Scientific Super- Thermometer II. This measuring chain (Thermistor + Super-Thermometer) has a global accuracy of ±0.002 K and was checked against the water triple point. A correction function for each thermocouple is determined from the on-site calibration procedure. At the end of the calibration, the water and wall thermocouples readings are within ±0.02 K of the reference temperature Figure 1.17.

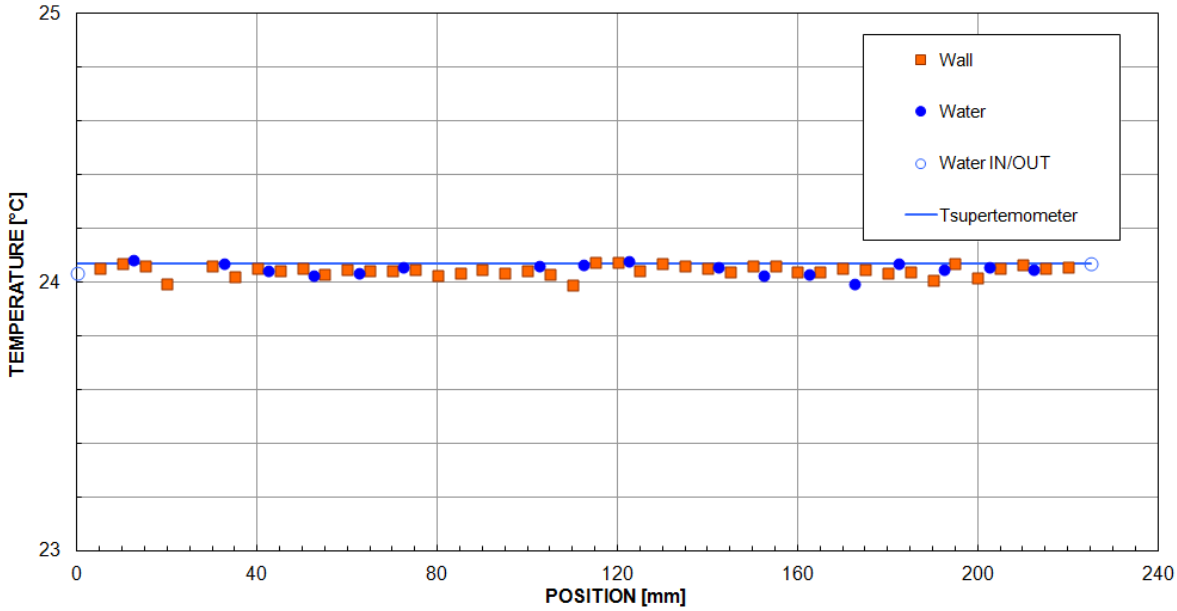

Figure 1.17. Wall and water temperature values recorded after a calibration test. Tsupertermometer is the temperature recorded from a Pt100 inserted in the water inlet pipe.

As a second check of the experimental apparatus, the refrigerant temperature at inlet to the measuring sector is measured during two-phase flow by means of a copper–constantan thermocouple. This temperature is compared to the saturation temperature obtained from the pressure measurement: the disagreement is typically below 0.2 K, which is within the uncertainty range of the two instruments.

The energy balance in the test section is checked by comparing the water side heat transfer rate to the one determined on the refrigerant side when superheated vapor enters the test section and subcooled liquid exits. In this case the agreement found was very good, within 1%.

Prior to collecting measurements, an ad-hoc investigation on the influence of the ambient temperature on measurements has been performed. Since the total heat transfer rate in the pre-section or in the measuring sector may be in the range of a few watts at certain operating conditions, some tests have been performed to check the heat transfer between the water and the ambient air at varying water-to-air temperature difference. This heat dissipation was found to be negligible at low and high refrigerant mass velocities.

Regarding the error analysis, the procedure used is the same previously reported in Paragraph 1.4.3. Combining Eq. (1.23) and Eq. (1.25), the heat transfer coefficient results:

$$\alpha(z) = \frac{-\dot{m}_w \cdot c_{pw} \cdot \dfrac{\mathrm{d}T_w(z)}{\mathrm{d}z}}{p_i \cdot \left[T_{sat}(z) - T_{wall}(z)\right]} = f\left(\dot{m}_w, p_i, \frac{\mathrm{d}T_w(z)}{\mathrm{d}z}, T_{sat}(z) - T_{wall}(z)\right) \tag{1.28}$$

The combined heat transfer coefficient uncertainty was calculated as a function of 4 parameters:

$$u_{\alpha(z)} = \sqrt{\left(\frac{-c_{pw}\cdot\frac{dT_w(z)}{dz}}{p_i\cdot\Delta T_{ref-wall}(z)}\cdot u_{\dot{m}_w}\right)^2 + \left(\frac{\dot{m}_w\cdot c_{pw}\cdot\frac{dT_w(z)}{dz}}{p_i^{\,2}\cdot\Delta T_{ref-wall}(z)}\cdot u_{p_i}\right)^2 + \left(\frac{-\dot{m}_w\cdot c_{pw}}{p_i\cdot\Delta T_{ref-wall}(z)}\cdot u_{\frac{dT_w(z)}{dz}}\right)^2 + \left(\frac{\dot{m}_w\cdot c_{pw}\cdot\frac{dT_w(z)}{dz}}{p_i\cdot\left(\Delta T_{ref-wall}(z)\right)^2}\cdot u_{\Delta t(z)}\right)^2}$$

(1.39)

As it can be seen in Figure 1.18 the percent uncertainty terms associated to the heat transfer area (cross section perimeter) and the temperature difference (T_{ref}-T_{wall}) are pretty uniform along the test section. On the contrary, the uncertainty associated to the heat transfer rate strongly depends on the axial position (with minimum values in the middle of the channel) on mass flux and vapor quality.

The uncertainty of the heat transfer coefficient is estimated as low as 3% in the middle of the test section and it never exceeds 6% for mass velocities higher or equal to 200 kg m^{-2} s^{-1} and vapor quality between 0.15 and 0.9. Only during test condensation at 100 kg m^{-2} s^{-1}and very low vapor quality the uncertainty in the heat transfer coefficient reached 10 %.

The uncertainty can also be calculated for the vapor quality: at low mass velocity (G = 100 kg m^{-2} s^{-1}) the uncertainty associated with vapor quality is equal to ±0.04, whereas at higher mass velocity ($G \geq$ 200 kg m^{-2} s^{-1}it is never greater than ±0.02.

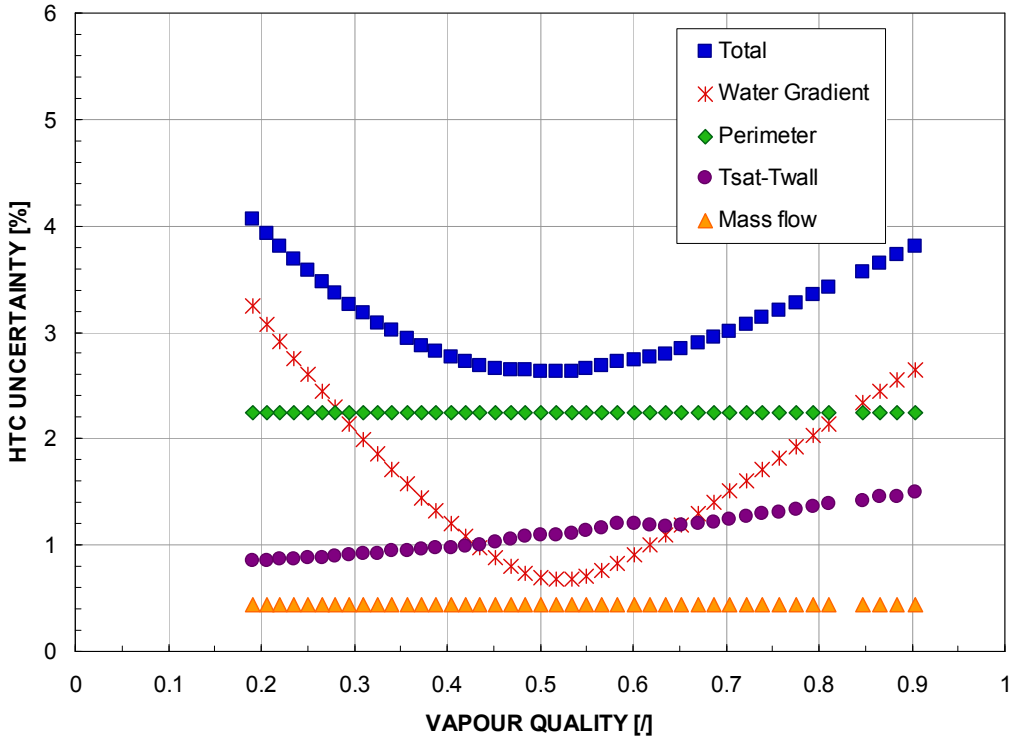

Figure 1.18. Relative heat transfer coefficient uncertainty at G=600 kg m^{-2} s^{-1}

1.5.4 Condensation of R1234yf in the square minichannel

Figure 1.19 reports the experimental heat transfer coefficients measured during condensation of R1234yf at 40 °C saturation temperature, correspondent to 1018 kPa saturation pressure, at mass velocities from 100 to 800 kg m^{-2} s^{-1} over the entire range of vapour quality. Each dot in the diagram corresponds to one experimental value of the wall temperature and is obtained as the ratio of heat flux to saturation minus wall temperature; readings from the first and the last wall thermocouple are not used since they may be affected by axial boundary effects. Furthermore, as it can be seen in Figure 1.19, some values are missing for middle vapour qualities: this is due to the fact that three water thermocouples were not working.
The heat transfer coefficients display the usual trend that one would expect for condensation inside plain tubes: it decreases as the condensation proceeds and the vapour quality decreases in the channel. Besides, the heat transfer coefficient increases with mass velocity, implying that condensation must be dominated by shear stress at these operating conditions.

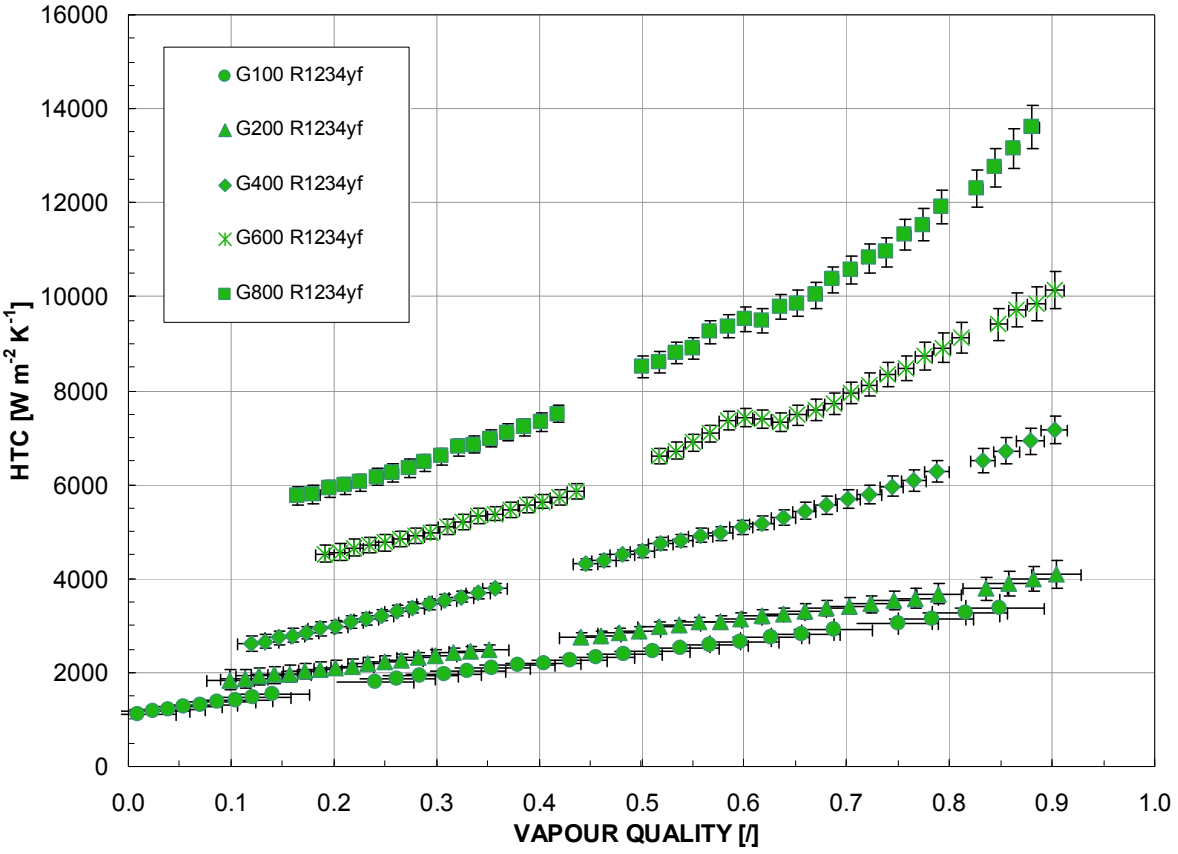

Figure 1.19. Local experimental condensation heat transfer coefficients versus vapour quality for R1234yf at mass velocities ranging from 100 to 800 kg m^{-2} s^{-1}.

1.5.4.1 Comparison with Models

The comparison with seven different models for macroscale condensation is here reported.
The first correlation is the one by Cavallini *et al.* (2003): this model is based on the analogy of heat and momentum transfer. It has been designed for any flow regime and for reduced pressures higher than 0.75. In the present work the value of the reduced pressure is 0.3; nevertheless, as depicted in Figure 1.20, the correlation by Cavallini *et al.* (2003) predicts the present experimental heat transfer coefficients within 20% at mass flux between 200 and 800 kg $m^{-2}s^{-1}$.

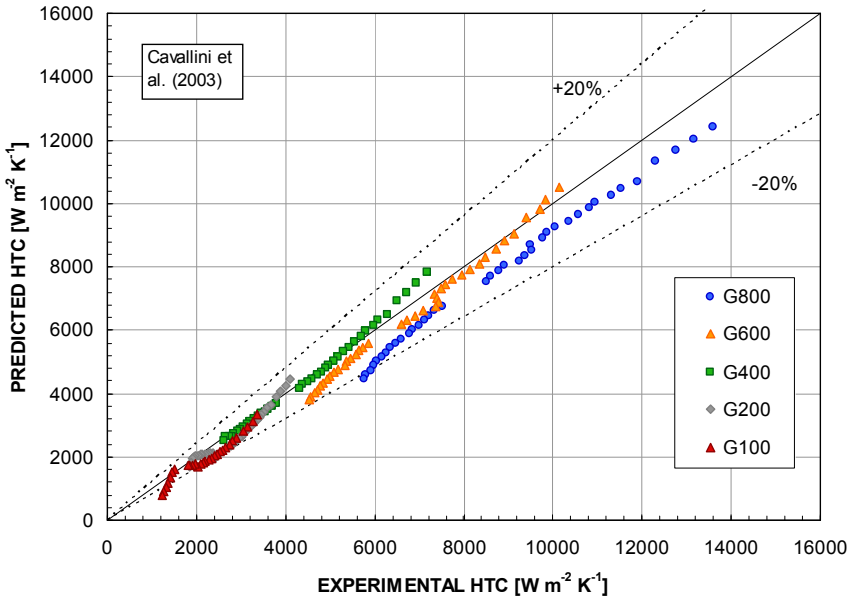

Figure 1.20. Comparison with Cavallini et al. (2003) model

In Figure 1.21 a comparison between experimental HTC and Cavallini *et al.* (2005) model has been presented. All the data at mass velocities grater than 200 kg m^{-2} s^{-1} are well estimated by the model. On the contrary, at lower mass flux the heat transfer coefficients are under predicted on average by 13%: at 200 kg m^{-2} s^{-1} and 42%: at 100 kg m^{-2} s^{-1}. This trend is expected since the correlation for macro scale condensation is not supposed to predict the heat transfer enhancement due to the surface tension in the square minichannel at 200 kg m^{-2} s^{-1} and 100 kg m^{-2} s^{-1}.
The Cavallini *et al.* (2005) model was developed for condensation heat transfer coefficient prediction during condensation of refrigerants inside minichannels. Proper selection of the experimental data has been performed in order to fit the desired range of applicability. The model was designed for annular and annular-mist regime. Systematic underprediction of the experimental results at high dimensionless gas velocities of the previous model (Cavallini *et al.* (2003)) has been adjusted by the introduction of the liquid entrainment. The results relative to square minichannels have been successfully modeled with this model.
The fourth model is the Cavalini *et al.* (2006), which was developed for macroscale condensation inside pipes with hydraulic diameters higher or equal to 3 mm. This model accounts for the transition from ΔT-independent to ΔT-dependent region. As presented later in Paragraph 1.4.5.2, one should expect that the stratified flow region is reduced in the case of minichannel as compared to conventional tubes.

Figure 1.22 reports the comparison between experimental HTC and predicted HTC using the correlation of Cavallin *et al.* (2006): data are underpredicted by this correlation at low and high mass velocity.

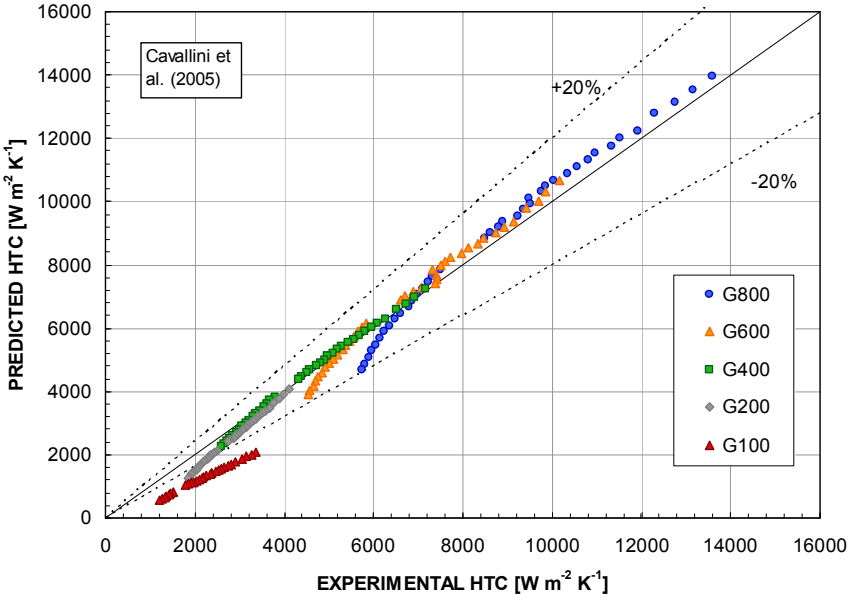

Figure 1.21. Comparison with Cavallini et al. (2005) model

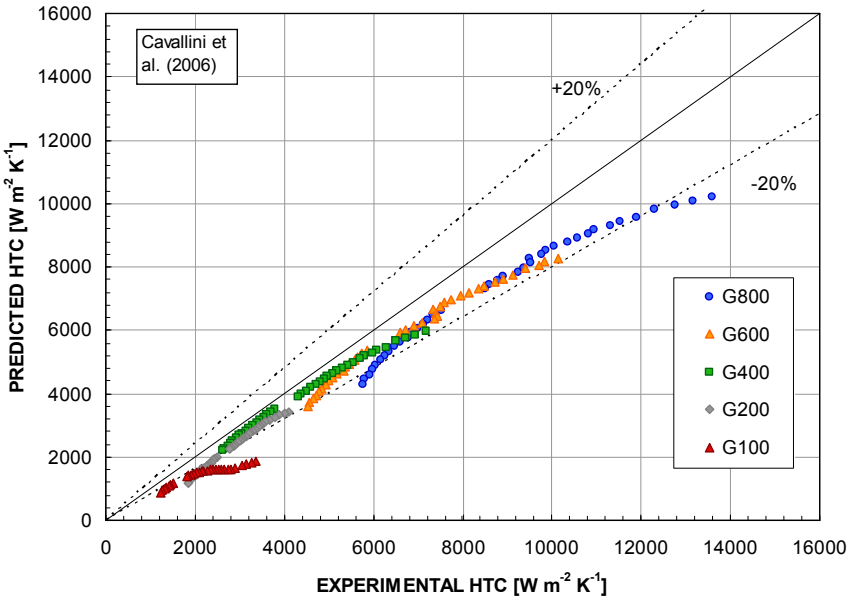

Figure 1.22. Comparison with Cavallini et al. (2006) model

Akers *et al*. (1959) developed a correlation for forced convective condensation within conventional tubes. The comparison between the values predicted by this model and the experimental ones is reported in Figure 1.23: the model underpredicts experimental data on average by 60%: at 100 kg m^{-2} s^{-1} and 40%: at 800 kg m^{-2} s^{-1}.

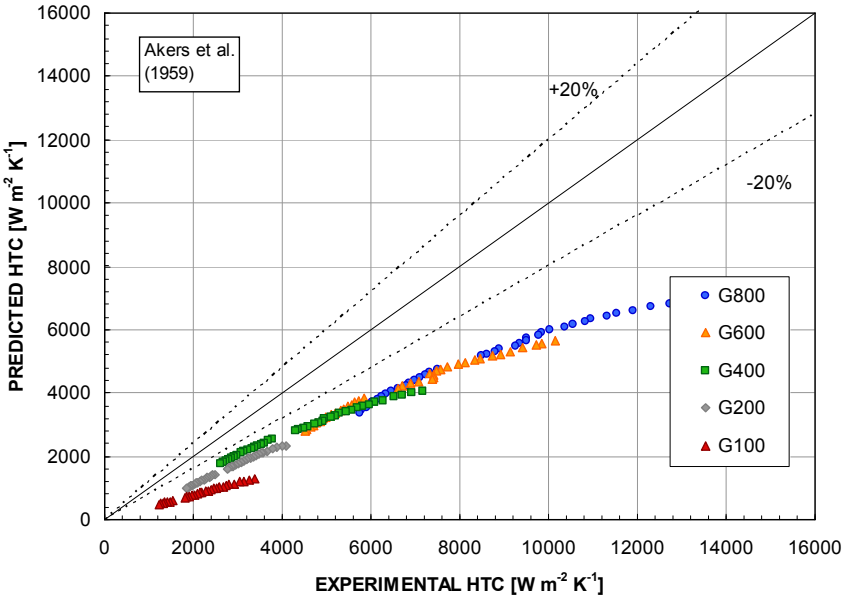

Figure 1.23. Comparison with Akers et al. (1959) model

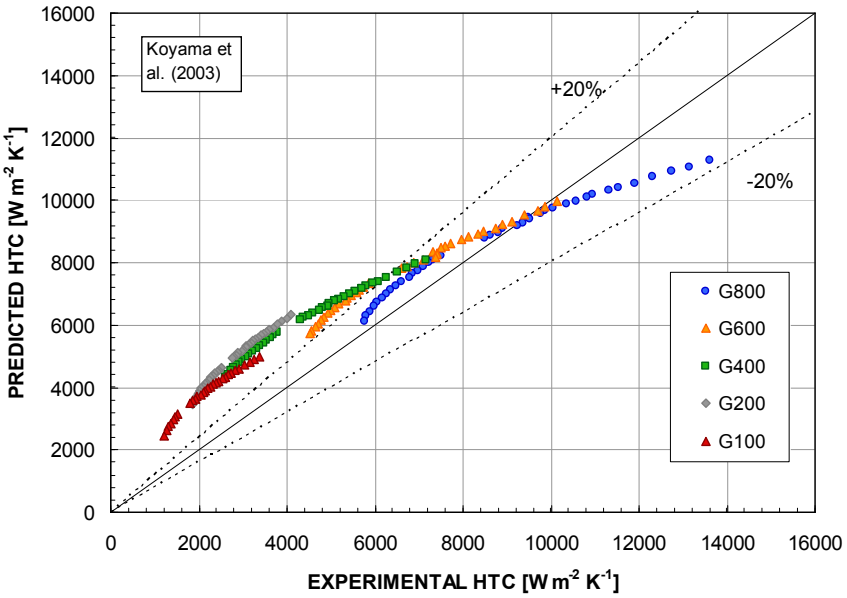

Figure 1.24. Comparison with Koyama et al. (2003) model

The model by Koyama *et al.* (2003), which was developed for minichannels, is used in the comparison presented in Figure 1.24. This model does not give an accurate prediction of the present data, mainly because it is not able to catch the experimental trend of the data versus mass velocity. Also the model proposed by Wang *et al.* (2002) does not catch the trend of the data as reported in Figure 1.25.

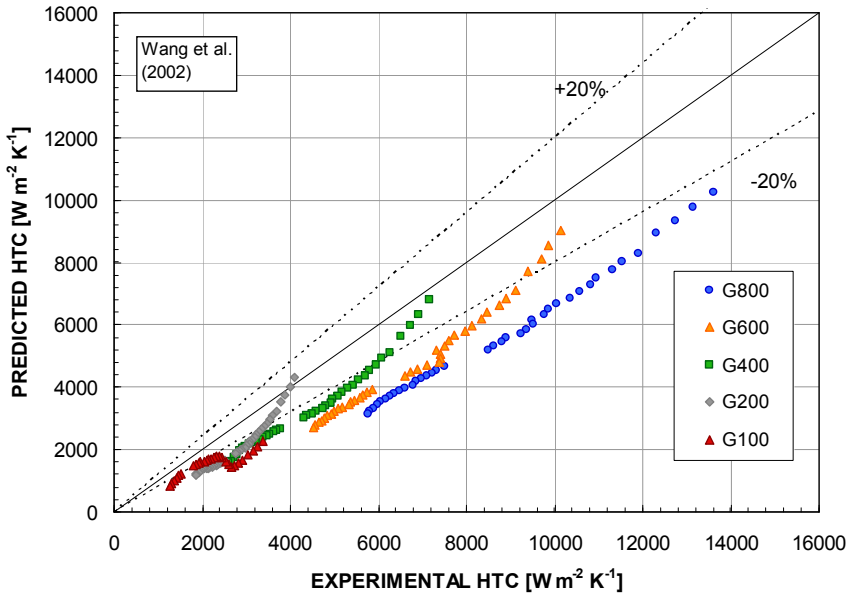

Figure 1.25. Comparison with Wang et al. (2002) model

In Figure 1.26 the predicted heat transfer coefficient is calculated from the model by Moser *et al.* (1998) applied along with the correlation by Zhang and Webb (2001) for pressure gradient in small diameter channels. The correlation, which has been developed for annular flow conditions, is able to catch the experimental trend of data, but it under predicts the data points.

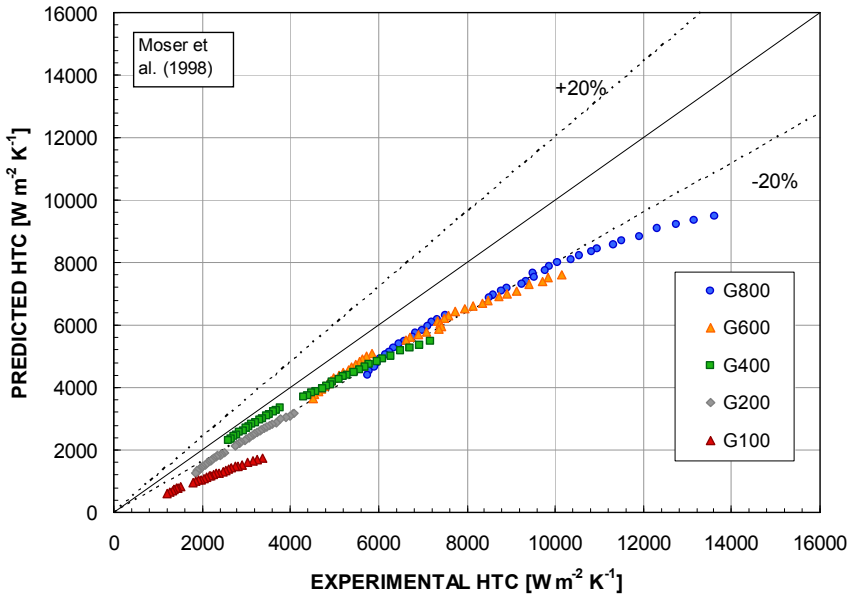

Figure 1.26. Comparison with Moser et al. (1998) model

1.5.4.2 Sensitivity to inlet vapour conditions

Since the purpose of the present apparatus is to accurately measure the local heat transfer coefficient, several tests have been run to check repeatability.
Figure 1.27 shows the experimental heat transfer coefficient measured at 400 kg m^{-2} s^{-1} by imposing different inlet conditions to the refrigerant entering the test section. In the test runs, the refrigerant has been fed at 98% of vapour quality and down to 71% quality: as it can be seen, the local heat transfer coefficient determined in the different test runs perfectly overlaps. That is, the present apparatus provides exactly the same value of the heat transfer coefficient at the same refrigerant conditions, no matter which location this coefficient is measured along the channel.

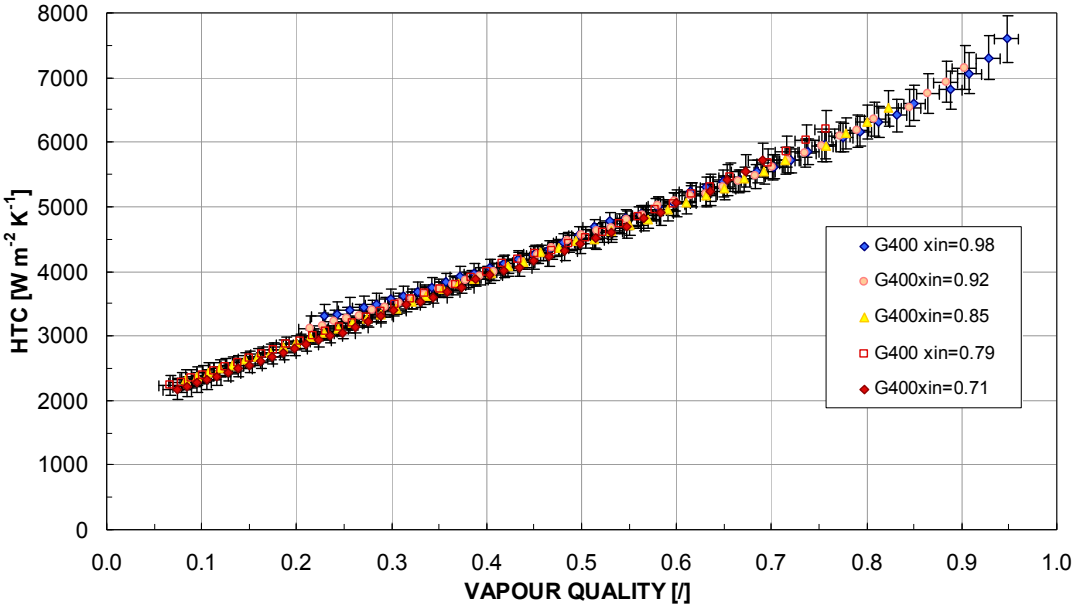

Figure 1.27. Experimental local heat transfer coefficients versus vapour quality for R1234yf at 600 kg m^{-2} s^{-1} at different inlet vapour conditions.

1.5.4.3 Sensitivity to coolant conditions

Figure 1.28 presents the database plotted in the flow pattern map of Cavallini *et al.* (2006). Operating conditions occurring during condensation in plain tubes are divided in two main regions, depending whether the heat transfer coefficient is ΔT-dependent or ΔT-independent, where ΔT stands for the saturation to wall temperature difference in the channel. As it can be seen, only at 100 kg m^{-2} s^{-1} the stratified flow is predicted during condensation tests, while for higher mass velocity the flow regime is annular. This means that the heat transfer coefficients should result independent from the difference between the wall and saturation temperature at mass velocity higher than 100 kg m^{-2} s^{-1}.
Because of the peculiar design of the coolant channel, the dominant thermal resistance is on the refrigerant side and therefore these variations of the coolant temperature imply a consequent significant change in the wall temperature and thus in the saturation to wall temperature difference.

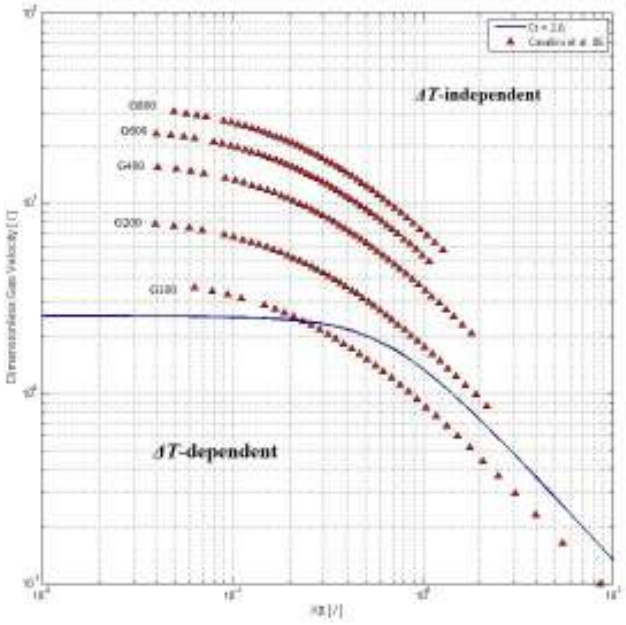

Figure 1.28. Flow regime map of Cavallini et al. (2006) for the refrigerant R1234yf

The heat flux in Figure 1.29 varies between 52 and 21 kW m^{-2} at 0.8 vapor quality and between 36 and 21 kW m^{-2} at 0.3 vapor quality. The results of tests at varying inlet water temperature are plotted in Figure 1.29, showing no effect of the temperature difference on the heat transfer coefficient at 200 kg m^{-2} s^{-1}: the differences among heat transfer coefficient curves are within the experimental uncertainty. These results confirm that the effect of gravity at this mass flux is not significant in comparison with the other forces influencing the condensation heat transfer.

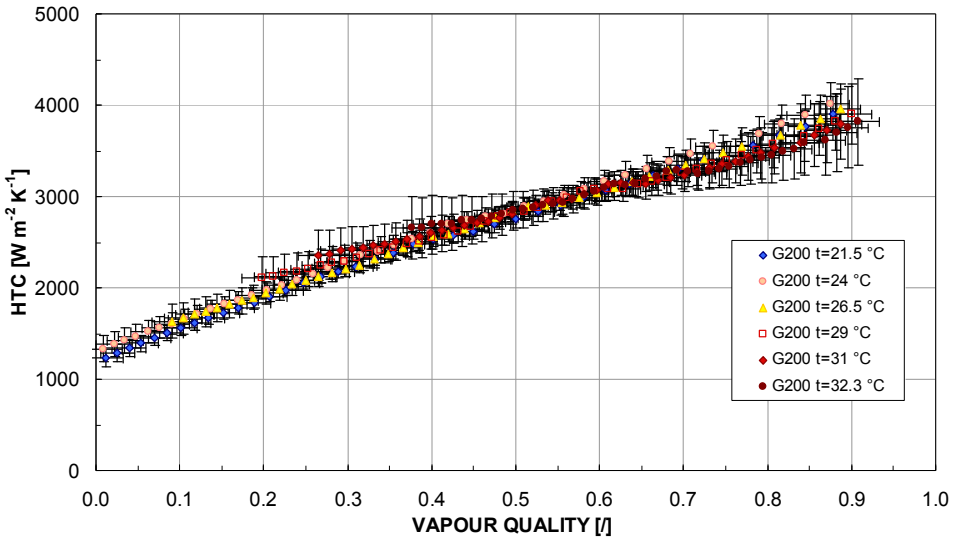

Figure 1.29. Experimental local heat transfer coefficient during condensation of R1234yf at 200 kg m^{-2} s^{-1} when varying the inlet water temperature.

1.5.5 HTC comparison during condensation of R1234yf and R134a

In Figure 1.30 the local heat transfer coefficients measured during condensation of R1234yf at 40°C saturation temperature and at four different mass velocities are compared to the ones of R134a at the same operating conditions. Except for the lowest values of vapour quality, R134a displays a heat transfer coefficient higher than R1234yf for all three values of mass velocities.
At 200 kg $m^{-2}s^{-1}$, the heat transfer coefficient of R1234yf is lower than that with R134a by 20% at vapour quality of 0.2 and 30% at 0.8. A similar trend is found at 400 and 800 kg m^{-2} s^{-1} mass velocity with lower values by 15% and 10% at x=0.2 respectively, and 20% and 15% at x=0.8.

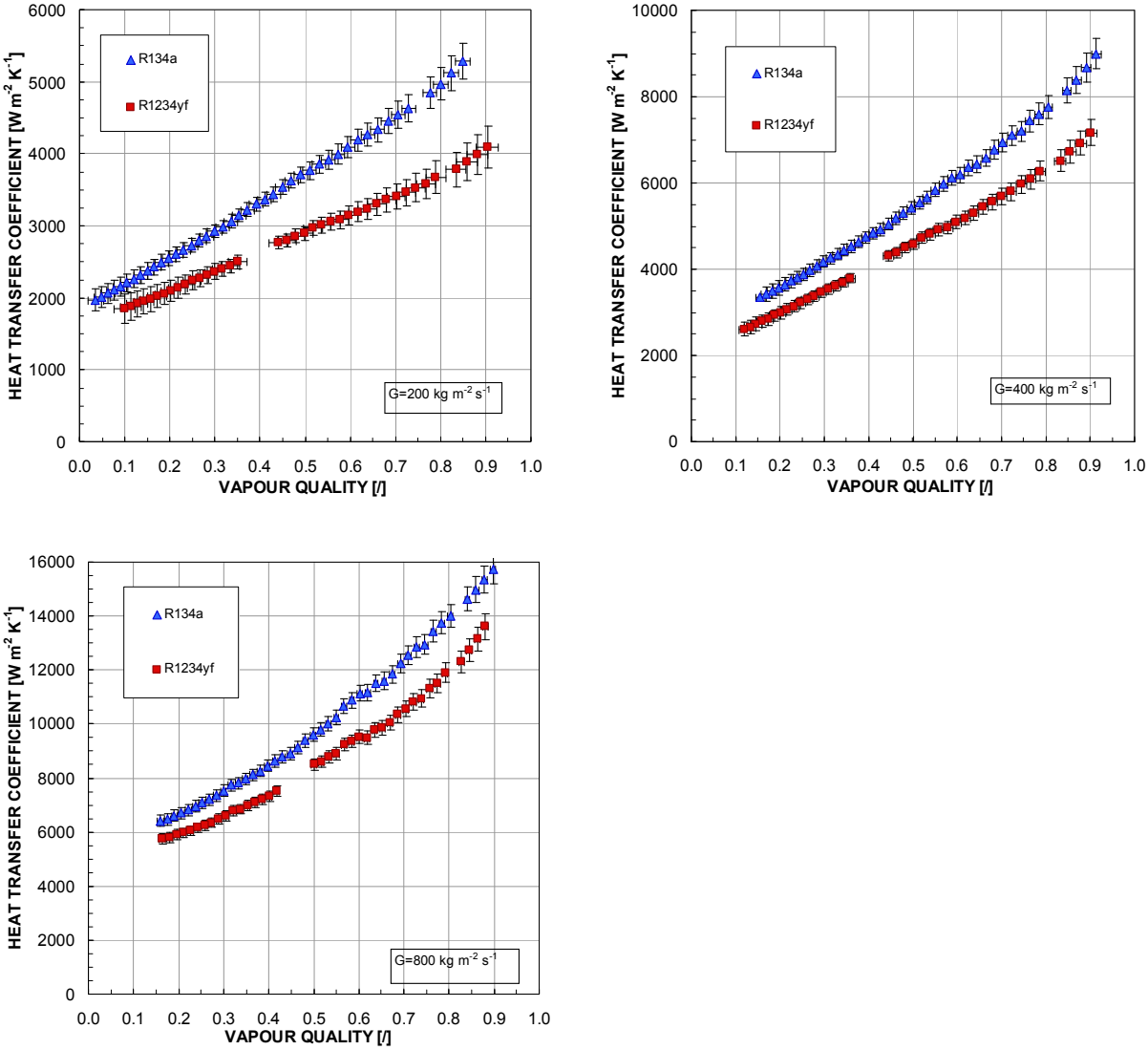

Figure 1.30. Experimental local heat transfer coefficients versus vapour quality for R1234yf and R134a at 200, 400 and 800 kg $m^{-2}s^{-1}$ mass velocity.

2 VAPORIZATION INSIDE MINICHANNELS

2.1 Abstract

In this Chapter, the local heat transfer coefficients measured during flow boiling of R1234yf in a 0.96 mm diameter circular minichannel and a square 1.23 mm hydraulic diameter minichannel are reported. During flow boiling tests, the heat is provided to the boiling fluid by using hot water as a secondary fluid. Therefore the heat flux is not imposed but instead it is the result of the inlet temperatures of the two fluids and the thermal resistances on the two sides, as it occurs in actual heat exchangers for automotive and air-conditioning applications.
Flow boiling tests have been carried out at 31°C saturation temperature and mass fluxes ranging between 200 and 600 kg m^{-2} s^{-1}, in the circular channel and between 200 and 500 kg m^{-2} s^{-1} in the square one.
Data obtained in the circular section with R1234yf are compared to the ones measured with R134a in the same channel at the same operating conditions, displaying roughly the same values. No significant differences between the flow boiling heat transfer performances of R1234yf and R134a have been measured.

2.2 Introduction

Very few data on heat transfer during vaporization of R1234yf have been published so far in the open literature. Park and Jung (2010) measured nucleate boiling heat transfer coefficient of R1234yf and R134a on a flat plain and low fin surfaces. They measured very similar nucleate boiling heat transfer coefficients between the two fluids: test runs conditions were at 7 °C pool temperature, with heat flux varying from 10 kW m^{-2} to 200 kW m^{-2}. Recently Park *et al.* (2011) have also studied R1234yf and R134a condensation on a plain, low fin, and Turbo-C tubes at the saturated vapor temperature of 39°C. Dang *et al.* (2010) have experimentally investigated the boiling heat transfer of the refrigerant R-1234yf, flowing in a smooth horizontal tube with an inner diameter of 2 mm. The test tube was heated by Joule effect, using a DC power supply. The measured heat transfer coefficient of R-1234yf was compared with that of R-134a. The results showed that, in a wide vapour quality region, the difference between the heat transfer coefficient of R-1234yf and R-134a is small. They also studied the effect of mass velocity and heat flux on the heat transfer coefficient, and they observed that heat transfer coefficient increases as mass velocity and heat flux increase. The effect of vapour quality on heat transfer coefficient was also considered, and they observed that heat transfer coefficient increases as increasing vapour quality up to $x \approx 8$; for higher vapour qualities, the heat transfer coefficient decreases. In practical applications, the heat flux may be an independent variable as under Joule-effect heating or it may be a dependent variable when it is transferred from a secondary fluid. However, most of the data available were measured by adopting Joule effect heating and thus by imposing the heat flux.
In the present investigation, vaporization of R1234yf is not performed using electrical heating to promote the boiling heat transfer: the heat is transferred to the evaporating fluid by using a secondary circuit (this is the case of automotive and domestic air conditioning, where the heat is removed from the air). In this way, the inlet temperatures of the two fluids are imposed while the local heat flux comes out as a result (it is a dependent variable).

The heat flux is determined from the temperature profile of the secondary fluid in the measuring sector. The wall temperature is directly measured along the test section and the saturation temperature is measured in the adiabatic segments at the inlet and outlet of the test tube by means of pressure transducers.

2.3 State of the art of convective flow boiling inside minichannels

2.3.1 Flow boiling inside minichannels

Heat transfer realized by flow boiling inside minichannels is one of the main topics in researches about heat transfer. The need of studying this phenomenon derives by the recent applications of electronic industry, which require the dissipation of high thermal fluxes from small areas. Moreover, the electronic devices need their working temperature to be maintained sufficiently low. In a few years the need of heat dissipation has increased from 30 W cm^{-2} to 100 W cm^{-2}, and probably it will reach 300 W cm^{-2} in a short period. The vaporization of refrigerants flowing inside conventional macrochannels, whose diameter range from 6 to 20 mm, cannot achieve these performances: it allows exchanging about 6 W cm^{-2}.
Cooling through vaporization of a refrigerant in a minichannel heat sink allows compactness, minimal refrigerant usage, high heat transfer coefficients (especially at low vapour qualities) and a constant temperature dictated by the coolant saturation temperature. For these reasons, a worldwide study aims at determining the methods to design and optimize minichannels heat sinks.
So far, the studies that have been carried out about vaporization inside minichannels have shown that the models which properly describe this phenomenon in the macroscale are not able to predict the same data as the channel diameter decreases. The same thing happens for the maps that describe the flow regimes. Beside this, despite of many recent researches about flow boiling in minichannel, the amount of available data in literature is still slight with regard to the wide range of applications of flow boiling inside minichannels. Moreover, a general agreement about the mechanisms involved in the heat transfer phenomena in the microscale has not been reached yet.
In practical applications of flow boiling inside minichannels, the exchanged heat flux can be an independent variable as well as a dependent variable. Heat flux is an independent parameter when heat is supplied through Joule effect, while it is a dependent parameter when heat is provided by a secondary fluid. The first case is typical of electronic applications, while the latter case is typical of cooling systems like air-conditioning in vehicles.
Most of the available data in literature deals with vaporization in minichannels in the case of heating through Joule effect, therefore with imposed heat flux. On the contrary, literature data dealing with flow boiling under conditions of non-imposed heat flux are only a few. Such type of data is obtained by measuring heat flux by means of an energy balance on a secondary fluid. However, most of these data is gained by using multiple parallel minichannels, so that the heat transfer coefficient, which is indirectly measured, represents only a mean value for all the parallel minichannels, and it does not give any information about the single minichannel.

2.3.2 Classification of minichannels

In flow boiling through channels, as the channel size decreases to approach the bubble diameter, physical confinement begins to modify the influence of the different governing forces, resulting in different behavior of boiling in minichannels compared to that in conventional-size channels.

Kandlikar and Grande (2003) classified channels basing merely on their dimensions and not on the physical behavior. They called "macrochannels" those channels with hydraulic diameter greater than 3 mm; "minichannels" those channels with hydraulic diameter between 3 and 0.02 mm; "microchannels" those channels with hydraulic diameter smaller than 0.02 mm.
Kew and Cornwell (1997) proposed a criterion for a threshold hydraulic diameter below which the two-phase flow in microchannels is characterized by confined bubbles; the available models for macroscale boiling were found to be unsuitable for the prediction of heat transfer and pressure drops at these small channel sizes. According to them, for hydraulic diameters lower than d*, the two-phase flow is confined:

$$d^* = \sqrt{\frac{4 \cdot \sigma}{g \cdot (\rho_l - \rho_g))}} \tag{2.1}$$

where ρ_l is the liquid density [kg m^{-3}], ρ_g the vapour density [kg m^{-3}], σ the surface tension [N m^{-1}] and g the acceleration of gravity [m s^{-2}].
Our test runs are performed by keeping the saturation temperature of the refrigerant at the constant value of 31°C. Thus, using R-1234yf, d^*=1.47 mm, while using R-134a, d^*=1.61mm. So, according to this criterion, our channels, that have an inner diameter of 0.96 mm and 1.23 mm, are considered as a minichannel, since the vaporization process is affected by confinement effects.
Harirchian and Garimella (2010) observed that a confinement criterion should consider mass flux as well as hydraulic diameter and fluid properties.
The Bond number represents the ratio of buoyancy forces to surface tension forces, and becomes important in microscale boiling. It is defined as follows:

$$Bo = \frac{g \cdot (\rho_l - \rho_g)) \cdot d^2}{\sigma} \tag{2.2}$$

where d is the hydraulic diameter of the channel.
According to Harirchian and Garimella (2010), for channels of small cross-sectional area and at low mass fluxes, vapour confinement is observed, while for larger microchannels and at high mass fluxes, the flow is not confined. They proposed a distinctive criterion based on the convective confinement number:

$$Bo^{0.5} \cdot \mathrm{Re} = \frac{1}{\mu_l} \cdot \left(\frac{g \cdot (\rho_L - \rho_G)}{\sigma} \right)^{0.5} \cdot G \cdot d^2 \tag{2.3}$$

where G is the mass velocity [kg m^{-2} s^{-1}], μ_l is the dynamic viscosity of liquid [Pa s] and Re is the Reynolds number. This new flow boiling transition criterion recommends that for $Bo^{0.5} \cdot Re$<160, vapour bubbles are confined and the channel should be considered as a microchannel (see Figure 2.1). For larger convective confinement numbers, the flow does not experience physical confinement by the channel walls and the channel can be considered as a conventional (macroscale) channel (Harirchian and Garimella (2010)).

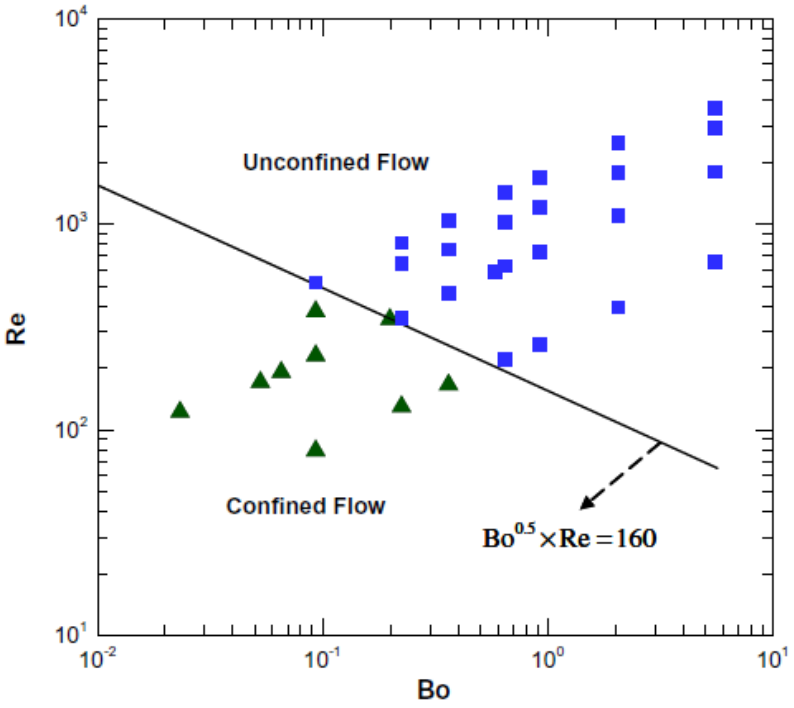

Figure 2.1. Transition from unconfined to confined flow (Harirchian and Garimella (2010)).

Since the inner diameter of the circular channel is 0.96 mm and since G varies between 200 and 600 kg m^{-2} s^{-1} the vaporization test runs presented below (at 31°C saturation temperature), the convective confinement number ranges from 1730 to 5190 if R-1234yf is used and from 1260 to 3790 in the case of R-134a. Thus, according to this criterion, vapour bubbles are not confined in our circular channel, which can be considered as a conventional channel. The same is for the square channel: in the range 200-500 kg m^{-2} s^{-1} of the specific mass flux, the convective confinement number ranges from 2809 to 7023 if we use R-1234yf

2.3.3 Flow regimes

Cornwell and Kew (1992) conducted experiments with R-113 flowing in 1.2 × 0.9 mm rectangular channels. They observed three flow patterns, which are illustrated in Figure 2.2:

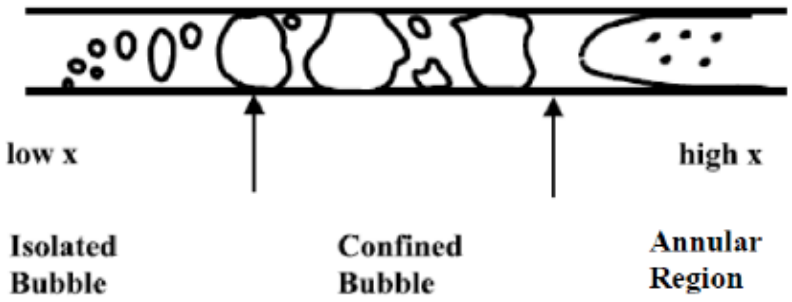

Figure 2.2. Flow patterns observed by Cornwell and Kew (1992).

In the isolated bubble region was found that $HTC=f(q^{0.7})$, indicating the dominance of nucleate boiling. When the bubble occupied the entire cross-section in the confined bubble region, the dependence of the heat transfer coefficient on heat flux decreased: the convection effects were dominant in the annular-slug region.

Kasza *et al*. (1997) studied the nucleation activity in a rectangular channel of 2.5×6 mm cross-section with the aid of a high speed video camera. They observed vapour slugs separated from the wall by a thin liquid film with a 0.67 mm average thickness (see Figure 2.3). Nucleation was observed in this liquid film. They noticed that the heat transfer in the thin liquid film underneath the bubbles improved the heat transfer. They concluded that the increased bubble activity at nucleation sites in the thin liquid film is responsible for high heat transfer coefficients in minichannels.

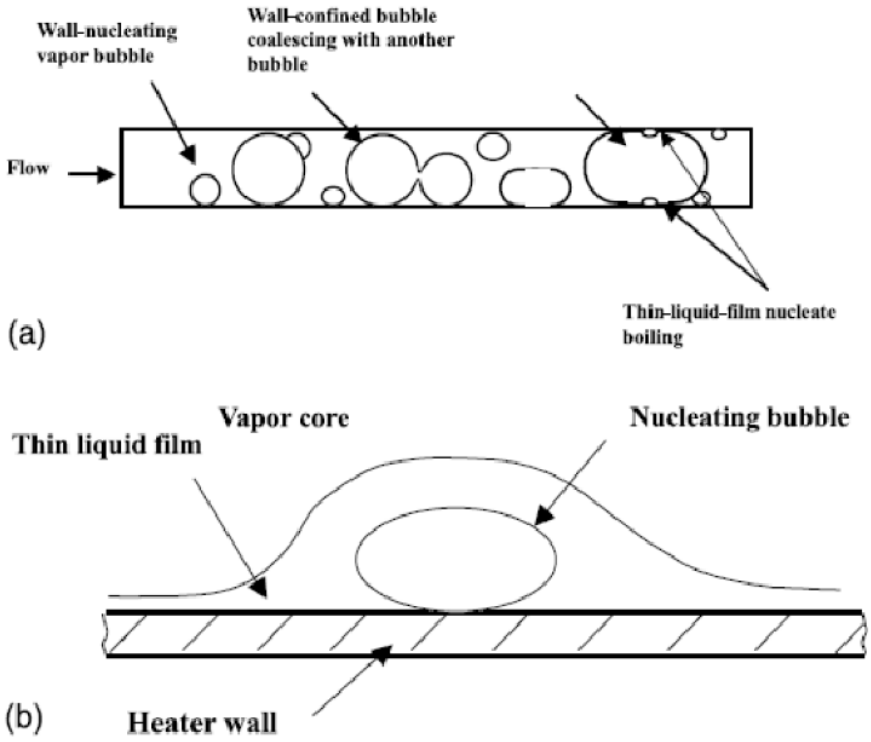

Figure 2.3. Flow patterns and bubble nucleation observed by Kasza et al. (1997): (a) flow patterns, (b) bubble nucleation in the thin liquid film under a vapour slug.

Thome and Consolini (2010) studied the flow patterns during vaporization inside minichannel and found four main regimes: bubbly flow (at very low vapour qualities), slug flow (describing the passage of long bubbles separated by liquid slugs), churn flow (a transition mode between slug flow and fully annular flow), annular flow (occurring at the highest gas superficial velocities).

However, Harirchian and Garimella (2009), who observed boiling flow patterns via highspeed visualizations in parallel microchannel of widths ranging from 0.1 to 5.85 mm, all of 0.4 mm in depth, described five main flow regimes: bubbly, slug, churn, wispy-annular, and annular flows were identified. A post-dry-out regime of inverted-annular flow was also identified. Representative images of these six flow regimes are illustrated in Figure 2.4; a sketch of the flow pattern is added on the right side of each image.

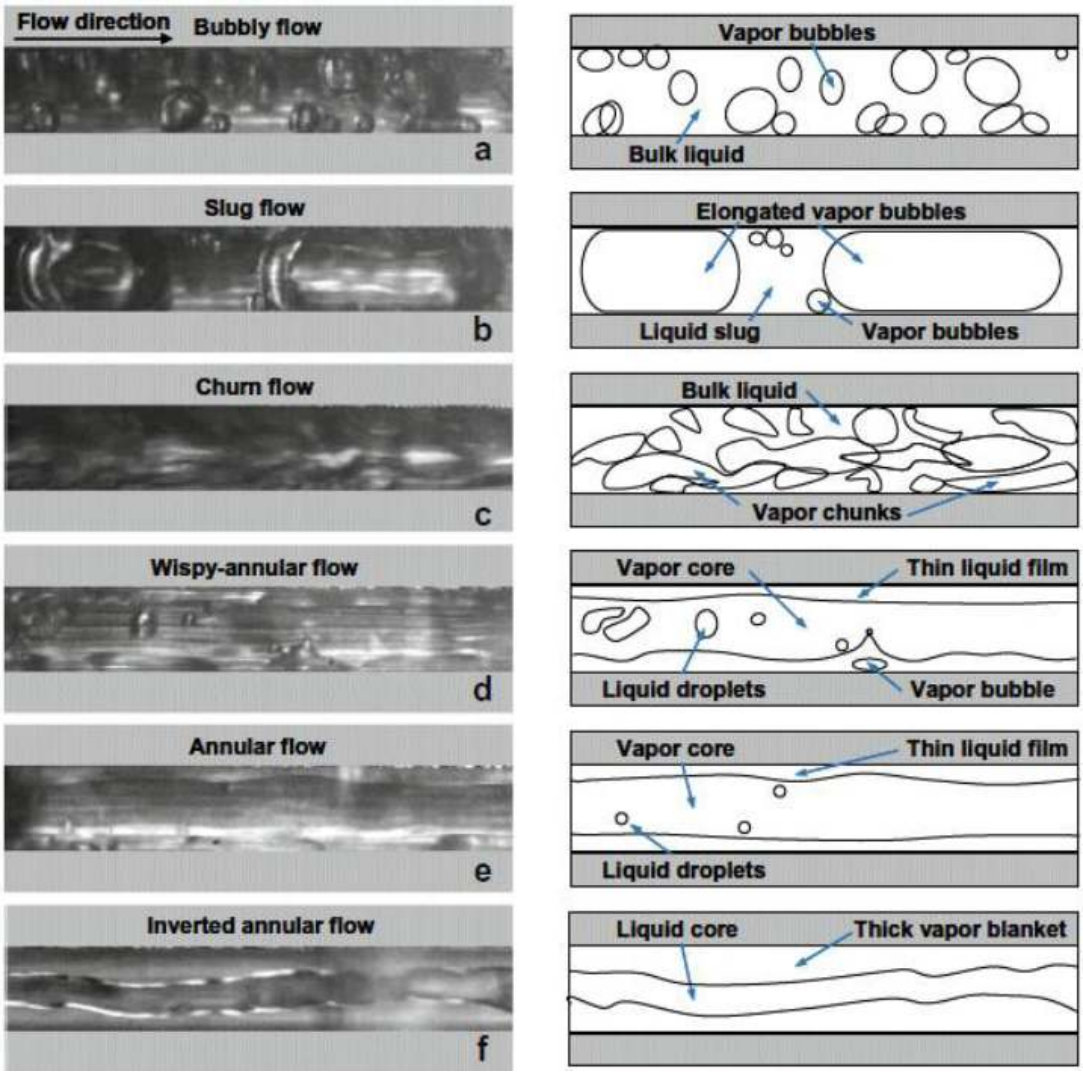

Figure 2.4. Description of boiling flow regimes. This figure is taken from Harirchian and Garimella (2009).

Figure 2.4a shows bubbly flow: isolated round and elongated bubbles that are smaller than the minichannel cross-section can be seen. Bubbles generally nucleate at the microchannel walls and detach after growing. As the heat flux increases, or as the vapour quality increases, the bubble generation rate at the walls increases and bubbles become larger as a result of coalescence between bubbles. At higher heat fluxes or vapour qualities, or in smaller minichannels, bubbles occupy the entire cross-section, resulting in slug flow as shown in Figure 2.4b; small bubbles exist in the liquid slugs between the elongated bubbles. The churn flow regime is illustrated in Figure 2.4c. It consists of vapour chunks moving downstream and large bubbles nucleating at a high rate; however, at high heat fluxes, the nucleation at the walls may be suppressed. In wispy-annular flow, as shown by Figure 2.4d, a vapour core is separated from the channel walls by an unstable liquid film. Large, irregular droplets are entrained into the vapour core. Very few nucleation sites remain in the liquid film and produce small vapour bubbles in the liquid layer. In annular flow (Figure 2.4e), the liquid layer is thinner than in wispy-annular flow, and the interface between the vapour core and the liquid film can become wavy. The liquid film thickness decreases as the heat flux increases, or as the vapour quality increases. Small, round droplets are entrained into the vapour core, while no vapour bubbles are observed in the liquid film. At very high heat fluxes, when critical heat flux is reached,

the walls can completely dry out under certain conditions and a vapour blanket forms at the walls around a liquid core flowing through the centre of the minichannel. This flow regime is called inverted-annular flow (Figure 2.4f) and is to be avoided since it involves a sudden rise in the wall temperature and a significant drop in the heat transfer coefficient.
Harirchian and Garimella (2010) developed a comprehensive flow regime map basing on two non-dimensional parameters: the convective confinement number $Bo^{0.5}\cdot Re$ and the product $B_l\cdot Re$ where B_l is called boiling number:

$$B_l = \frac{q}{G \cdot h_{lv}} \tag{2.4}$$

where q is the specific heat flux [W m^{-2}] and h_{lv} is the latent heat of vaporization [J kg^{-1}].
This map distinguishes four regions: confined slug flow, churn/confined annular flow, bubbly flow and churn/annular/wispy-annular flow. It is plotted in Figure 2.5. The vertical transition line is given by $Bo^{0.5}\cdot Re=160$, which represents the transition from unconfined to confined flow. The other transition line is given by:

$$B_l \cdot \mathrm{Re} = 0.017 \cdot \left(B_0^{\ 0.5} \cdot \mathrm{Re}\right)^{0.7} \tag{2.5}$$

This means that, for low heat fluxes ($B_l\cdot R_e<0.017\cdot(B_o^{0.5}\cdot Re)^{0.7}$), flow patterns of slug (if $B_o^{0.5}\cdot Re<160$) or bubbly (if $B_o^{0.5}\cdot Re>160$) flow exist in the microchannels. At higher heat fluxes ($B_l\cdot R_e>0.017\cdot(B_o^{0.5}\cdot Re)^{0.7}$) vapour bubbles coalesce, resulting in a continuous vapour core in the alternating churn/annular or churn/wispy-annular flow regimes.

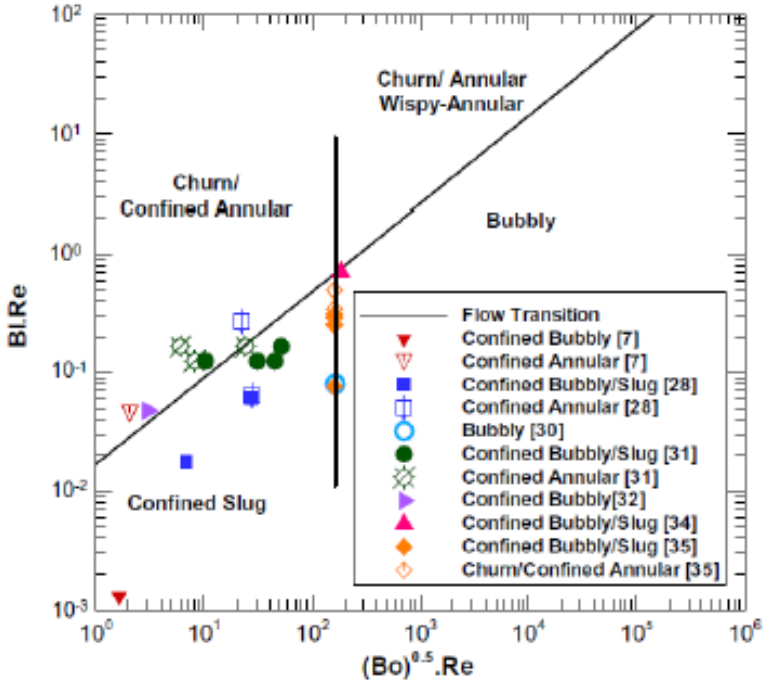

Figure 2.5. Comparison of the comprehensive flow regime map with the experimental data from literature. This diagram is taken from Harirchian and Garimella (2010). It shows experimental points from a wide database of observations of flow regimes coming from different authors.

2.3.4 Mechanisms of heat transfer during flow boiling inside minichannels

An important purpose of studies on two-phase heat transfer is to understand the mechanisms that control the flow boiling process.
The earliest results of Lazarek and Black (1982), who investigated flow boiling of R-113 in a single vertical tube of 3.1 mm diameter, showed that the heat transfer coefficient was not affected by vapour quality, but was a function of heat flux. This led them to conclude that nucleate boiling was the dominant heat transfer mechanism, as in macroscale flow boiling.
Cornell and Kew (1992) affirmed that nucleate boiling dominates in the isolated bubble region, while convective effects dominate in the annular flow region.
Wambsganss *et al.* (1993) conducted experiments of flow boiling with R-113 in a 2.92 mm diameter tube. They found that heat transfer coefficients were sensitive both to heat flux and mass velocity. This indicates the contributions from both nucleate boiling and convective boiling mechanisms.
Tran *et al.* (1996) studied R-12 flow boiling in circular and rectangular channels both of 2.46 mm hydraulic diameter. Convective boiling was found to be dominant at lower wall superheats, and nucleate boiling at higher wall superheats. Their data showed that, for a sufficiently high wall superheat (above 2.75 °C) the heat transfer coefficient was unaffected by vapour quality and mass velocity but increased significantly with heat flux.
Thome and Consolini (2010) affirmed that, during slug flow, nucleate boiling is completely suppressed and heat is transferred primarily by conduction through the thin evaporating film surrounding the elongated bubbles. They developed a *three-zone* flow boiling model wich is based on this assumption, producing a physical-based alternative to the models derived from Chen's superposition model (Chen (1966)). These models (as the one proposed by Zhang *et al.* (2004)) share the same structure: the heat transfer coefficient is estimated as sum of two contributes: the nucleate boiling term, which is dominant at low vapour qualities, and the convective vaporization term, which is dominant at high vapour qualities.
Thome and Consolini (2010) summarize the mechanisms of heat transfer during flow boiling as follows: (i) in bubbly flow, nucleate boiling and liquid convection would appear to be dominant; (ii) in slug flow, the thin film evaporation of the liquid film trapped between the bubble and the wall and convection to the liquid and vapour slugs between two successive bubbles are the most important heat transfer mechanisms; (iii) in annular flow, laminar or turbulent convective evaporation across the liquid film should be dominant.

2.3.5 Heat transfer coefficient measurements in flow boiling inside minichannels

Several studies have been reported in the recent years on vaporization in microchannels. Some experimental studies show that the heat transfer coefficients obtained during vaporization in microchannels, are not a function of vapour quality nor mass velocity (in contrast with the macro-channel trend), but are a function of heat flux and saturation pressure (Kandlikar (2004), Thome (2004b), Thome (2006)). Other experimental studies demonstrate that the heat transfer coefficient also depends on vapour quality and mass velocity. Some experimentalists conclude that flow in small channels is dominated by nucleate boiling while forced convection evaporation is less important. Instead, Thome (2004) suggests that transient evaporation of the thin liquid films surrounding elongated bubbles is the dominant heat transfer mechanism. Lee and Mudawar (2005) reported a list of studies on this matter showing that researchers are divided into two groups. The first group shares the view that nucleate boiling is dominant and therefore dictates overall heat transfer inside the channel. A second group shares the observation that the local heat transfer coefficient is a function of vapour quality and mass velocity in addition to heat flux. Of course, the

understanding of dominant mechanisms during flow boiling in mini-channels is the fundamental basis for the development of an accurate predicting method. In addition, the heat transfer during vaporization may depend on the surface quality. In fact, surface roughness is a key parameter affecting nucleation; and it also affects the thickness of the liquid films surrounding elongated bubbles as demonstrated by Thome (2004b). However there is still a lack of experimental results regarding the effect of surface roughness in microchannel flow boiling. Harirchian and Garimella (2008) investigated the local flow boiling heat transfer of a dielectric fluid, Fluorinert FC-77, in a microchannel heat sink. In this study seven different test pieces consisting of parallel microchannels with widths ranging from 100 to 5850 μm and a depth of 400 μm are considered; experiments are performed for heat flux up to 300 kW m-2. The results show that for microchannels of a width grater then 400 μm, the heat transfer coefficient at a fixed heat flux are independent of channel size. Also heat transfer coefficients are independent of mass flux in nucleate boiling region; when convective boiling dominates, the heat transfer coefficient increases with increasing mass flux.
Bertsch *et al*. (2009) studied flow boiling heat transfer with the refrigerants R134a and R245fa in copper microchannel cold plate evaporators. Arrays of microchannels of hydraulic diameter 1.09 and 0.54 mm are considered with an aspect ratio of the rectangular cross section equal to 2.5. The heat transfer coefficient is measured at saturation temperature ranging from 8 to 30 °C, mass flux from 20 to 350 kg m^{-2} s^{-1}, and heat flux from 0 to 220 kW m^{-2}. It was found that heat transfer coefficient vary significantly with heat flux and vapour quality, but only slightly with saturation pressure and mass flux. They found that, for R-245fa, at a fixed heat flux, the heat transfer coefficient increases up till a vapour quality of 0.1; then it stays almost constant up to a vapour quality of 0.5 before it starts to drop-off more rapidly towards higher vapour qualities. A different trend was found by Consolini and Thome (2009) during flow boiling of R245-fa in a single microchannel of 510 μm internal diameter with heat flux ranging from 0 to 110 kW m^{-2}. The heat transfer coefficient appears to be sensitive to heat flux only up to intermediate vapour qualities, beyond which the data points for different values of heat fluxes merge and exhibit a monotonic increase with vapour quality. Shiferaw *et al*. (2009) recently published flow boiling experiments in a 1.1 mm tube inside diameter using R134a; the parameters were varied in the range: mass flux 100-600 kg m^{-2} s^{-1}; heat flux 16-150 kW m^{-2} and pressure 6-12 bar. In their data, the heat transfer coefficient increases with heat flux, but does not change with vapour quality when the quality is less than about 30 to 50%. For vapour quality values greater than 50% and at high heat flux, the heat transfer coefficient decreases with vapour quality. According to Thome and Consolini (2010), a significant number of studies found decreasing curves in the plane, and even some increasing trends.

2.4 Flow boiling of R124yf in the circular minichannel

2.4.1 Experimental apparatus

The experimental apparatus used in the present study was designed and realized to measure local heat transfer coefficients during phase change with a secondary fluid, as it occurs in common refrigeration and air-conditioning applications. The test rig used for the experimental tests is depicted in Figure 2.6. It is the same already described in Chapter 1 but the operative conditions durig vaporization tests is different. In fact, the fluid is pumped through the Coriolis-effect mass flow meter into the test section as a subcooled liquid. Then it enters the test section, which is made of two counter-flow heat exchangers: the first one (pre-section) is used to achieve desired inlet subcooling and the second one is the actual measuring sector.

The pressure is gauged through two digital strain gauge pressure (absolute and differential) transducers, connected to manometric taps to measure the fluid pressure upstream and downstream of the test tube.
Two refrigerated thermal baths are used in the flow boiling tests: the first one provides the hot water entering the measuring section, the second one provides the coolant for the postcondenser. When necessary, the water entering the presection can be maintained at a different temperature through an additional electrical heater.

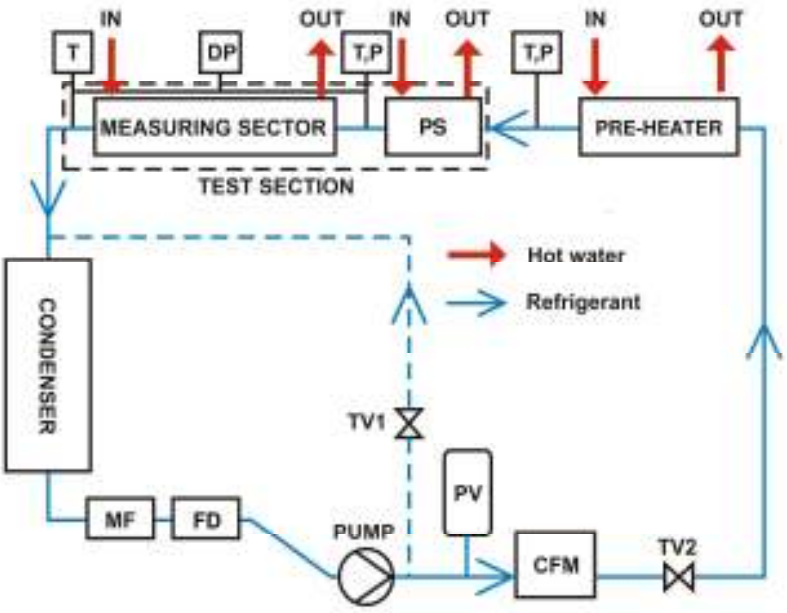

Figure 2.6 Experimental test-rig. (PS.=presection, MF=mechanical filter, FD= filter drier, PV=pressure vessel, CFM=Coriolis-effect mass flow meter, TV=valve, P=pressure transducer, T=thermocouple, DP=differential pressure transducer).

The test section is designed for measurement of local two-phase heat transfer coefficients by measuring the local wall temperature and the water temperature profile along the channel. Therefore, the measuring sector is equipped with a high number of thermocouples, both in the wall and in the water.
The thermocouples embedded in the wall are installed in 0.6 mm diameter cylindrical holes, machined 0.5 mm far from the internal tube surface.
The measuring sector is thermally separated from the pre-section and the exit tube through adiabatic stainless steel capillary tubes.
The water flow rates, in the pre-section and in the measuring section, are measured by means of two Coriolis-effect mass flow meters and the total temperature difference of water across both sectors are measured with two multiple junction copper-constantan thermopiles.

2.4.2 Data reduction

In the present setup, the heat flux is determined from the temperature profile of the coolant in the measuring sector. The wall temperature is measured by means of 11 thermocouples embedded in the copper tube. The saturation temperature is directly measured in the adiabatic segments at the inlet and outlet of the test tube, by means of a T-type thermocouple and a four-junction thermopile, soldered to the stainless steel adiabatic capillary tubes.

Figure 2.7 reports refrigerant, wall and water temperature measurements along the measuring sector during flow boiling of R1234yf at mass velocity G = 500 kg m^{-2} s^{-1}. The refrigerant enters the test channel at 32.8 °C saturation temperature with 5.2 K subcooling. At the exit, saturation temperature is decreased of 1.6 K due to pressure drop. The water enters from the opposite side of the test tube at 38.7 °C and its temperature decreases due to the heat transfer to the boiling refrigerant. As the vaporization proceeds, the wall temperature increases uniformly up to the end of the test section. 0 also shows the standard deviation of the temperature measurements in the wall (each temperature measurement is the average value of fifty readings taken in fifty seconds): those deviations are pretty much the same in the channel.
The local heat flux (q') is determined from the temperature profile of the coolant in the measuring sector. Since the heat flux is not fixed, it must be obtained indirectly, from the slope of the secondary fluid temperature profile:

$$q'(z) = \dot{m}_w \cdot c_{p,w} \cdot \frac{1}{\pi d_i} \frac{\mathrm{d}t_w}{\mathrm{d}z} \tag{2.6}$$

where z is the axial coordinate along the tube and dtw/dz is the derivative of the water temperature along z. A polynomial function is used to interpolate the water temperature profile along the channel and the polynomial coefficients are determined using the minimum square method.

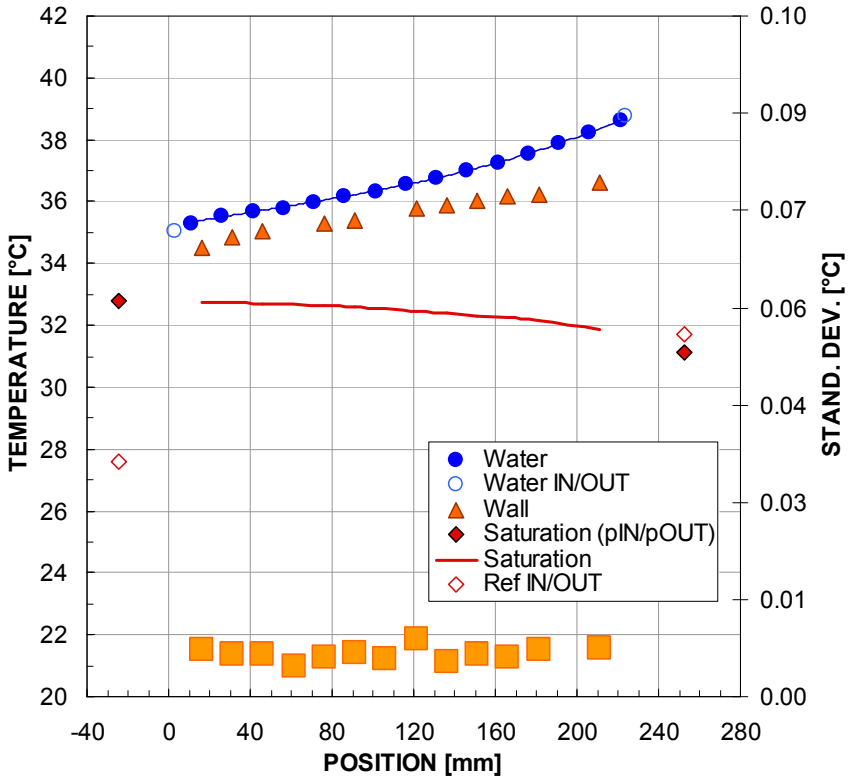

Figure 2.7. Water, wall and saturation temperature during a boiling process of R1234yf in the 0.96 mm diameter channel at G = 500 kg m^{-2} s^{-1}. The big square dots represent the standard deviation of the wall temperature measurements.

Two different independent procedures have been adopted for the determination of the fitting polynomial equation of the water temperature and thus the calculation of the heat flux (Eq. 2.6). The first criterion, dubbed as physical, is based on the assumption that all the calculated values by the polynomial interpolation of the water temperatures should be below ± 0.05 °C with respect to

the experimental values, and 68% of the predicted values should be inside the ± 0.03 °C prediction boundary. Beside this, a statistical method based on the choice of the simplest fitting polynomial have been used. This statistic approach uses the R^2 statistic parameter, and adjusts it on the basis of the residual degrees of freedom: this is the reason of the name R^2_{adj} (Rawlings *et al.*, (1998)).
For the 68% of tests, the two methods have given the same grade for the interpolation polynomial. In the remaining 32% of cases, the HTC values have been taken into consideration only when the disagreement between the two methods is below 10%.
Once the heat flux is known, the local heat transfer coefficient inside the microchannel is obtained as the ratio of heat flux to temperature difference:

$$HTC(z) = \frac{q'(z)}{\left[t_{wall}(z) - t_{sat}(z)\right]} \tag{2.7}$$

The wall temperature (t_{wall}) is measured by means of thermocouples embedded in the copper tube. The saturation temperature (t_{sat}) is the local value in the exact position where the wall temperature is measured and the heat transfer coefficient is determined. The saturation temperatures at inlet and outlet are obtained from the pressure measurements. During vaporization, the vapor quality changes along the microchannel and therefore the pressure gradient varies in the measuring sector; for this reason, a linear interpolation of the saturation temperature between inlet and outlet may lead to errors in the determination of the heat transfer coefficient. Instead, in the present work the pressure is measured at inlet and outlet of the channel and the pressure profile along the microchannel is calculated by implementing the Cavallini *et al.* (2009) two-phase pressure gradient correlation. The calculated total pressure drop is corrected multiplying it by a factor, in order to match the total pressure drop to the value measured by the differential pressure transducer. The vapor quality x at any axial position z is obtained from:

$$x = \frac{q - \dot{m}_r \cdot (h_{SL} - h_{sub})}{\dot{m}_r \cdot h_{LG}} \tag{2.8}$$

as a function of the total heat flow rate q up to that location, the specific enthalpy of saturated liquid (h_{SL}), the specific enthalpy of the subcooled liquid (h_{sub}) and the latent heat (h_{LG}). The enthalpy of the subcooled refrigerant is determined from the inlet pressure and temperature, while the total heat flow rate transferred to the refrigerant is obtained by integrating the local heat flux *q'* from 0 (refrigerant inlet) to *z*.

$$q = \pi \cdot d_i \cdot \int_0^z q' \,\mathrm{d}z \tag{2.9}$$

2.4.3 Error analysis

An uncertainty analysis on the heat transfer coefficient was performed. The experimental uncertainty is made up by two parts: the first component is the type A uncertainty that derives from repeated observations, the second one is type B uncertainty that derives from instruments calibration and manufacturer's specifications.
Type B experimental uncertainties of the measured parameters are reported in Table 2.1. In the case of thermocouples, the reported uncertainty comes from the off-site calibration tests. However, additional on-site calibrations of the thermocouples installed in the wall and in the water channel have been carried out, in order to improve the accuracy of the measurements. The thermocouples calibration is performed by means of two thermistors (Standard AS115) coupled with a Hart Scientific Super-Thermometer II. This measuring chain (Thermistor + Super-Thermometer) has a global accuracy of ±0.002 K.

Temperature	± 0.05 °C (on-site calibration)
Temperature difference	± 0.03 K (thermopile)
Water flow rate	± 0.15 % of flow rate
Refrigerant flow rate	± 0.25 to ± 0.35 % of flow rate
Absolute pressure	± 5 kPa
Pressure difference	± 0.1 kPa

Table 2.1. Type B experimental uncertainty of measured parameter.

The major contribution to the experimental uncertainty of the heat transfer coefficient is due to the uncertainty associated with the heat flux, which in turn depends on the uncertainty of the water temperature gradient. The other components of the overall uncertainty are associated with the wall to saturation temperature difference, the hydraulic diameter and the refrigerant mass flow rate.
The uncertainty associated with the channel diameter is determined from an enlarged image of the microchannel obtained by a microscope. The diameter uncertainty, that includes dimensional and geometric tolerances, is equal to ±0.02 mm. Fluid properties have been calculated using NIST Refprop Version 9.0 (2010); in particular Refprop 9.0 implements for refrigerant R1234yf the Equation of State by Richter *et al*. (2011).
All the experimental measurements (temperature, pressure, mass flow rate) are taken as a mean value of 50 readings with a time step of 1 s.
In the case of a temperature measurement, for instance, the average value and the standard deviation for n=50 repeated observations will be expressed as reported below:

$$\bar{t} = \frac{1}{n}\sum_{k=1}^{n} t_k \tag{2.10}$$

$$s(t) = \sqrt{\frac{1}{n-1}\sum\nolimits_{k=1}^{n}\left(t_k - \bar{t}\right)} \tag{2.11}$$

According to the ISO Guide to the Expression of Uncertainty in Measurement (1995), the Type A standard uncertainty is given by the experimental standard deviation of the mean as follows:

$$u(t) = s(\bar{t}) = \frac{s(t)}{\sqrt{n}} \tag{2.12}$$

Similarly, the average values, the standard deviations and the related uncertainties can be calculated also for the pressure and the mass flow rate.
When the searched parameters are not directly measured, it is necessary to know the function linking each parameter to measured quantities. As an example, in the case of the heat transfer coefficient *α(z)*, the function is:

$$\alpha(z) = \frac{\bar{q}(z)}{\pi d_i\left[t_{wall}(z) - t_{sat}(z)\right]} = \frac{\dot{m}_w c_{p,w}\dfrac{\mathrm{d}t_w(z)}{\mathrm{d}z}}{\pi d_i\left[t_{wall}(z) - t_{sat}(z)\right]} = f\left(\dot{m}_w, \frac{\mathrm{d}t_w}{\mathrm{d}z}, t_{sat}, t_{wall}, d_i\right) \tag{2.13}$$

As a first step, the Type A and Type B uncertainty of each measured parameter (water flow rate, water temperature gradient, saturation and wall temperatures, channel perimeter) must be determined.
The combined standard uncertainty $u_c(\alpha)$ on the heat transfer coefficient is obtained by combining appropriately the Type A and Type B standard uncertainties of each measured quantities xi and then by propagating the experimental uncertainty associated to each term (Eq. 2.15):

$$\alpha = f\left(x_1, x_2, .., x_5\right) \tag{2.14}$$

$$u_c(\alpha) = \sqrt{\sum_{i=1}^{5} \left(\frac{\partial f}{\partial x_i} \right)^2 u^2(x_i)} \tag{2.15}$$

The expanded uncertainty on the heat transfer coefficient U_M is obtained by multiplying the combined standard uncertainty $u_c(\alpha)$ by a coverage factor k=2 with an interval having a level of confidence of approximately 95%.

$$U_M = k\, u_c(\alpha) \tag{2.16}$$

As it can be seen from Eq. (2.13), the heat transfer coefficient uncertainty is essentially independent on the refrigerant properties, since the only refrigerant parameter requested to determine the heat transfer coefficient is the saturation temperature, which can be determined from the pressure and also checked with direct measurement.

The components of the overall uncertainty are associated with the water temperature gradient, the wall-to-saturation temperature difference, the hydraulic diameter and the refrigerant mass flow rate.

The average experimental uncertainty associated with the heat flux can be estimated equal to ±5% and the mean uncertainty associated with the wall minus saturation temperature difference is ±6%; the experimental uncertainty of the heat transfer coefficient is within ±10% for 80% of the data points.

2.4.3.1 Temperature gradient uncertainty

The procedure that has been implemented for determining the uncertainty related to temperature gradient is the weighted least square – WLS (Press *et al.* (2007)) regression method.

The water temperatures t_w for each test run have been fitted to a n-degree polynomial; the form of this polynomial is given by the following equation:

$$t_w(z) = \sum_{j=0}^{n} a_j z^j \tag{2.17}$$

where a_k are the polynomial coefficients that minimize the merit figure χ^2. In Eq. (2.18) z_i is the i-th axial location along the channel at which water temperature is measured; i ranges between 1 to m_{bd}, where m_{bd} is the number of water thermocouples before dryout and it assumes the maximum value m_{bd} = 15 if dryout does not occur (e.g. z_1 = 16 mm, z_{15} = 220 mm). In the Eq. (2.18) $t_{w,i}$ is the water temperature measured at the i-th location, and $u_i(t_w)$ is the experimental uncertainty associated with water temperature at the i-th location.

$$\chi^2 = \sum_{i=1}^{m_{bd}} \left[\frac{t_{w,i} - \sum_{j=0}^{n} a_j z_i^j}{u_i(t_w)} \right] \tag{2.18}$$

Let **A** be an $m_{bd} \times n$ matrix whose elements are obtained as reported in Eq. (2.19):

$$A_{ij} = \frac{z_i^{j-1}}{u_i(t_w)} \tag{2.19}$$

A vector **b** of m_{bd} elements is also defined as the ratio between the water temperature measured at the i-th location and the correspondent uncertainty:

$$b_i = \frac{t_{w,i}}{u_i(t_w)} \tag{2.20}$$

and finally let **a** the vector whose components are the parameters to be fitted a_j.

The minimum of Eq. (2.16) occurs where the derivative of χ^2 with respect to all parameters a_j is equal to zero. This condition yields the following equation in the matrix form:

$$\left(\mathbf{A}^T \cdot \mathbf{A}\right) \cdot \mathbf{a} = \mathbf{A}^T \cdot \mathbf{b} \tag{2.21}$$

The inverse matrix

$$\mathbf{C} = \left(\mathbf{A}^T \cdot \mathbf{A}\right)^{-1} \tag{2.22}$$

is related to the standard uncertainty of the estimated parameters a_j; the diagonal elements of **C** are the square uncertainties of the fitted parameters a

$$u^2\left(a_j\right) = C_{jj} \tag{2.23}$$

and the off-diagonal elements C_{jk} are the covariances between the estimated parameters a_j and a_k

$$\operatorname{cov}\left(a_j, a_k\right) = C_{jk} \tag{2.24}$$

The uncertainty related to temperature gradient $u(dt_w/dz)$ is obtained from the uncertainty of fitted parameters (Eq. (2.23)) and from the covariances between fitted parameters (Eq. (2.24)) by applying the law of propagation of uncertainty as reported in Eq. (2.25) and (2.26)

$$g(z) = \frac{\mathrm{d}t_w}{\mathrm{d}z} = \sum_{j=1}^{n} j a_j z^{j-1} \tag{2.25}$$

$$u_c\left(g\right) = \sqrt{\sum_{j=1}^{n}\left(\frac{\partial g}{\partial a_j}\right)^2 u^2\left(a_j\right) + 2\sum_{j=1}^{n-1}\sum_{k=j+1}^{n}\left(\frac{\partial g}{\partial a_j}\right)^2\left(\frac{\partial g}{\partial a_k}\right)^2 \operatorname{cov}\left(a_j, a_k\right)} \tag{2.26}$$

2.4.4 Flow boiling tests

Flow boiling tests have been performed with R1234yf at mass velocity ranging between 200 and 600 kg m^{-2} s^{-1}, around 31 °C saturation temperature, in the 0.96 mm round channel.

During the test runs, mass velocity and inlet fluid temperature can be maintained constant, while the heat flux varies along the test section. In some of the test runs, the refrigerant exits as superheated vapor or saturated vapor with quality close to one. In this case, the heat flux increases with vapor quality in the channel up to a certain point, where the wall starts to dry up and the wall temperature deviates from its trend to approach the water temperature. The onset of dryout is determined from the standard deviation of the wall thermocouples, as described in Del Col *et al*. (2008) and Cavallini *et al.* (2007). The wall temperature in fact displays larger fluctuations in the zone where dryout occurs, which are related to the presence of a liquid film drying up at the wall with some kind of an oscillating process. These temperature fluctuations are detected by means of the standard deviation of the thermocouple readings. All the data points reported in the present paper refer to boiling conditions before the dryout occurs.

At constant mass velocity and saturation temperature, some test runs have been performed by varying the inlet temperature of the water in order to vary the heat flux. The test runs have been performed in a double mode: first by increasing the temperature difference between inlet water and saturated refrigerant and then by decreasing it. All the experimental points reported in the paper are taken decreasing the water temperature when all nucleation sites have been activated. The measurement of the wall temperature along the channel allows calculating the contribution of the axial conduction in the copper wall. The effect of axial conduction on the heat transfer coefficient can be determined from an energy balance at each elementary segment of the wall between the radial heat flux *q'* from water to R1234yf and the axial heat flux; this allows to calculate the actual heat flux to be used in the evaluation of the heat transfer coefficient. It was determined that the axial

conduction does not affect the values of heat flux neither the heat transfer coefficient, provided that locally dryout is not occurring in the channel.

2.4.5 Effect of heat flux

The graph in Figure 2.8 shows the heat flux plotted versus vapor quality for all the R1234yf tests performed in the channel. The vapor quality varies between 0.05 and 0.75, while the heat flux ranges from 10 up to 130 kW m^{-2}. The experimental data points are measured at five different refrigerant mass velocities *G* varying the inlet water temperature. The heat flux is not directly controlled but it is a result of the fluids (water and R1234yf) inlet conditions. Since refrigerant and water flow in counter-current, most of the data at low vapor quality display low heat flux (Figure 2.8) because at the entrance of the channel (low vapor quality region) the difference between saturation temperature and wall temperature is lower.

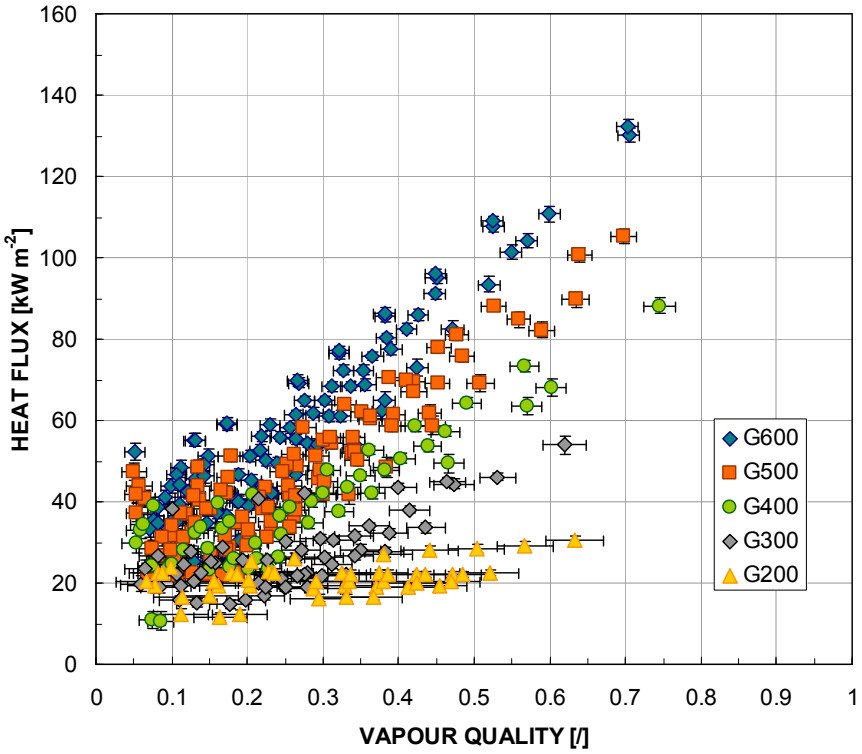

Figure 2.8. Flow boiling data of R1234yf at t_{sat}=31°C: local heat flux versus vapor quality.

When the same database is plotted as heat transfer coefficient vs. heat flux (Figure 2.9), the present data points display a dependence of the heat transfer coefficient on the heat flux: the higher the heat flux, the higher the heat transfer coefficient. From Figure 2.9, it can be seen that at a given heat flux, the corresponding heat transfer coefficients range in a band, which means that they also depend on other parameters such as vapor quality. The variation of the heat transfer coefficient at constant heat flux and constant mass velocity shows that the heat transfer coefficient is dependent on the vapor quality.

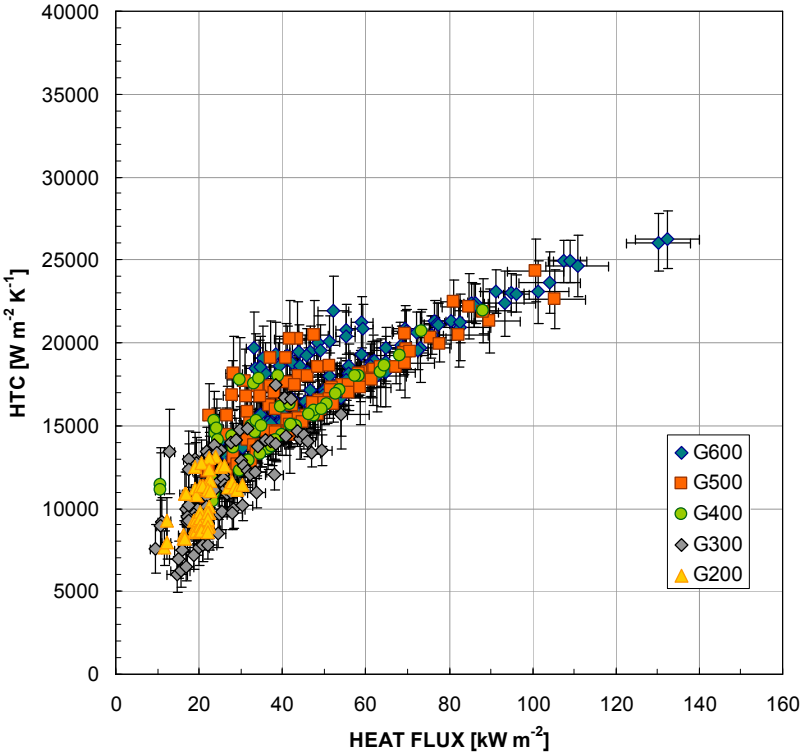

Figure 2.9 Flow boiling data of R1234yf at t_{sat}=31°C: local HTC versus heat flux.

In the present data analysis, it must be considered that the average roughness in the channel is equal to *Ra*=2.34 μm. The surface roughness is known to be important in the nucleation process: the smoother the surface, the larger the nucleation superheat (and heat flux) required to activate boiling sites. Similarly, the surface roughness must play a role in microchannel boiling, although its effect is not completely understood and agreed upon yet.

2.4.6 Effect of vapor quality and mass velocity

By comparing data points at constant heat flux and mass velocity, it is possible to get some information on the influence of vapor quality.
Figure 2.10 shows the experimental trend of heat transfer coefficients at constant heat flux (q = 30 kW m^{-2}) and mass velocity ranging between 200 and 600 kg m^{-2} s^{-1}. Furthermore, in Figure 2.11 the heat transfer coefficient has been reported as a function of vapor quality at a higher heat flux q = 50 kW m^{-2} and 400 kg m^{-2} s^{-1} < G < 600 kg m^{-2} s^{-1}. The heat transfer coefficient decreases with vapor quality for all the mass velocities and heat fluxes.
In Figure 2.12 the heat transfer coefficients have been plotted versus heat flux at nearly constant vapor quality x = 0.07-0.11; besides, in Figure 2.13, the heat transfer coefficients have been reported at nearly constant vapor quality x = 0.28-0.31. As can be seen, the experimental heat transfer coefficient is strongly dependent on heat flux while mass velocity does not affect it.

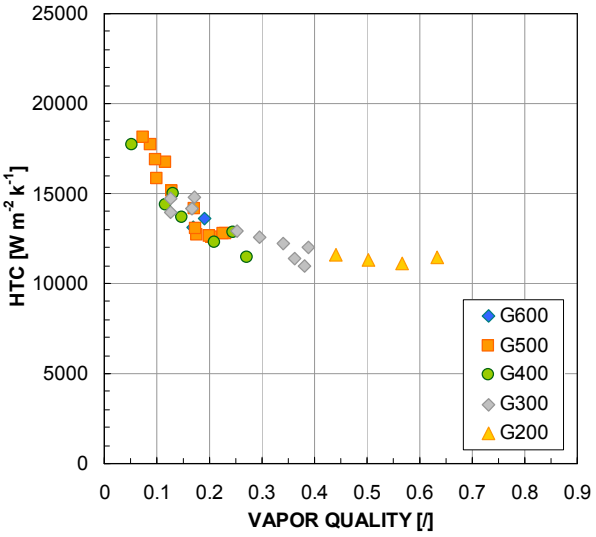

Figure 2.10. Local heat transfer coefficients versus vapor quality at constant heat flux (q = 30 kW m^{-2}).

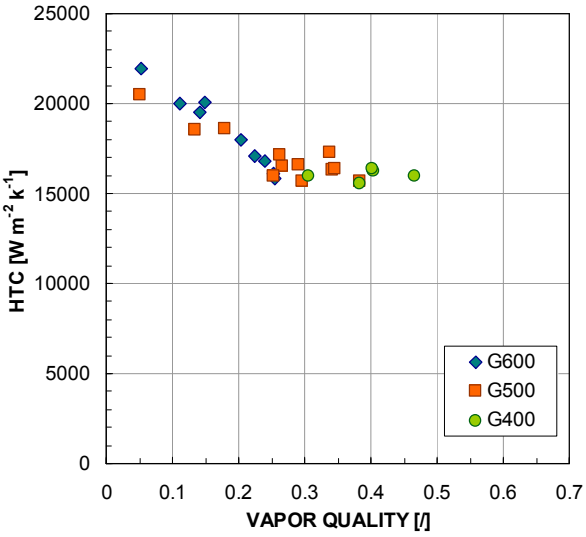

Figure 2.11. Local heat transfer coefficients versus vapor quality at constant heat flux (q = 50 kW m^{-2}).

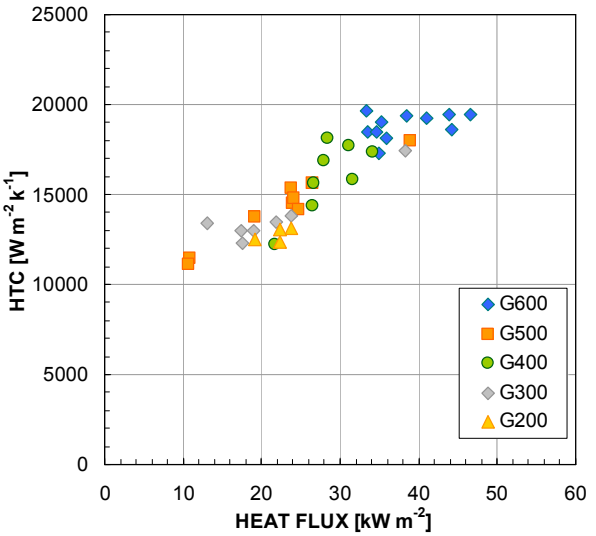

Figure 2.12. Local heat transfer coefficients versus heat flux at constant vapor quality (x = 0.07-0.11).

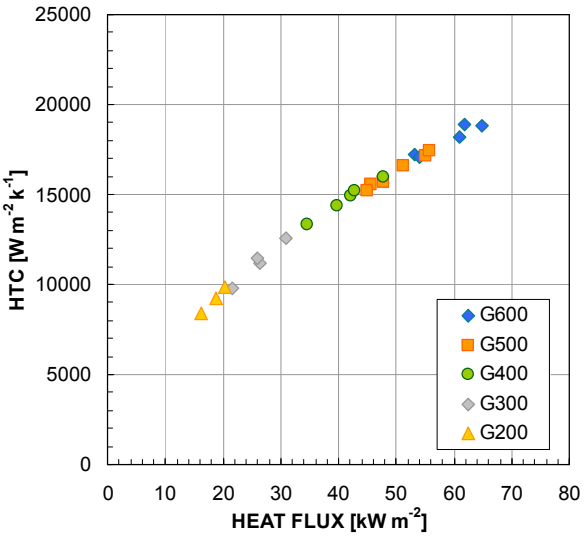

Figure 2.13. Local heat transfer coefficients versus heat flux at constant vapor quality (x = 0.28-0.31).

2.4.7 HTC comparison during vaporization of R1234yf and R134a

Since R1234yf has emerged as the global replacement refrigerant for R134a in mobile air conditioning, it is of great interest to compare its heat transfer characteristics to the ones of R134a at the same operating conditions. This is feasible because the heat transfer coefficients during vaporization were measured inside the same channel.
In Table 2.2, properties of saturated R134a and R1234yf at 30°C calculated using NIST Refprop 9.0 (2010) have been reported.

	p [bar]	p_R [/]	ρ_l [kg m^{-2}]	ρ_v [kg m^{-2}]	σ[mN m^{-1}]	h_{LG} [kJ kg^{-1}]
R1234yf	7.83	0.23	1073.3	43.73	5.561	141.2
R134a	7.70	0.19	1187.5	37.53	7.417	173.1

Table 2.2. Properties of saturated R1234a and R134a at 30°C.

Figure 2.14 compares the local heat transfer coefficients measured during boiling of R1234yf at 31°C saturation temperature and G = 300 kg m^{-2} s^{-1} to the ones of R134a at the same operating conditions; in Figure 2.15 R1234yf and R134a flow boiling data have been compared among them at an higher mass velocity G = 500 kg m^{-2} s^{-1}. In each figure, the uncertainty on the heat flux and on the heat transfer coefficient, calculated as described in Paragraph 2.4.3, has also been reported.
When comparing the heat transfer coefficient of R1234yf to the one measured for R134a at same values of heat flux and vapor quality, one can see that the two fluids display similar values of the heat transfer coefficient at the same operating conditions. From these graphs, a significant increase or decrease of the heat transfer coefficient of R1234yf as compared to R134a it is not observed.

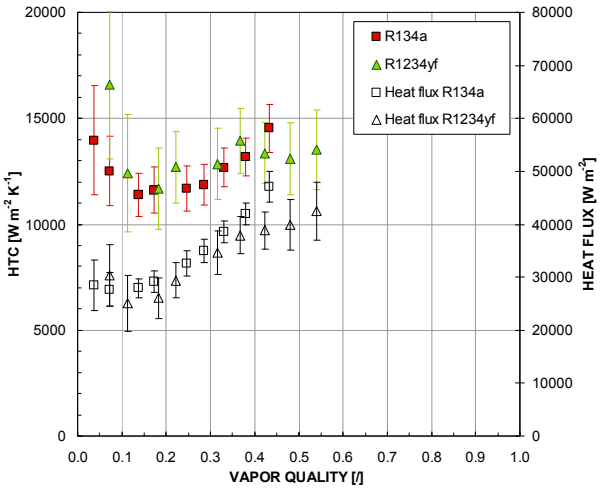

Figure 2.14. HTC comparison during vaporization of R1234yf and R134a at G = 300 kg m^{-2} s^{-1}; the experimental uncertainty bars are also reported.

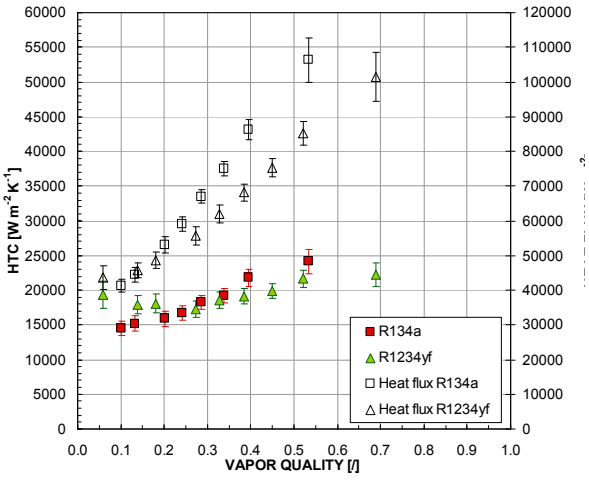

Figure 2.15. HTC comparison during vaporization of R1234yf and R134a at G = 500 kg m^{-2} s^{-1}; the experimental uncertainty bars are also reported.

2.5 Flow boiling of R1234yf in the square minichannel

In the following paragraphs, data reduction technique, uncertainty analysis and experimental results during convective boiling of R1234yf in the square (d_h=1.23 mm) minichannel will be presented. As previously seen for the circular minichannel, the heat is transferred to the evaporating fluid by using a secondary circuit and thus by imposing temperatures and not the heat flux. Thanks to the higher number of thermocouples in the water path (16) and in the copper wall (46), a more detailed investigation of the physical phenomena is possible in this new test section.
A description of the square minichannel test section could be found in Paragraph 1.5.1.

2.5.1 Data reduction

Figure 2.16 reports refrigerant, wall and water temperature measurements along the measuring sector during flow boiling of R1234yf at mass velocity $G = 400$ kg m^{-2} s^{-1}. The refrigerant enters the test channel at 31.6 °C saturation temperature with 9.6 K subcooling. At the exit, saturation temperature is decreased of 0.5 K due to pressure drop. The water enters from the opposite side of the test tube at 38.8 °C and its temperature decreases due to the heat transfer to the boiling refrigerant. Figure 2.16 also shows the standard deviation of the temperature measurements in the wall (each temperature measurement is the average value of fifty readings taken in fifty seconds): those deviations are pretty much the same in the channel.

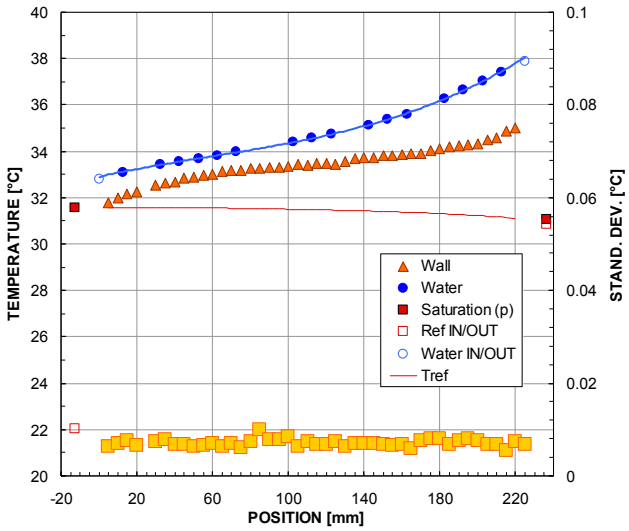

Figure 2.16. Water, wall and saturation temperature during a boiling process of R1234yf in the 1.23mm hydraulic diameter square channel at G = 400 kg m^{-2} s^{-1}. The big square dots represent the standard deviation of the wall temperature measurements.

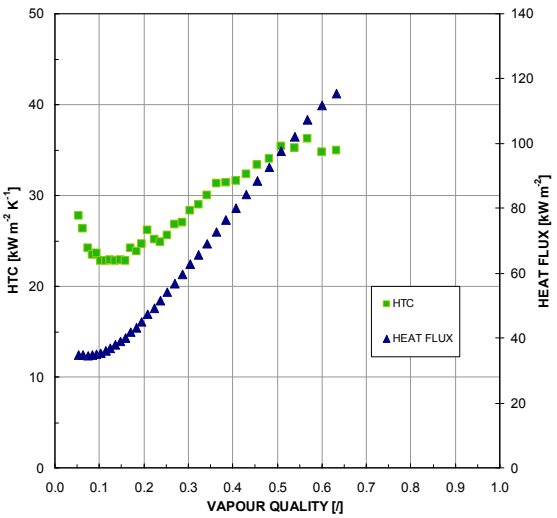

Figure 2.17. Heat transfer coefficient and heat flux versus vapour quality during R1234yf boiling at G = 400 kg m^{-2} s^{-1}.

The saturation temperature is directly measured in the adiabatic segments at the inlet and outlet of the test tube, by means of a T-type thermocouple and a four-junction thermopile, soldered to the stainless steel adiabatic capillary tubes.
In the test section there are 46 thermocouples embedded in the copper tube for measuring the wall temperature, and 16 in coolant path from which the local heat flux (q') is determined as:

$$q'(z) = \dot{m}_w \cdot c_{p,w} \cdot \frac{1}{p_i} \cdot \frac{dT_w}{dz} \tag{2.27}$$

where z is the axial coordinate along the tube and dTw/dz is the derivative of the water temperature along z and p_i is the perimeter of the square cross section. The water temperature profile along the channel is obtained interpolating the measured values using the minimum square method.
The heat flow rate transferred to the secondary fluid up to a certain position z is obtained by integrating the local heat flux q' from 0 (refrigerant inlet) to z

$$q(z) = p_i \cdot \int_0^z q'(z)\,\mathrm{d}z \tag{2.28}$$

Two different independent procedures have been adopted for the determination of the fitting polynomial equation of the water temperature and thus the calculation of the heat flux (Eq. 2.27). The first criterion, dubbed as physical, is based on the assumption that all the calculated values by the polynomial interpolation of the water temperatures should be below ± 0.05 °C with respect to

the experimental values, and 68% of the predicted values should be inside the ± 0.03 °C prediction boundary. Beside this, a statistical method based on the choice of the simplest fitting polynomial has been used. This statistic approach uses the R^2 statistic parameter, and adjusts it on the basis of the residual degrees of freedom: this is the reason of the name R^2_{adj} (Rawlings *et al.*, (1998)).
For the 93% of tests where no dryout condition was observed, the two methods have given the same grade for the interpolation polynomial. In the remaining 6% of cases, the HTC values have been taken into consideration only when the disagreement between the two methods is below 5%.
Once the heat flux is known, the local heat transfer coefficient inside the microchannel is obtained as the ratio of heat flux to the wall and refrigerant temperature difference:

$$\alpha(z) = \frac{q'(z)}{[T_{wall}(z) - T_{sat}(z)]} \tag{2.29}$$

While the wall temperature (T_{wall}) is directly measured, the saturation temperature (T_{sat}) in the exact position where the wall temperature is measured, is indirectly determined. In fact, during vaporization, the vapor quality changes along the microchannel and therefore the pressure gradient varies in the measuring sector; for this reason, a linear interpolation of the saturation temperature between inlet and outlet may lead to errors in the determination of the heat transfer coefficient. For this reason the pressure profile along the microchannel is calculated by implementing the Cavallini *et al.* (2009) two-phase pressure gradient correlation starting from the pressure measured at inlet and outlet of the channel. The calculated total pressure drop is corrected multiplying it by a factor, in order to match the total pressure drop to the value measured by the differential pressure transducer. Figure 2.16 reports the saturation temperature calculated from the pressure profile obtained in the just described way.
The vapor quality x at any axial position z is obtained from:

$$x(z) = \frac{q(z) - \dot{m}_{ref} \cdot (H_L - H_{SUB})}{\dot{m}_{ref} \cdot H_{LG}} \tag{2.30}$$

as a function of the total heat flow rate *q(z)* up to that location (Eq. 2.28), the specific enthalpy of saturated liquid (H_{SL}), the specific enthalpy of the subcooled liquid (H_{sub}) and the latent heat (H_{LG}). The enthalpy of the subcooled refrigerant is determined from the inlet pressure and temperature.
Figure 2.17 reports heat transfer coefficient and heat flux refereed to the test run of Figure 2.16: since in the test no dryout was observed, the heat flux increases till the end of the minichannel while the heat transfer coefficient first decrease till a vapor quality of 0.15 and then increases. Different is the case reported in Figure 2.19: it refers to a test run at 400 kg m^{-2} s^{-1} during dryout, which temperature profiles are reported in Figure 2.8.

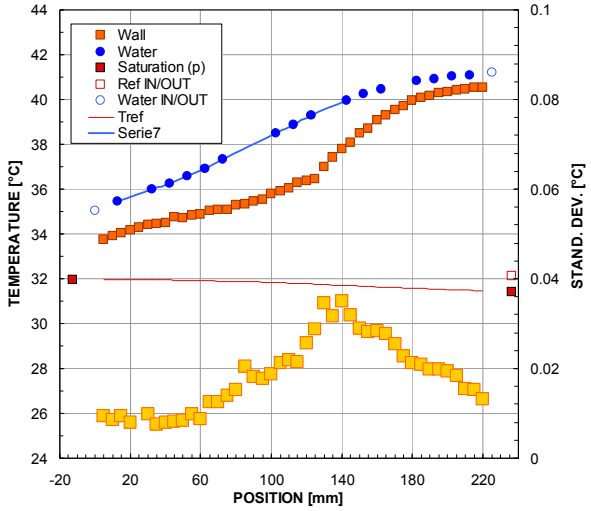

Figure 2.18. Water, wall and saturation temperature during a dryout boiling test of R1234yf in the 1.23mm hydraulic diameter square channel at G = 400 kg m^{-2} s^{-1}. The big square dots represent the standard deviation of the wall temperature measurements.

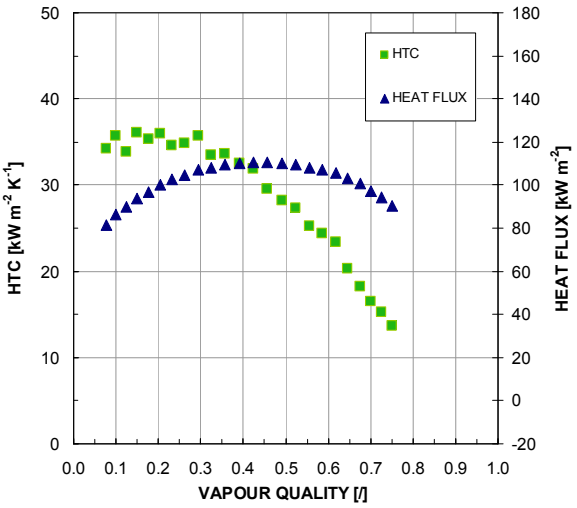

Figure 2.19. Heat transfer coefficient and heat flux versus vapour quality during R1234yf boiling at G = 400 kg m^{-2} s^{-1}.

As shown in Figure 2.19, the heat flux increases with vapour quality up to a certain value, which is equal to around 0.4 vapour quality. Up to this point the heat transfer coefficient is almost constant, while it starts to sharply decrease at higher vapour quality. It is interesting to observe the position where the wall temperature readings display a jump in terms of standard deviation: this occurs in the position z=135 mm far from the inlet of the test tube. Instead the maximum heat flux corresponds to the position z=95 mm: this means that the position where the deviation standard shows the maximum value is not the same where the heat flux reaches its maximum, which is 40 mm before. For the reduction of the dryout test, the water temperature profile has been calculated using the water thermocouples till the first one after the point where the maximum wall temperature deviation value has been observed.

2.5.2 Corrections for thermocouple position and axial conduction

The heat transfer coefficient is determined as described in the previous paragraph. Moreover, the measurements of the wall temperature along the channel allow calculating the contribution of the axial conduction in the copper wall. The effect of axial conduction on the heat transfer coefficient can be determined from an energy balance at the wall, as depicted in Figure 2.20: this allows determining the actual heat flux to be used in the evaluation of the heat transfer coefficient. As it can be seen in Figure 2.20, where the right axis shows the percent deviation of the corrected heat flux from the measured heat flux, the correction for the axial conduction does not significantly affect the values of the heat flux.
Furthermore, another correction has been introduced to take into account the real position of the wall thermocouple. In fact, the wall thermocouples are positioned at a distance of 1.2 mm from the wall of the minichannel. For this reason, during vaporization tests, the value of the wall temperature to be used in the calculation of the heat transfer coefficient is lower than the measured value. As it can be seen in Figure 2.20, this correction is more important at high heat flux, but in never more than 0.2 K.

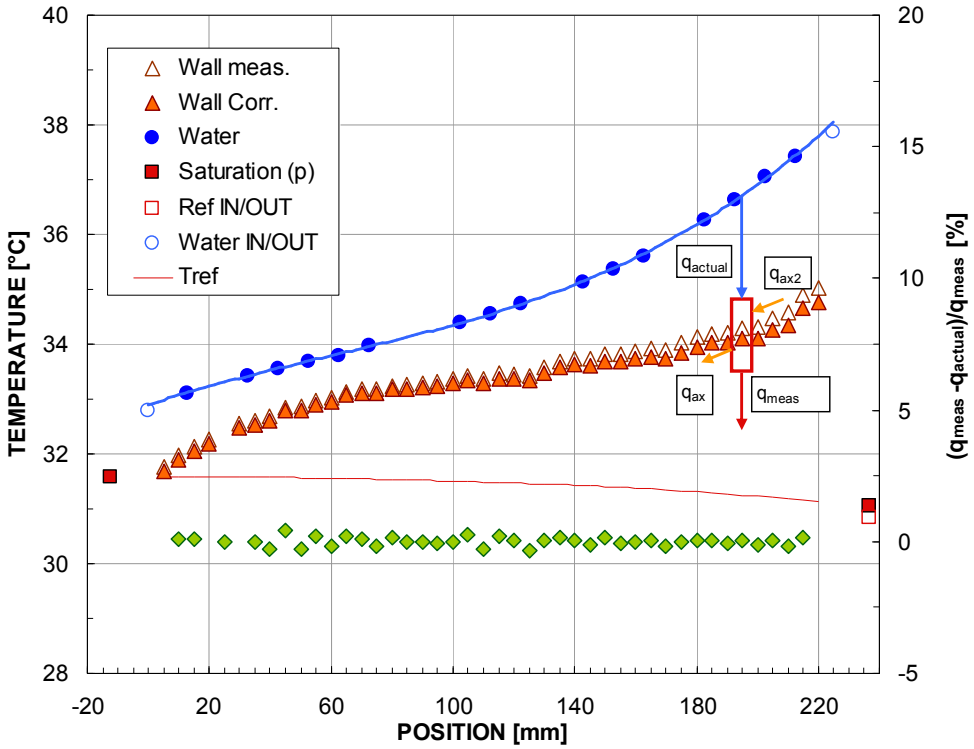

Figure 2.20. Water, wall and saturation temperatures during a flow boiling test run. Full triangles represent the corrected wall temperatures, while circles represent percent different between measured heat flux and actual value corrected for the axial conduction.

2.5.3 Error analysis

The experimental uncertainties of the measured parameters are reported in Table 2.3. In the case of thermocouples, the reported uncertainty comes from the off-site calibration tests. However, additional on-site calibrations of the thermocouples installed in the wall and in the water channel have been carried out, in order to improve the accuracy of the measurements.

Temperature	± 0.05 °C (on-site calibration)
Temperature difference	± 0.03 K (thermopile)
Water flow rate	± 0.15 % of flow rate
Refrigerant flow rate	± 0.25 to ± 0.35 % of flow rate
Absolute pressure	± 5 kPa
Pressure difference	± 0.1 kPa

Table 2.3. Type B experimental uncertainty of measured parameter.

The uncertainty associated with the channel length and the corner radius is equal to ±0.02 mm. Fluid properties have been calculated using NIST Refprop Version 9.0 (2010); in particular Refprop 9.0 implements for refrigerant R1234yf the Equation of State by Richter *et al.* (2011).
An uncertainty analysis on the heat transfer coefficient was then performed. The experimental uncertainty is made up by two parts: the first component is the Type A uncertainty that derives from repeated observations, the second one is Type B uncertainty that derives from instruments

calibration and manufacturer's specifications. All the experimental measurements (temperature, pressure, mass flow rate) are taken as a mean value of 50 readings with a time step of 1 s.
For each measured parameter, according to ISO Guide to the Expression of Uncertainty in Measurement (1995), the Type A standard uncertainty is given by dividing the experimental standard deviation by the root mean square of the number of observations.
Since the heat transfer coefficient is a function of several measured quantities:

$$\alpha(z) = f\left(\dot{m}_w, \frac{dT_w}{dz}, T_{sat}, T_{wall}, p_i\right) \tag{2.31}$$

the combined standard uncertainty $u_c(y)$ is calculated for each measured quantity by combining appropriately the Type A and Type B standard uncertainties of the measured parameters $u(x_i)$ as follows:

$$y = f\left(x_1, ..x_n\right) \qquad u_c\left(y\right) = \sqrt{\sum_{i=1}^{n}\left(\frac{\partial f}{\partial x_i}\right)^2 u^2\left(x_i\right)} \tag{2.32}$$

A specific procedure has been implemented for determining the uncertainty associated with the heat flux which depends on the water temperature gradient. The procedure that has been implemented for determining the uncertainty related to temperature gradient is the weighted least square – WLS (Press *et al*. (2007)) regression method as reported in Paragraph 2.4.3.1. In this case the value m_{bd} = 16 if dryout does not occur (e.g. z_1 = 12.5 mm, z_{16} = 212.5 mm).
The expanded uncertainty U_M is obtained by multiplying the combined standard uncertainty by a coverage factor k=2 with an interval having a level of confidence of approximately 95% ($U_M = k \cdot u_c(y)$).
The expanded uncertainty of the heat transfer coefficient results:

$$\delta_{\alpha(z)} = k \cdot \sqrt{\left(\frac{c_{pw} \cdot T'_w(z)}{p_i \cdot \Delta T} \cdot u_{\dot{m}_w}\right)^2 + \left(-\frac{c_{pw} \cdot \dot{m}_w \cdot T'_w(z)}{p_i^{\,2} \cdot \Delta T} \cdot u_{p_i}\right)^2 + \left(\frac{\dot{m}_w \cdot c_{pw}}{p_i} \cdot u_{T'_w(z)}\right)^2 + \left(-\frac{c_{pw} \cdot \dot{m}_w \cdot T'_w(z)}{p_i \cdot \Delta T^2} \cdot u_{\Delta T}\right)^2} \tag{2.33}$$

where ΔT is the difference between the wall and the saturation temperature. As it can be seen from Eq. (2.33), the HTC uncertainty is essentially independent on the refrigerant properties, since the only refrigerant parameter requested to determine the heat transfer coefficient is the saturation temperature, which can be determined from the pressure and also checked with direct measurement.
Figure 2.21 reports the four terms of Eq. (2.33) calculate during the same test at G=400 kg m^{-2} s^{-1} reported in Figure 2.20: while the contribution due to the uncertainties in the perimeter and in the water mass flow rate are constant and equal to 2.2% and 0.3 % respectively, the terms due to ΔT the and the water gradient play a major role.

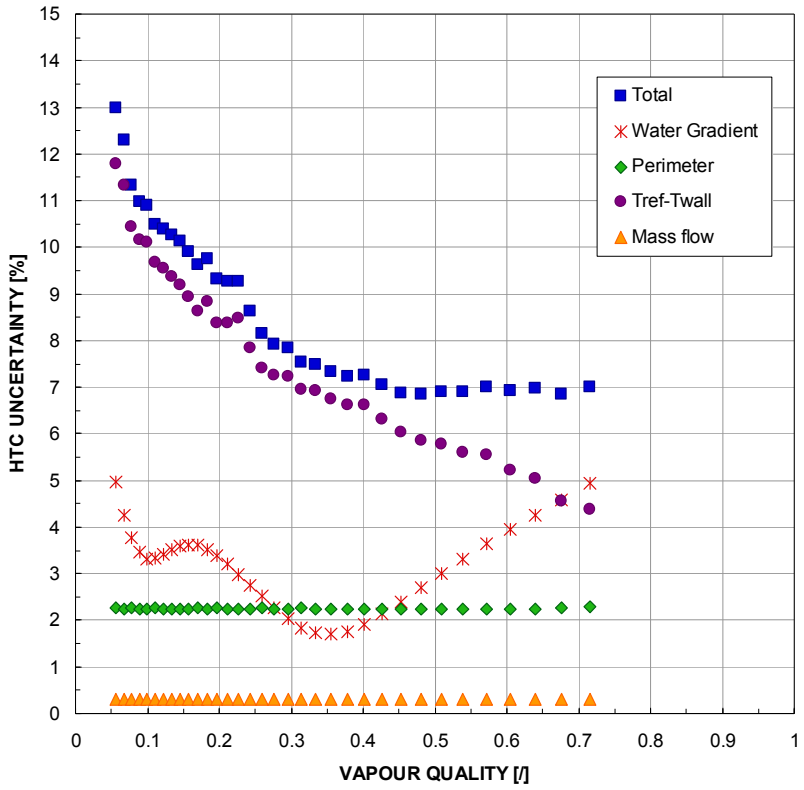

Figure 2.21. Contributions of water gradient, Perimeter, T_{sat}-T_{wall} and mass flow terms in the heat transfer coefficient uncertainty.

The lower is the mass velocity the higher results the experimental uncertainty. In particular, the higher contribute to the total uncertainty is due to the ΔT: at 600 kg m^{-2} s^{-1}, its mean value is around 7%, while at 300 kg m^{-2} s^{-1} it ranges around 8% and 10 % at 200 kg m^{-2} s^{-1}.
On the other hand, the uncertainty due to the water gradient, which depends on the interpolation polynomial used for the water temperature profile, has always the trend reported in Figure 2.21 with the lower value in the middle of the channel. It is not a monotonic decreasing function in the first part of the channel because two consecutive water thermocouples, at z=82.5 mm and z=92.5 mm were not working during the tests and then their values have not been used for the interpolation of the water profile.
All the experimental data presented below have a heat transfer coefficient uncertainty below 15% and is within ±10% for 50% of the data points. The average experimental heat transfer uncertainty associated to the heat flux can be estimated equal to ±6% and the mean uncertainty associated with the wall minus saturation temperature difference is ±8%.

2.5.4 Flow boiling tests

Flow boiling tests have been performed with R1234yf at mass velocity ranging between 200 and 500 kg m^{-2} s^{-1}, around 31 °C saturation temperature, in the 1.23 mm square channel.
During the test runs, mass velocity and inlet fluid temperature can be maintained constant, while the heat flux varies along the test section. In some of the test runs, the refrigerant exits as superheated vapor or saturated vapor with quality close to one. In this case, the heat flux increases with vapor quality in the channel up to a certain point, where the wall starts to dry up and the wall temperature

deviates from its trend to approach the water temperature. In order to exclude any effects of due to the dryout, all the data points reported in the present paper refer to experimental tests were this phenomenon was not observed.
The test runs have been performed first by increasing the temperature difference between inlet water and saturated refrigerant and then by decreasing it. All the experimental points reported below, if it is not specify, have been taken decreasing the water temperature when all nucleation sites have been activated.
The graph in Figure 2.22 shows the heat flux plotted versus vapor quality for all the R1234yf tests performed in the square channel. The error bars are also displayed.

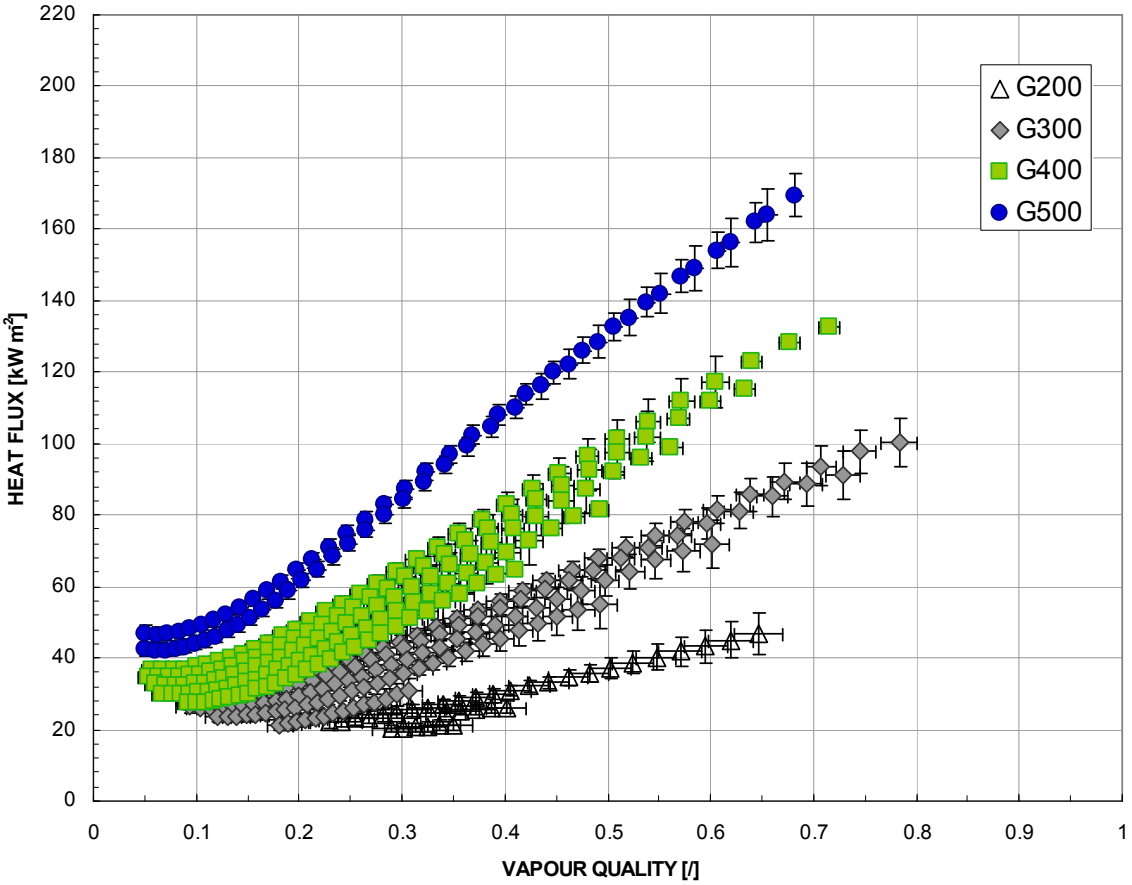

Figure 2.22. Flow boiling data of R1234yf at t_{sat}=31°C: local heat flux versus vapor quality.

The vapor quality varies between 0.05 and 0.75, while the heat flux ranges from 20 up to 170 kW m^{-2}. The experimental data points are measured at four different refrigerant mass velocities *G* varying the inlet water temperature. A clear dependence of the heat flux can be observed in Figure 2.22: for all the mass velocities the heat flux increases with the increasing of the vapour quality.
When the same database is plotted as heat transfer coefficient vs. heat flux (Figure 2.23), the present data points lay in a pretty narrow band, showing a clear dependence of the heat transfer coefficient on the heat flux: the higher the heat flux, the higher the heat transfer coefficient. From Figure 2.23, it can be seen that at a given heat flux, the corresponding heat transfer coefficients range in a band, which means that they also depend on other parameters such as vapor quality. The

variation of the heat transfer coefficient at constant heat flux and constant mass velocity shows that the heat transfer coefficient is dependent on the vapor quality.

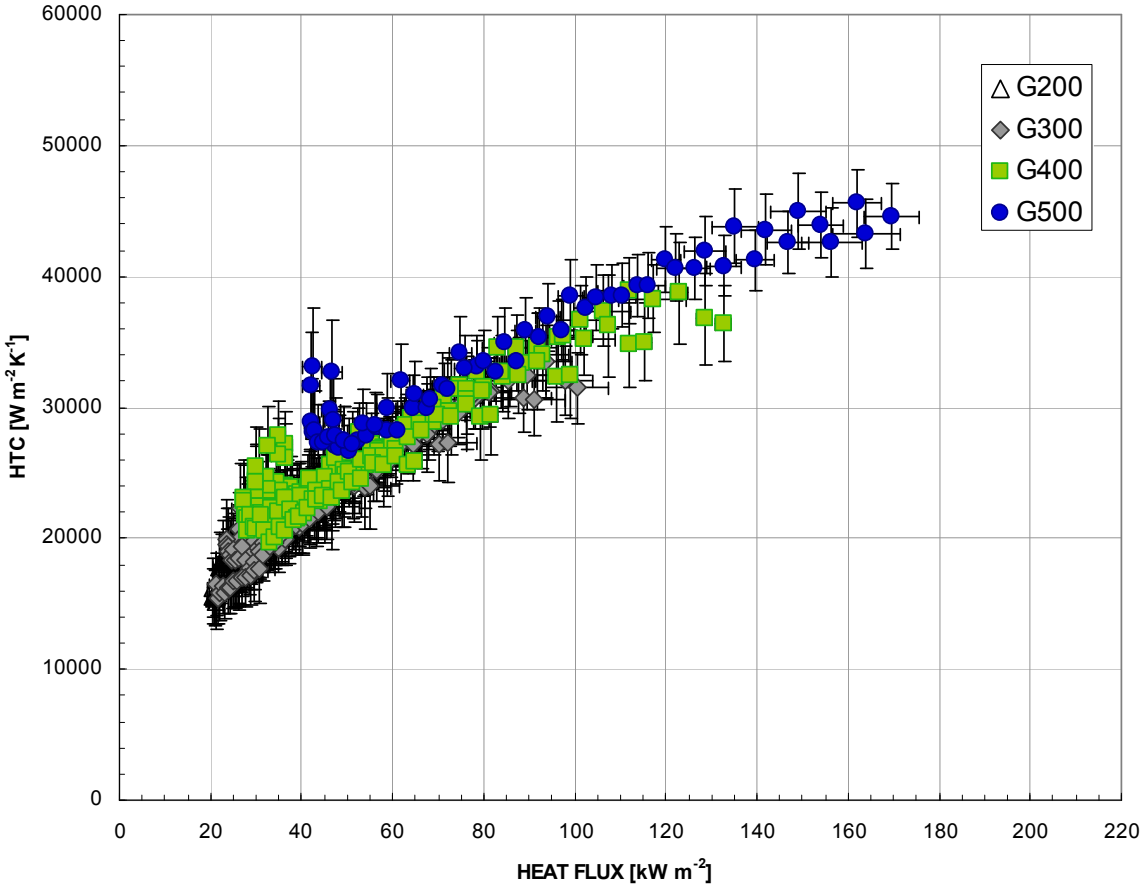

Figure 2.23. Flow boiling data of R1234yf at t_{sat}=31°C: local HTC versus heat flux.

In the present data analysis, it must be considered that the average roughness in the channel is equal to *Ra* = 1.02 μm. The surface roughness is known to be important in the nucleation process: the smoother the surface, the larger the nucleation superheat (and heat flux) required to activate boiling sites. Similarly, the surface roughness must play a role in microchannel boiling, although its effect is not completely understood and agreed upon yet.

2.5.5 Effect of vapor quality and mass velocity

By comparing data points at constant heat flux, it is possible to get some information on the influence of vapor quality.
Figure 2.24 shows the experimental trend of heat transfer coefficients at three different values constant heat flux (q = 30, 50 and 80±5% kW m^{-2}) and mass velocity ranging between 200 and 500 kg m^{-2} s^{-1}. When moving at q = 30 kW m^{-2} constant heat flux, vapour quality ranges between 0.05 and 0.4. The corresponding values of heat transfer coefficient show a limited variation, between 25 and 18 kW m^{-2} for the entire span of mass velocities.

At higher heat flux, 50 kW m^{-2}, the vapour quality goes from 0.05 to 0.45. As shown in the heat transfer coefficient displays little variation with vapour quality and mass velocity. It slightly decreases when increasing vapour quality. The same trend is found at higher heat flux, 80 kW m^{-2}. The heat transfer coefficient decreases with vapor quality for all the mass velocities and heat fluxes.

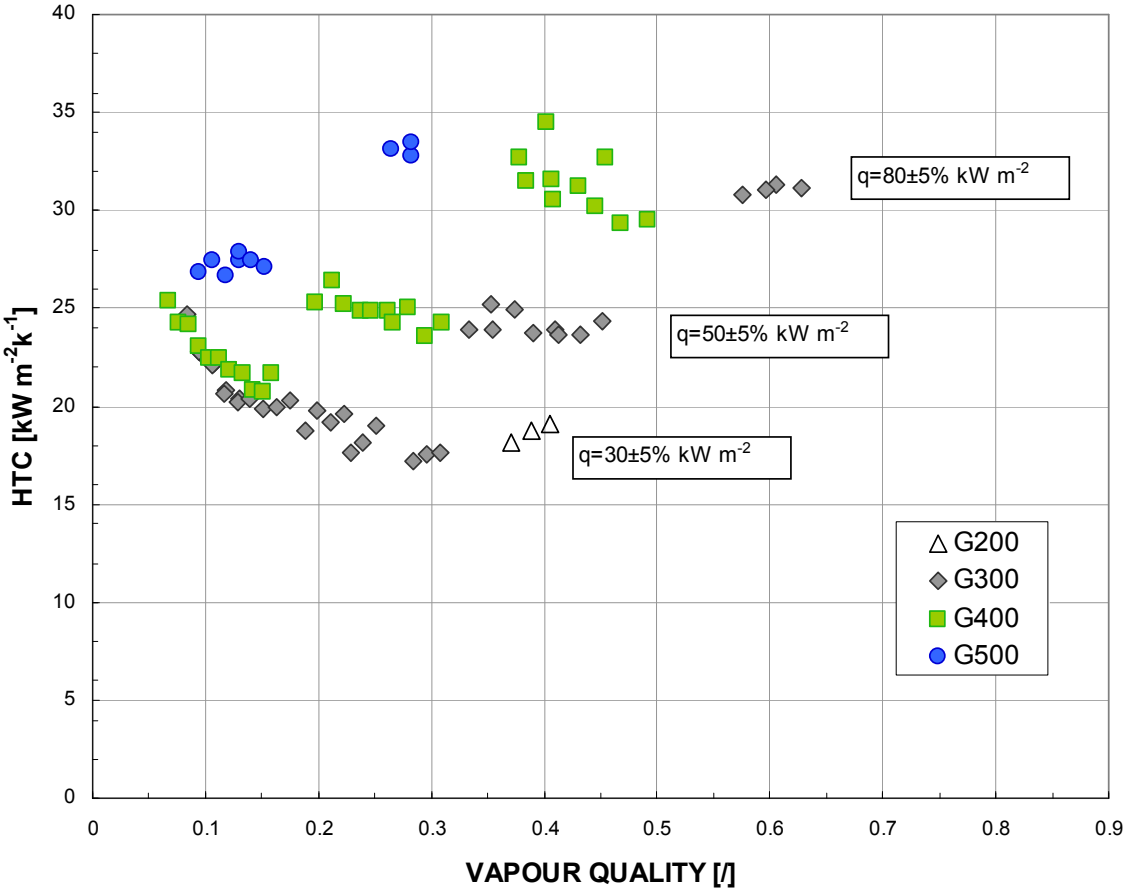

Figure 2.24. Local heat transfer coefficients versus vapor quality at constant heat flux (q = 30, 50 and 80 ±5% kW m^{-2}).

In Figure 2.25 the heat transfer coefficients have been plotted versus heat flux at nearly constant vapor quality x = 0.15-0.25; besides, in Figure 2.26, the heat transfer coefficients have been reported at nearly constant vapor quality x = 0.45-0.55. The experimental heat transfer coefficient is strongly dependent on heat flux but no effect of the mass flux seems to be present: at a constant vapour quality the heat flux increases and all the data at different mass flux could be interpolated by a straight line. In fact, if a heat flux of 35 80 kW m^{-2} and a constant vapour quality (x=0.15-0.25) are considered in Figure 2.25, values for the heat transfer coefficient at G400 and G500 are overlapped. Such a behavior could be observed also in Figure 2.26 considering values for the heat flux of 80 kW m^{-2}: the are no differences between G300 and G400 at x=0.45-0.55.
As shown comparing Figure 2.25 and Figure 2.26, this effect does not depend on the considered vapour quality range.

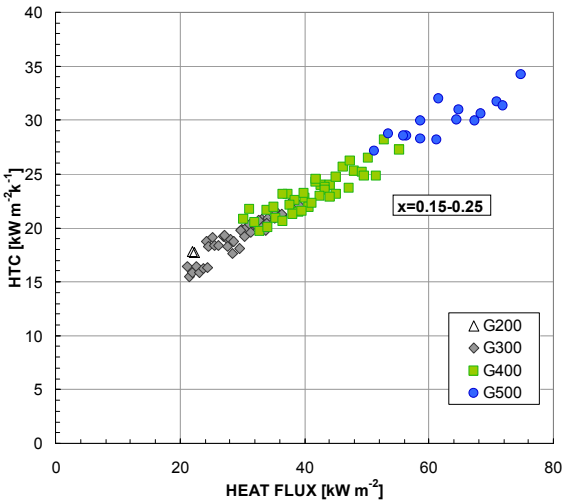

Figure 2.25. Local heat transfer coefficients versus heat flux at constant vapor quality (x = 0.15-0.25).

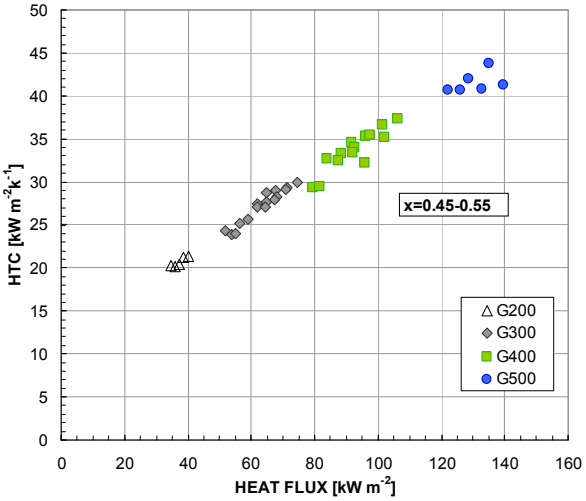

Figure 2.26. Local heat transfer coefficients versus heat flux at constant vapor quality (x = 0.45-0.55).

2.5.6 Hysteresis

For each value of the mass velocity the test runs have been performed first by increasing the temperature difference between inlet water and saturated refrigerant, till to reach the dryout condition in more of the half of the channel, and then by decreasing it. All the data reported up to now have been measured during the decreasing phase of the water temperature. Instead, Figure 2.27 reports the heat transfer coefficient in function of the heat flux measured both during the increasing and decreasing phase without the data recorded during dryout tests. It can be clearly seen the difference between the two phases: when all the nucleating points have been activated the heat flux and heat transfer coefficient where sensibly higher respect to a test which have been recorded during the increasing phase, with the same conditions for the secondary fluid. For a heat flux of 40 kW m^{-2} the heat transfer coefficient has been increased by 40%.

This behavior have been observed for all the mass velocities with the exception of G=200 kg m^{-2} s^{-1}. Figure 2.28 reports the measured heat flux in function of the wall superheating recorded in a fixed position in the channel (z=130 mm from the inlet) during the increasing and decreasing phase at 200 kg m^{-2} s^{-1}: triangles refers to tests which have been recorded during the increasing phase, while diamonds during the decreasing phase. The circles highlight tests in which the same inlet conditions of the water has been imposed: as it can be seen, there are non differences and the values perfectly overlaps, meaning that for this test run no hysteresis has been observed. Tests have been performed in order to have the same inlet conditions, mass flow and temperature, for the secondary fluid, and the same inlet conditions, temperature and pressure, for the refrigerant. In 0 are also reported the vapour quality values referred to each value.

Different is the case reported in Figure 2.29: test run has been done at G=400 kg m^{-2} s^{-1} in the same way of G=200 kg m^{-2}. In this case at the same heat flux, a different value of the wall superheating has been recorded during the two phases. A lower value by 40% of the ΔT has been measure, which means a higher value by the same amount for the heat transfer coefficient.

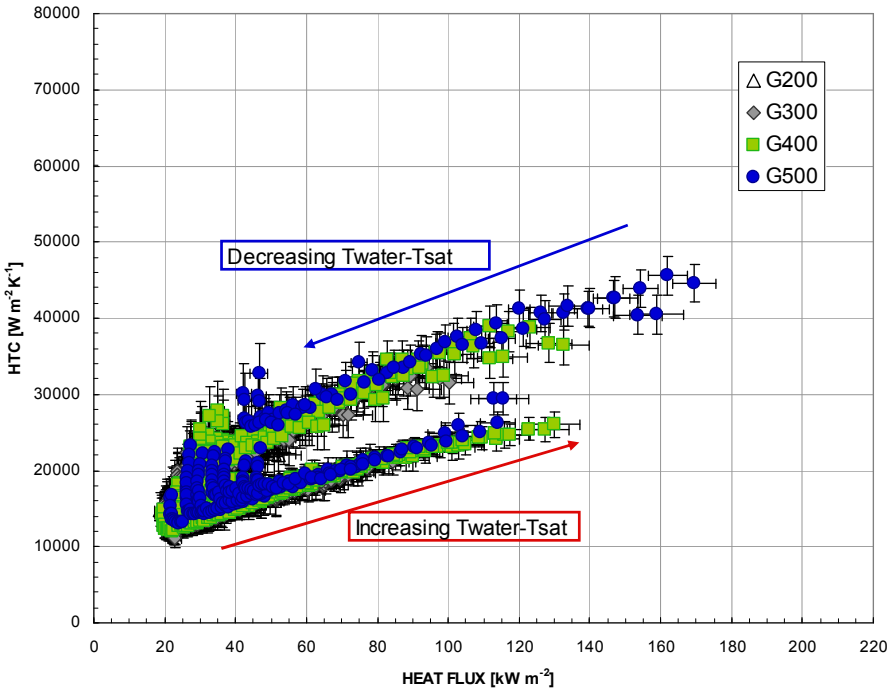

Figure 2.27. Flow boiling data of R1234yf at t_{sat}=31°C: local HTC versus heat flux: values measured during the increasing and decreasing of the water temperature.

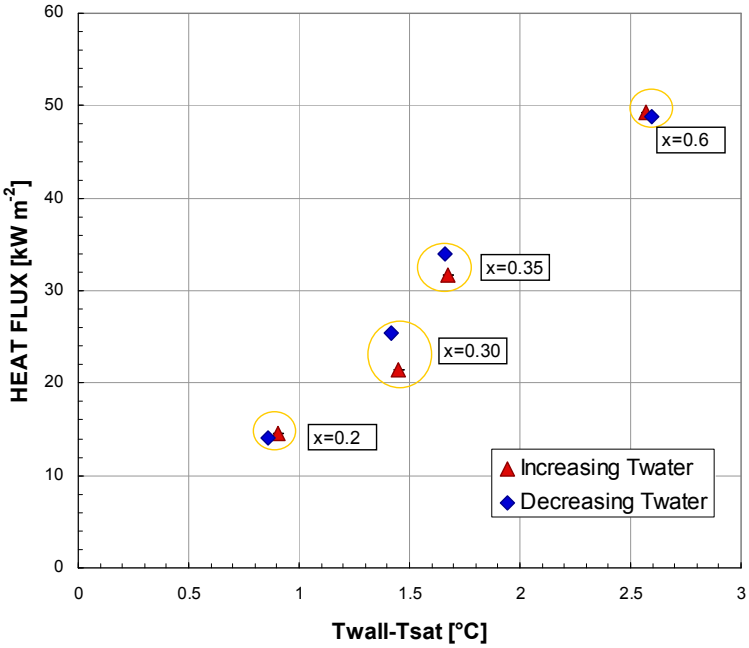

Figure 2.28. Heat flux in function of the wall superheating at z=130 mm during vaporization test of R1234yf at G 200 kg $m^{-2}s^{-1}$. Circled values refer to tests in which the conditions for the inlet water were the same.

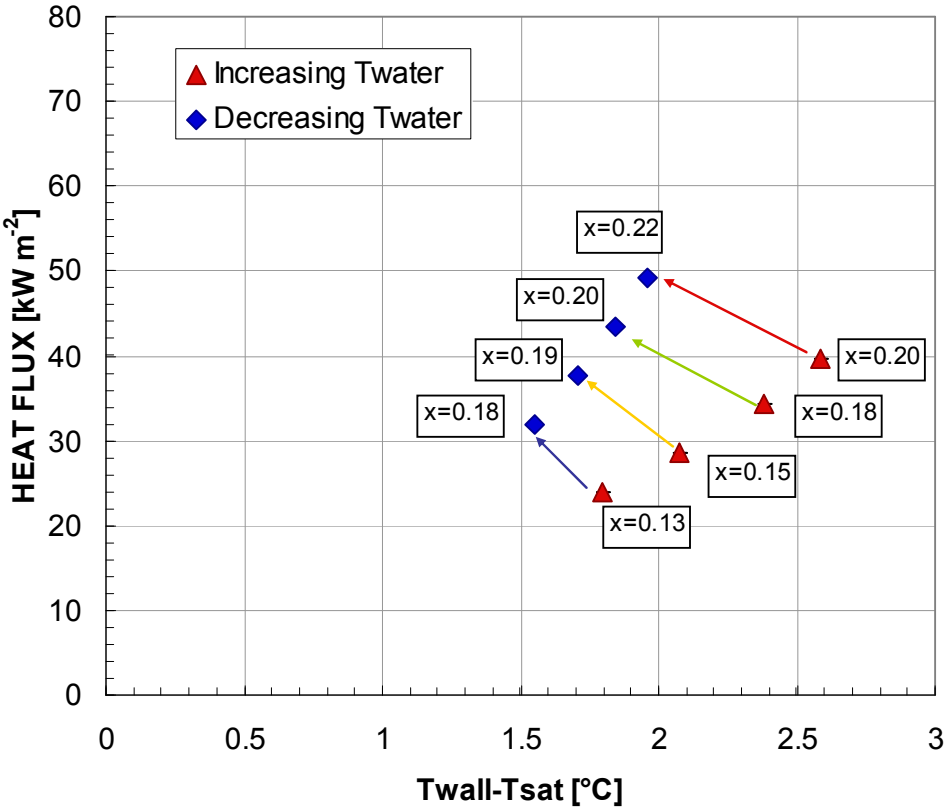

Figure 2.29. Heat flux in function of the wall superheating at z=130 mm during vaporization test of R1234yf at G 400 kg $m^{-2}s^{-1}$. Arrows refer to tests in which the conditions for the inlet water were the same.

The hysteresis has been observed also at *G*=300 and 500 kg m^{-2} s^{-1}. A possible explanation to why the hysteresis was present only at *G*=200 kg m^{-2} s^{-1} may be found in the different subcooling grade of the refrigerant at measuring sector inlet. While for all the other mass flux the temperature of the refrigerant was 7 K below the saturation temperature, at *G*=200 kg

3 SINGLE PHASE AND TWO PHASE PRESSURE DROP IN MINICHANNELS

3.1 Abstract

The present Chapter reports a study of single phase and two phase pressure drop in different minichannels. Tests were performed during single phase and two phase flow of R134a and R1234yf inside the circular and square test section presented before in Chapters 1 and 2. Experimental results are compared with classical models available for the macroscale in order to verify their validity in the miniscale. An ad-hoc section has been used for the validation of an indirect technique for determining the hydraulic diameter of ducts from the pressure drop measurement in laminar flow. This method has been used for the determination of the geometrical parameters of the square minichannel described before in Paragraph 1.5.1. Furthermore, two new circular minichannels, with 0.96 and 2 mm inner diameter, and a new presection have been designed and realized specifically for single phase and two phase pressure drop measurements. Proper installation of the pressure ports has been realized in order to avoid any correction factors in the data reduction. Tests performed during liquid and vapour single phase flow of R134a which have been done in these new sections are reported. The good agreement between the Hagen-Poiseulle law and the Balusius models in the laminar and turbulent flows confirms the validity of the classical theory in the small scale. A good capacity of prediction has been found also in some two phase pressure drop models like the Cavallini *et al.* (2009) and Friedel (1979).

3.2 Introduction

An earnest interest in microchannel flows began with the pioneering work on direct chip cooling with water by Tuckerman and Pease (1981). Recently, a number of investigators including Li *et al*. (2000), Celata *et al*. (2002) and Steinke and Kandlikar (2005) critically evaluated the available literature and presented explanations for the large deviations from the classical theory reported by some of the researchers.

Since measuring the local pressure along the flow is difficult in microchannels, researchers have generally measured the pressure drop across the inlet and outlet manifolds. The resulting pressure drop measurement represents the combined effect of the losses in the bends, entrance and exit losses, developing region effects, and the core frictional losses. Judy *et al*. (2002) achieved an excellent agreement between the laminar flow theory and experimental results obtained in 15–150μm round and square microchannels made of fused silica and stainless steel with distilled water, methanol and isopropanol. Similar agreement was obtained by Bucci *et al*. (2004) in 172, 290 and 520μm diameter stainless steel circular tubes with water in the fully developed laminar flow region. Niklas and Favre-Marinet (2003) analyzed the flow of water in a network of triangular microchannels with d_h =110μm. The contributions due to various losses were carefully analyzed in both their numerical as well as experimental work. They concluded that the classical theory is applicable to modeling the flow through the entire system.

In these first paragraphs single-phase pressure drop experiments that were performed intentionally to have critical insight into the test section hydraulic performance are presented.

3.3 Single-phase pressure drop

3.3.1 Circular minichannel

Conventional approach was used for roughness representation and calculation of its effect. If not noted differently, all friction factors expressed here are in the form of Fanning friction factor, which is four times less than Darcy friction factor.
Since stainless steel capillaries were assumed smooth, Hagen-Poiseuille and Blasius laws were used to calculate the pressure losses within those tubes. Even though short, the two adiabatic lengths are associated to a significant pressure drop due to the smaller hydraulic diameter (0.72 mm) compared to the test section (0.96 mm). When laminar flow was assumed for the two sectors, Hagen-Poiseuille law was used to calculate resistance coefficient.

$$f = \frac{16}{\mathrm{Re}} \tag{3.1}$$

Therefore, pressure gradient in the laminar region can be written:

$$\frac{dp}{dl} = 2f \cdot \frac{G^2}{d_h \cdot \rho} = \frac{32}{\mathrm{Re}} \cdot \frac{G^2}{d_h \cdot \rho} = \frac{128 \cdot \dot{m} \cdot \mu}{\pi \cdot \rho} \cdot \frac{1}{d_h^{\,4}} \tag{3.2}$$

It can be seen from Eq. (3.2) that pressure gradient during laminar flow is inverse proportional to the hydraulic diameter over exponent 4, which implies rather big impact of tube diameter on overall pressure loss. Similarly, frictional coefficient at higher values of Re number was assumed to follow Blasius curve for smooth tubes.

$$f = \frac{0.0791}{\mathrm{Re}^{0.25}} \tag{3.3}$$

Pressure gradient for the second region of the transition regime can be calculated.

$$\frac{dp}{dl} = 2f \cdot \frac{G^2}{d_h \cdot \rho} = \frac{2 \cdot 0.0791}{\mathrm{Re}^{0.25}} \cdot \frac{G^2}{d_h \cdot \rho} = \frac{2.5312}{\sqrt{2}} \cdot \frac{\dot{m}^{1.75} \cdot \mu^{0.25}}{\pi^{1.75} \cdot \rho} \cdot \frac{1}{d_h^{\,4.75}} \tag{3.4}$$

Pressure gradient in smooth tubes and high Reynolds numbers from Eq. (3.4) is inverse proportional to the hydraulic diameter over exponent 4.75. The high dependency of the pressure gradient from the hydraulic diameter requires a precise examination of the internal diameter.

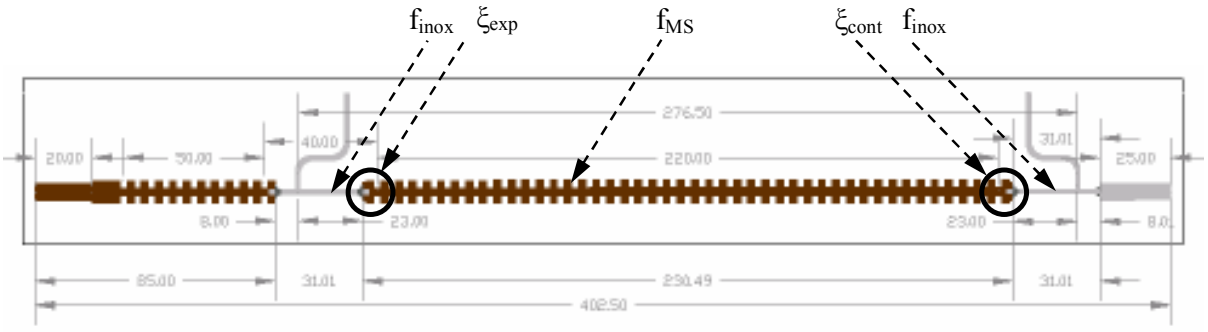

Figure 3.1. Geometry of the TS tubing. Total pressure loss refers to 276.5 mm long region that consists of two considered smooth 24 mm long adiabatic sectors and 228.5 mm long measuring sector.

Since in the turbulent region it depends on the surface roughness, the internal surface roughness of the copper channel has been measured with the digital surface roughness machine ZEISS-TSK Surfcom 1400A. The measurements have been performed moving axially at different

circumferential positions. The mean roughness *Ra*, as defined by the ISO 4287:1997, ranges between 2.01 μm and 2.76 μm, with a mean value equal to 2.34 μm.

3.3.1.1 Local Pressure Drop

Local pressure losses during single phase fluid flow are mostly characterized with geometry dependent coefficients only. Moreover, shock losses usually depend on flow cross section shape, flow distribution, orientation, scaling ratio, inlet and outlet conditions and on Reynolds number within distinguished flow regimes. Local pressure drop was calculated for two geometry changes: the abrupt enlargement of the studied minichannel from 0.762 mm diameter adiabatic sector to assumed 0.96 mm circular measuring sector (Eq. (3.5) to Eq. (3.8)) and back to adiabatic sector (Eq. (3.9) to Eq. (3.13)) as depicted in Figure 3.1.
The fluid flow through the abrupt enlargement of the studied minichannel was according to Handbook of Hydraulic Resistance (Idelchik 1996) introduced as a sudden expansion of a flow having a uniform velocity distribution. The friction coefficient below ς_{exp} and ς_{cont} are in form of the Darcy friction factor.

For Re < 10

$$\varsigma_{\exp} \approx \frac{30}{\mathrm{Re}} \tag{3.5}$$

For $10 \le \mathrm{Re} < 500$

$$\varsigma_{\exp} = \sum_{i=0}^{3} \left\{ \frac{1}{(\log(\mathrm{Re}))^i} \cdot \left[b_{i1} + b_{i2} \cdot \left(1 - \frac{d_{inox}^2}{d_{MS}^2} \right)^2 + b_{i3} \cdot \left(1 - \frac{d_{inox}^2}{d_{MS}^2} \right)^4 \right] \right\} \tag{3.6}$$

i	b_{i1}	b_{i2}	b_{i3}
0	3.62536	10.744	-4.41041
1	-18.13	-56.77855	33.40344
2	30.8558	99.9542	-62.78
3	-13.217	-53.9555	33.8053

Table 3.1. Numerical values for b_{i1}, b_{i2}, b_{i2}, from Eq. (3.6):

For $500 \le \mathrm{Re} \le 3.3\mathrm{x}10^3$

$$\varsigma_{\exp} = \sum_{i=0}^{2} \left\{ (\log(\mathrm{Re}))^i \cdot \left[c_{i1} + c_{i2} \cdot \left(1 - \frac{d_{inox}^2}{d_{MS}^2} \right)^2 + c_{i3} \cdot \left(1 - \frac{d_{inox}^2}{d_{MS}^2} \right)^4 \right] \right\} \tag{3.7}$$

i	c_{i1}	c_{i2}	c_{i3}
0	-8.4456	-26.163	-5.38086
1	6.007	18.5372	3.9978
2	-1.02318	-3.0916	-0.680943

Table 3.2. Numerical values for c_{i1}, c_{i2} and c_{i3} from Eq. (3.7).

For $\mathrm{Re} > 3.3\mathrm{x}10^3$

$$\varsigma_{\exp} = \left(1 - \frac{d_{inox}^2}{d_{MS}^2} \right)^2 \tag{3.8}$$

The fluid flow through the abrupt contraction of the studied minichannel was according to Handbook of Hydraulic Resistance (Idelchik 1996) introduced as a sudden contraction in transition and laminar regions.

For (Re < 10):

$$\varsigma_{cont} \approx \frac{30}{\mathrm{Re}} \tag{3.9}$$

For $10 \leq \mathrm{Re} < 10^4$

$$\varsigma_{cont} = A \cdot B \cdot \left(1 - \frac{d_{inox}^2}{d_{MS}^2}\right) \tag{3.10}$$

$$A = \sum_{i=0}^{7} a_i \cdot (\log(\mathrm{Re}))^i \tag{3.11}$$

$$\mathrm{B} = \sum_{\mathrm{i}=0}^{2} \left\{ \left[\sum_{\mathrm{j}=0}^{2} \mathrm{a_{ij}} \cdot \left(\frac{\mathrm{d_{inox}^2}}{\mathrm{d_{MS}^2}} \right)^{\mathrm{j}} \right] \cdot \left(\log(\mathrm{Re}) \right)^{\mathrm{i}} \right\} \tag{3.12}$$

$\mathbf{a_0}$	$\mathbf{a_1}$	$\mathbf{a_2}$	$\mathbf{a_3}$	$\mathbf{a_4}$	$\mathbf{a_5}$	$\mathbf{a_6}$	$\mathbf{a_7}$
-25.12458	118.5076	-170.4147	118.1949	-44.42141	9.09524	-0.9244027	0.03408265

Table 3.3. Numerical values for a_i from Eq. (3.11).

	$\mathbf{10 \leq Re \leq 2x10^3}$			$\mathbf{2x10^3 < Re < 10^4}$		
i / j	**0**	**1**	**2**	**0**	**1**	**2**
0	1.07	1.22	2.9333	0.5443	-17.298	-40.715
1	0.05	-0.51668	0.8333	-0.06518	8.7616	22.782
2	0	0	0	0.05239	-1.1093	-3.1509

Table 3.4. Numerical values for a_{ij} from Eq. (3.12).

And for fully developed quadratic region ($\mathrm{Re} > 10^4$)

$$\varsigma_{cont} = 0.5 \cdot \left(1 - \frac{d_{inox}^2}{d_{MS}^2}\right)^{3/4} \tag{3.13}$$

Once we have calculated linear resistance coefficient for adiabatic sectors, local resistance coefficient for expansion and contraction, we can obtain resistance coefficient for the measuring sector experimentally.

Since the overall pressure drop is measured, the searched pressure loss is obtained from subtraction of the other two calculated values, the sum of the local pressure drops and frictional pressure drop within the stainless steel capillaries, from the total pressure loss.

$$\Delta p_{MS} = \Delta p_{tot} - \sum \Delta p_{loc} - \Delta p_{ss} \tag{3.14}$$

Once the local resistance coefficients are calculated, the pressure loss in the measuring section are easy obtained.

$$\Delta p_{MS} = \Delta p_{tot} - \left(\varsigma_{\exp} + \varsigma_{cont} + 4 \cdot f_{inox} \cdot \frac{l_{inox}}{d_{h_{inox}}} \right) \cdot \frac{G_{inox}^2}{2 \cdot \rho} \tag{3.15}$$

At the end, the resistance coefficient can be calculated from Eq. (3.16):

$$f_{MS} = \frac{\rho \cdot d_{h_{MS}} \cdot \Delta p_{MS}}{2 \cdot G_{MS}^2 \cdot l_{MS}} \tag{3.16}$$

All single phase pressure drop experiments are here reported for adiabatic flows. Low Re number data refer to subcooled liquid tests, whereas data at high Reynolds were carried out with superheated vapor.
Figure 3.2 reports the friction factor in function of the Reynolds number calculated during single phase flow of R1234yf in the circular minichannles, while in Figure 3.3 are reported the values obtained with R134a.

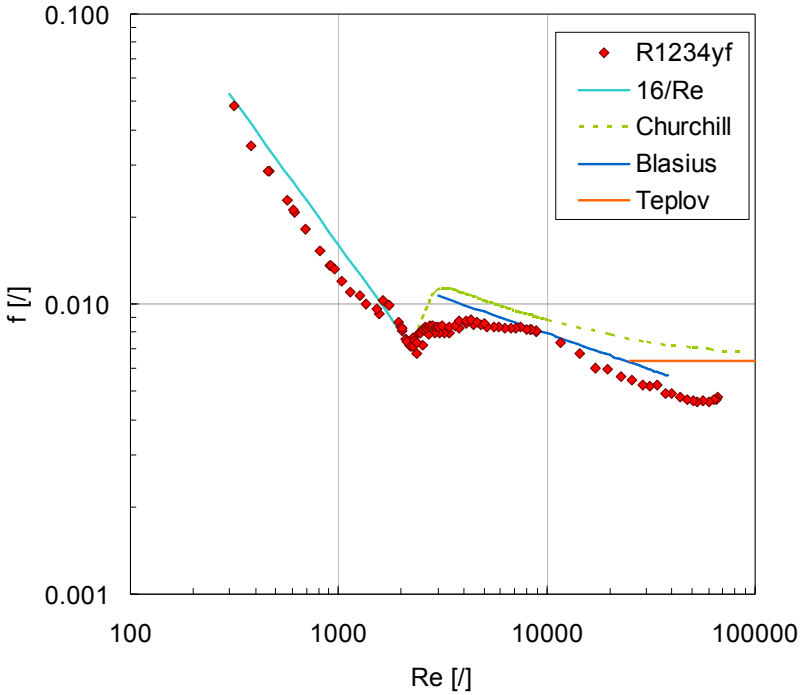

Figure 3.2. Experimental and calculated frictional resistance coefficient for R1234yf during single phase flow versus Reynolds number. The experimental coefficient was obtained from subtraction of measured pressure loss and sum of local pressure drops and pressure losses inside the stainless steel capillaries.

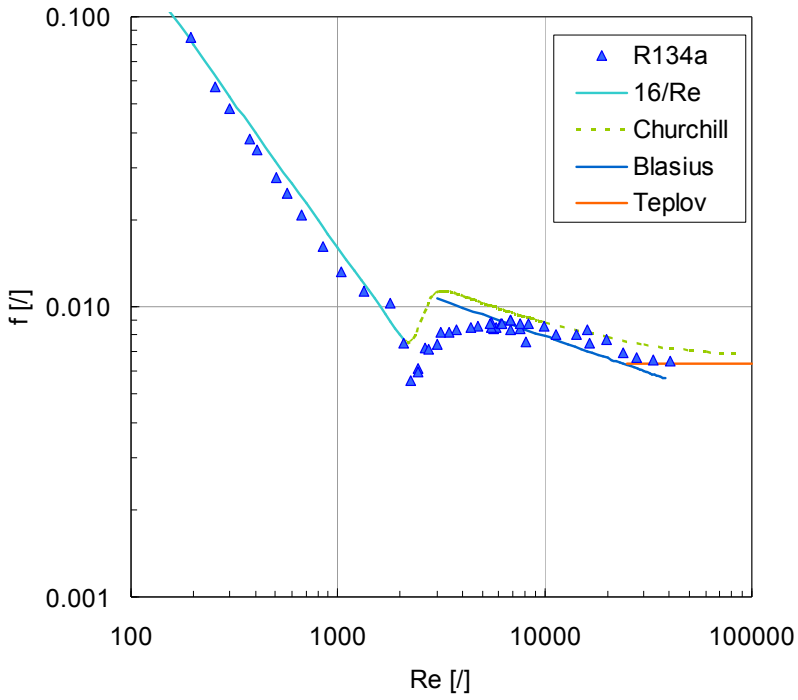

Figure 3.3. Experimental and calculated frictional resistance coefficient for R134a during single phase flow versus Reynolds number. The experimental coefficient was obtained from subtraction of measured pressure loss and sum of local pressure drops and pressure losses inside the stainless steel capillaries.

In Figure 3.2 and Figure 3.5Figure 3.3 are also reported Churchill (1977) and Teplov friction factors: the first model covers laminar, transition and turbulent zone and takes into consideration also the mean wall roughness R_a

$$f_{CHURCHILL} = 2 \cdot \left[\left(\frac{8}{\mathrm{Re}} \right)^{12} + \left[\left(2.457 \cdot \ln \left(\frac{1}{\frac{5.762}{\mathrm{Re}^{0.9}} + 0.27 \cdot \left(\frac{Ra}{d_h} \right)} \right) \right)^{16} + \left(\frac{37530}{\mathrm{Re}} \right)^{16} \right]^{-\frac{3}{2}} \right]^{\frac{1}{12}} \tag{3.17}$$

While the second one, valid only in the turbulent flow, is obtained as

$$f_{TEPLOV} = \frac{1}{\left[1.8 \cdot \log \left(\frac{8.3 \cdot d_h}{R_a} \right) \right]^2} \tag{3.18}$$

It can be clearly seen that for both the fluids, the classical Hagen-Poiseuille model for the friction factor in the laminar region, overestimates the experimental values. The disagreement is worse particularly for the R1234yf. This could be due to several reasons:

- the procedure used for the data reduction take into account several corrections factors which could causes this disagreement. In Figure 3.4 (left) are reported the experimental friction factors for R134a reduced without the corrections for the local pressure drops in the stainless steel pipes. Pressure drops are calculated from the experimental ones with:

$$\Delta p_{MS} = \Delta p_{tot} - \Delta p_{ss} \tag{3.19}$$

As in can be seen in Figure 3.4 the agreement between the Hagen-Poiseuille model and the measured values is improved.

- the flow after the expansion due to the enlargement of the duct from the 0.762 mm diameter to 0.96 mm is considered hydrodinamically developed without taking into account that there is a length (for the developed flow) for witch the traditional correlation are not suitable;

- the hydraulic diameters in the adiabatic sector is 0.762 mm, 25% less than the diameter of the copper tube (d_h=0.96 mm). This means that during test in laminar regime inside the copper tube, in the stainless steel pipe there could be a transition regime. Since the correlations used for the local pressure losses sand frictional pressure drops are very sensible to the flow regimes, this could affect the data reduction;

- the properties of R1234yf (calculated with REFPROP 9) may have still some uncertainties: in fact, when using a lower viscosity by 15% in the Re number, friction factor data would lay on the theoretical curve (Figure 3.4 right)

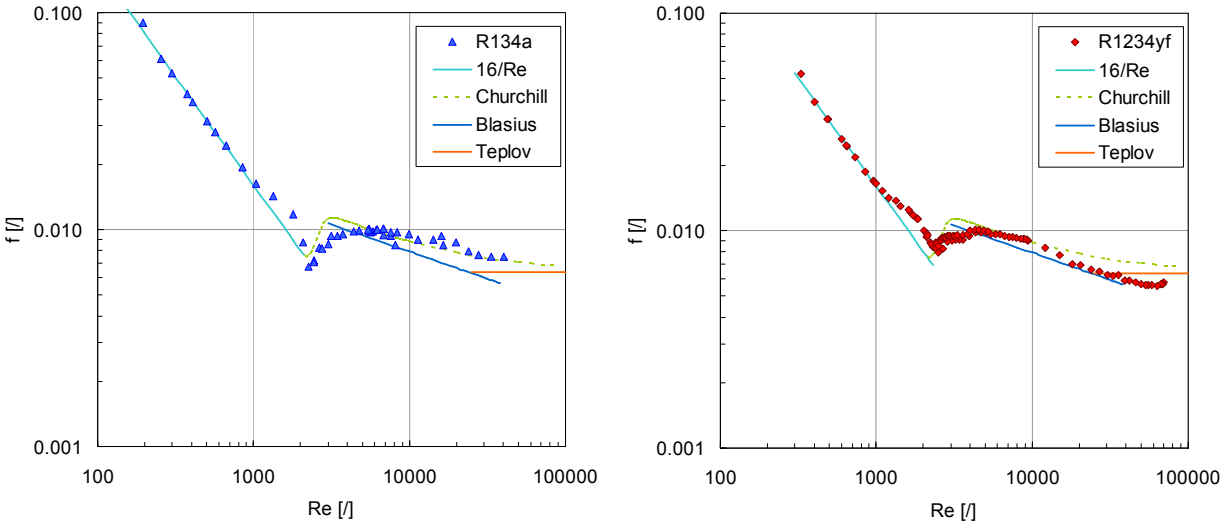

Figure 3.4. Experimental and calculated frictional resistance coefficient for R1234yf and R134a during single phase flow versus Reynolds number. In the left side are reported the values for R134a reduced without the corrections for the local pressure losses at the inlet and outlet of the test section. In the right side are reported the R134yf values obtained without the corrections for the local pressure losses at the inlet and outlet of the test section and using a lower viscosity by 5% with respect to the value given by REFPROP 9.

In order to clarify this disagreement, it has been decided to do an experimental study in another minichannel, where the pressure ports are inserted directly in the measuring sector at proper distance from the inlet and outlet for assuring the developed flow condition. In this way the corrections for the inlet and outlet local expansion and contractions and for the friction losses present in the circular minichannel are avoided.

3.3.2 Single phase pressure drop in a new semi square test section

A new test section has been realized from a copper rod with the same technique adopted for the square minichannel used for heat transfer measurements. The specifications given to the manufacturer were to build a square cross section minichannel with 0.96 mm side length and a

curvature radius of each corner equal to 0.15 mm. This would have lead to a hydraulic diameter of 1 mm. In this section, as already mentioned before, the pressure ports were designed directly in the channel contrary to the circular section. A picture of the new section is reported in Figure 3.6.

3.3.2.1 Friction factor for laminar flow

Single phase pressure drop tests were performed using water, R134a and R1234yf. The data reduction resulted very simple. In fact, the friction coefficient f is calculated

$$f = \frac{\rho \cdot d_h \cdot \Delta p}{2 \cdot G^2 \cdot L} \tag{3.20}$$

were Δp is the value measure between the two pressure ports, l is the distance between the two pressure ports equal to 227 mm, to each other, d_h is the hydraulic diameter equal to 1 mm, ρ is the fluid density and G is the specific mass flux.

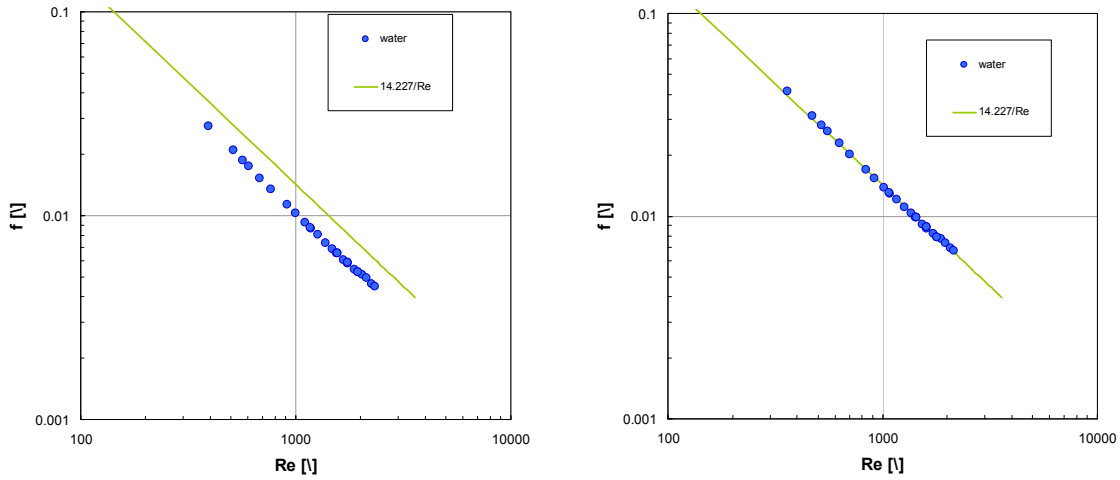

Figure 3.5. Friction factor versus Reynolds number for water. (left)Data reduced considering l=0.96mm, R=0.15 mm and dh=1 mm. (Right) Data reduced considering l=1.04mm, R=0.15 mm and dh=1.088 mm.

Figure 3.5(Left) reports the friction factor values obtained during laminar flow of water. It is also reported the Hagen-Poiseuille law for square section channel:

$$f = \frac{C}{\mathrm{Re}} = \frac{14.227}{\mathrm{Re}} \tag{3.21}$$

There is no agreement between the experimental values and the predicted ones. The real value of the constant in Eq. (3.21) should be even higher if the curved edges are considered. With the assumption of a square section with curve edge having a curvature radius of 0.15 mm, it has been estimate a value of 1.088 mm for the hydraulic diameter in order to have the agreement with the classical theory (see Figure 3.5 Right).
According to Celata *et al.* (2002) investigation, there is no influence of the surface roughness in the friction factor during laminar flow inside minichannles.
Furthermore, the laminar region is very sensitive to a minimum variation in the value used for the hydraulic diameter: from Eq. (3.20), explicating the specific mass flux in terms of the hydraulic diameter we obtain:

$$f = \frac{\rho \cdot \Delta p \cdot \pi^2}{32 \cdot L \cdot \dot{m}^2} \cdot d_h^5 \tag{3.22}$$

In the laminar flow region the friction factor is a function of the hydraulic diameter at the fifth power.

It has been decided, in order to better understand the cause of the disagreement, to cut the section and measure directly the geometrical parameters. In particular two cuts have been done, one after the first pressure port, and another one before the second pressure port. Figure 3.6 reports the microscope images which have been taken from the two cuts.

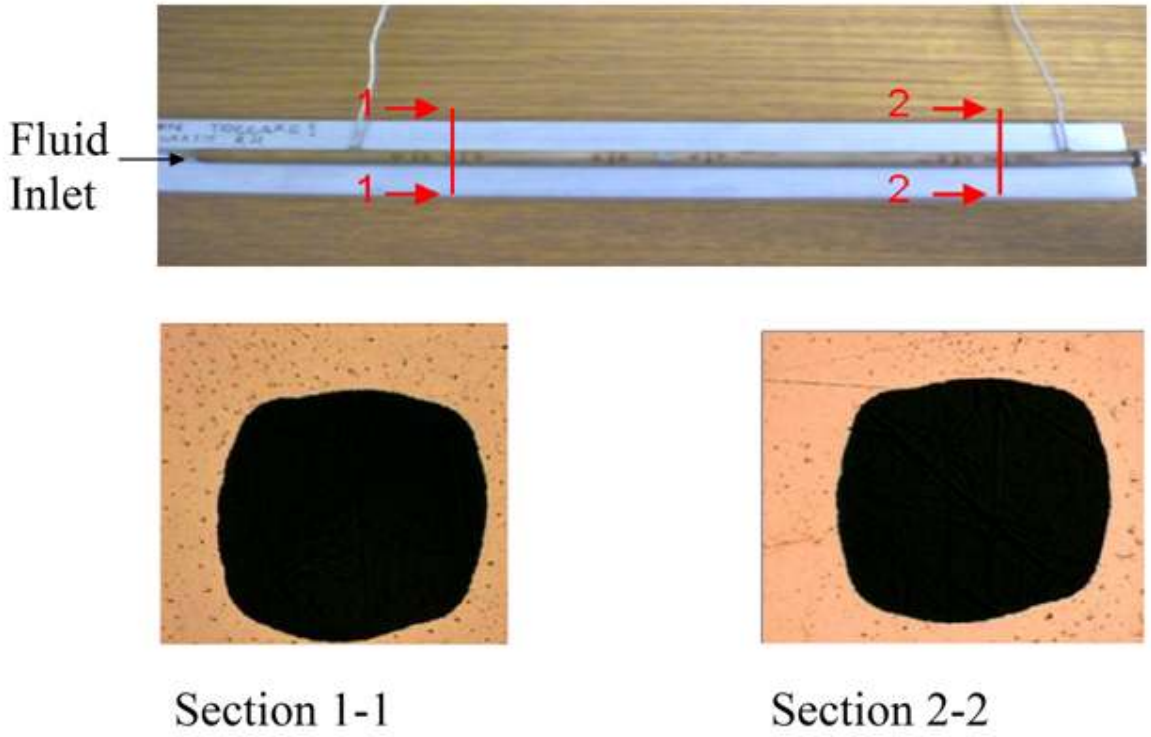

Figure 3.6. Section view of the test section.

From Figure 3.6 it is clear that the cross section is not a perfect square. Nevertheless, the shape is the same in all the length of the channel. In fact in Figure 3.7 the two section are superimposed and thy overlaps perfectly.

Figure 3.7. Overlapping of Section 1-1 and Section 2-2.

From the same images it has also been possible to measure the real values for the perimeter and cross section area. Table 3.5 summarized the measured values in the two sections; for the later considerations the mean values will be taken into account.

	Area [m^2]	Perimeter [m]	Hydraulic diameter[m]
Section 1-1	1.06E-06	0.003953	0.001073
Section 2-2	1.10E-06	0.004036	0.001087
Mean values	1.08E-06	0.003994	0.00108

Table 3.5. Measured mean values of the area, perimeter and hydraulic diameter for the two sections

Using the mean values reported in Table 3.5, the experimental data have been reduced again.
Interpolating the values of the friction factor versus the Reynolds number in the laminar region it has been obtained the value of the constant C in Eq. (3.21). In fact, in a logarithm graph, the relation between f and Re is a straight line, and the intercept represents the constant C:

$$\log(f) = \log(C) + \log(\mathrm{Re}) \tag{3.23}$$

For the two sections the calculate values for the intercept are:

	C
Section 1-1	13.56
Section 2-2	14.55
Mean values	14.06

Table 3.6. Calculated values of the constant C in Eq. (3.21)

In the literature the value of the C constant has been calculated for different type of geometry like for rectangular, triangular ducts, etc. Shah and London (1978) reported an analytical expression which allows calculating the value of C for other geometries considering a fully developed flow on an incompressible fluid. This expression will be presented in the next section and will be adopted for the evaluation of C for the sections reported in Figure 3.6.

3.3.2.2 Determination of the Hagen-Poiseuille constant for a particular geometry

Flow is laminar when the velocities are free of macroscopic fluctuations at any point of the flow field. For steady-state laminar flow, all velocities at a stationary point in the flow field remain constant with respect to time, but velocities may be different at different points. Laminar flow, also referred to as viscous or streamline flow, is characteristics of a viscous flow at low Reynolds number.
Laminar flow in a two-dimensional stationary straight duct is designed as *hydrodynamically fully developed* when the fluid velocity distribution at a cross section is independent of the axial distance x as shown in 0:

$$u = u(y, z) \tag{3.24}$$

$$v, w = 0 \tag{3.25}$$

where u is the fluid axial velocity, in x direction, y and z are Cartesian coordinates across the flow cross section while v is the fluid velocity component in y direction and w is the fluid velocity component in z direction. The fluid particles move in definite paths called streamlines, and there are no components of fluid velocity normal to the duct axis. In a fully developed laminar flow, the fluid appears to move by sliding laminae of infinitesimal thickness relative to adjacent layers. Fully

developed laminar flow persists up to Re<2300 for a duct length greater then the hydrodynamic entry length.

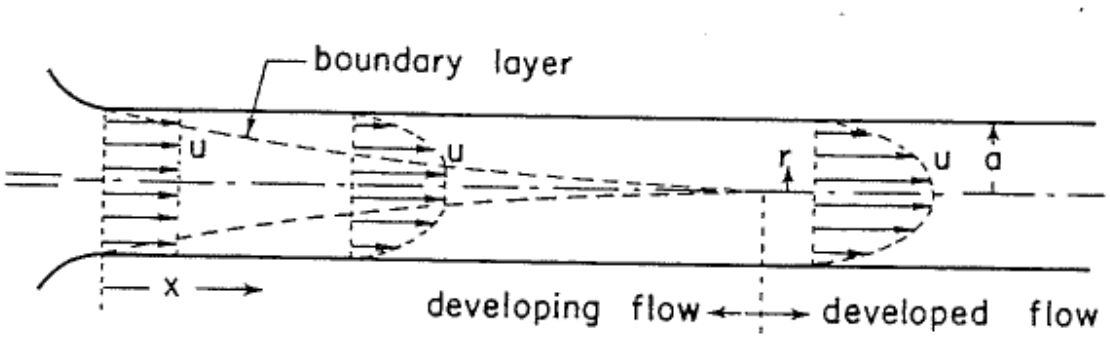

Figure 3.8. Developed and developing laminar flow. Image taken from Shah and London (1968).

3.3.2.3 Velocity problem for hydrodynamically developed flow

Consider a fully developed, steady-state laminar flow in a two-dimensional stationary duct with the boundary Γ (as in 0).

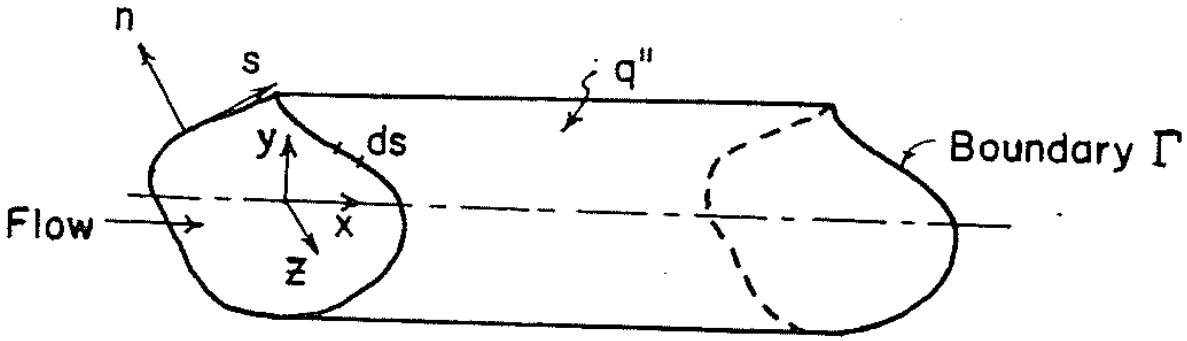

Figure 3.9. Duct of constant cross-sectional area. Image taken from Shah and London (1968).

The fluid is idealized as liquid or low-speed gas with the flow properties ρ, μ, and *cp*, constant (independent of fluid temperature). Moreover, body force such as gravity, centrifugal, Coriolis, and electromagnetic do not exists. The applicable momentum equation is:

$$\nabla^2 u = \frac{\partial^2 u}{\partial y^2} + \frac{\partial^2 u}{\partial z^2} = c_1 \tag{3.26}$$

The boundary condition for the velocity problem is the non slip condition, namely:

$$u = 0 \text{ on } \Gamma \tag{3.27}$$

where c_1 is defined as a pressure drop parameter.

The pressure drop in fully developed flow is caused by the wall shear. Fluid mean axial velocity and wall shear stress are two important physical quantities in the laminar flow problem.

The fluid mean axial velocity is defined as the integral average axial velocity with respect to the flow area *A*:

$$u_m = \frac{1}{A}\int_A u dA \tag{3.28}$$

where the velocity distribution *u* for a given duct geometry id determined from the Eq. (3.26).

The local wall shear stress for a Newtonian fluid flowing through the duct is expressed as the average wall shear stress with respect to the perimeter of the duct:

$$\tau_x = -\mu \cdot \left(\frac{\partial u}{\partial n} \right)_{w,m} \tag{3.29}$$

The flow length average wall shear stress is then defined as:

$$\tau_m = \frac{1}{x} \int_0^x \tau_x dx \tag{3.30}$$

The ratio of wall shear stress τ to the kinetic energy per unit volume is defined as the Fanning friction factor. The peripheral average axially local Fanning friction factor in then expressed as:

$$f_x = \frac{\tau_x}{\rho \cdot u_m^2 / 2} \tag{3.31}$$

For the case of fully developed flow through a duct, the velocity profile is invariant across any flow cross section. Consequently, the wall shear stress does not change axially, and the average friction factor is the same as the local friction factor. In this case, the constant-density pressure drop across two flow sections, separated by a distance *L*, takes the following form:

$$\frac{\Delta p}{\rho \cdot u_m^2 / 2} = f \cdot \frac{4 \cdot L}{d_h} \tag{3.32}$$

In the fully developed region, Eq. (3.32) may be rearranged using the definition of Re and using the constant *c1* from Eq. (7-3), so that

$$f \cdot \mathrm{Re} = - \cdot \frac{c_1 \cdot d_h}{2 \cdot u_m} \tag{3.33}$$

Also, based on the solution of the differential equation (3.26), it can be shown that

$$f \cdot \mathrm{Re} = C \tag{3.34}$$

where *C* is a constant value dependent on the geometry of the channel cross section.

Steady state fully developed laminar flow of an incompressible fluid through a stationary circular duct is referred to as Hagen-Poiseuille flow. For a circular tube the friction factor-Reynolds number product is:

$$f\,\mathrm{Re} = 16 \tag{3.35}$$

This procedure has been used for determining the *C* constant for the duct reported in Paragraph 3.3.2.2. A matlab code was written in order to solve the differential equation (3.26), with an arbitrary value of the constant c1 and the boundary conditions given by Eq. (3.27). One the real geometry profile was imported, the partial differential equation (3.26) was resolved using finite elements method.

The resulting velocity field is reported in Figure 3.10. The fluid mean axial velocity *um* has been calculated by Eq. (3.28) and finally the friction factor-Reynolds product has been obtained by Eq. (3.33) for the two sections:

	C
Section 1-1	14.11
Section 2-2	14.09
Mean values	14.10

Table 3.7. Calculated C values on the real section 1 and Section2 profiles of Figure 3.6.

In order to test the numerical procedure, the friction factor-Reynolds product was also calculated for a circular channel and for a square channel. The numerical results perfectly agree with Hagen Poiseuille equation (3.35) for the circular channel.

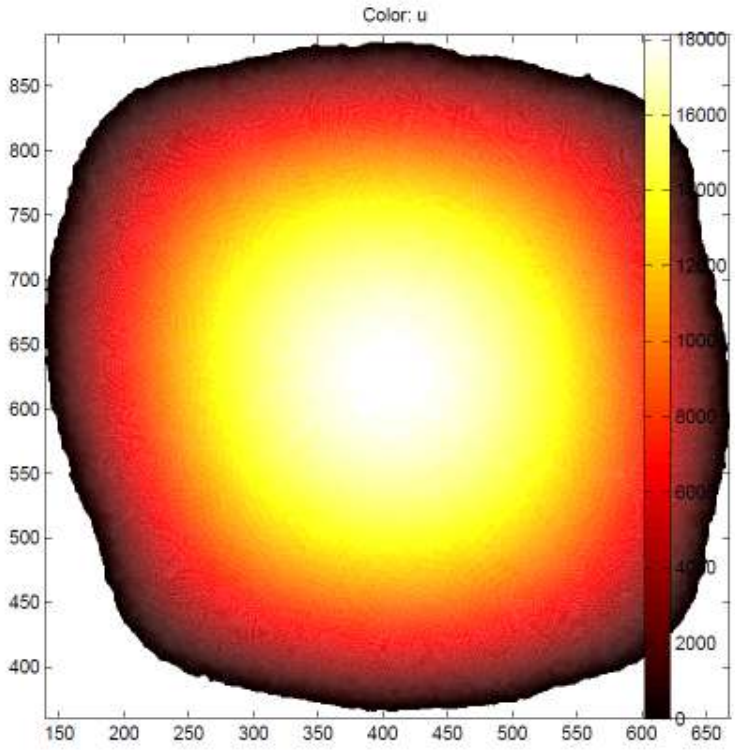

Figure 3.10. Velocity profile obtained from the solution of Eq. (3.26). Velocity is represented in Pixel/s.

3.3.2.4 Experimental results

The experimental friction factor has been obtained from pressure drop and mass flow rate measurements as reported in Eq. (3.20). The distance between the pressure ports L is 0.227 mm.
Tests with R134a and R1234yf have been done in the same section during liquid and vapour single phase flow. In the turbulent region 4000<Re<10000 the friction factor has been compared with the classical formula presented by Blasius for circular ducts:

$$f = \frac{0.079}{\mathrm{Re}^{0.25}} \tag{3.36}$$

Figure 3.11 reports the experimental values measured with water, R134a and R1234yf and reduced considering the real hydraulic diameter (1.08 mm). In the laminar region it is represented the classical theory with the constant C calculated as described before. It can be seen the good agreement in the laminar region with the correlation f Re =14.10; in the turbulent region a good estimation is obtained by the Blasius equation (3.36).
Comparing the mean values of C obtained from the intercept of the friction factor curve and the calculated one through the solution of Eq. (3.33), the disagreement is of -0.26%.
These good results allow to draw the following conclusions:
- classical correlations developed for conventional channels can predict frictional factor in laminar flow also for minichannels;

- corrections used in Eq.(3.15) for the local pressure drops at the inlet and outlet of the circular minichannel may be the cause of the poor agreement between the Hagen-Poiseuille equation and the R134a data reported in Figure 3.3;
- if the cross section geometry of a duct is known , i.e. circular, square, rectangular, etc, the pressure drops measurements in the laminar region could be used as an indirect method for determining the hydraulic diameter of the duct.
- R1234yf data seems to be in less agreement with the classical theory respect to water and R134a: this confirm that there is still a lack of precision in the estimation of its properties. In fact, when using a lower viscosity by 5% in the Re number, friction factor data would lay on the theoretical curve.

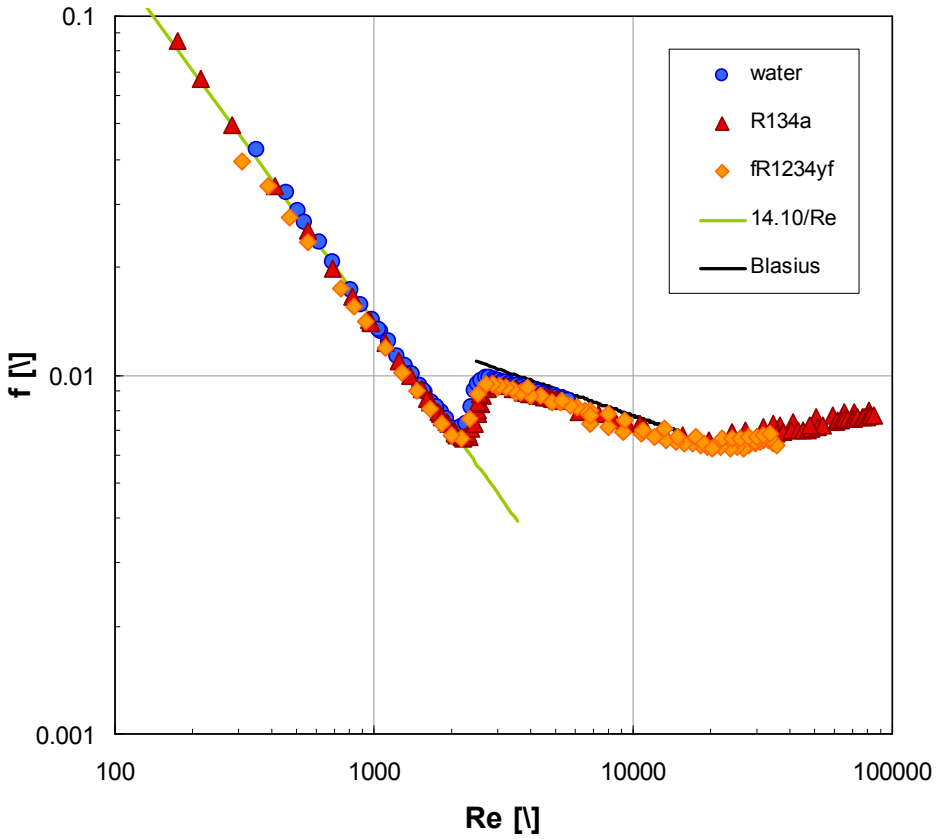

Figure 3.11. Friction factor versus Reynolds number for water, R134a and R1234yf. Data have been reduced with the measured geometric parameter.

3.3.3 Single-phase pressure drop in the square minichannel

3.3.3.1 Geometrical parameters definition

In the previous paragraph (3.3.2), it has been defined and validated an indirect technique for determining the hydraulic diameter of ducts with pressure drops measurements during laminar

single phase flow. This technique has been applied for the characterization of the square minichannel used during two phase heat transfer measurements.
It has been assumed a square cross section (Figure 3.12 reports an image taken with a micro endoscope inside the minichannel) and a curvature radius R equal to 0.15 mm (as declared from the manufacturer of the minichannel).
An iterative procedure has been applied in order to define the hydraulic diameter d_h of the channel:

1) Hypothesize a first tentative value for d_h
2) Calculation of the C value through resolution of Eq. (3.33)
3) Verify agreement between experimental values and predicted with the classical theory Eq. (3.34)
4) If the test is positive the geometrical parameters are corrected otherwise continue with the iterations assuming another value for d_h.

After some iterations, it has been found that the square minichannel has the following characteristics (see Figure 3.12):
-side length L=1.18 mm
-hydraulic diameter D_h= 1.23 mm obtained as:

$$d_h = \frac{4 \cdot A}{P}$$
$$A = L^2 - R^2 \cdot (4 - \pi)$$
$$P = 4 \cdot L - R \cdot (8 - 2 \cdot \pi) \qquad (3.37)$$

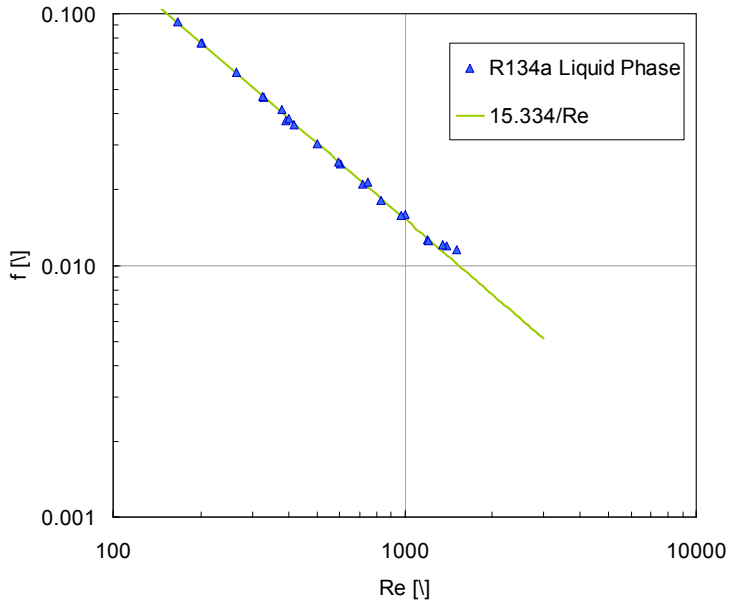

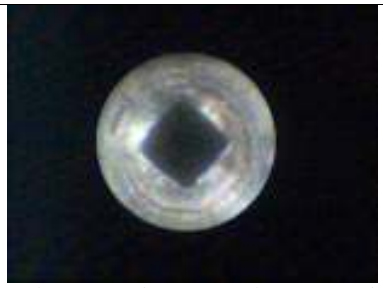

Micro endoscope image of the minichannel inside

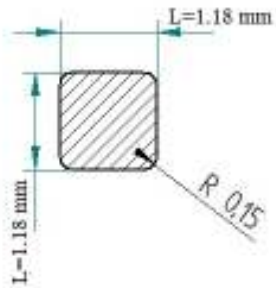

Figure 3.12. Friction factor versus Reynolds number for R134a (left). Data reduced considering the geometric parameters reported in the right side L=1.18mm, R=0.15 mm and dh=1.23 mm.

The resolution of Eq. (3.33) for the cross section just defined resulted in a value of 15.334 for the C constant.

$$f \cdot \mathrm{Re} = 15.334 \qquad (3.38)$$

As it can be seen in Figure 3.12 the experimental values measured with R134a follow very well the laminar theory for the friction factor. As for the square section analyzed in the previous paragraph (3.3.2), the reduction of experimental data is easier compared to the circular section: in fact, the pressure ports are inserted in two stainless steel pipes before and after the copper pipe, but they have the same cross section area of the measuring channels. Therefore, no corrections for local pressure drops have to be applied.

3.3.3.2 Experimental results

The friction factor has been measured during adiabatic flow of R134a and R1234yf in subcooled liquid state and in superheated vapour state. The distance L between pressure ports is equal to 0.249 m. Since in the turbulent region it depends on the surface roughness, the internal surface roughness of the copper channel has been measured with the digital surface roughness machine ZEISS-TSK Surfcom 1400A. The measurements have been performed at different positions. The mean roughness Ra, as defined by the ISO 4287:1997, ranges between 0.80 μm and 1.32 μm, with a mean value equal to 1.02 μm.
The experimental friction factor has been obtained from pressure drop and mass flow rate measurements as reported in Eq. (3.20).
The fully developed turbulent friction factor is compared against the classical Blasius's formula corrected for the square cross section of the minichannel. According to Bhatti and Shah (1987) for rectangular ducts, in the range $5000<Re<10^7$, the friction factor should be given by:

$$f = \left(1.0875 - 0.1125 \cdot \alpha^*\right) \cdot f_c$$

$$\alpha^* = b/a \qquad (3.39)$$

Where f_c is the friction factor of Blasius give by (3.36), while a and b are the lengths of a rectangular ducts. In this case, a=b and therefore $\alpha^* = 1$.

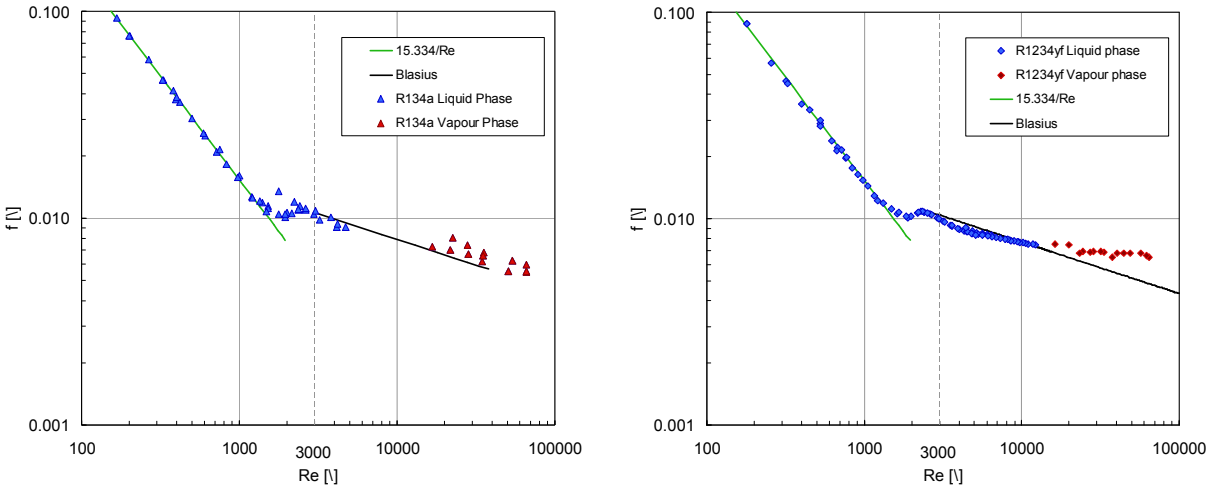

Figure 3.13. (Left) Friction factor versus Reynolds number for R134a. (Right) Friction factor versus Reynolds number for R1234yf

In Figure 3.13 the measured friction factor is reported as a function of Reynolds number. Two different symbols are used in order to distinguish experimental points measured during vapour phase and liquid phase flow: in the left side of the figure are reported the values measured with

R134a, while in the right side the ones measured with R1234yf. In the laminar region experimental data are in good agreement with the correlation (3.38). In the turbulent zone a good estimation of the experimental points is obtained by the Blasius equation corrected for square channel as indicated in Eq. (3.39) for both fluids.

3.3.4 New circular test sections for single and two phase pressure drop measurements

In all the experimental pressure drops results presented up to now, during the data reduction several correction factors have been introduced for taking into account local phenomena due to cross section shape changes, etc.. Even if the square minichannel (d_h=1.23 mm) has the pressure ports in two inox adiabatic sectors having the same cross section of the copper tube, single phase and two phase pressure drops measurements should account for the frictional pressure drops in these adiabatic areas, which should be subtracted to the total Δp measured value. If during laminar flow the roughness doesn't play any effects, different is the case in turbulent conditions. The mean roughness value (Ra_{cu}) for the copper in square minichannel has been measured as 1.02 μm, which is 8% higher than the value measured in the inox area: in fact the mean inox roughness (Ra_{inox}) is 0.93 μm. In order to study the effect of the roughness during single and two phase flow in minichannels, it has been decided to build two new circular test sections made by copper, with the pressure ports directly inserted in the copper tube, like for the semi square minichannel with a hydraulic diameter of 1.08 mm. Furthermore a new pre-section has been design in order to avoid the limits for the maximum water temperature (40°C) presents in the circular and square minichannel pre-sections. Figure 3.14 reports a sketch of the new pre-section. It is a counter flow heat exchange made by a brass cylinder where the refrigerant flows inside a stainless steel pipe (d_h=1.7 mm) and the water flows outside. The water path has been designed in order to reduce the external thermal resistant: from the inlet to the outlet water is forced to follow a coil path formed by the refrigerant pipe (which has been rolled up to a PTFE cylinder) and the internal wall of the brass cylinder. In the right side of Figure 3.14 is represented a detail of the internal design.
With the new pre-section it is possible to vaporize or condensate the refrigerants without any constrains for the temperature of the secondary fluid. In this way, the gap presents in the two phase graphs previously reported at some vapour quality ranges values could be filled.
Refrigerant state is defined at the inlet of the pre-section from the measurements of its temperature and pressure. The outlet conditions are calculated from the heat exchanged with the water. In fact, two thermocouples, at the inlet and outlet of the water side and a thermopile are installed. The exchanged heat results:

$$Q = \dot{m}_w \cdot cp_w \cdot \left(\Delta T_w\right) \tag{3.40}$$

where ΔT_w is recorded with the thermophile and cp_w (hysobaric heat capacity) is calculated from the water temperature measured at the inlet. The refrigerant state at the pre-section outlet results from the heat balance

$$\dot{m}_{ref} \cdot \left|\Delta h_{ref}\right| = \dot{m}_w \cdot cp_w \cdot \left|\Delta T_w\right| \tag{3.41}$$

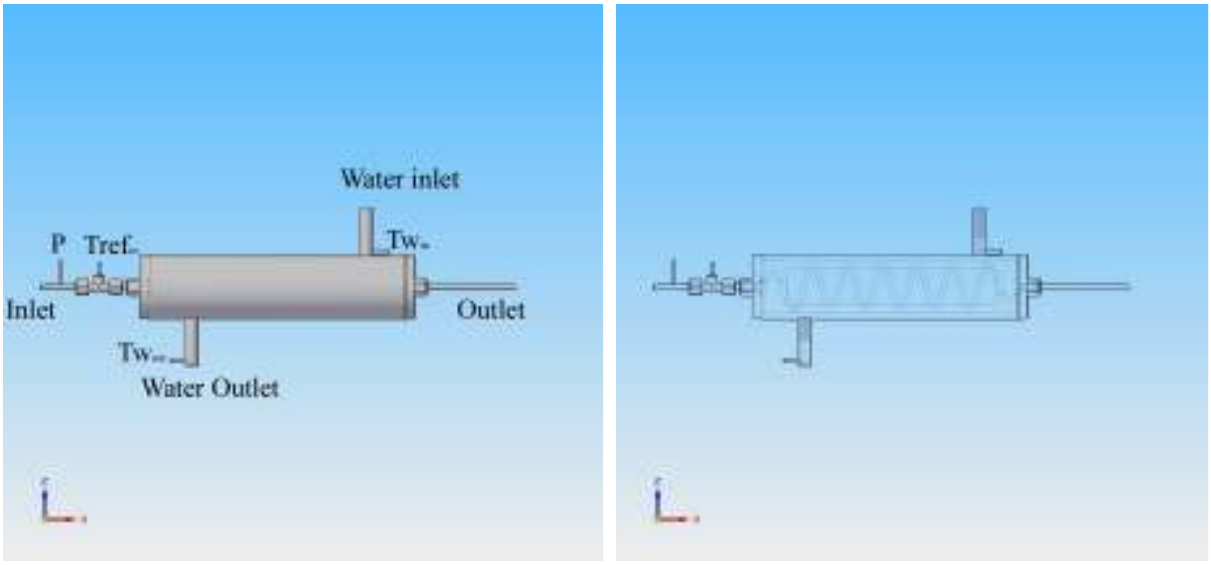

Figure 3.14. (Left) New pre-section rendering. (Right) Pre section view of the refrigerant and water paths

Two circular channels with 0.96 and 2 mm hydraulic diameter have been designed and realized with the aim of performing single and two phase pressure drops measurements. The length of the new sections have been decided upon some pressure drops estimations with the Friedel (1979) and Cavallini *et al.* (2009) models. Table 3.8 reports the calculate pressure drops according the two models for the circular minichannels with 0.96 mm internal diameter and a length between the pressure ports of 0.22 m. The optimal length has been chosen as the solution that allows having the experimental pressure drops in the range between 100 and 10^5 Pa, in order to be able to measure them with the differential pressure transducers already installed in the test set-up. Figure 3.15 reports the technical drawing of the 0.96 mm section.

	Friedel (1979)		**CAVALLINI *et al.* (2009)**	
G	**DpMax**	**DpMin**	**DpMax**	**DpMin**
[kg m^{-2} s^{-1}]	**[kPa]**	**[kPa]**	**[kPa]**	**[kPa]**
200	4.4572	0.3784	4.2966	0.2838
400	14.1944	1.2056	14.168	1.0032
600	28.0192	2.4024	28.0368	2.112
800	45.408	3.8984	44.792	3.5904
1000	66.0968	5.6848	63.096	5.412
1200	89.8392	7.7352	85.4216	7.5328

Table 3.8. Calculations of pressure drops with Friedel (1979) and Cavallini *et al.* (2009) models for the 0.96 mm circular minichannels with a length of 0.22m

The same procedure has been done for the 2 mm circular section and the length between the pressure ports has been calculated to be 0.44 m (see Figure 3.16).

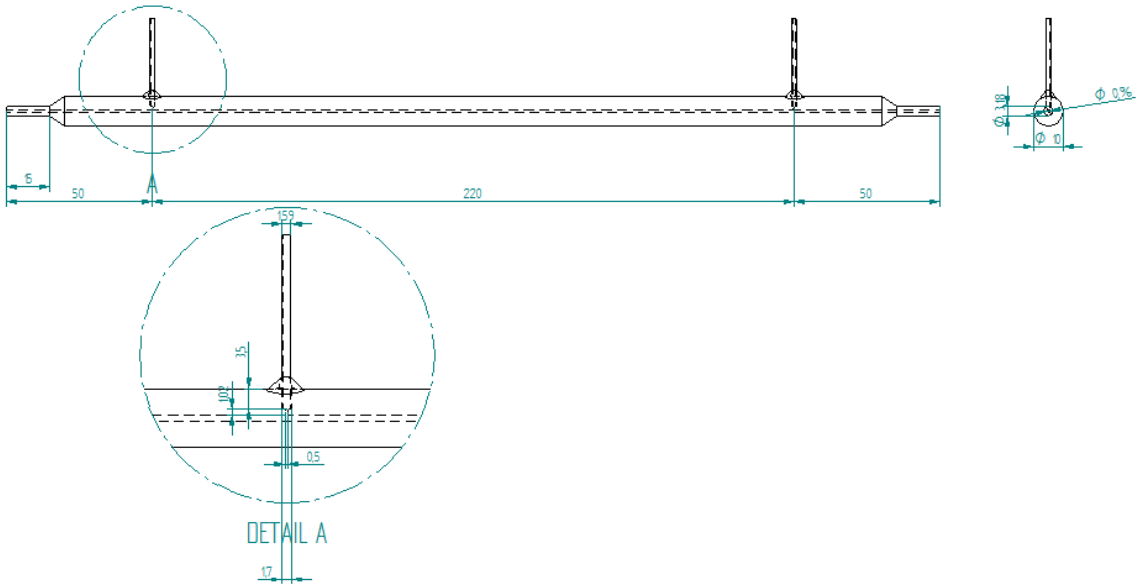

Figure 3.15. Sketch of the 0.96 mm inner diameter circular test section. Dimensions are in mm.

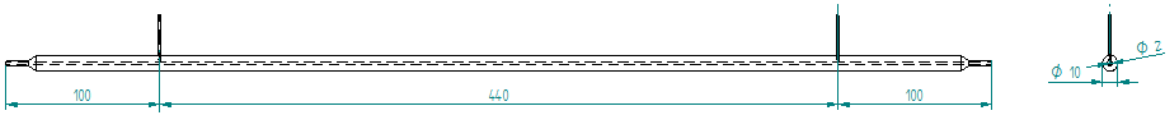

Figure 3.16. Sketch of the 2 mm inner diameter circular test section. Dimensions are in mm.

3.3.4.1 Realization of the stainless steel pressure ports

The most crucial part in realizing the two new sections was how to make the pressure ports, in order to be sure not to influence the measurements. The firs decision was the distance from the inlet and the outlet of the channel. To be out of the developing flow length, the two pressure ports have been made at a distance equal to 50 times the hydraulic diameter from the inlet and the outlet. The copper channels were then predrilled with holes of 0.5 mm for the pressure ports accommodation (see Detail A in Figure 3.15 and Figure 3.17 Left). To avoid eventual melted material from obstructing the flow passage and to reduce oxidation of the test tube, soldering was performed at constant nitrogen flow within the Minichannel and on external side of the tube (see Figure 3.17 Right). Several samples of the same size were soldered in this way to check the quality of the joint and any residual left inside the channel. All samples were joined successfully using this technique, which was deemed highly effective for soldering capillaries. Moreover, nitrogen played triple role in the soldering process. First, the oxidation process was inhibited, second, internal overpressure prevented melted material from entering the minichannel and last, the flowing gas cooled down the heated spots more rapidly, which helped to maintain tensile strength of the materials “unchanged”.

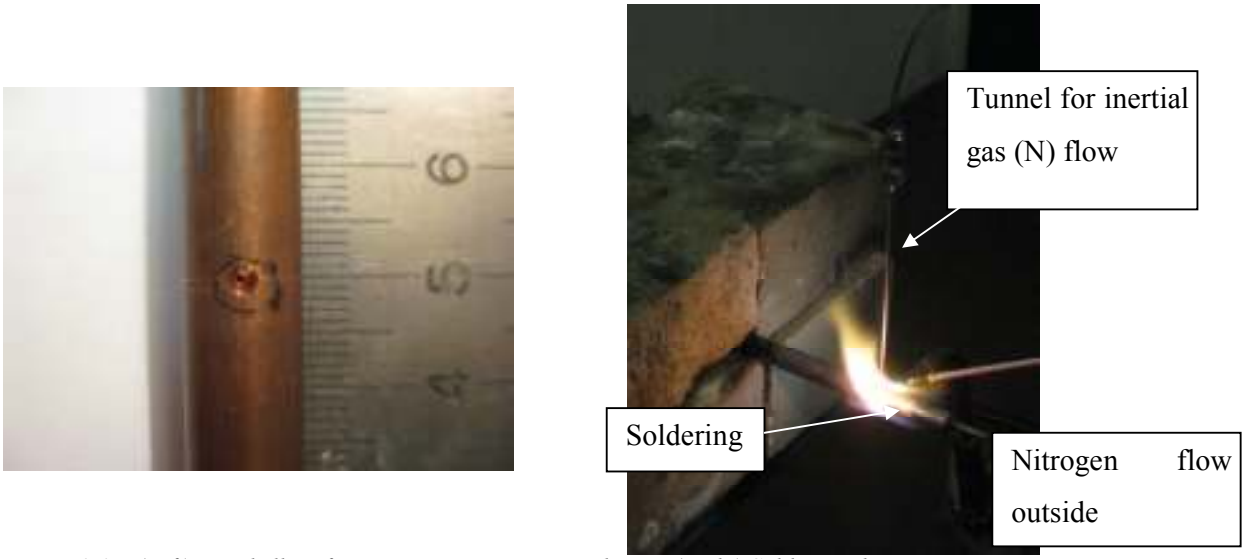

Figure 3.17. (Left) Pre-drilling for pressure port accommodation. (Right) Soldering the pressure ports

3.3.4.2 Experimental results

Single phase pressure drop experiments were performed during adiabatic flow of R134a in both the new sections. Data at low Re number were recorded during subcooled liquid tests: refrigerant from the post-condenser was sent through the dehumidifier and was pumped through the Coriolis-effect mass flow meter directly inside the test sections. Data at high Reynolds were carried out with superheated vapor: in this case the refrigerant before entering the measuring sector was vaporized and superheated in the evaporator.

Figure 3.18 and Figure 3.19 report the experimental friction factor measured during adiabatic single phase flow of R134a in the 0.96 mm and 2 mm circular minichannels respectively. The experimental friction factor has been obtained from pressure drop and mass flow rate measurements as reported in Eq. (3.20).

In both cases the agreement with the Hagen-Poiseuille model is very good in the laminar region. For Re<1000 the distance from the inlet of he pressure tap is in both case is higher than the length of the hydrodynamic developing region L_h given by Kandlikar *et al.* (2006) by the following equation:

$$L_h = 0.05 \cdot \mathrm{Re} \cdot d_h \tag{3.42}$$

Interesting is also the analysis of the transition region. Some of the initial studies indicated an early transition to turbulent flow in microchannels. However, a number of recent studies showed that the laminar-to-turbulent transition remains unchanged. Bucci *et al*. (2004) found that the transition occurred around Ret =2000 for circular microtubes 171–520 μm in diameter. The results of Baviere *et al*. (2004) also indicate that the laminar-to-turbulent transition in smooth microchannels is not influenced by the channel dimensions and occurs around 2300. Similar results were reported by a number of investigators, including Bucci *et al*. (2004), Schmitt and Kandlikar (2005), for minichannels with d_h <1 mm; and Li *et al.* (2000) for 80μm≤ d_h ≤166.3μm.

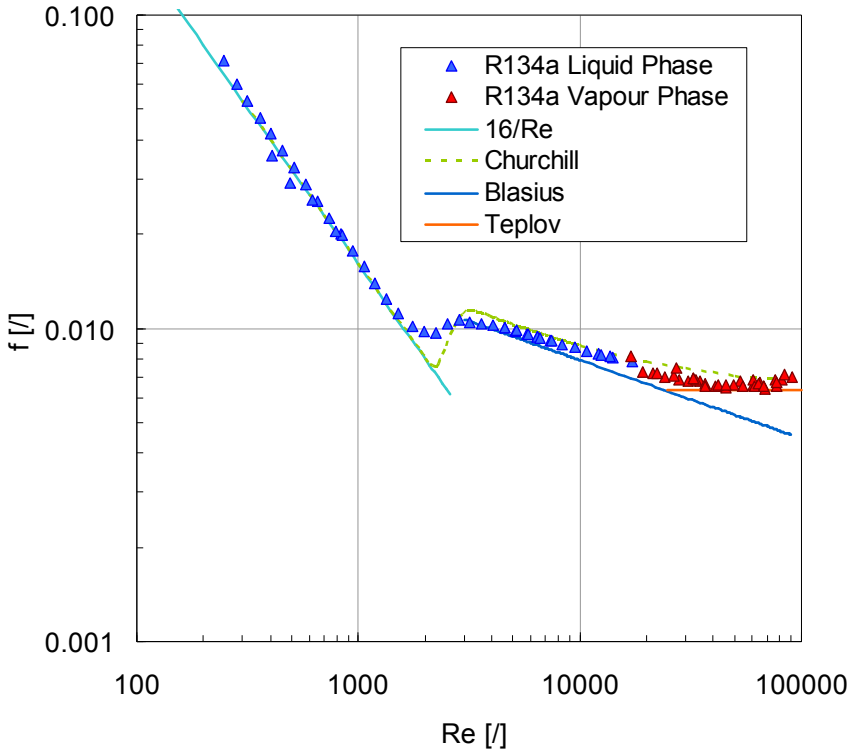

Figure 3.18. Friction factor versus Reynolds number for R134a flowing in the 0.96 mm circular minichannel.

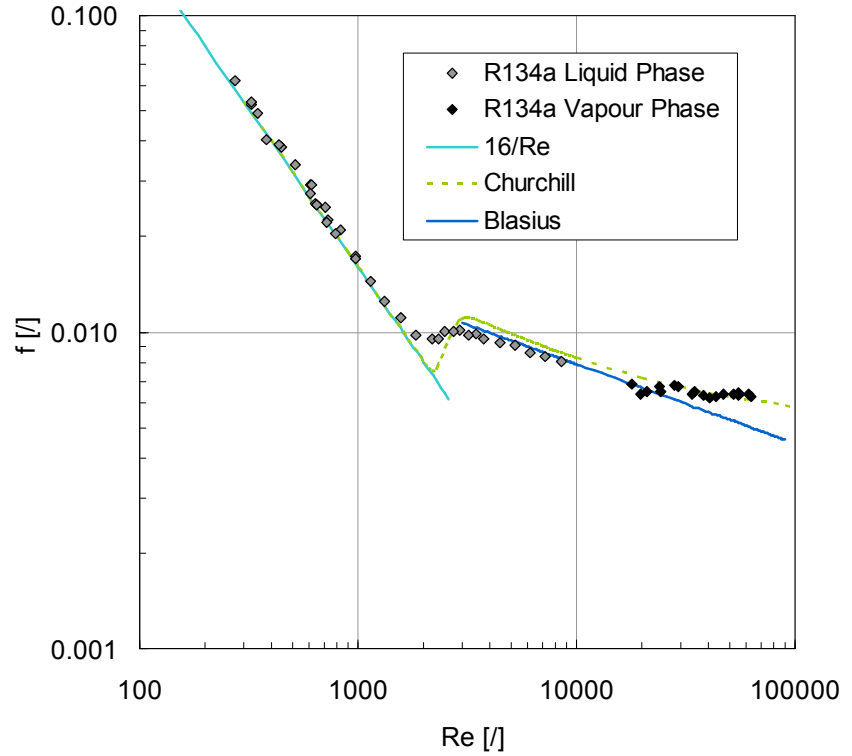

Figure 3.19. Friction factor versus Reynolds number for R134a flowing in the 2 mm circular minichannel.

Figure 3.20 reports the comparison between the friction factors data measured in the two sections. It can be seen that the transition is not influenced by the hydraulic diameter and occurred at *Ret* =1800.

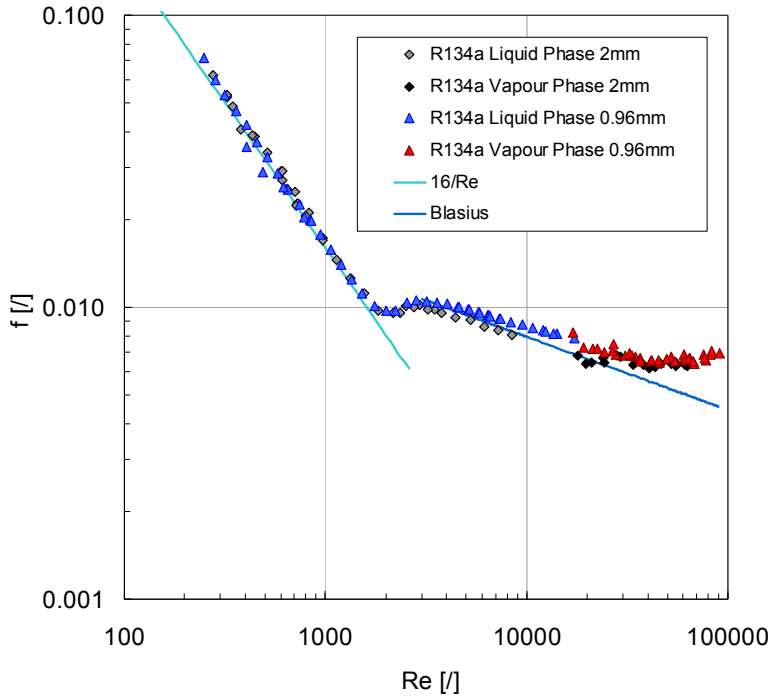

Figure 3.20. Friction factor versus Reynolds number: comparison between 0.96 mm and 2 mm diameter minichannels.

Schmitt and Kandlikar (2005) conducted careful experiments with plain and saw tooth roughened channels with air and water. Their results for smooth rectangular channels showed a transition Reynolds number between 2000 and 2300, but for increasing relative roughness values there was a decreasing transition Reynolds numbers. Then, roughness is an important parameter to take into account not only in the turbulent flow regime but also in the transition from laminar to turbulent. From Figure 3.18 and Figure 3.19 it can also be noted the slightly different behavior of the two minichannels in the turbulent regime: wile the 0.96 mm channel seems to follow the Churchill (1977) model, the 2 mm channel is very closed to the Blasius model for Re<22000 and then, for higher turbulence, is very closed to the Churchill one.
In order to better understand the influence of roughness in the flow regime and the in the friction factor measurements, the internal profile of several samples from the new test sections will be analyzed. Furthermore, from two phase pressure drop tests, it will be also possible to analyze the influence of the surface profile during adiabatic two phase flow inside minichannles. This part of the work is under consideration and il not reported in the present thesis.

3.4 Two phase pressure drop

3.4.1 Pressure drop during adiabatic vapour-liquid flow in the circular (d_h=0.96 mm) minichannel

During experimental test for measuring two phase pressure drops, subcooled refrigerant from the post-condenser was sent through the dehumidifier and was pumped through the Coriolis-effect mass flow meter into the evaporator. There, the fluid was heated up, vaporized and superheated. Superheated refrigerant entered the test section, where pressure and temperature were measured allowing to determine the superheated degree. Desired vapor quality at the inlet of the measuring sector was controlled with the heat output in the desuperheater. The vapour quality was calculated from the following equations:

$$x_{in\,MS} = \frac{H_{inMS} - H_L}{H_V - H_L} \tag{3.43}$$

$$H_{inMS} = HinPS - \frac{(\dot{m}_{wPS} \cdot cp_w \cdot \Delta T_{wPS}) + qdiss_{PS}}{\dot{m}_{ref}} \tag{3.44}$$

$$qdiss_{PS} = 0.16 \cdot (T_{wmeanPS} - T_{amb}) + 0.03 \tag{3.45}$$

where Eq.(3.45) represents the heat losses to the ambient of the water flowing in the pre-section and H_L and H_V are the saturate liquid and vapour enthalpies.

Pressure loss within the measuring circular section was obtained in analogous way to single-phase experiments. After the linear pressure losses for adiabatic sectors and the sum of local pressure drops for the two abrupt geometry changes were calculated (Paliwoda (1992)), the difference from overall experimental pressure loss was attributed to the measuring sector.

$$\Delta p_{MS} = \Delta p_{tot} - \left(\varsigma_{\exp} \cdot \beta_{\exp} + \varsigma_{cont} \cdot \beta_{cont} + 4 \cdot f_{inox} \cdot \frac{l_{inox}}{d_{h_{inox}}} \cdot \Theta \right) \cdot \frac{G_{inox}^2}{2 \cdot \rho} \tag{3.46}$$

where β_{cont}, Θ are two phase multipliers.

Since the pressure losses were obtained as a difference of experimental measurements and three important calculated values, the obtained results are associated to a significant experimental error. Therefore, it is preferred in this case to present pressure drop measurements as cumulative pressure drop rather than "semi experimental" discrete pressure drop values associated to linear loses within the measuring sector. Figure 3.21 reports the contributes to the total pressure losses due to abrupt geometry changes, frictional losses in the inox and in the copper areas during two phase adiabatic flow of R134a in the circular minichannel at 40 °C saturation temperature. The contribute of the local losses is around 5%, while the linear pressure losses in the two inox sectors and in the copper minichannel are 32 and 56% respectively.

Figure 3.22 shows the total experimental pressure drop measured with R1234yf and R134a at 40 °C saturation temperature at three different values of mass velocity: 400, 600 and 800 kg $m^{-2}s^{-1}$. The total pressure drop reported in the graph is the sum of the frictional pressure drop in the 228.5 mm long copper tube, the frictional pressure drop in the two 24 mm stainless steel tubes and the pressure losses due to change of cross area (from 0.76 mm diameter to 0.96 mm diameter and vice-versa).

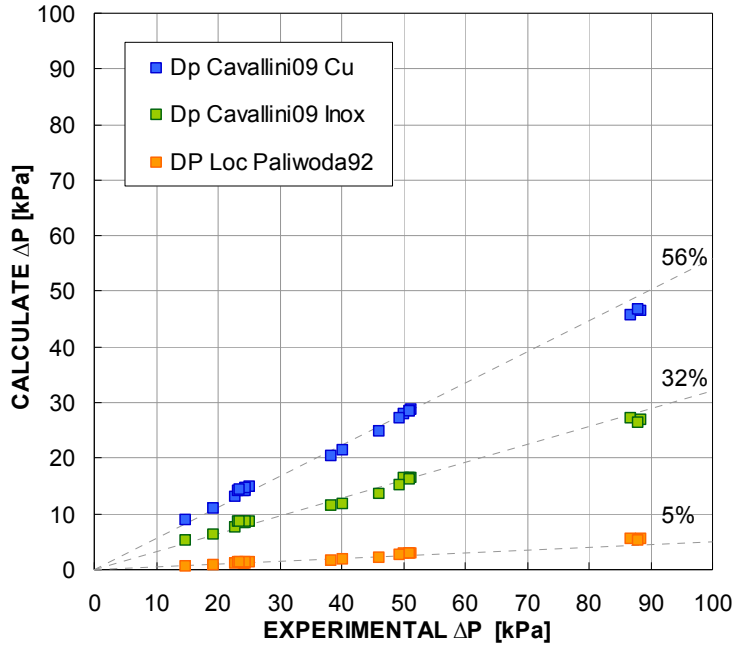

Figure 3.21. Calculated pressure drop within the studied geometry vs. experimental data. The linear pressure losses were calculated from Cavallini et al. (2009) model whereas Paliwoda (1992) was applied for local pressure drop calculation.

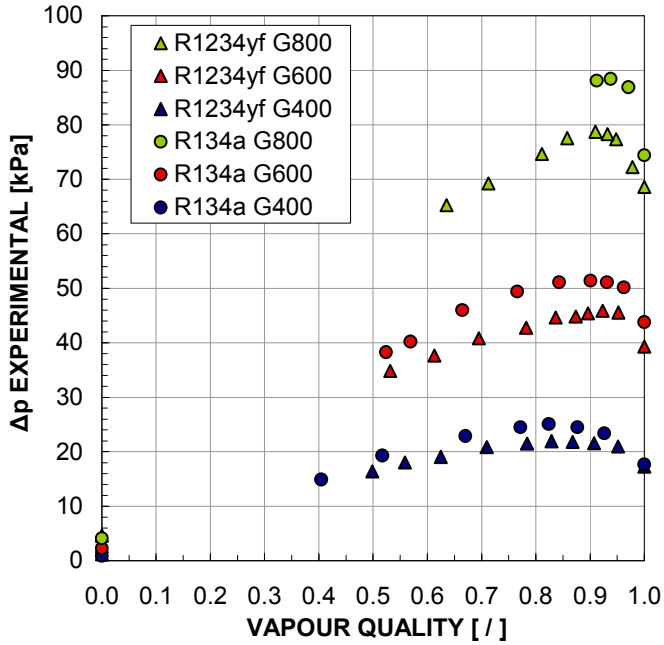

Figure 3.22. Experimental pressure losses during adiabatic two-phase flow of R1234yf and R134a at 40° C saturation temperature and at three different values of mass velocity (400, 600 and 800 kg $m^{-2}s^{-1}$) in the circular minichannel.

It can be seen that the fluid R1234yf displays a lower pressure drop by 10-12 % as compared to R134a, at the same operating conditions. This may be explained by looking at Table 1.2 at the reduced pressure of R1234yf, which is greater by 20% than that of R134a at 40 °C saturation temperature. Therefore, from this point of view R1234yf performs better than R134a.

3.4.1.1 Comparison against models

All the experimental data previously reported in Figure 3.22 were compared against fifteen different models available from the accessible literature. Linear pressure losses within the stainless steel capillaries and the measuring sector were calculated separately for each model and summed together with the two local pressure drops calculated by Paliwoda (1992). Overall calculated data were then compared against experimental measurements. The results of the comparison are reported from Figure 3.23 to Figure 3.33.

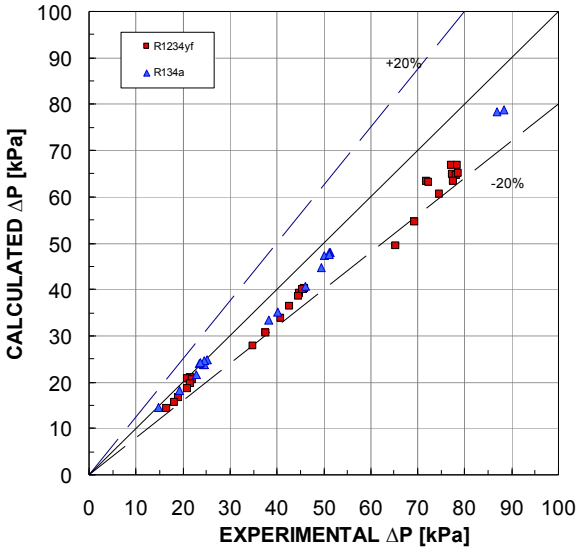

Figure 3.23. R134a and R1234yf data compared against Cavallini et al. (2009) model.

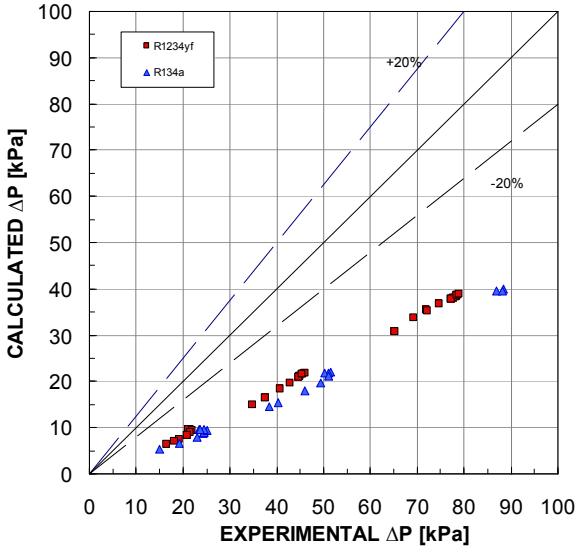

Figure 3.24. R134a and R1234yf data compared against Chen et al. (2001) model.

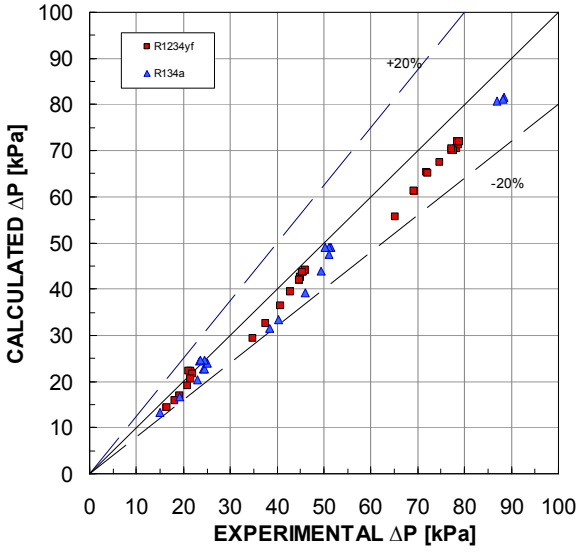

Figure 3.25. R134a and R1234yf data compared against Friedel (1979) model.

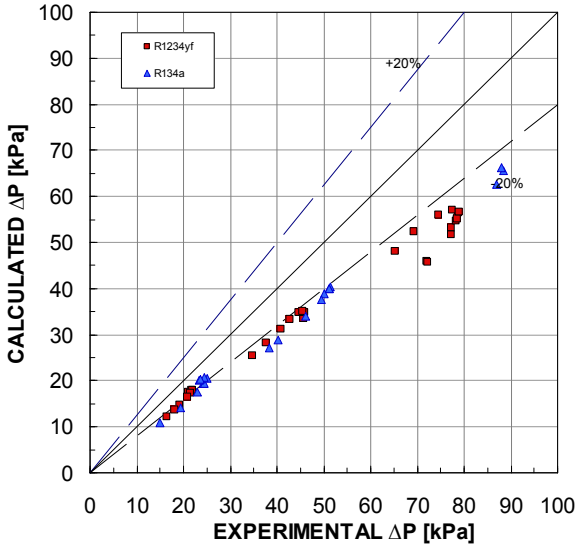

Figure 3.26. R134a and R1234yf data compared against Garimella et al. (2004) model.

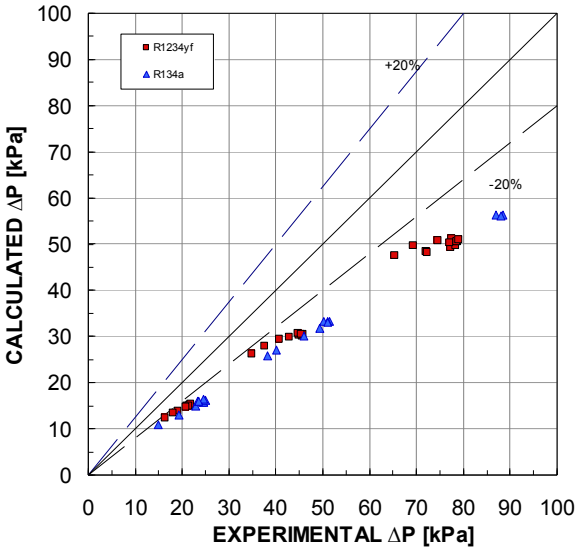

Figure 3.27. R134a and R1234yf data compared against Koyama et al. (2003) model.

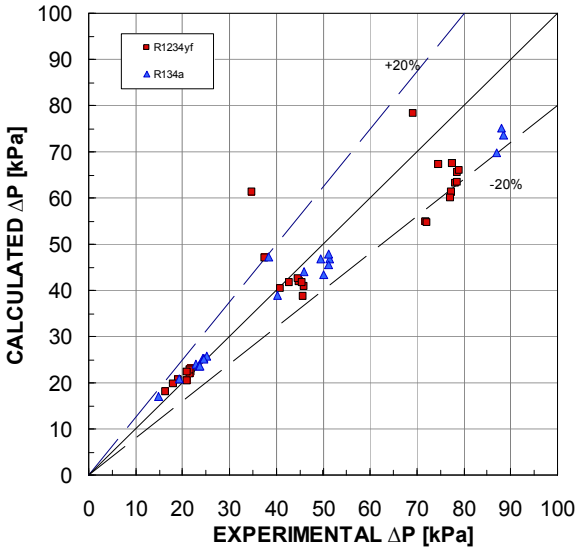

Figure 3.28. R134a and R1234yf data compared against Lockhart and Martinelli (1949) model.

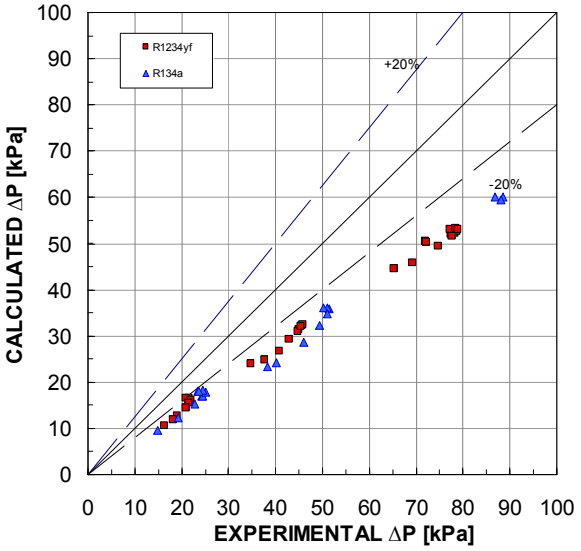

Figure 3.29. R134a and R1234yf data compared against Mishima and Hibiki (1996) model.

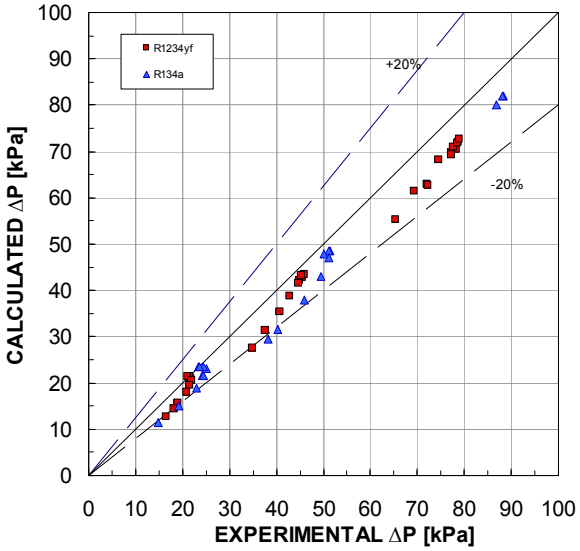

Figure 3.30. R134a and R1234yf data compared against Mueller Steinhagen and Heck (1986).

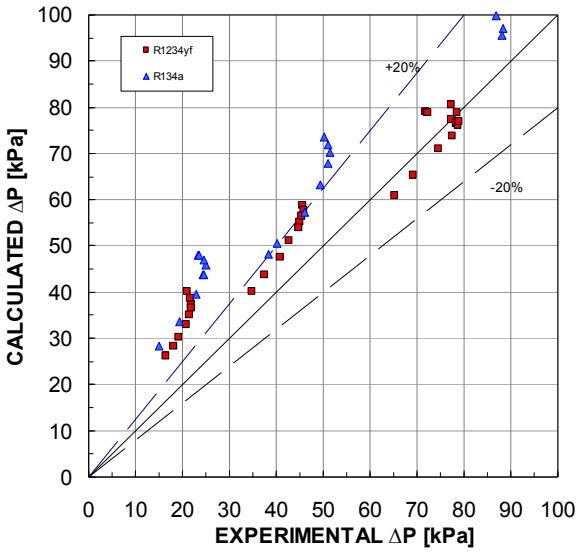

Figure 3.31. R134a and R1234yf data compared against Yan and Lin (1999) model.

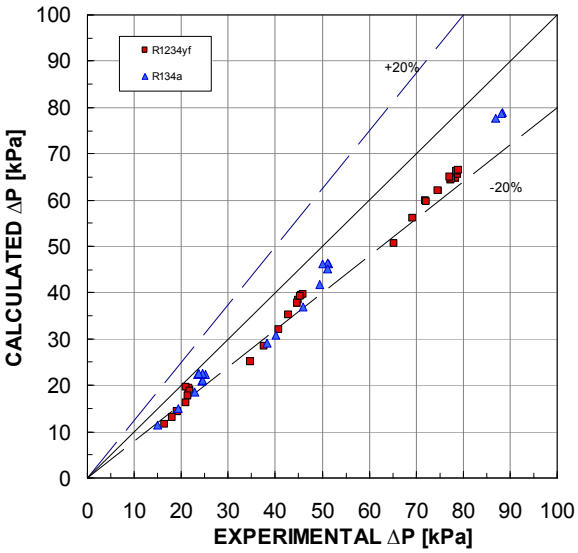

Figure 3.32. R134a and R1234yf data compared against Zhang and Webb (2001) model.

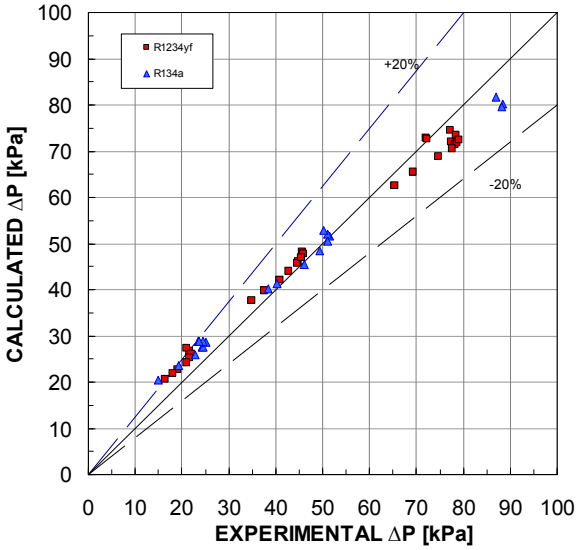

Figure 3.33. R134a and R1234yf data compared against Revellin and Thome (2007) model.

3.4.2 Pressure drop during adiabatic vapour-liquid flow in the semi square (d_h=1.08 mm) minichannel

Two phase pressure drop experiments during liquid-vapour adiabatic flow of R134a were performed in the semi square (d_h=1.08 mm) minichannel presented before in Paragraph 3.3.2. Subcooled refrigerant from the post-condenser was sent through the dehumidifier and was pumped through the Coriollis-effect mass flow meter into the evaporator where it was superheated. Then it entered the circular (d_h=0.96) test section where it was condensate using the pre-section and/or the measuring section in order to have the desired vapour quality at the inlet of the semi square

minichannel. In fact, this section was installed in series to the circular one as reported in Figure 3.34 and the equations used for the data reduction are the Eq. (3.44). Vapour enthalpy at the inlet of the circular presection were determined from the measured temperature and pressure. The water heat balance in the pre-section and in the measuring section allowed calculating the vapour conditions at the circular minichannel outlet. Furthermore, heat losses to the ambient in the length between the outlet of the circular test section and the inlet of the semi square minichannel were determined during single phase test and introduced in the data reduction.

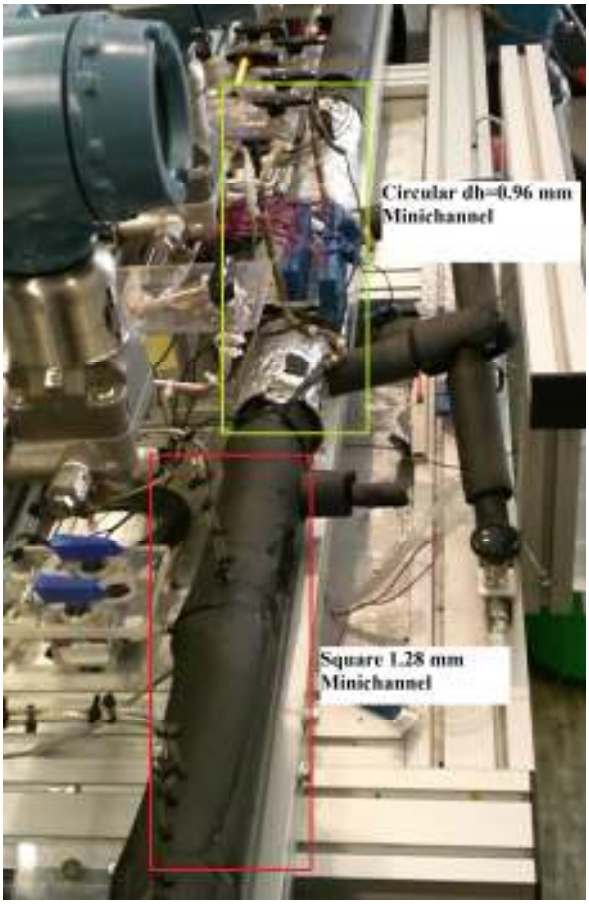

Figure 3.34. Photo of the semi square minichannel installed in series after the circular test section

$$x_{in} = \frac{H_{IN,TS} - H_L}{H_V - H_L}$$

$$H_{IN,TS} = H_{IN,CircularPS} - \left(\frac{Q_{CircularPS} + Q_{CircularMS}}{\dot{m}_{ref}} \right) + - \frac{Qdiss_{OutCircular-InSemiSquare}}{\dot{m}_{ref}}$$

$$H_{IN,CircularPS} = f\left(P_{IN,CircularPS}, T_{IN,CircularPS}\right)$$

$$Q_{CircularPS} = \dot{m}_{wPS} \cdot cp_{wPS} \cdot \Delta T_{wPS}$$

$$Q_{CircularMS} = \dot{m}_{wMS} \cdot cp_{wMS} \cdot \Delta T_{wMS}$$

Eq. (3.44): Equations used for data reduction.

In Figure 3.35, Figure 3.37 and Figure 3.39 are reported the experimental pressure losses in function of the vapour quality measured with R134a at 200, 400 and 600 kg m^{-2} s^{-1}. Furthermore, for the first two mass fluxes, tests were performed at 30 and 40 °C saturation temperature. The saturation temperature influences the two-phase frictional pressure drop: in particular, the higher the saturation temperature, the lower the two-phase frictional pressure drop is. When increasing the saturation temperature, the vapor density increases, which means that the vapor velocity decreases and by consequence the two-phase frictional pressure drop decreases. The results presented below show the expected tendency from macroscale theory.

In each graph is also reported the comparison with the pressure drop predicted from the model of Cavallini *et al.* (2009) and Friedel (1979).

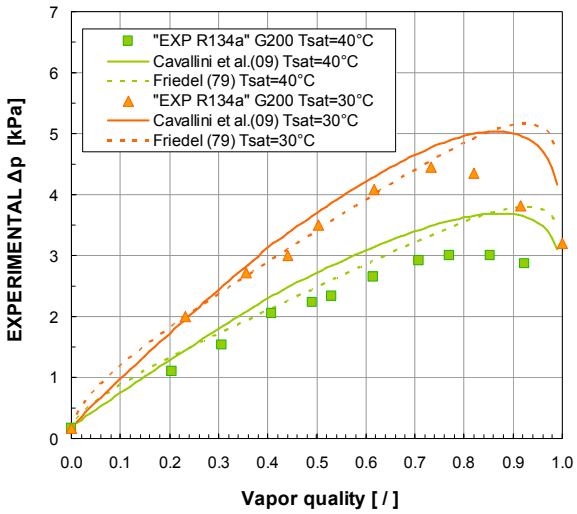

Figure 3.35. Experimental pressure loss of R134a at 200 kg m^{-2} s^{-1} and Tsat=30 and 40 °C. Lines refer to calculated trends by Cavallini et al. (2009) and Friedel (1976).

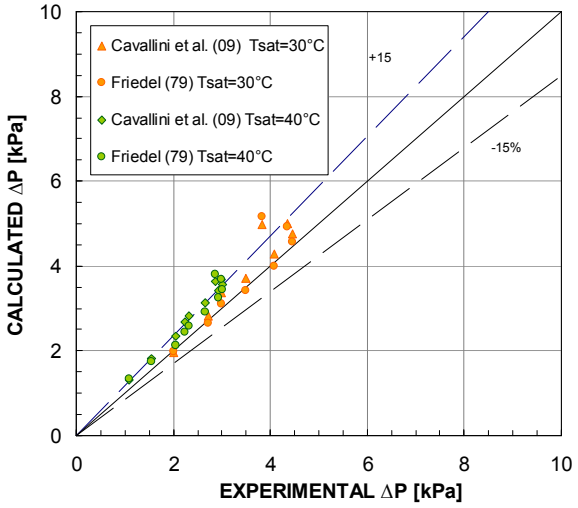

Figure 3.36. Calculated pressure drop within the studied geometry vs. experimental data. The pressure drop was calculated from Cavallini et al. (2009) and Friedel (1976).

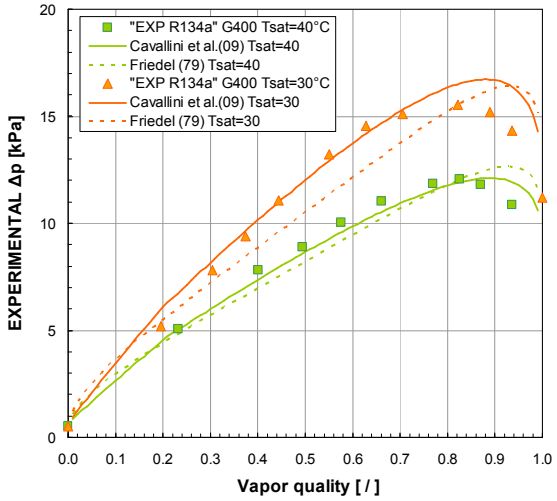

Figure 3.37. Experimental pressure loss of R134a at 400 kg m^{-2} s^{-1} and Tsat=30 and 40 °C. Lines refer to calculated trends by Cavallini et al. (2009) and Friedel (1976).

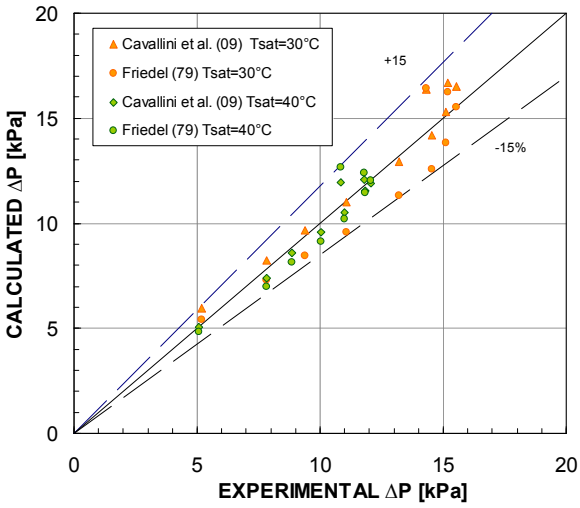

Figure 3.38. Calculated pressure drop within the studied geometry vs. experimental data. The pressure drop was calculated from Cavallini et al. (2009) and Friedel (1976).

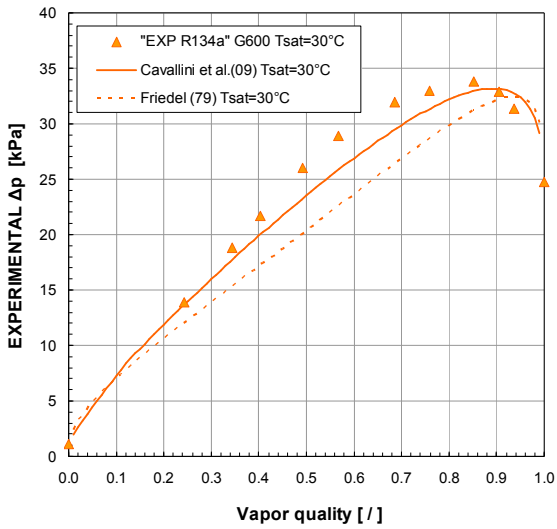

Figure 3.39. Experimental pressure loss of R134a at 600 kg m^{-2} s^{-1} and Tsat=30 °C. Lines refer to calculated trends by Cavallini et al. (2009) and Friedel (1976).

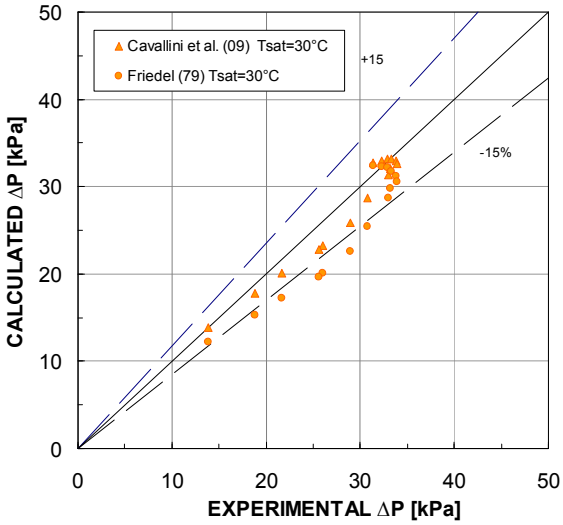

Figure 3.40. Calculated pressure drop within the studied geometry vs. experimental data. The pressure drop was calculated from Cavallini et al. (2009) and Friedel (1976).

Figure 3.36, Figure 3.38 and Figure 3.40 report the comparison between the experimental values and the calculated ones with the models of Cavallini *et al*. (2009) and Friedel (1979). Both models are able to catch the trend of data, but if at 400 kg m^{-2} s^{-1} the agreement is very good, at 200 kg m^{-2} s^{-1} they overestimate the measured values while, at 600 kg m^{-2} s^{-1} they underestimate them.

3.4.3 Pressure drop during adiabatic vapour-liquid flow in the square (d_h=1.23 mm) minichannel

As for the circular minichannel, during two phase flow pressure drop measurements in the square minichannels, subcooled refrigerant was heated up, vaporized and superheated before entering the test section where desired vapor quality at the inlet of the measuring sector was controlled with the heat output in the desuperheater. The vapour quality was calculated from the Eq. (3.40); in the square minichannels no heat dissipations: were observed fro the water side and then, contrary to the circular minichannel, no corrections were introduced.
In Figure 3.41 the experimental two phase pressure drops measured with R134a are compared to the ones measured with R1234yf. It can be seen that the fluid R1234yf displays a lower pressure drop by 20 % as compared to R134a, at the same operating conditions, as already seen fro the circular minichannel in Paragraph 3.4.1.

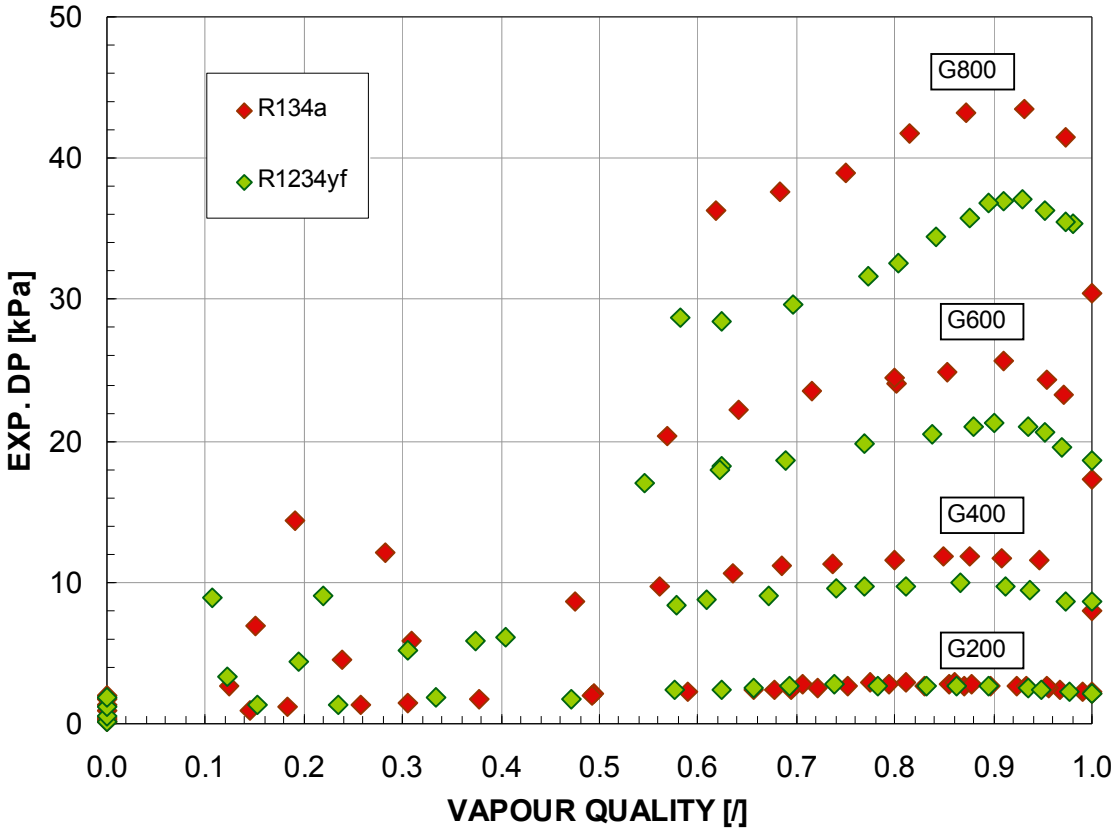

Figure 3.41. Experimental pressure losses during adiabatic two-phase flow of R1234yf and R134a at 40° C saturation temperature and at three different values of mass velocity (400, 600 and 800 kg $m^{-2}s^{-1}$) in the square (d_h=1.23 mm) minichannel

3.4.3.1 Comparison against models

In this paragraph the total experimental pressure drops measured during adiabatic two phase flow of R134yf and R134a in the square channel (d_h=1.23 mm) are compared against different models. For the comparison with the Cavallini *et al.* (2009) model, frictional pressure drops within the stainless steel capillaries and in the copper tube have been calculated separately considering the proper roughness value and summed together.

Most of the models reported here were developed for conventional tubes. Since most of the minichannel modeling is based on modeling well accepted driving mechanisms from conventional tubes, all the models reported here are applied regardless the range of applicability. Even though some exceed the "allowed" range of test conditions, the agreement was still found satisfactory

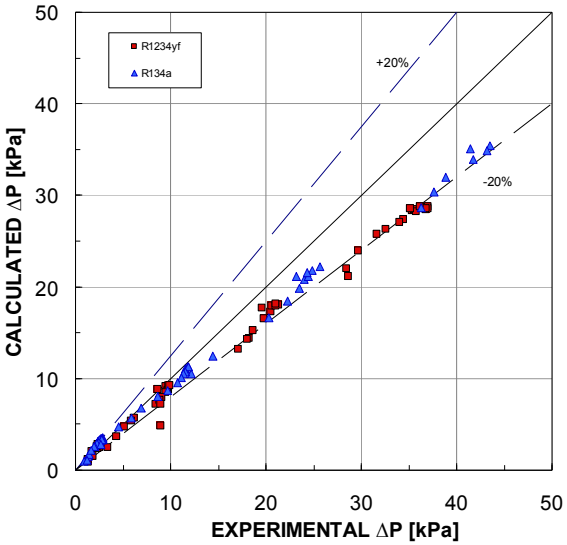

Figure 3.42. R134a and R1234yf data compared against Cavallini et al. (2009) model

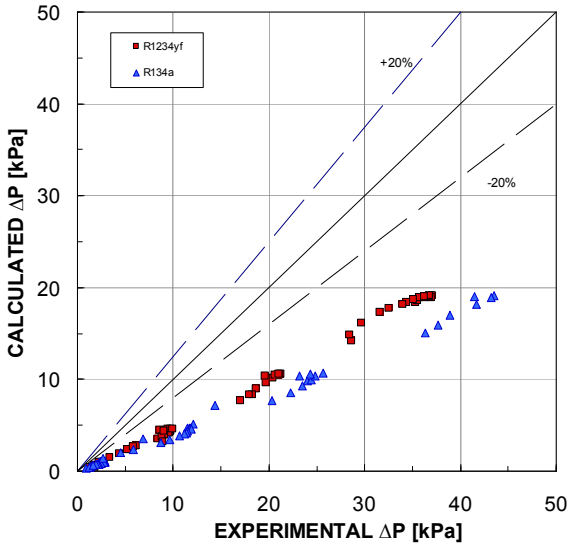

Figure 3.43. R134a and R1234yf data compared against Chen et al. (2001) model.

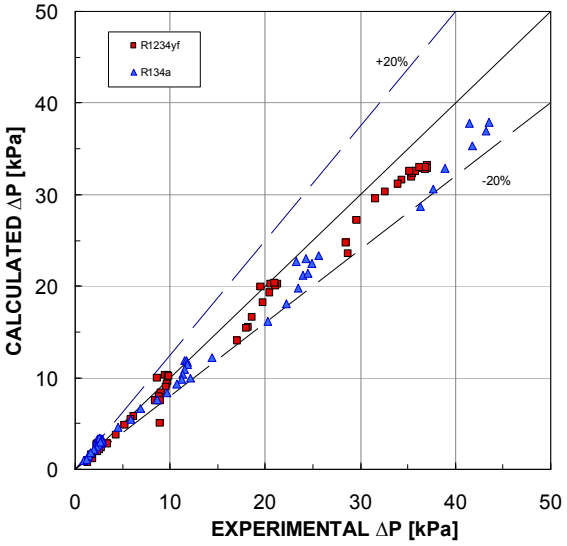

Figure 3.44. R134a and R1234yf data compared against Friedel (1979) model

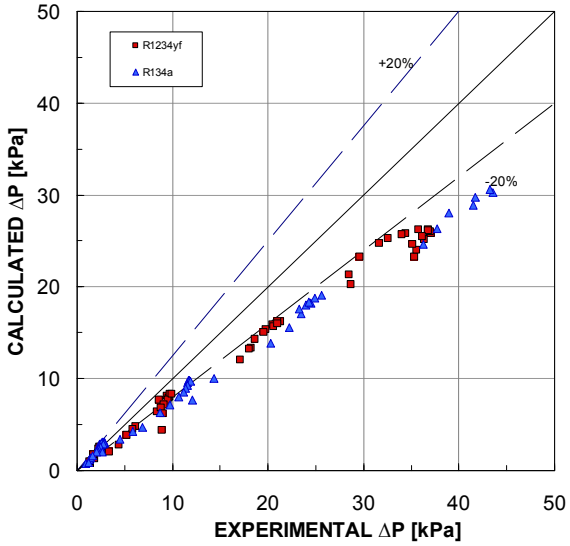

Figure 3.45. R134a and R1234yf data compared against Garimella et al. (2004) model

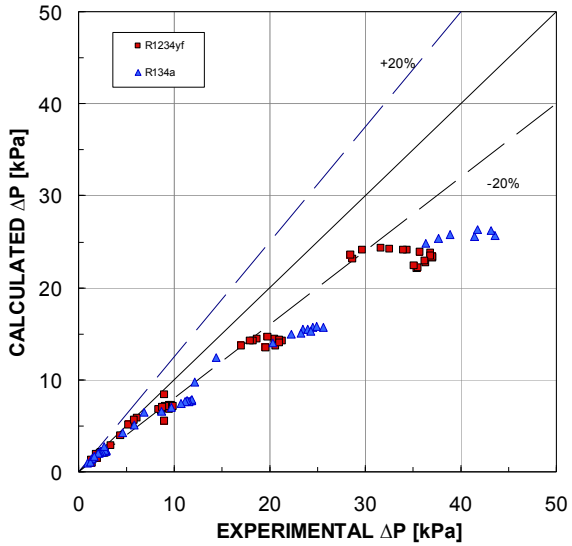

Figure 3.46. R134a and R1234yf data compared against Koyama et al. (2003) model

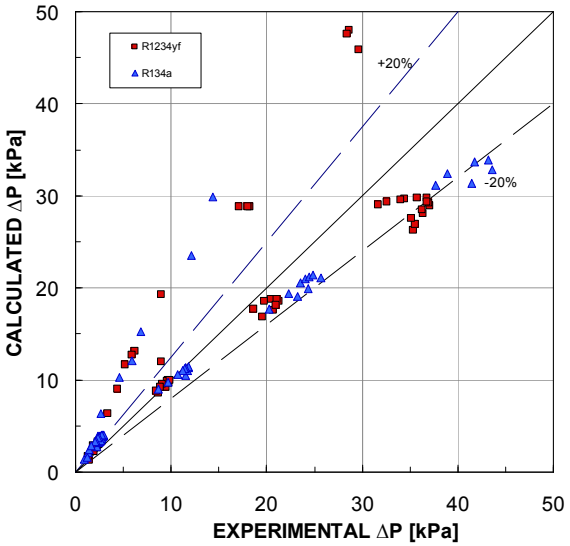

Figure 3.47. R134a and R1234yf data compared against Lockhart and Martinelli (1949) model

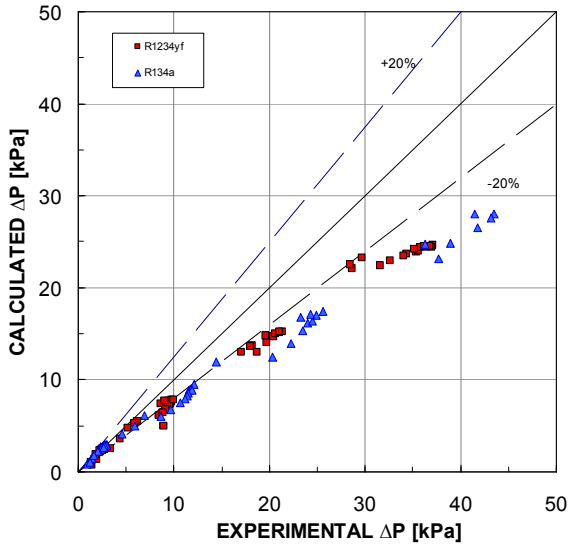

Figure 3.48. R134a and R1234yf data compared against Mishima and Hibiki (1996) model

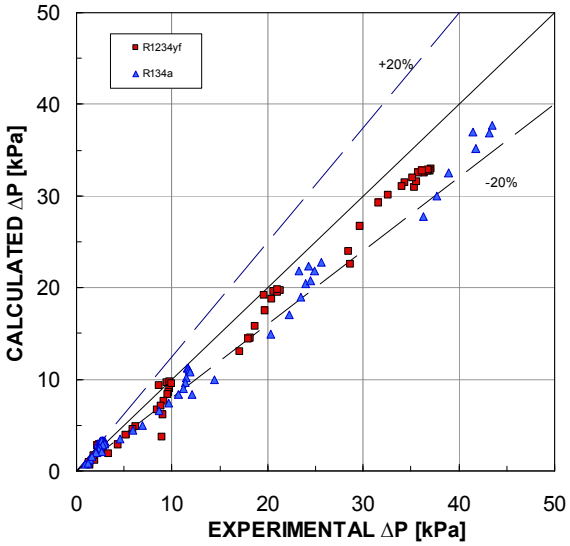

Figure 3.49. R134a and R1234yf data compared against Mueller Steinhagen and Heck (1986)

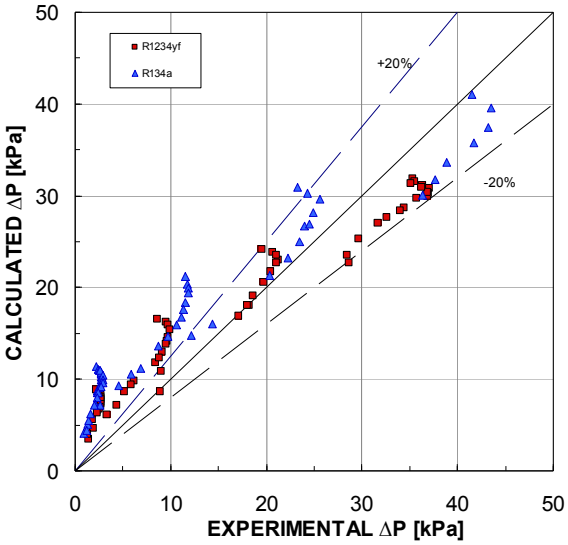

Figure 3.50. R134a and R1234yf data compared against Yan and Lin (1999) model

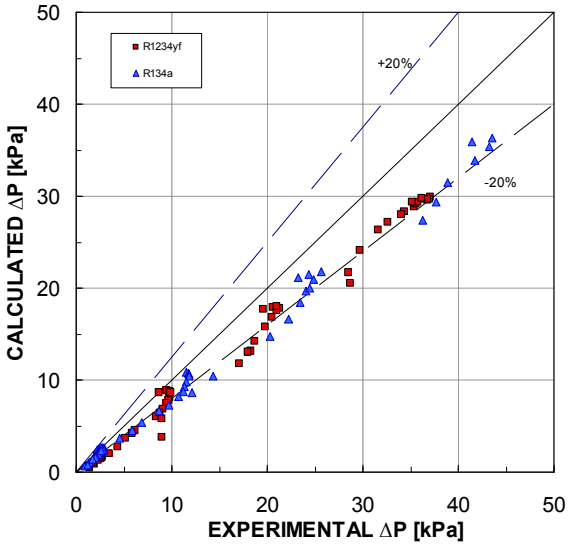

Figure 3.51. R134a and R1234yf data compared against Zhang and Webb (2001) model

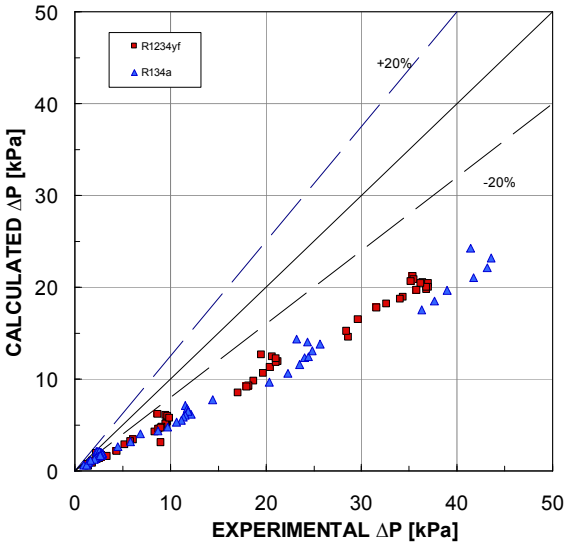

Figure 3.52. R134a and R1234yf data compared against Homogeneous model

4 NANOENGINEERED SURFACES FOR PROMOTING DROPWISE CONDENSATION AND ENHANCING HEAT TRANSFER

4.1 Abstract

In the present Chapter nanoengineered copper surfaces are investigated with the aim of enhancing the heat transfer coefficient during steam condensation by promoting the dropwise condensation mode (DWC) instead of the film mode. A wet-chemical fabrication process is used to modify the wettability of a copper surface by rendering it superhydrophobic at ambient conditions using an oxidation and surface functionalization approach. The superhydrophobic sample is tested in a new experimental apparatus which allows the measurement of heat transfer coefficient during condensation and the visualization of the droplets movements. A small hydraulic diameter of the test section (d_h=3.6 mm) was to investigate the effect of the vapour velocity. Heat transfer performances of polished and superhydrophobic copper samples are investigated during steam condensation at 110 °C saturation temperature. Experimental data shows that the superhydrophobic sample does not improve the heat transfer performance as expected from the higher contact angle (165°) with respect to a polished copper sample (80°), but promote the DWC for longer time while the polished sample turns to the filmwise mode after few days. The effect of the vapour velocity during DWC is found negligible at very low degree of subcooling. However, with a decrease in the wall temperature, an increase in vapor velocity results in a reduction in the diameter at which the drops begin to depart on the surface, thereby enhancing the heat transfer coefficient. In addition, an increase in vapour velocity also promotes an earlier transition from the DWC to the FWC mode during condensation on the superhydrophobic sample.

4.2 Introduction

Condensation is widely used in many industries and engineering process, such as power industry, refrigerating process, etc. With the motivation for improved energy efficiency and miniaturization of the heat exchanger, an extensive research has been undertaken in the area of enhanced condensation heat transfer since the report of Schmidt *et al.* (1930) who first recognized that during dropwise condensation the heat transfer coefficients were between 5 and 7 times those found with film condensation. Until the 1960s, there were wide discrepancies between the results of different investigators: error in the data was primarily due to the presence in the steam of air as well as, in some cases, to insufficient accuracy in the measurement of the surface temperature. The extreme sensitivity of the dropwise condensation heat transfer coefficient to even minute quantities (a few ppm) of air in the steam has been demonstrated in several investigations (i.e. Detz *et al.* (1976)). Subsequently, more accurate measurements have shown good consistency and the mechanism and theory of the dropwise condensation have become better understood. Accurate measurements, free from error due to the presence of noncondensable gases, show that the heat transfer coefficient during dropwise condensation increases with vapour–surface temperature difference or heat flux reaching an almost constant value: this behavior is due to the increase in numbers of active nucleation sites with increase in vapour–surface temperature difference (Rose (2002)).

The ability of dropwise condensation to increase heat transfer coefficients over filmwise condensation is well established. The main mechanism responsible for the heat transfer enhancement in dropwise condensation heat transfer is related to droplets mobility. In fact, the sweeping and renewal in the droplets' growth process, encouraged by poor wall wettability, produces an augmentation of both the heat and the mass transfer coefficient as compared to the film condensation condition, where the liquid layer adjacent to the wall causes a large thermal resistance. The surface properties, in particular the surface energy of the material and the correlated contact angle phenomena, play a crucial role in determining the onset of filmwise or dropwise condensation modality. Typically, hydrophobic surfaces are expected to promote dropwise condensation, while hydrophilic ones more easily induce filmwise condensation.

Over the past few decades, considerable attention has been paid toward the development of suitable DWC promoters. The method so far mostly employed to produce hydrophobic surfaces is to coat the metallic surface with a thin layer of a material with a smaller surface energy. Such coatings could be organic compounds polymer film hard coatings or the formation of surface alloys. The use of organic promoter requires strong, long-term adhesion forces between the coating and the metal substrate. Usually, the thicker is the coating, the better its resistance to corrosion/erosion. However, due to very low thermal conductivity, thick organic coatings add to the heat transfer resistance that deteriorates the DWC performance. Moreover, the coating material, if inadvertently removed from the condenser surface, may contaminate the system. A very interesting method of modifying the wetting properties of a surface is to use self-assembled-monolayer (SAMs). Self-assembled monolayer is composed of a single layer of organic molecules adsorbed onto a surface to form a coating. Being only a monolayer-thick (10–15 Å), these coatings give negligible heat transfer resistance. In addition, they are very stable and should last over long periods of time (Bonner (2010)). SAM can be used to create gradient surfaces by varying areal concentration of molecules with low surface energy. In this way the motion of droplets from the hydrophobic to hydrophilic side of a surface is possible, also against gravity.

In the recent years, thanks to the developments in the material science, new techniques have been discovered which allows constructing superhydrophobic surfaces by mimicking the surface of the lotus leaves. Nanoengineered superhydrophobic surfaces appear to be a viable and promising solution to promote dropwise condensation but its feasibility is still to be demonstrated. The present study is focused on copper surfaces which have many applications in industrial fields, especially in the heat exchange area. Many different synthetic strategies have been developed to fabricate artificial superhydrophobic surfaces on copper to date. Some examples of these methods are electrodeposition (Xi *et al.* (2008)), electroplating (Xi *et al.* (2009)), chemical etching (Quian and Shen (2005)), sandblasting (Zhang *et al.* (2010)), sol-gel processing (Huang *et al.* (2007)), ions implantation (Rausch *et al.* (2008), Zhao *et al.* (1991)).

Dropwise condensation on rough superhydrophobic surfaces has been reported in the literature (Dorrer and Rhuhe (2007), Narthe and Beysens (2004), Varanasi *et al.* (2009)). The detailed mechanism of drop formation and growth are still being investigated. Although there has been a study with the specific intent of developing efficient heat transfer surfaces based on dropwise condensation (Chen *et al.* (2007)), few data are available for heat transfer rate. Recently Zhong *et al.* (2011) report heat transfer measurements on a superhydrobobic nanostructured copper sample and compare them to a mirror polished sample. They find that the nanostructured substrate do not improve the dropwise condensation heat transfer performance as expected by the higher contact angle. Dietz *et al.* (2010) reported a study of the dynamic condensation on a superhydrophobic sample. Droplet departure frequency was investigated using environmental scanning electron microscopy on a tilted (30°) superhydrophobic surface formed by cupric hydroxide nanostructures. Comparing these results with a nonstructered hydrophobic surface, they found that the droplets tend to depart the surface at reduced diameter. Since droplets with diameter less than 10 μm provide the

most significant contribution to the heat transfer during dropwise condensation and the formation of new droplet occurs only once large drops have departed from the surface, they concluded that the larger surface renewal frequency of the superhydrophobic surface leads to an increase in the heat transfer coefficient. They estimate an increase by a factor two but no measurements have been done.
Berndt *et al.* (2008) presented an experimental and theoretical study of dropwise condensation of vapour in a three channels plate heat exchanger with the plates coated with hydrophobic Ni-P-PFA. They showed an increase in heat flux of up to 20%, and an enhancement of about 100% in term of heat transfer coefficients with respect to the filmwise mode. However, this enhancement was limited at low subcooling (<6°C) since for higher value they observe a transit to the filmwise regime
In the present study DWC of steam on a superhydrophobic copper sample with the effect of the vapour flow is investigated, in order to reproduce the real conditions that occur inside a plate heat exchanger.

4.2.1 Effect of vapour velocity on dropwise condensation

The heat transfer coefficient of dropwise condensation is dependent upon the distribution of drop sizes on the condensing surface. Several models are available in the literature showing that a condensation surface covered by small drops provides a better condensation than the same surface covered by large drops (Chen (2001)). What largely determines the drop size distribution is the maximum drop diameter or the departing drop diameter, together with the fraction of the area covered by sliding drops. Vapor velocity, the physical and chemical characteristics of the surface (such as roughness and wettability), and the inclination and the height of the surface are some of the factors that have an influence upon the heat transfer coefficient of dropwise condensation. Kim *et al.* (2011) developed a mathematical model to predict the dropwise condensation phenomenon on nonwetting surfaces having hydrophobic and superhydrophobic features. They showed that high contact angles reduce the size of departure drops, allowing more condensing surface for small drops. Tanasawa *et al.* (1976) measured the dependence of the heat transfer coefficient on the departing drop diameter, using the gravitational, centrifugal, and steam shear forces to change the departing drop diameter. The result is shown in Figure 4.1: as it can be seen, the heat transfer coefficient is proportional to the departing drop diameter to the power of about -0.3, no matter what kind of force may be used to prompt drop departure**.** The same conclusions were derived theoretically by Tanaka (1975a) and Rose (1976).

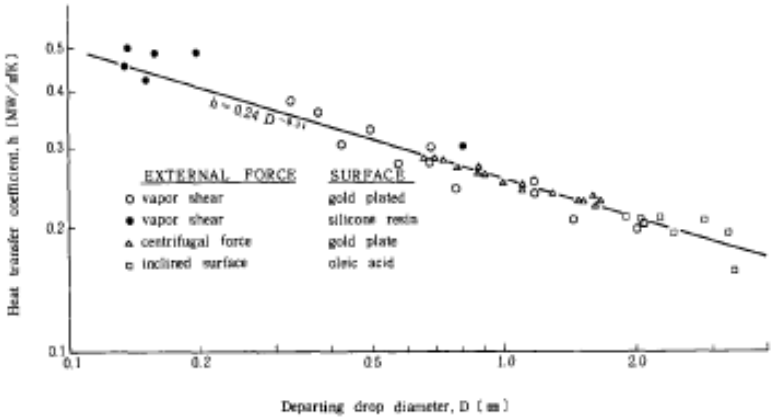

Figure 4.1. Dependence of the heat transfer coefficient on the departing drop diameter. Image taken from Tanasawa (1976).

4.2.2 Condensation Curves

In pool boiling, it is well known that the mode of heat transfer shifts from convection to nucleate boiling, then to transition boiling, and finally to film boiling, with the increase in the degree of surface superheat. The curve that represents the change of heat flux with the superheat is called the boiling curve and was first obtained by Nukiyama (1966). According to this curve, the heat flux varies with the superheat: it increases in the convective and nucleate part and then decreases with the superheating in the transition region till to reach the film boiling where it starts to increase again.

In dropwise condensation, a similar curve, which may be called a "condensation curve," has been observed for the first time during condensation of organic vapours (aniline, ethanediol, and nitrobenzene) by Takeyama and Shimizu (1974) with a vapour velocity of 2.2 m s^{-1}. Results are shown in Figure 4.2, represented with as a thin, solid line. The other curves are the results obtained using a condensing surface with a special configuration of a concave sphere by Tanasawa and Utaka (1983). Dropwise condensation was promoted applying oleic acid to the condensing surface. Steam velocities from 4 to 76 m s^{-1} were investigated: at the same subcooling the heat flux increases with the vapour velocity. It can be seen that the shapes of the condensation curves are similar to those of the boiling curves, whereas the maximum heat fluxes are higher, exceeding 10 MW m^{-2}. Dropwise condensation has been maintained from a lower degree of surface subcooling up to the maximum heat flux. At a much larger surface subcooling, the condensate begins to accumulate on part of the condensing surface and a state of pseudofilm condensation has been observed. When the surface temperature is lowered below 0 °C, a layer of ice was formed on the surface and film condensation occurs on the layer (on-ice condensation).

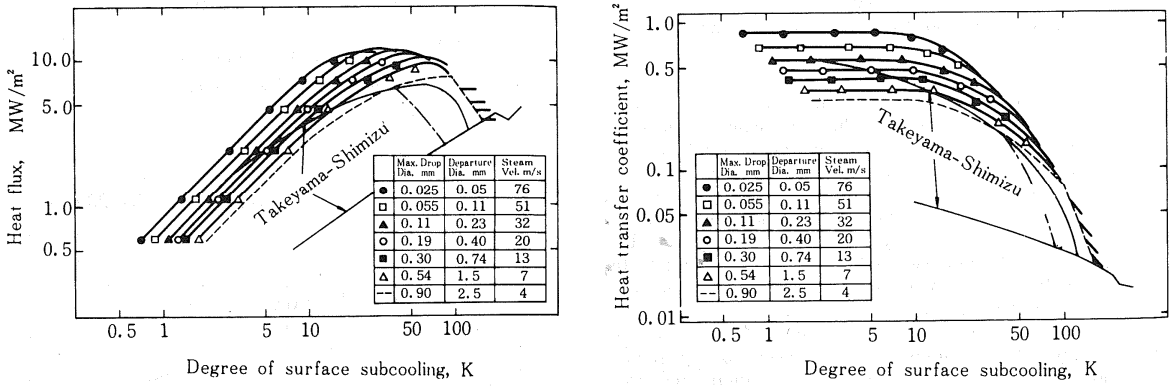

Figure 4.2. Condensation curves during dropwise condensation of steam at atmospheric pressure with the effect of the vapour velocity. Results obtained by Takeyama and Shimizu (1974) and Tanasawa and Utaka (1983). Axis scales are logarithmic.

Tanner *et al.* (1965) investigated the effect of vapour velocity during dropwise condensation of steam on copper surfaces promoted by montan wax. Results are reported in Figure 4.3: the effect of the vapour shear diminishes with increasing heat flux becoming negligible below about 50000 Btu ft^{-2} h^{-1} (160 kW m^{-2}). According to Tanner *et al.* (1965) observations, increased steam velocity produced a radical change in the appearance of the condensing surface both at high and low heat flux. At all heat fluxes the effect of increasing velocity was to decrease the amount of condensate on the surface and the average drop size. In view of this the small effect of velocity on coefficient at low heat fluxes was somewhat unexpected.

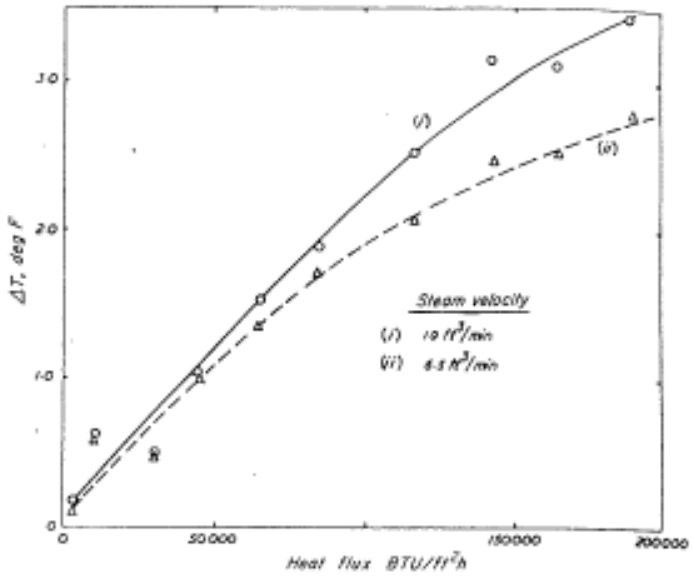

Figure 4.3. Variation of ΔT with heat flux at two steam flow rates during dropwise condensation. Image taken from Tanner et al. (1965).

O'Bara *et al.* (1967) determined experimentally dropwise condensation of steam on a vertical surface using cupric oleate as a promoter. They investigated the effect of the vapour velocity and pressure. Observations indicated that the vapor velocity across the condensing surface has a significant effect on the equivalent transfer coefficient with the coefficient exhibiting a maximum with increasing vapor velocity. Figure 4.4 reports the heat transfer coefficient in function of the vapour velocity at different subcooling grade.

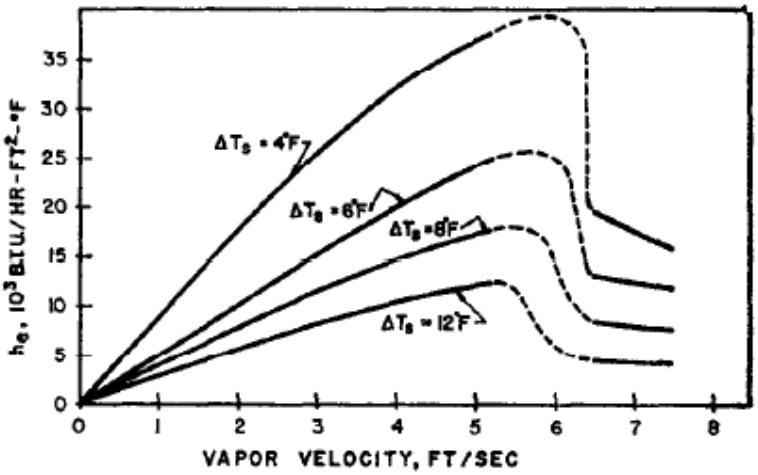

Figure 4.4. Influence of vapour velocity on the heat transfer coefficient. Image taken from O'Bara et al. *(1967).*

According to the authors, the reason a maximum vapor velocity exists in dropwise condensation appears to be an effect of the shear stress between vapour and drops. As the vapor velocity increases, the shear stress also increases and tends to disrupt the drops, inducing coalescence and, hence, the formation of a liquid film. The shift in the maximum value is explained by the fact that at low AT, drops are relatively small and drop growth rate is low so that more shear stress is necessary to bring about this transition. In contrast, at higher AT, the drops are larger and growth rate higher so that less shear stress, i.e. lower vapor velocity, is required to produce the same effect.

4.3 Theoretical background

In this section, theoretical models of wettability are discussed. First, the Young, Wenzel, and Cassie equations of wetting of a rough surface are introduced. Then the contact angle hysteresis is discussed as a measure of energy dissipation during liquid flow, transition between the wetting regimes, and hierarchical surfaces.

4.3.1 Wetting of Flat and Rough Surfaces: The Governing Equations

From the thermodynamic point of view, wetting of a rough solid surface is governed by Young, Wenzel, and Cassie equations that relate the contact angle between liquid and solid to interface free energies and to surface roughness.

4.3.1.1 The Young equation

Figure 4.5 reports a liquid in contact with a solid in presence of vapor, with the free surface energies of the solid–liquid, solid–air, and liquid–air interfaces equal to γ_{SL}, γ_{SA}, and γ_{LA}, respectively. When a liquid front comes in contact with a flat solid surface under the contact angle θ, the propagation of the liquid front for a small distance ds results in a net energy change of

$$dE = ds \cdot (\gamma_{SL} - \gamma_{SA} + \gamma_{LA} \cdot \cos\vartheta) \quad (4.1)$$

Therefore, for the liquid front to be at equilibrium (dE/ds=0), the Young equation should be satisfied:

$$\gamma_{LA} \cdot \cos\vartheta = \gamma_{SA} - \gamma_{SL} \quad (4.2)$$

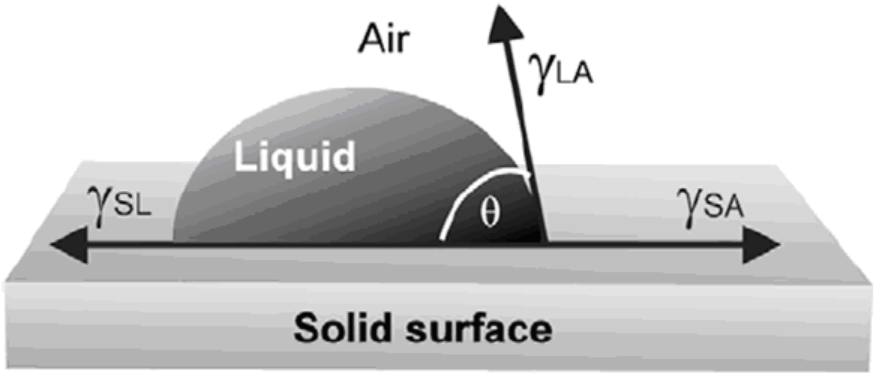

Figure 4.5. Wettability of solid surfaces. θ represents the contact angle, while γ are the interfacial surfaces energies. The subscripts L stands for liquid, A for air and S for solid.

The Young equation allows the calculation of the contact angle for given values of the interface energies. It is obvious from Eq. (4.2) that three situations are possible. If $(\gamma_{SA} - \gamma_{SL})/\gamma_{LA}$=1, complete wetting takes place with the liquid fully adsorbed by the solid surface (θ = 0). If $(\gamma_{SA} - \gamma_{SL})/\gamma_{LA}$ =-1, complete rejection of the liquid by solid surface takes place (θ = 180◦). The most common situation is the intermediate situation of partial wetting ($-1 < (\gamma_{SA} - \gamma_{SL})/\gamma_{LA} < 1$, $0 < \theta < 180°$). A liquid that has the contact angle $\theta < 90°$ is often referred to as a "wetting liquid," while that with $\theta > 90°$ is "a nonwetting liquid." Corresponding surfaces are called, in the case of the contact with water, "hydrophilic" and "hydrophobic," respectively. The free interface energies can also be viewed as surface tension forces. These forces are applied to the three-phase contact line

(the triple line) and directed toward the corresponding interface. The surface tensions are measured in force units per length of the contact line, N m^{-1}, the same units as the interface energy, J m^{-2}. Historically, the Young equation was formulated in early 1800s in terms of forces, after the thermodynamic concept of free energy in general and free surface energy in particular was introduced since the middle and in the second half of the 19th century by Helmholtz, Gibbs, and other scientists. Note that Young's formulation implies that the solid is nondeformable and insoluble, so that only the horizontal projection of the tensions is considered.

Young's equation does not take into account a number of factors, which can significantly affect the contact angle at the micro and nanoscale. It is emphasized that the contact angle provided by the Young equation is a macroscale parameter, so it is sometimes called "the apparent contact angle" (APCA). The actual angle under which the liquid–vapor interface comes in contact with the solid surface at the micro and nanoscale can be different. There are several reasons for that. First, water molecules tend to form a thin layer upon the surfaces of many materials. This is because of a long-distance Van Der Waals adhesion force that creates the so-called disjoining pressure. This pressure is dependent upon the liquid layer thickness and may lead to the formation of stable thin films or precursors. In this case, the shape of the drop near the triple line gradually transforms from a spherical surface into a precursor layer, and thus the nanoscale contact angle is much smaller than the apparent contact angle. In addition, adsorbed water monolayers and multilayers are common for many materials.

Second, even carefully prepared atomically smooth surfaces exhibit certain roughness and chemical heterogeneity. Water tends to cover at first the hydrophilic spots with high surface energy and low contact angle. The tilt angle of the surface due to roughness can also contribute to the APCA.

Third, Young's equation provides the value of the so called static contact angle that ignores any dynamic effects related to the change of the drop's shape. The very concept of the static contact angle is not well defined. For practical purposes, the contact angle, which is formed after a drop is gently placed upon a surface and stops propagating, is considered the static contact angle. However, depositing the drop involves adding liquid while leaving, which may involve evaporation, so it is difficult to avoid dynamic effects.

Fourth, for a small drop and curved triple lines, the effect of the contact line tension may be significant. Molecules at the surface of a liquid or solid phase have higher energy because they are bonded to fewer molecules than those in the bulk. This leads to surface tension and surface energy. In a similar manner, molecules at the edge have fewer bonds than those at the surface, which leads to line tension and the curvature dependence of the surface energy. This effect becomes important when the radius of curvature is comparable with the Tolman's length. However, the triple line at the nanoscale can be bending, and the radius of curvature can be very small, so that the line tension effects become important. Thus while the contact angle is a convenient macroscale parameter, wetting is governed by interactions at the micro and nanoscale, which determine the contact angle hysteresis and other wetting properties.

4.3.1.2 The Wenzel and Cassie equations

The Wenzel equation relates the contact angle of a water drop upon a rough solid surface θ (Figure 4.9), with that upon a smooth surface, θ_0, through the nondimensional surface roughness factor, $Rf \geq 1$, equal to the ratio of the surface area to its flat projection:

$$\cos\vartheta = Rf \cdot \cos\vartheta_0 \qquad (4.3)$$

The equation was originally derived for the homogeneous solid–liquid interface (no air pockets) (Figure 4.6) using the surface force balance and empirical considerations; however, it was later put in a proper thermodynamic framework. It is important that according to Wenzel model the

inherently hydrophilic flat surface will be more hydrophilic when rough, and inherently hydrophobic surface will become more hydrophobic.

For a surface composed of two fractions, one is with the fractional area f_1 and the contact angle θ_1 and the other with f_2 and θ_2, respectively ($f_1+f_2=1$), the contact angle is given by the Cassie equation:

$$\cos\vartheta = f_1 \cdot \cos\vartheta_1 + f_2 \cdot \cos\vartheta_2 \qquad (4.4)$$

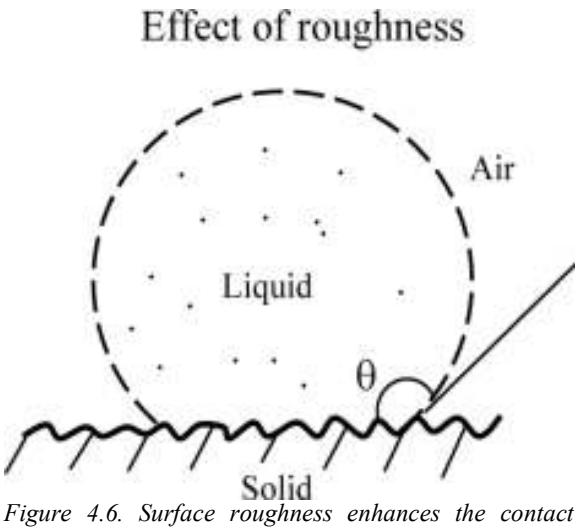

Figure 4.6. Surface roughness enhances the contact angle.

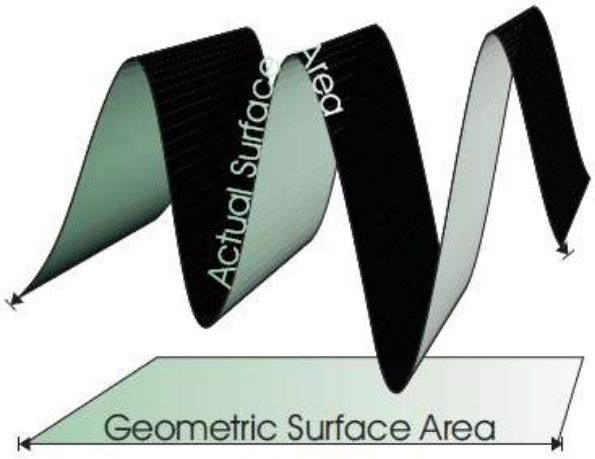

Figure 4.7. Schematic drawings of the actual and projected area of a rough surface.

$$Rf = \frac{Actual\_Surface\_Area}{Geometric\_Surface\_Area}$$

For the case of a composite interface (b), consisting of the solid–liquid fraction ($f_1=f_{SL}$, $\theta_1=\theta_0$) and liquid–vapor fraction ($f_2=1-f_{SL}$, $\cos\theta_2=-1$), substituting in the Eq. (4.4) yields the Cassie–Baxter equation:

$$\cos\vartheta = -1 + f_{SL} \cdot (\cos\vartheta_0 + 1) \qquad (4.5)$$

Eq. (4.5) predicts an enhancement of hydrophobicity ($\theta>\theta_0$) and a jump in the contact angle can often be observed once air trapping occurs. Eq. (4.5) is sometimes used for the homogeneous interface instead of Eq. (4.2), if the rough surface is covered by holes filled with water (Figure 4.8c).

The same equation could be explained in this way: a drop on a flat solid makes an angle θ, while it does not spread at all on a pure film of air (contact angle of π), and the average value it takes on the patchwork is an average on the cosines weighted by the respective proportions of solid and air below the drop f_{SL}.

Gao and McCarthy (2007) showed experimentally that the contact angle of a drop is defined by the triple line and does not depend upon the roughness under the bulk of the drop. Gao and McCarthy (2007) concluded that the Wenzel and Cassie equations "should be used with the knowledge of their fault." The question remained, however, under what circumstances the Wenzel and Cassie equations can be safely used and under what circumstances do they become irrelevant.

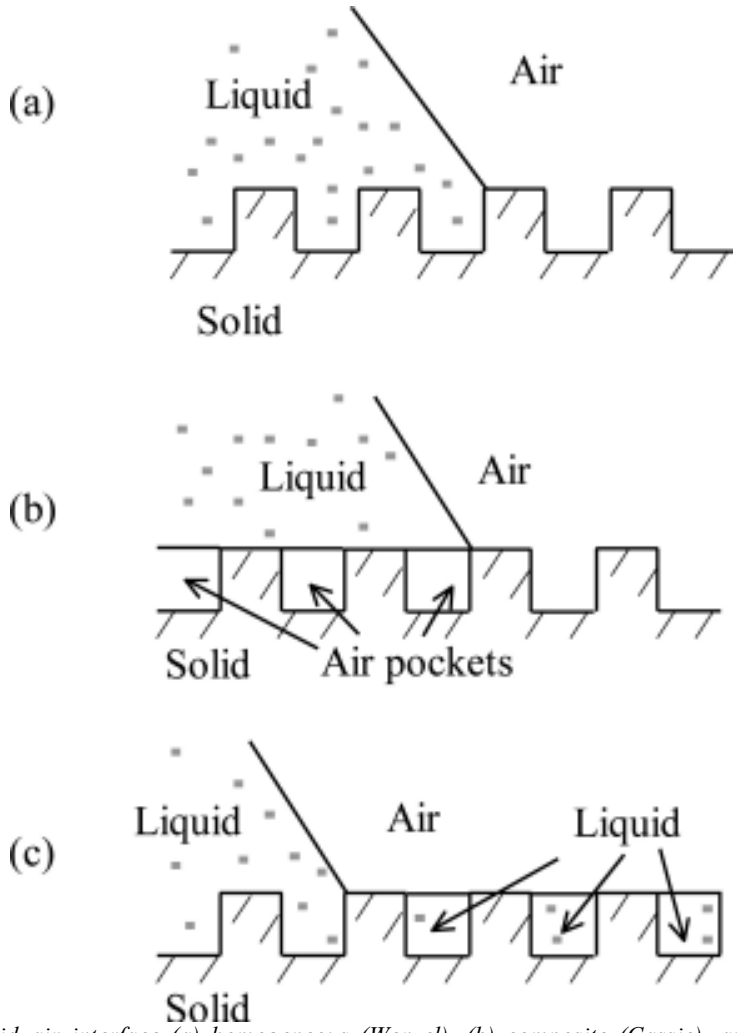

Figure 4.8. Solid–liquid–air interface (a) homogeneous (Wenzel), (b) composite (Cassie), and (c) with filled holes (Cassie with water penetration).

4.3.2 Contact angle hysteresis

Most solids are naturally rough, often at a micrometric scale. Processes of fabrication (such as lamination) may generate striations or microgrooves. Materials resulting from the compaction of grains exhibit roughness at the scale of the grains. Coating can also induce roughness, in particular when the coating film dewets, thus producing microdrops at the surface. Conversely, very few solids are molecularly flat. Most often, molecularly flat solids result from solidifying a liquid film, either free or suspended on another liquid; in such cases, the roughness can correspond to the thermal roughness of a liquid interface, generally of the order of a few angstroms. This is the case of glass, solidified from its molten state after deposition onto a bath of molten tin.

Gibbs pointed out that defects on a solid can pin a contact line. As a consequence, droplets on an incline stay at rest; the front and rear contact nonwetting and wetting defects, respectively. The resulting asymmetry in contact angles creates a Laplace pressure difference between the front (of high curvature) and the rear (of smaller curvature) and, thus, a force able to resist gravity provided that the drop is small enough. Both chemical heterogeneities and roughness can act as pinning sites.

It has been shown that a force, most often gravity, must be applied to overcome the surface tension forces holding the liquid to the surface.

$$m \cdot g \cdot \sin\alpha = k \cdot w \cdot \gamma_{LV} \cdot (\cos\vartheta_{\mathrm{Re}c} - \cos\vartheta_{Adv}) \quad (4.6)$$

where m is the droplet mass, g is the acceleration of gravity, k is a constant, w is the droplet contact diameter, θ_{Rec} and θ_{Adv} are the receding and advancing contact angles respectively (see Figure 4.9), and γ_{LV} is the liquid vapor surface tension, can be used to predict α, the minimum tilt angle required for the droplet to move. This equation predicts that by decreasing contact angle hysteresis, the difference between the advancing and receding contact angles, the inclination angle required to induce drop motions is decreased. In fact, if there is no hysteresis, then a droplet of liquid should move spontaneously on a horizontal surface. However, if the hysteresis is high enough, then a droplet will remain pinned even though the static contact angle is grater than 160° on a vertical surface. Contact angle hysteresis on hydrophobic rough surfaces can vary dramatically depending on how the liquid wets the surface. Wenzel described a wetting regime where the liquid penetrates between the surface asperities on a rough surface. It was later shown that such surfaces often have high contact angle hysteresis: the three-phase contact line remains pinned because there are high-energy barriers between metastable states that the contact line can adopt. A liquid droplet can also rest on top of surface features as described by Cassie and Baxter. In this wetting regime, the hysteresis is generally lower because the droplet is sitting on a composite surface of air and solid and the energy barriers limiting the discontinuous contact line movement are small. Therefore, according to Eq. (4.6), a droplet would move more easily (at a lower tilt angle) on the low hysteresis surface in the Cassie-Baxter wetting regime than on the higher-hysteresis Wenzel-type surface. Recently, it has been shown that a transition from the Cassie- Baxter to Wenzel wetting regime can be observed on some superhydrophobic surfaces. Condensation on superhydrophobic surfaces has also been shown to decrease drop mobility and increase hysteresis. Surfaces with low hysteresis but minimal roughness (i.e., not superhydrophobic) would be more appropriate choices for applications where liquid droplet mobility needs to be maintained during condensation (Wier and McCarthy (2006)).

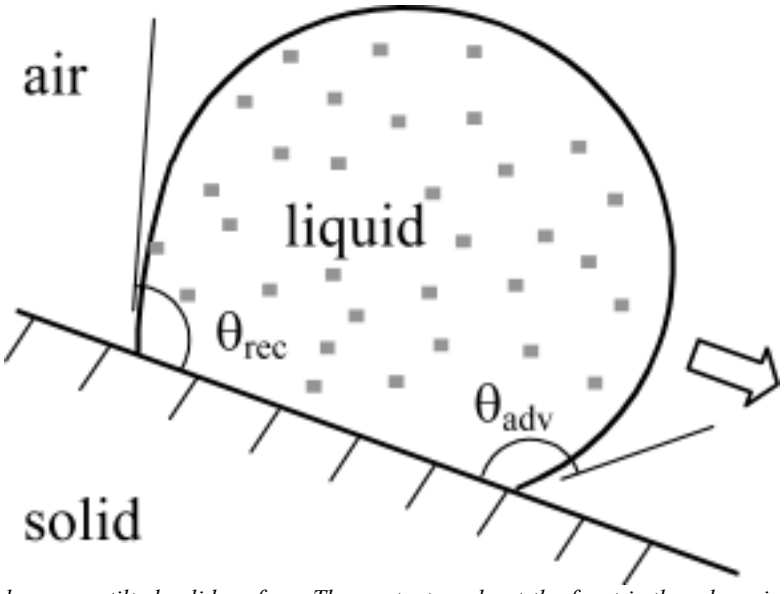

Figure 4.9. A water drop on a tilted solid surface. The contact angle at the front is the advancing contact angle, θ_{adv}, whereas that at the back is the receding contact angle, θ_{rec}. The difference, $\theta_{adv}-\theta_{rec}$, constitutes adhesion hysteresis.

4.4 Theory of the DWC phenomena

The experimental evidence of Umur and Griffth (1965) that the surface area between condensate drops during vapour condensation remains dry, with no indication of a microfilm, opened a new perspective on this phenomenon. Like in the heterogeneous nucleation of vapour bubbles on superheated surfaces in boiling, a cyclic process of droplet nucleation at active sites occurs during DWC. The nucleated droplets grow by mass addiction due to condensation, coalescence due to surface tension effects and finally are removed by body force or shear drag. This "nucleation model", since its early proposal, have been further developed and confirmed by other authors, Rose (1981), and is widely accepted.
It has been reported that dropwise condensation on a hydrophobic surface enhances heat transfer by an order of magnitude compared with filmwise condensation (Schmidt *et al.* (1930)). Dropwise condensation occurs on surfaces which are not strongly wetted by the liquid and so the drops do not spread out over the surface. They grow until they became so large that they run off the surface by gravity or are blow off by the flowing vapor. Surfaces with strong hydrophobicity are believed to allow effective dropwise condensation, due to the promotion of the drop movement and departure and consequently accelerating surface renewal, allowing small drops to form. Neumann *et al.* (1978) investigated the effect of the contact angle hysteresis on the heat transfer characteristics during DWC. It was found that the heat transfer during DWC is related to the contact angle hysteresis of the surface. Superhydrophobic surfaces exhibit high contact angle between 150° and 180° and low water contact angle hysteresis. For this reasons they seem likely to promote dropwise condensation much more than other kind surfaces.
The superhydrophobicity derives from a combination of two factors:

- hierarchical roughness scale
- hydrophobic coating

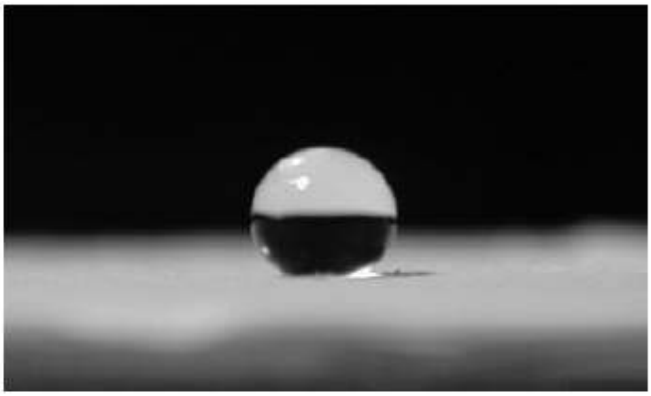

Figure 4.10. On a surface which is both rough and hydrophobic, the contact angle of water is observed to be very high (typically between 160° and 170°)

A combination of these two factors is necessary, because of the practical difficulty of achieving flat surfaces with large hydrophobicity (Bico *et al.* (2002)).
These two characteristics allow water droplets to rolls easily and the phenomenon is called "Lotus effect" which involves two important properties that are typical for many water-repellent plant leaves: the superhydrophobicity and self-cleaning. A surface with the water contact angle θ greater than 150° and with low contact angle hysteresis is called superhydrophobic. The SEM study reveals that the lotus leaf surface is covered by "bumps," more exactly called *papillae* (papillose epidermal

cells), which, in turn, are covered by an additional layer of epicuticular waxes. The wax is hydrophobic with water contact angle of about 95°–110°, whereas the experimental values of the static water contact angle with the lotus leaf were reported as about 160°. The increase of the contact angle is a result of the surface roughness due to the papillae (Figure 4.11, left). On the right side is reported the picture of a water droplet on a lotus leaf. The bottom of the drop (blue-greyish colors) reflects sky, an indication of the additional air layer underneath the drop, causing total reflection of the light at the air-water interface. Thanks to this air layer, the drop is highly mobile on the surface.

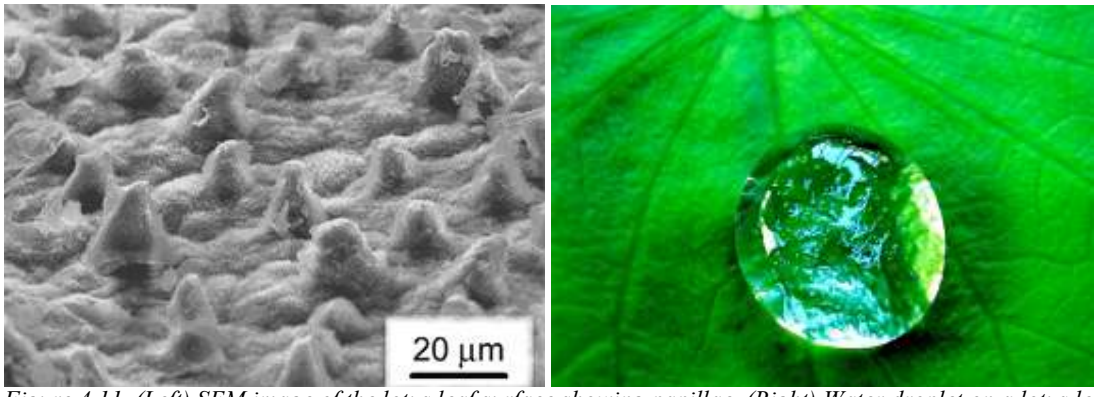

Figure 4.11. (Left) SEM image of the lotus leaf surface showing papillae. (Right) Water droplet on a lotus leaf

There are many other examples in nature of superhydrophobic leaves. Neinhius and Bartthlott (1997) reported the study of about 200 plants, which have all three common features:

- They are coated by an epitacular film of wax that makes them hydrophobic
- They have a textured surface made by bumps at a typical scale of 10 µm
- They have also a secondary texture, much smaller in size than the previous one (around 1 µm) often superimposed on the first one

Also many animals, like for examples water striders, ducks, butterflies have optimal water repellency characteristics, and their structure confirms that the hydrophobicity of a solid is enhanced by textures (Quéré (2005)). In the recent years, many researchers have become interested in superhydrophobic surfaces because a variety of experimental techniques allow the preparation of samples with controlled roughness. A review of these processes has previously presented in Paragraph 4.2.

4.4.1 Criteria for determining suitable DWC surfaces

As explained before in Chapter 4.4, the main mechanism responsible for the heat transfer enhancement in dropwise condensation heat transfer is related to droplet mobility. Then the question that arises is how to evaluate if a surface is suitable for promoting the condensation in the dropwise mode.
Contact angle has sometimes been used to predetermine the condensation mode on a specific solid surface. However, the contact angle measured at room temperature and in equilibrium with an air environment has been proven not to be useful for determining the wettability of systems where mass transfer takes place. For example, the contact angle of water on a polytetrafluoroethylene (PTFE) surface is 88° under the condensation condition at atmospheric pressure but 108° at room temperature with an air environment (Ponter (1992)). Condensation on superhydrophobic surfaces

has been shown to decrease drop mobility and increase hysteresis. Quere *et al.* (2003) reported experiments of water condensation where the contact angle hysteresis was nearly 110°, compared to about 5° on the dry surface. Also some tests of condensation on a lotus leaf showed an increase in the contact angle hysteresis (Narhe and Beyesen (2004)). Wier and McCarthy (2006) observed the condensation of water on ultrahydrophobic surfaces containing hydrophobized silicon pillars. They found that water condenses both between and on the top of the surface features: a macroscopic water drop coalesces with the water and undergoes a wetting transition from sitting on the top of the posts (Cassie-Baxter State) to wetting between them (Wenzel State). That causes an increase in contact angle hysteresis and a decrease in macroscopic water drop mobility. They concluded that surfaces with low hysteresis but minimal roughness would be more appropriate choices for applications where liquid droplet mobility needs to be maintained during condensation.

Figure 4.12 represents the Wenzel and Cassie-Baxter model for the hydrophobicity. Above a certain surface roughness, it becomes energetically more favorable for the liquid to span the asperities of the surface texture, so that the interface is in the Cassie-Baxter state. It has been suggested that a critical contact angle (θ_c) for the transition between both regimes can be found by equating Eq. (4.2) and Eq. (4.5), resulting in:

$$\vartheta_c = -\frac{1-f_{SL}}{R_f - f_{SL}} \tag{4.7}$$

Out of Wenzel and Cassie-Baxter states the one with lowest energy should prevail. In practice, however, the interface is not always in the energetically most favorable state. Very often a composite state is observed where a noncomposite state would be favorable. This state is metastable, and applying pressure to the drop causes a transition of the interface to a noncomposite state (Quere *et al.* (2003)). It is therefore possible that both states coexist on the same substrate for different drops. A pressure applied to the drop of liquid can cause an irreversible transition to the Wenzel's regime, but also the condensation has been shown to decrease drop mobility and increase hysteresis. For moderate roughness and hydrophobicity Wenzel angles are expected to be smaller than Cassie ones (see Figure 4.12). But the most important fact is the increase of the contact angle hysteresis. This can be understood because, in Wenzel state, ad liquid recedes, is in contact with water trapped inside the texture. The contact angle should be given by an average between θ and 0, yielding a very low value for the receding angle. Thus, rather than a small difference in contact angles, the main difference between both superhydrophobic states lies in the adhesion properties: a Wenzel drop will adhere efficiently to its substrate, in spite of high contact angle. In Figure 4.13 are reported the receding and advancing contact angles measure by Johnson and Dettre (1964) on a wax substrate with different roughness r. Contact angle hysteresis $\Delta\theta$ first increases with r and then decreases; in this regime, in spite of numerous defects, the contact angle hysteresis is lesser than on the smoothest surface. If this is true during water contact angle measurements, it is not valid anymore during vapor condensation.

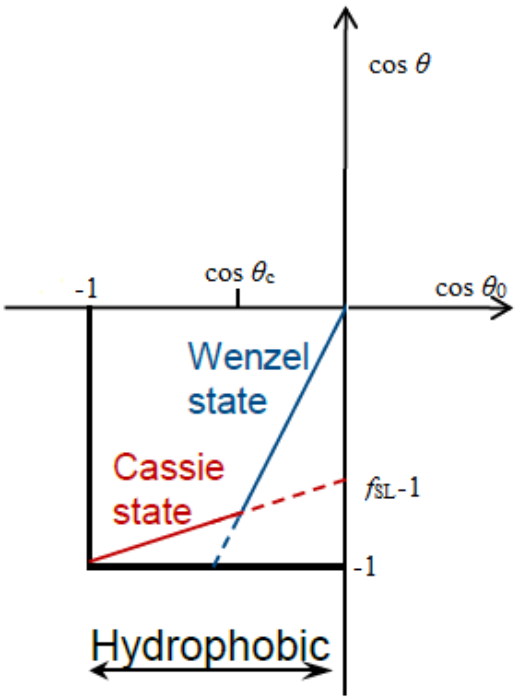

Figure 4.12. Different models of superhydrophobicity: for 90°<θ<θc the Wenzel model should be selected, while for θ>θc, air should be trapped below the drop, and the Cassie-Baxter model followed.

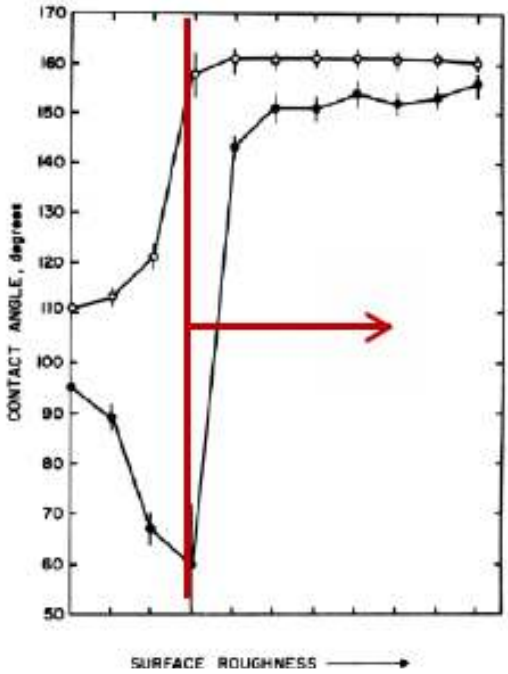

Figure 4.13. Contact angle of water on wax substrates: advancing (○) and receding angle (●) as a function of a qualitative roughness measure. Johnson and Dettre (1964).

Rausch *et al.* (2010) suggested a condensation model based on droplet nucleation and growth on elevated precipitates, resulting in short-term steam entrapment after droplet coalescence (see Figure 4.14). According to the wetting theory, this transition state corresponds with the contact angle model suggested by Johnson and Dettre (1964) which combines the approaches by Wenzel and Cassie and Baxter: gas or steam entrapment enhances the macroscopic contact angle and thus increases the tendency for stable dropwise condensation. Therefore, the wettability parameters determined at dry conditions are not capable of predicting condensation forms on surfaces suitable for the suggested condensation mechanism.

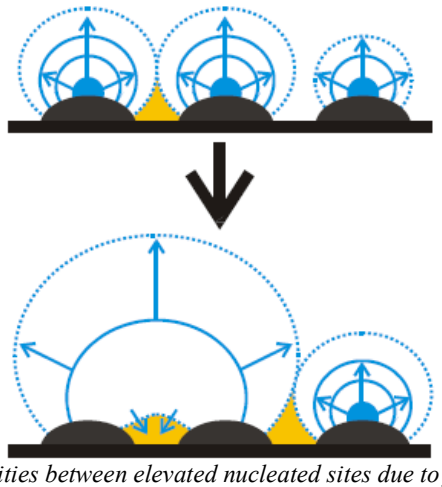

Figure 4.14. Steam entrapment in cavities between elevated nucleated sites due to fast droplet coalescence.

Rausch *et al.* (2010) postulated the initial droplet formation on elevated locations according to previous works with promoters like gold or organics (Detz *et al. (*1976)) showed that droplet formation preferentially takes place on geometric nucleation sites like pits or scratches.
Also Lan *et al*. (2010) considered the effect of surface energy and nanostructures on dropwise condensation. Self-assembled monolayers coatings of *n*-octadecyl mercaptan were prepared on mirror-polished (SAM-2) and the nanostructured (SAM-1) copper substrates to promote the DWC. According to modified Cassie–Baxter model, the SAM-1 surface would show a better performance of superhydrophobicity and a larger apparent contact angle in the air-steam environment. However the DWC heat transfer coefficients for SAM-1 surface are lower than those of SAM-2, because DWC takes place in a composite surface, comprising SAM-1 surface and condensate.
According to Ma *et al* (2010), in a pure steam condensation process, usually the condensate filled the cavities of roughness induced coated surface without air. During the condensation of pure steam, the micro-nanostructures, which are important for superhydrophobic surfaces, would not adsorb and trap air to show superhydrophobicity. The condensate droplets are in a new condensate wetting mode with condensate stagnating in the cavities of the micro-nanostructures, resulting in an increase in the thermal resistance and a decrease in heat transfer performance. This is in contrast with the model of Rausch *et al.* (2010) who started from the hypothesis that the initial droplet formation takes place on elevated sites, resulting in short-term steam entrapment after droplet coalescence.
Chen *et al.* (2007) have recently reported continuous dropwise condensation on a superhydrophobic surface with short carbon nanotubes deposited on micromachined posts, a two-tier texture mimicking lotus leaves. Superhydrophobicity is retained during and after condensation and rapid drop removal is enabled with a hexadecanethiol coating.
Much work is needed to quantitatively understand the dynamic condensation process down to the nanoscale. Boreyko and Chen (2009) reported continuous dropwise condensation spontaneously occurring on a superhydrophobic surface without any external forces. The spontaneous drop removal results from the surface energy released upon drop coalescence, which leads to surprising out-of-plane jumping motion of the coalesced drops at a speed as high as 1 m s^{-1}. They prepared a superhydrophobic substrate composed of two tier roughness with carbon nanotubes deposited on silicon micropillars (height 8 μm, width 3.7 μm and centre to center separation 8.3 μm) and coated with hexadecanethiol. As a control case they also prepared a smooth silicon substrate coated with hexadecanethiol. During the condensation tests, the saw conventional dropwise condensation with a continuous grow of the droplets on the smooth hydrophobic sample, while, in the superhydrophobic sample, the drops were autonomously removed. This is the first example of sustained Cassie state reported during condensation.

4.4.2 Design: dropwise condensation

Up to know all examples of superhydrophobic surfaces have been reviewed because such surfaces are believed to bead up water drops and to let them to roll off easily. These surfaces are obtained through a combination of chemical hydrophobic treatments and surface roughness. But what is the best configuration for promoting stable DWC?
Patankar (2010) presented an analysis of the thermodynamic of phase change and concluded that the best surface should be made by long slender pillars with hydrophobic sides and hydrophilic tops. In this way, the hydrophilicity in the top of the pillars promotes drops nucleation there, avoiding the condensation in the grooves or cavities that can leas to drops in the Wenzel state which do not slide off easily. The main goal is to control the heterogeneous nucleation controlling the local intrinsic wettability of a surface.

Varanasi *et al.* (2009) reported the first attempt to control the nucleation process. They first proved that on a plain surface, the large different in the intrinsic wettability of hydrophilic and hydrophobic segments results in preferential nucleation and subsequent droplet growth on hydrophilic segments. This is due to the free nucleation barrier for the formation of a liquid nucleus on a flat surface which continuously increases with contact angle. Then they prepared a textured surface consisting of an array of hydrophobic posts with hydrophilic tops as reported in Figure 4.15. They demonstrated that nucleation and subsequent growth of droplets occur preferentially on the hydrophilic post tops of the hybrid surface when compared to the random nucleation of droplets on the identically textured superhydrophobic surface with uniform wettability. The condensation experiments of Varanasi *et al.* (2009) have been done in an ESEM, on a horizontal surface: no external forces were present for removing the condensed droplets from the surface.

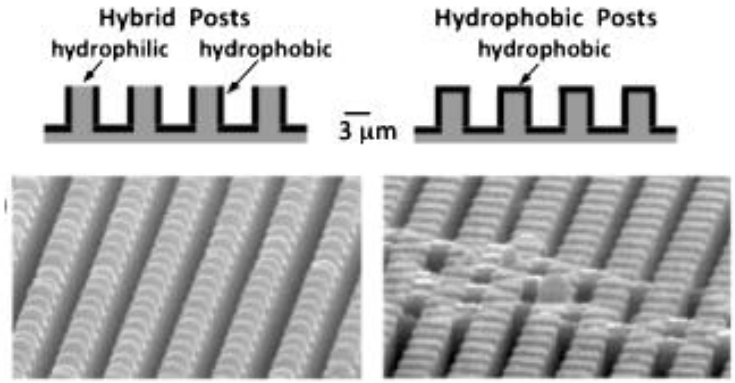

Figure 4.15. Comparison of the condensation behavior on a hybrid surface (Left) consisting of hydrophobic posts (110°) and hydrophilic tops (25°) with that of a superhydrophobic surface consisting of superhydrophobic posts (Right). Image taken from Varanasi et al. (2009).

These works are a guideline in the realization of new surfaces for promoting stable dropwise condensation. But, if such principles have to be transferred in the realization of superhydrophobic surfaces for the promoting of dropwise condensation in the heat exchangers industry, some easy to do and costless treatments should be found. For this reason, as it will present later in next Paragraph 4.5, in this study a very simple method has been applied for producing a superhydrophobic copper surface.

4.5 Superhydrophobic sample preparation

In the present paragraph the technique used for modifying the copper wettability into superhydrofobicity is described. The method is very simple, requires less than two hours and could be done at ambient conditions without special equipment.
A simple immersion process is used to create $Cu(OH)_2$ crystal based superhydrophobic surfaces. Before starting the process, the sample is finely polished: in Figure 4.16 is reported an SEM image taken on a polished sample. The contact angle of water droplet on this surface is about 80°.
The process consists of two steps. During the first one, the copper sample is ultrasonically cleaned in ethanol and deionized water for about 5 min respectively, followed by immersion in an aqueous solution of 2.5 M/L NaOH and 0.1 M/L $(NH_4)_2S_2O_8$ for 12 min. Then the copper sample is fully rinsed with deionized water and dried in nitrogen stream. After this first step, wire-like $Cu(OH)_2$

nanotubes uniformly cover the whole surface of the copper substrate (Figure 4.18), dotted with some microspheres with diameters of about several micrometers (for more details refer to Chen *et al.* (2009)). At this point the copper surface is completely superhydrophilic.
In the second step, the modified copper is immersed in an ethanol solution of 1 mM/L 1H,1H,2H,2H-perfluorodecanethiol (molecular formula $CF_3(CF_2)_7CH_2CH_2SH$) for 30 min followed by washing in ethanol for 30 min and repeated washing with ethanol thereafter.
In this way a monolayer is self-assembled onto the $Cu(OH)_2$ film which results in a surface with water droplet contact angle of around 165°.

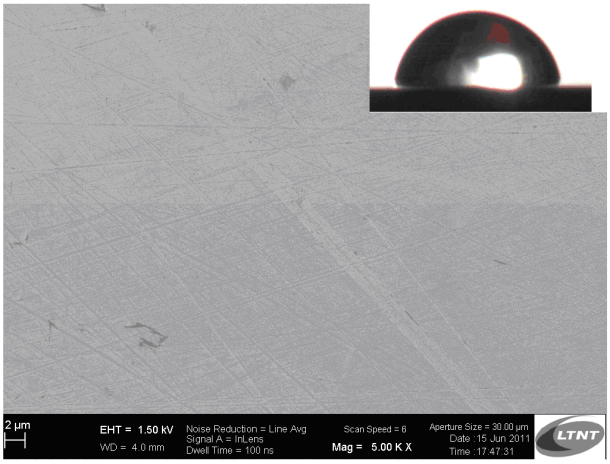

Figure 4.16. SEM image at 2 µm resolution and contact angle measurement on polished copper.

An investigation for determining the optimum solution immersion time that allows the superhydrophobicity and, at the same time, the smallest thermal resistance due to the thickness of the $Cu(OH)_2$ film has been done. In Figure 4.17 the SEM images obtained varying the immersion time from 60 to 450 s are reported. As it can be seen, the process is very fast and after just 60 s some $Cu(OH)_2$ are growing on the copper surface. Anyway, when the immersion time is very short, the dispersion is not uniform, but increasing the time, the nanowires become longer and grow more uniformly.

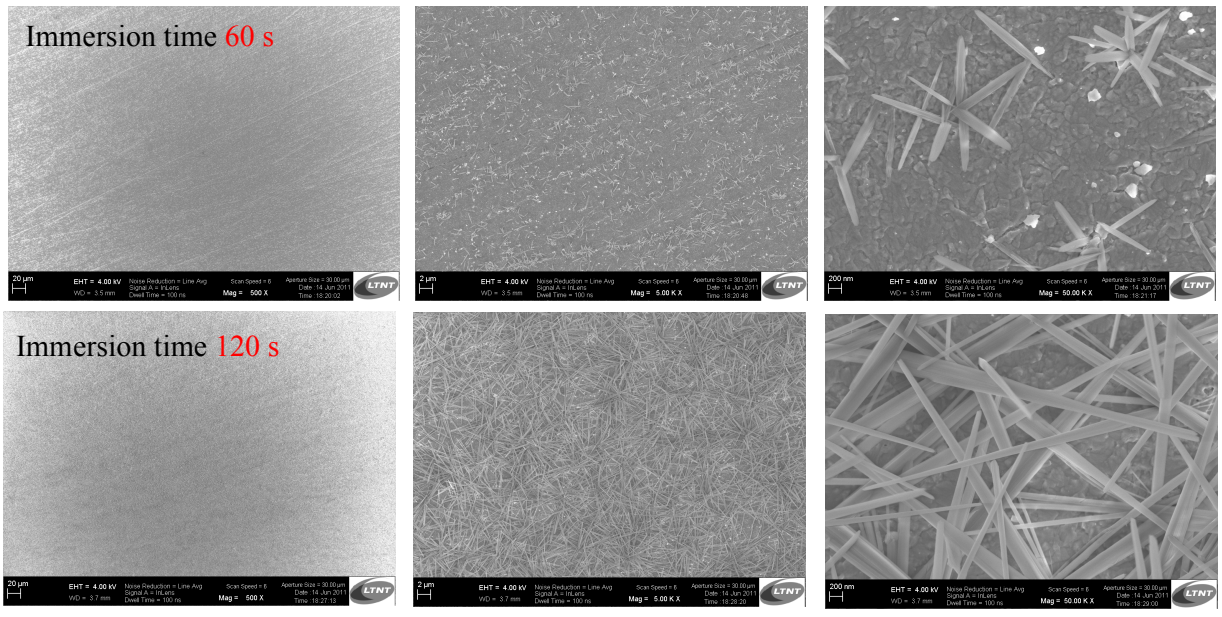

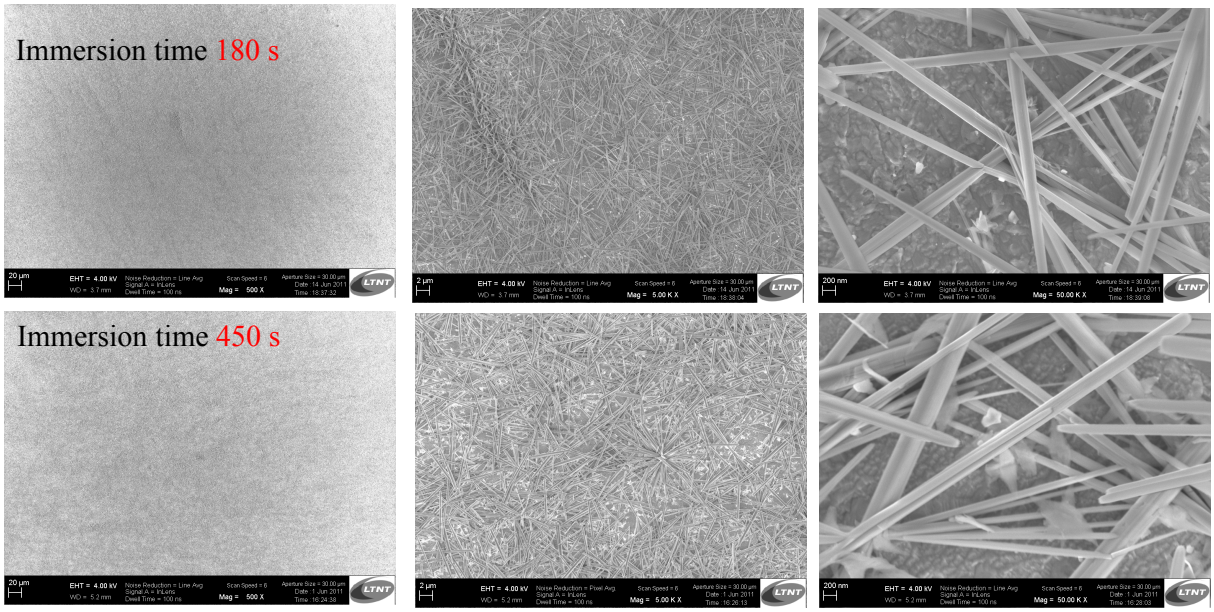

Figure 4.17. SEM images at different immersion times during the first step. For each step there magnification are reported: 20 μm, 2 μm and 200 nm.

The optimum immersion time is found to be 12 min: it guarantees the superhydrophilicity, but also a good mechanical stability tested blowing nitrogen at high velocity on the sample. The SEM images of the sample obtained with the optimum time are reported in Figure 4.18.

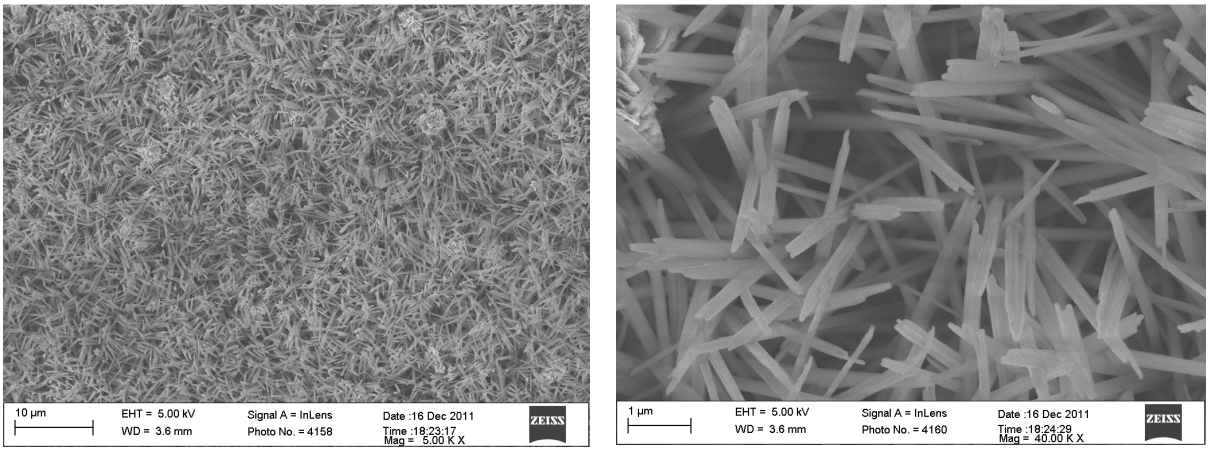

Figure 4.18. SEM images of the copper sample after 12 min immersion time at 10μm and 1μm magnifications.

On such a sample, after the second step, the surface shows superhydrophobic characteristic: the measured contact angle results to be around 165° (Figure 4.19):

Figure 4.19. 4μL water droplet on the superhydrophobic copper sample.

The as described treatment is very simple and requires less than two hours to have a superhydrophobic copper sample. The reproducibility is very good: several samples have been produced in the same way, no problems were found. Moreover, after being stored in air for about 7 months, modified $Cu(OH)_2$ nanowires still maintain a contact angle of about 165°, showing stable superhydrophobicity in a long term.

4.6 Experimental apparatus

In this Paragraph is reported a description of the thermosyphoning test rig and the new test section designed for the study of dropwise condensation of steam on nanoengineered surfaces with the effect of the vapour shear.

4.6.1 Test apparatus

A thermosyphoning two-phase test loop has been designed to measure the condensation heat transfer coefficients attained during steam condensation. Figure 4.20 reports a scheme of the test rig used for the experimental tests. It consists of three main parts: the evaporator, the test section and two cooling water loops. Steam is generated in a stainless steel cylindrical boiler of 0.2 m diameter and 0.3 m height at a maximum pressure of 3 bars gage. The boiler contains immersion heaters connected in parallel with a maximum heating power of 4 kW. The produced steam flows in the vapor line made by a stainless steel flexible pipe with an inside diameter of 0.019 m and length of 1.5 m. Then it enters the test section where are inserted two copper specimens with a diameter of 0.02 m on which the condensation of the vapor takes place. The coppers samples are cooled on the backside by water or a mixture of water and ethanol which is circulated in a closed system by a water bath. Steam not condensed in the test section passes into an auxiliary condenser. The secondary condenser is made by a stainless cylinder with an internal coil in which cold water, supplied from an independent water bath, flows. The subcooler, condenses the balance of steam, collects all condensate and returns the subcooled condensate to the boiler through a gravity drain. A needle valve is inserted at the boiling chamber inlet: its purpose is to make the flow more stable with a proper regulation.
Another important component installed in the test rig is the hydraulic accumulator: it is used for regulating the internal pressure during tests and also in the starting and closing operations. In fact, adjusting the pressure from the gas side it is possible to increase or decrease the pressure inside the test rig. This allows leaving the system in overpressure when no tests are done avoiding air to enter: in this way experiments could be done in consecutive days, without vacuuming and filling the test rig every time before of each test.
A filling line is also installed: when the system has to be filled, after proper vacuuming from the upper valve close to the test section, water from a supplying tank is pumped with a centrifugal pump inside the test rig.
All the components of the test rig, with the exception of the test section, are made by stainless steel in order to avoid contamination of the fluid. Steam components, boiling chamber and the stainless steel line are very well insulated in order to avoid heat loss to the ambient. In particular, in the last 0.5 m of the inlet vapour line, an electrical heater is installed around the stainless steel pipe. The power supplied to this heater is adjusted with a variac in order to avoid the condensation of vapour that could lead to flow instabilities.

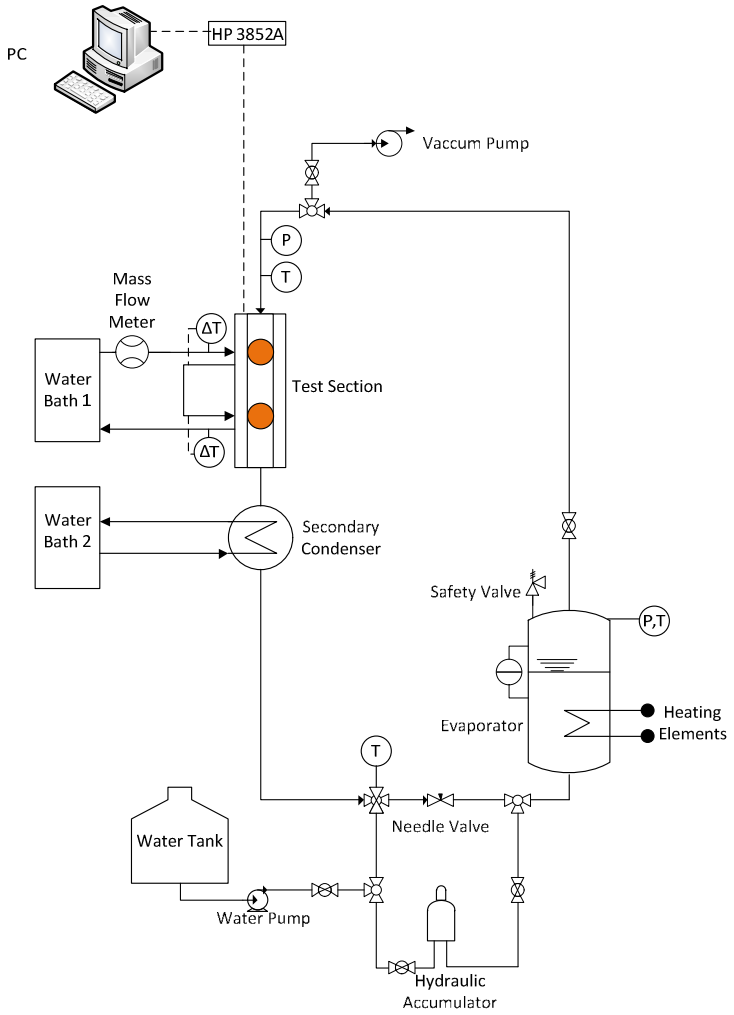

Figure 4.20. Schematic diagram of the experimental system.

Since it has been decided not to install a circulating pump, several considerations have been made in order to assure the natural convection of the fluid. The design steps are described below.
The first decision has been to define the dimensions of the evaporator. The criterion used was to have not a small boiler with respect to the volume occupied by the liquid and the vapor in the transports lines and in the post-condenser. This is very important because the electrical heaters must always be wet by the water. It has been decided to use a cylindrical boiler of 0.2 m diameter and 0.3 m height (11 dm^3), with the heaters (maximum power 4 kW) inserted in the half bottom part of it. It is very important that at least 5 dm^3 of water are always present in the boiling chamber to avoid burning of the electrical heaters. Anyway the boiling chamber is provided with an emergency sensor level that, in case of non-sufficient water inside, will turn off the power supply. The exit of the vapor and the entrance of the return liquid are located in the top and bottom part of the boiler respectively, with ¾" and ½" hose connections. The liquid return line has been sized with 0.01 m of internal diameter and a length of 1.5 m. As explained before, the sum of the liquid volume in the return line and in the post-condenser should not be greater than 5 dm^3. For this reason, on the side of safety, it has been decided to have a maximum internal volume of 2 dm^3 for the post-condenser. Assuming an internal diameter of 0.1 m, the resulting height is 0.25 m.
To guarantee the liquid return in the boiler, some evaluations have been made in order to establish the right position for the secondary condenser, covering the mass velocity range between 5-35 kg

m^{-2} s^{-1} inside the test section. The total pressure drop due to the sum of the frictional pressure losses in the vapor line (d_h=19 mm) and in the test section, plus the local pressure drops due to abrupt geometry changes have been calculated. With a mass velocity of 35 kg m^{-2} s^{-1} a value of 1768 Pa has been obtained with the main contribute of the local pressure drop due to the abrupt changes in the channel dimension at the inlet and outlet of the test section.

G [kg m^{-2} s^{-1}]	m_{steam} [kg/h]	ΔP_{TOT} [Pa]	[mm] H_2O
5	0.00022	64.6	6.9
10	0.00044	248.2	26.6
15	0.00066	526.1	56.4
20	0.00088	889.7	95.5
25	0.0011	1308.8	140.4
30	0.00132	1784.7	191.5
35	0.00154	1768.7	189.8

Table 4.1. Calculated total pressure losses (ΔP_{TOT}), sum of local and friction losses from the exit of the boiling chamber to the inlet of the subcooler, for the mass velocity range (G) between 5-35 kg m^{-2} s^{-1}. The last column (mm H_2O) represents the required height of the condensate inside the subcooler.

If P_{SAT} is the saturation pressure in the system and ΔP_{TOT} the sum of the local and distributed pressure losses from the boiling chamber exit to the post-condenser inlet, the pressure at the inlet of the post-condenser is:

$$P_{Subcooler,in} = P_{sat} - \Delta P_{TOT} \tag{4.8}$$

In order to assure the return of the liquid in the boiling chamber, the height ($H_{Subcooler}$) of the condensate in the post-condenser, with respect to the liquid level in the boiling chamber, should be:

$$H_{Subcooler} \geq \frac{\Delta P_{TOT}}{\rho_L \cdot g} \tag{4.9}$$

where ρ_L is the liquid density and g is the acceleration gravity term. In the last column of Table 4.1 are reported the minimum calculated values of $H_{Subcooler}$.

Even in the case of high mass velocity (i.e. G=35 kg m^{-2} s^{-1}) when the pressure losses are high, the condensate level inside the post condenser has to provide the necessary overpressure to assure its return in the boiling chamber. For this reason, working from the side of safety, it has been decided to position the bottom surface of the post-condenser 30 cm above the top surface of the boiling chamber. In any case, since the test section is connected to the test rig with flexible pipes, there is also the possibility to move the boiling chamber, increasing or decreasing its distance from the post-condenser.

Once it has been decided the position and dimensions of the subcooler, further considerations has been made in order to choose the Kv of a needle valve to install at the inlet of the boiling chamber. In fact, since the mass flow rate are very low, a local pressure drop which could be finely regulated, is necessary to stabilize the flow and guarantee stationary conditions. Calculations have been made considering that the maximum pressure drop admitted across the needle valve, is due to the difference between the sum of the ΔP_{TOT} and the pressure gain of the condensate column in the subcooler.

4.6.2 Description of the experimental section

The test section has been designed for measurements of heat transfer coefficients during condensation of steam with the possibility of direct visualization of the entire process. The main

part is made by a Teflon block having the following dimensions: 70x70x395 mm. This material has been chosen because of its very low thermal conductivity (0.23 W m^{-1} K^{-1}): since the steam temperature during operative conditions is around 110 °C, it is necessary to avoid heat loss to the ambient in order to prevent condensation due to dissipation phenomena. Furthermore, the PTFE ensure the one dimensional steady state conduction in the copper samples. A rectangular cross section grove of 22 mm width, 2 mm height and 230 mm length has been machined in one side of the block. The channel having a hydraulic diameter of 3.6 mm is then constituted by the grove in the PTFE and a glass which is press in contact with it. A viton gasket inserted in a cave on the PTFE face in contact with the glass prevents any leaks in between the glass and the block. The glass is a special one which could be electrically heated up in order to avoid the steam condensation on it: in this way it is possible to observe the condensation process occurring on the two copper surfaces aligned with the bottom part of the channel.
As it can be seen in Figure 4.21 , inlet and outlet of the fluid in the tests section are not aligned with the axis of the channel: the fluid, before entering the measuring rectangular channel (d_h=3.6 mm) deviates its flow passing first in a 1.9 mm diameter circular section to a rectangular 5x22 mm cross section, and then deviating again entering the measuring channel.

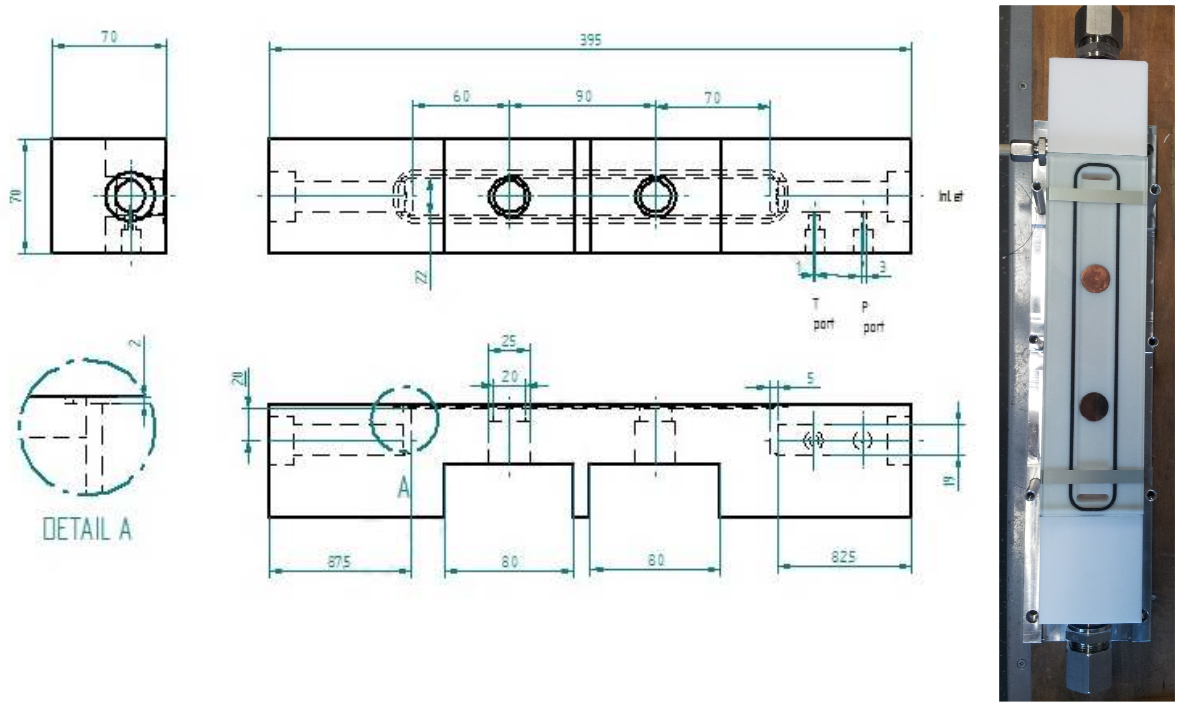

Figure 4.21. Sketch and picture of the test section. Dimension are in mm.

On the other side of the teflon block two holes are machined for accommodating the copper specimens and their cooling system. The copper cylinders have a diameter of 20 mm, a length of 38 mm and are inserted in the Teflon block with the top surface aligned with the bottom part of the channel. Figure 4.22 reports a sketch of them with the dimensions. To avoid any leaks between the channel and the PTFE a gasket is placed in a grove done in an enlargement of the specimen before the measurements. Simulations done in order to investigate the effects of these enlargements have confirmed that their effect is negligible in the heat flux measurement. As it can be seen, 5 holes having a diameter of 0.6 mm are drilled: the distance of the first hole from the top surface is 17.8 mm, while the distance between each hole is 3 mm. A very precise drilling machine has been used in order to have the minimum error in the distance between each other. This is very important since

the heat flux is determined from the slope of the temperature profile measured with the thermocouples inserted in the holes.
The first cylinder is inserted at a distance of 70 mm from the inlet of the channel while the second one is at 160 mm.
On the other side, the copper specimens are put in contact with the cooling system (Figure 4.23). This is made by a copper plate extended with 39 fins to mach the dropwise condensation heat capacity: the ratio between the enhanced surface and the condensation area is about 25.The plate is inserted in a teflon box in order to minimize heat loss: water entering from the side flows thorough the fins and the box. The geometry of the fins has been designed in order to change continuously the water path and break the boundary layer increasing the heat transfer coefficient. For each copper sample there is a cooling system: two thermocouples and a thermopile are inserted for measuring the inlet and outlet water temperature used in the calculation of the water heat balance.

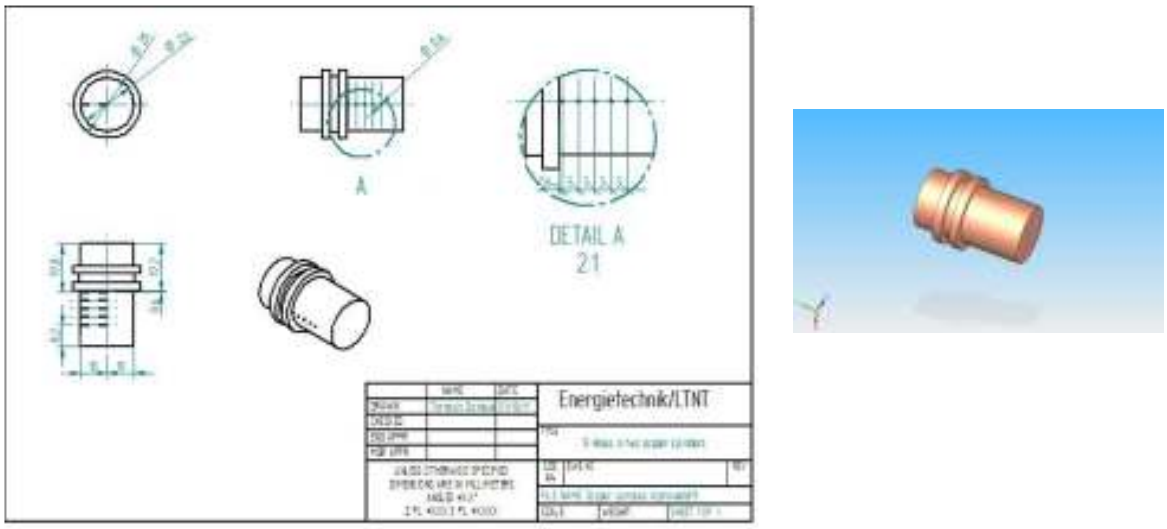

Figure 4.22. Sketch of the copper cylinders. Dimension are in mm.

In order to avoid heat loss to the ambient, a double glazing window unit is installed: in fact, the special glass in contact with the Teflon and forming the measuring channel is separated by a vacuum chamber to another external glass.

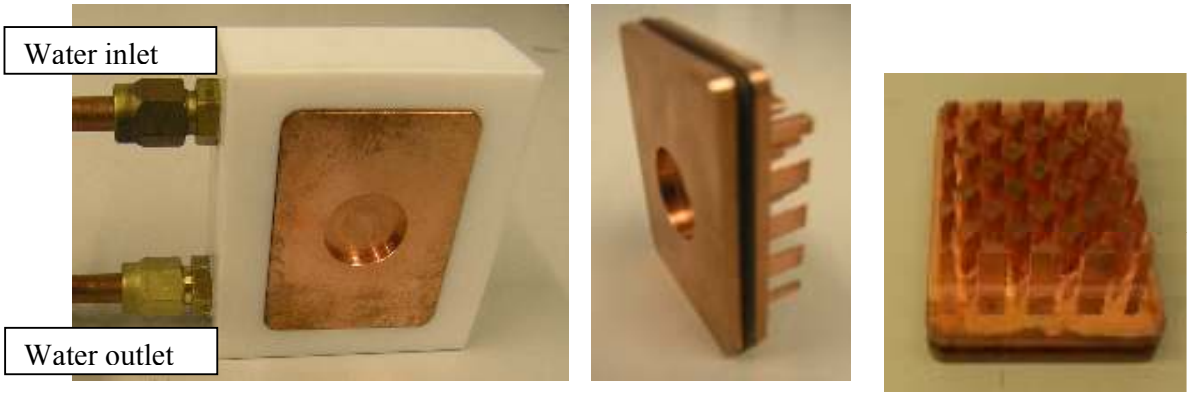

Figure 4.23. Images of the cooling system.

4.7 Data reduction

The present test apparatus allows to determine the heat flux extracted from the condensing vapour from the temperature profile measured in the copper cylinder. In particular, the slope of the profile is used to calculate the heat flux according to the Fourier's law:

$$q = -\lambda \frac{dT}{dz} \tag{4.10}$$

where z is the axial coordinate along the copper cylinder, and dT/dz is the slope of the linear equation interpolating the wall temperature along z. Copper thermal conductivity λ is assumed equal to 395 W m^{-1} K^{-1} (Tables of Physical & Chemical Constants, 2008).

Since the cooling water mass flux $\dot{m}_w$ is measured and also its inlet $T_{w,in}$ and outlet $T_{w,out}$ temperature, the heat flux can also be calculated from a heat balance in the cooling side

$$q = \frac{\dot{m}_w \cdot cp_w \cdot (T_{w,out} - T_{w,in})}{\pi \cdot D^2} \cdot 4 \tag{4.11}$$

The mean temperature of the condensing surface is calculated by extrapolating the temperatures measured inside the cylinder to the copper surface with the assumption of the validity of Fourier's law in its one-dimensional form, which is justified in the vertical center of the plate.

$$T_{wall} = \overline{T} + \frac{q}{\lambda} \cdot \bar{z} \tag{4.12}$$

where $\overline{T}$ is the mean measured temperature inside the cylinder and $\bar{z}$ is the mean thermocouple position along the copper.

The heat transfer coefficient can be obtained as the ratio of heat flux to saturation minus wall temperature difference:

$$\alpha = \frac{q}{(T_{sat} - T_{wall})} \tag{4.13}$$

In the present setup, no sensors for measuring the steam mass flow are installed. The steam flow rate is adjusted regulating the power of the boiling chamber. The stem flow rate could be could be determined from a heat balance to the boiling chamber

$$\dot{m}_{steam} = \frac{Q_{boilingchamber}}{(H_{L,sat} - H_{L,sub}) + H_{LV}} \tag{4.14}$$

where $H_{L,sat}$ is the saturation liquid enthalpy, $H_{L,sub}$ is the subcooled liquid enthalpy calculated from the measured temperature and pressure at the boiling chamber inlet and H_{LV} is the latent condensation heat. In the Eq. (4.14) is also required to know the power supplied to the boiling chamber $Q_{boilingchamber}$ which is directly measured with a NORMA AC Power Analyzer D 5255 S.

All the experimental measurements (temperature, pressure, mass flow rate) are taken as a mean value of 50 readings with a time step of 1 s. In Figure 4.24 is reported a temperature profile measured in the copper cylinder during a DWC test at 110°C saturation temperature and G=10 kg m^{-2} s^{-1}.

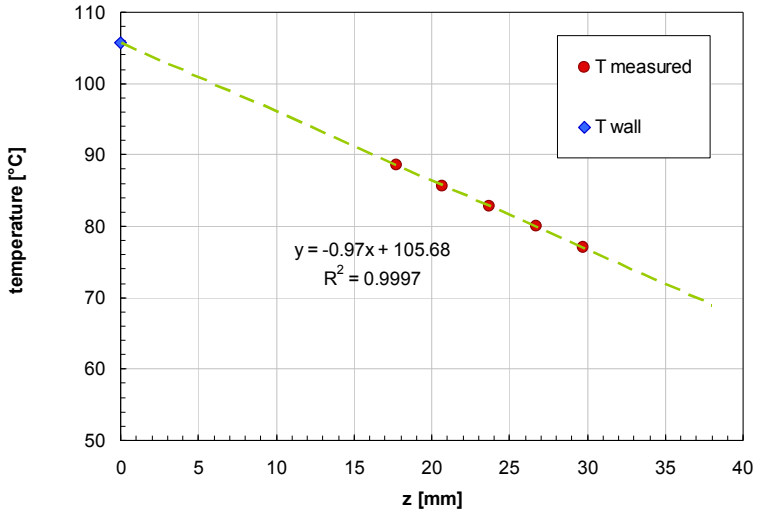

Figure 4.24. Wall temperatures measured during DWC of steam on a polished copper sample at 110°C and G=*10 kg m*$^{-2}$ *s*$^{-1}$*. It is also reported the linear interpolation line with the extrapolated value of the wall temperature.*

4.7.1 Error analysis

The experimental uncertainties are calculated as already seen in Chapter 1 and 2 following the general rules reported in ISO Guide to the Expression of Uncertainty in Measurement (1995). For each parameter, the combined uncertainty u_c is calculated considering "TypeA" and "TypeB" components.

The procedure that has been implemented for determining the uncertainty related to temperature gradient and the extrapolated wall temperature is the weighted least square – WLS (Press *et al.* (2007)) regression method.

The heat flux q is determined fitting with a liner interpolation the measured temperatures inside the copper cylinder which form is given by the following equation:

$$T(z) = a \cdot z + b \tag{4.15}$$

where a and b are the coefficients that minimize the merit figure χ^2 calculated as

$$\chi^2 = \sum_{i=1}^{5} \left[\frac{T_i - \sum_{j=1}^{5} (a \cdot z_j + b)}{u_i(T_i)} \right] \tag{4.16}$$

where j is the i-th location along the copper cylinder in which the temperature is measured, T_i is the water temperature measured at the i-th location, and $u_i(T_i)$ is the experimental uncertainty associated with the temperature at the i-th location.

Let **A** be an 5×*2* matrix whose elements are obtained as reported in Eq. (4.17):

$$A_{ij} = \frac{z_i^{\,j-2}}{u_i(T_i)} \tag{4.17}$$

A vector **b** of 5 elements is also defined as the ratio between the wall temperature measured at the i-th location and the correspondent uncertainty:

$$b_i = \frac{T_t}{u_i(T_i)} \tag{4.18}$$

and finally let **a** the vector whose components are the parameters to be fitted a and b.

The minimum of Eq. (4.16) occurs where the derivative of χ^2 with respect to the parameters *a* and *b* is equal to zero. This condition yields the following equation in the matrix form:

$$\left(A^T \cdot A\right) \cdot a = A^T \cdot b \tag{4.19}$$

The inverse matrix

$$C = (A^T \cdot A)^{-1} \tag{4.20}$$

is related to the standard uncertainty of the estimated parameters *a* and *b*; the diagonal elements of **C** are the square uncertainties of the fitted parameters

$$\begin{aligned} u^2(a) &= C_{11} \\ u^2(b) &= C_{22} \end{aligned} \tag{4.21}$$

and the off-diagonal elements C_{jk} are the covariances between the estimated parameters *a* and *b*

$$\operatorname{cov}(a,b) = C_{12} \tag{4.22}$$

The combined expanded uncertainty related to the heat flux *u(q)* is obtained, neglecting the uncertainty in the copper thermal conductivity, from the uncertainty *u(a)*

$$u_c(q) = k \cdot \sqrt{\left(-\lambda \cdot u\left(\frac{dT}{dz}\right)\right)^2} = k \cdot \sqrt{\left(-\lambda \cdot u(a)\right)^2} \tag{4.23}$$

where *k* is equal to 2 and is a coverage factor giving an interval having a level of confidence of approximately 95%.

The uncertainty in the heat transfer coefficient is obtained considering the covariances between the fitted parameters as:

$$u_c(\alpha) = k \cdot \sqrt{\begin{aligned} &\left(-\frac{\lambda}{\left(T_{sat} - T_{wall}\right)} \cdot u(a)\right)^2 + \left(\frac{\lambda \cdot \frac{dT}{dz}}{\left(T_{sat} - T_{wall}\right)^2} \cdot u\left(T_{sat}\right)\right)^2 + \left(-\frac{\lambda \cdot \frac{dT}{dz}}{\left(T_{sat} - T_{wall}\right)^2} \cdot u\left(T_{wall}\right)\right)^2 + \\ &+ 2 \cdot \operatorname{cov}(a,b) \cdot \left(-\frac{\lambda}{\left(T_{sat} - T_{wall}\right)}\right) \cdot \left(-\frac{\lambda \cdot \frac{dT}{dz}}{\left(T_{sat} - T_{wall}\right)^2}\right) \end{aligned}} \tag{4.24}$$

Table 4.2 reports the uncertainty of the measured parameters. The uncertainty in the thermocouples position is assumed to be zero.

Temperature	± 0.05 °C
Water flow rate	± 0.4 % of flow rate
Absolute pressure	± 7.5 kPa

Table 4.2. Type B experimental uncertainty of measured parameter.

In all the tests reported below, the mean uncertainty in the heat transfer coefficient is of 8.6 % and the major contribution is due to the uncertainty in the difference between the saturation and the wall temperature with a mean value of 8.4%. The mean uncertainty in the heat flux is less than 1%.
Furthermore in all the tests the disagreement between the heat flux calculated with Eq. (4.10) and (1.11) is always below 20% with a mean value of 7%.

4.8 Calibration of the set up and preliminary tests

Previous to any measurements, several actions have been undertaken in order to assure the accuracy of the results. Since the heat flux is calculated from the slope of the wall temperature, high attention has been dedicated in calibration and installation of the thermocouples. Simple short circuit soldering of 0.127 mm thick copper – constantan wires without using any additional bonding material was used to obtain the homemade T-type thermocouples.
All the thermocouples were electrically insulated and inserted with thermally conductive glue in the copper wall, where 0.6 mm diameter holes were made till the middle of the cylinder. Each thermocouple was checked against the tube wall, whether it was electrically insulated or not.
All thermocouples, on the other hand, were corrected for the constant shift value against Fluke 9142 calibration bath (see Figure 4.25 right), coupled with a reference probe: their nominal uncertainty was considered equal to ± 0.02 °C at 50 °C and ± 0.025 at 150 °C. All thermocouples were thus checked and calibrated in the temperature range 50-110 °C: a corrections function has been found for each thermocouple and inserted in the LABWIEV acquisition program.
After the installation of the thermocouples in the copper cylinder, adiabatic conditions were established making the vacuum inside the test section while water was flowing in the cooling system connected to the cylinders. Once the steady state operation was assured, all the thermocouples values resulted aligned and inside a band of ± 0.05 °C: Figure 4.25 reports a screen shot of the acquisition program with the thermocouples readings during a check test.

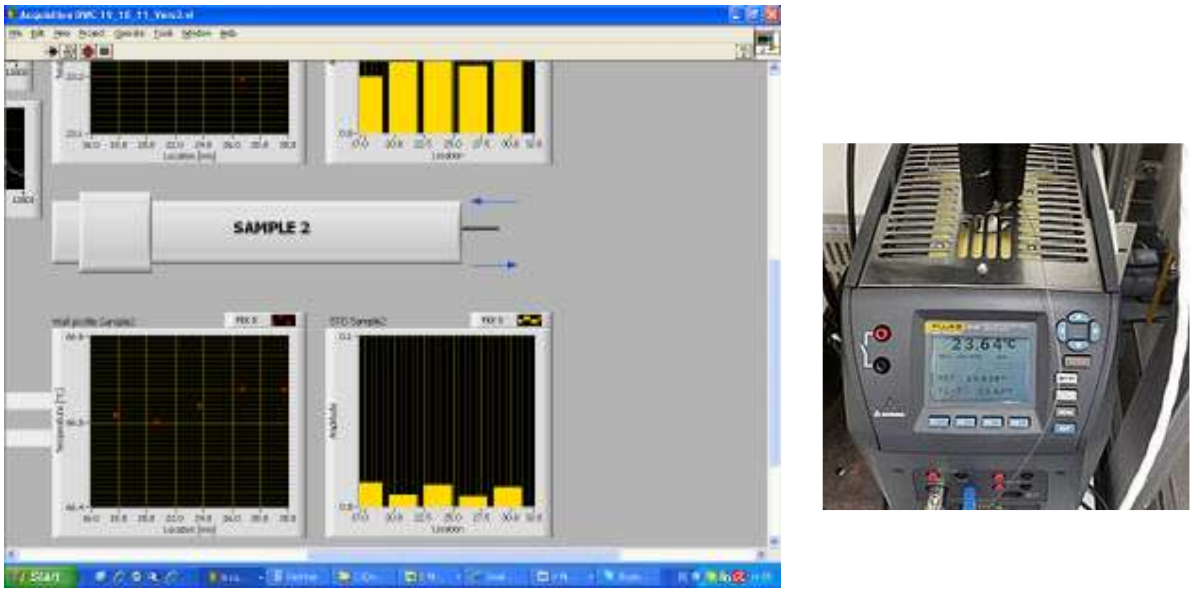

Figure 4.25. (Left)Thermocouples alignment with vacuum inside the section and water in the cooler. (Right) Fluke 9142 calibration bath.

Once the thermocouples have been calibrated, filmwise condensation tests on a naturally oxidized copper sample were performed in order to check the agreement with the Nusselt (1976) theory.
The results for the measured mean heat transfer coefficients are compared with those values calculated by the corrected form of Nusselt film theory:

$$\alpha = 1.15 \cdot \left[0.0206 \cdot \left(\frac{H_{LV} \cdot \mu_L}{\lambda_L \cdot (T_{sat} - T_{wall})} \right)^{\frac{1}{2}} + 0.79 \right] \cdot 0.943 \cdot \left[\frac{\rho_L \cdot (\rho_L - \rho_V) \cdot g \cdot H_{LV} \cdot \lambda_L^{\,3}}{\mu_L \cdot (T_{sat} - T_{wall}) \cdot 0.817 \cdot D} \right] \qquad (4.25)$$

where ρ_L is the condensate density, ρ_V is the densities of the steam, g is the acceleration of gravity, λ_L is the thermal conductivity of the condensate, μ_L is the dynamic viscosity of the condensate, T_{sat} and T_{wall} are the saturation and surface temperature respectively, and D is the condensing surface diameter. The last part of Eq. (4.25) represents the Nusselt (1916) film theory, which in the present has been corrected for taking into account the circular shape of the condensing plate. This is done with the term $0.817 \cdot D$ as suggested by Koch *et al.* (1997) which substitute the height of the condensing plate in the original formula. Furthermore, as wave formation was observed on the condensate film during the FWC experiments, the heat transfer enhancement due to this phenomenon has to be taken into account which can be adequately done by the correction factor 1.15 (Baehr and Stephan 2004).

Inertia effects, which are neglected in Nusselt's considerations, can be included by the empirically obtained second term in Eq. (4.25) as suggested by Depew and Reisbig (1964). The variation of the physical properties of the condensate with temperature has also to be considered.

Here, the viscosity shows the dominant effect which can be compensated by calculating all physical properties of the condensate at the mean temperature:

$$T_m = 0.75 \cdot T_{wall} + 0.25 \cdot T_{sat} \qquad (4.26)$$

while only the latent heat H_{LV} and the density of the saturated steam ρ_V are calculated at T_{sat} (Rose 1999).

Experimental results are reported in Figure 4.26 and compared with the original Nussel (1976) model and the modified one calculated with the formula (4.15). As it can be seen the agreement is good considering the very huge error bars: in fact, the temperature profile during these tests was not so stable and thermocouples values were oscillating quite a lot. This was due to the fact that the present set-up has been designed for studying the effect of vapour velocity: then, it is very difficult to perform very stable tests at low steam velocity, since the boiling chamber has to work at the minimum power.

Since even a few concentrations of non condensable gases in the vapour could lead to huge decrease in the thermal performance of the condensation process, several actions have been undertaken to avoid it. In particular it has been decide to operate always in overpressure conditions with respect to the ambient pressure in order to prevent air to go inside the test rig. Furthermore, before of each test run, the whole system was vacuumed; then the entire test rig was charged with deionized water coming from a supplying tank. When the pressure inside the setup was higher than the ambient pressure, water was released from the top valve in order to get rid of any non condensable gases still inside the setup while the filling pump continuing to run. After one minute of free water discharging the top valve was closed and then also the filling line. Subsequently, the boiler was started: when the water was heated up to the saturation temperature and boiled for several minutes, the vapour was released from the top valve. This procedure was repeated several times in order to get rid also of the gases dissolved in the water. In all these operations particular care was observed in order to be always in overpressure inside the test rig.

If non condensable gases where present inside the setup, a disagreement between the measured saturation pressure and the one calculated from the measured temperature should be observed. In particular, if NCG are present, the measured pressure should be grater then the calculated from the temperature. On the contrary, in all the data presented below, the calculate saturation pressure from the temperature is higher than the measured one, and inside the experimental uncertainty of the pressure transducer and the thermocouple.

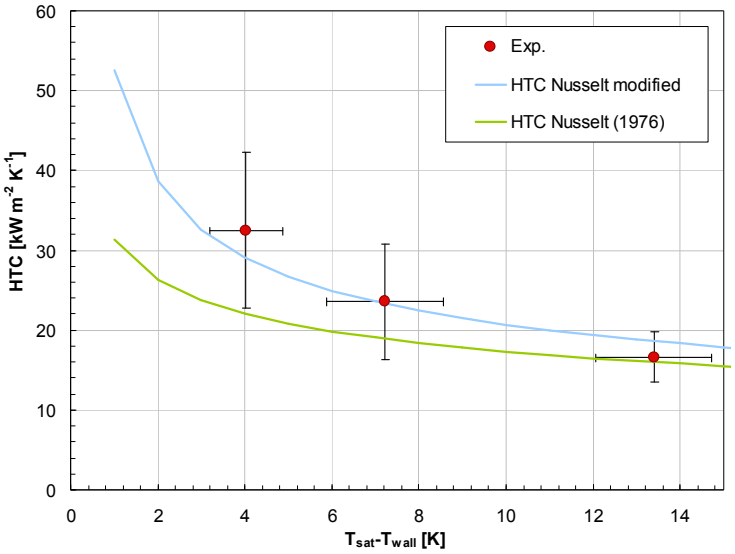

Figure 4.26. Comparison of the experimental values with the Nusselt theory: the two curves represent the original values calculated with the model by Nusselt (1976) and the corrected formula Eq. (4.25).

4.9 Condensation tests

Steam condensation tests have been performed at 1.43 bar (110 °C saturation temperature) on several copper samples. In the first paragraph, heat transfer measurements done on a naturally oxidized copper sample are presented. This sample was a polished copper cylinder which was naturally oxidized after having been in contact with air and water for one month. All the other measurements, with the exception of the ones presented in the last Paragraph 4.9.4, have been performed on polished copper sample.

4.9.1 FWC test on naturally oxidized copper: effect of the vapour velocity

As already said, the present setup has been designed for studying the effect of the vapour velocity during the dropwise condensation inside small channel (d_h in the miniscale range). Before any DWC tests, it has been decided to investigate the effect of the vapour velocity during filmwise condensation on a naturally oxidized copper sample which has been exposed to water and air for one month. Steam velocity has been regulated with adjusting the power supplied to the boiling chamber.
As already seen in Chapter 1 during the condensation study inside two minichannels, it is expect that the effect of increasing the mass velocity will be to increase the heat transfer coefficient.
According to Rose (1998), during condensation on a vertical plate, gravity effects begin to dominate when F (Eq. (4.27)) which measure the relative importance of gravity (through Gr) an d vapour velocity (through $\widetilde{\mathrm{Re}}$) is greater than 1, while vapour shear stress becomes more important than gravity when F<1.

$$F = \frac{1}{J} \cdot \left(\frac{Gr}{\widetilde{\mathrm{Re}}^2} \right) \tag{4.27}$$

$$Gr = \frac{\rho_L \cdot (\rho_L - \rho_V) \cdot g \cdot d_h^{\,3}}{\mu_L} \tag{4.28}$$

$$\widetilde{\mathrm{Re}} = \frac{u_\infty \cdot \rho_L \cdot x}{\mu_L} \tag{4.29}$$

where ρ_L is the condensate density, ρ_V is the densities of the steam, g is the acceleration of gravity, u_∞ is the vapour free steam velocity, μ_L is the dynamic viscosity of the condensate, d_h the duct hydraulic diameter and x the distance from top of the plate.

In the present study F is always below 1, meaning that the effect of the vapour shear is more important than gravity. This is confirmed by the experimental measured values of the heat transfer coefficient: it increases with the wall subcooling but also with the vapour velocity. Results are reported in Figure 4.27. Tests have been done at a saturation temperature of 110 °C and at three different mass fluxes: G 5, 10 and 15 kg m^{-2} s^{-1} correspondent to 6, 12 and 18 m s^{-1} calculated values for the vapour velocities. The increase is around 30% passing from $G5$ to $G10$ and around 20 % from $G10$ to $G15$. It is important also to notice that the difference is much less al low subcooling grade: this may be explained because the condensate film thickness is already small due to the low heat fluxes exchanged and then no appreciable improvements could be introduced increasing the vapour velocity. In Figure 4.27 is also reported the heat flux and heat transfer coefficient calculated according to the modified Nusselt theory (Eq. (4.25)). As it can be seen, even at the lower velocity the recorded values are higher than the predicted ones. This is expected since the Nusselt theory does not take into account the vapour velocity.

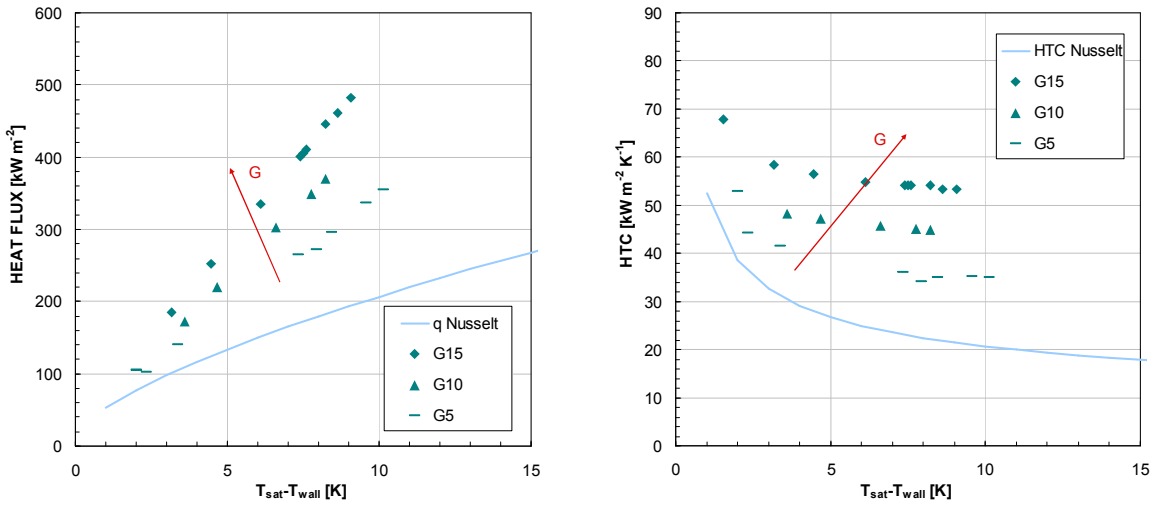

Figure 4.27. Heat Flux and Heat transfer coefficient in function of the wall subcooling during FWC of steam at G=5, 10 and 15 kg m^{-2} s^{-1} on a naturally oxidized copper sample.

4.9.2 DWC and FWC comparison on polished copper

In this Paragraph, three different modes of steam condensation, dropwise, mist dropwise and filmwise, filmwise (FWC), measured on copper samples are presented and compared. Dropwise condensation was observed on a polished copper sample: the entire surface was covered with drops and droplets (see Figure 4.28 Left) and the cyclic process of nucleation, coalescence and sweeping was recorded with a high speed camera which allowed understanding the physical mechanism

which dominates. It is well known that most metals when polished have a very low surface energy and then are surfaces where steam could condensate in the dropwise mode.

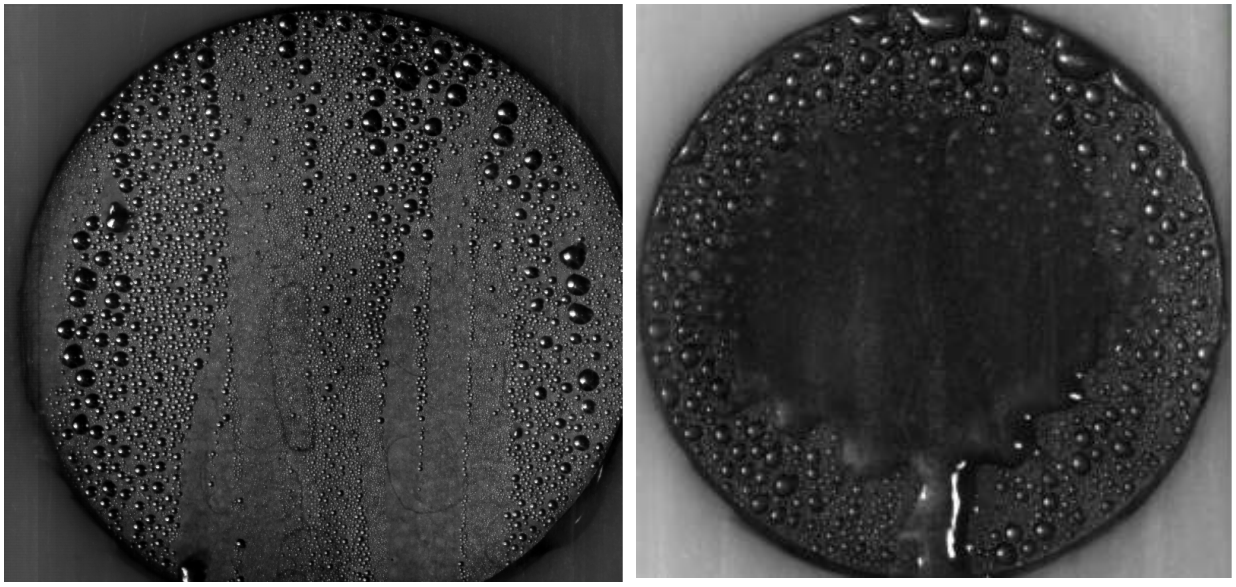

Figure 4.28. (Left) DWC on Polished copper G10 kg m^{-2} s^{-1} ΔT=2 °C, Tsat=109.6 °C, q=579 kW m^{-2}. (Right) DWC/FWC G10 kg m^{-2} s^{-1} ΔT=2.1 °C, Tsat=109.9 °C, q=254 kW m^{-2}

Figure 4.29 reports several frames of a video recorded during DWC with a frequency of 1000 fps. Time step between each image is 4 ms. Vapour is flowing in the direction indicate by the arrow. As it can be seen, at the beginning small droplets are growing on the cold surface (0 ms). Then, as they reach a certain size, start to coalesce into larger drops but the center of mass of the merging drops did not change appreciably before and after coalescence (4 ms). Only when the average drop diameter reached a critical value (24 ms), coalescence leads to mobilization and rapid removal of the merged drops from the surface. In that moment, drops sweep over the surface helped by the shear stress exerted by the flowing vapour, adsorbing and wiping small droplets in their path (32-44 ms). Then, new droplets from and grown on the wiped surface, but very often, these do not have the time to reach the critical radius because are wiped by other drops coming from the top part of the sample. These images confirms that, in the case of dropwise condensation with the effect of the vapour shear, the surface area between condensate drops remain dry with no indication of a microfilm: this is in perfect agreement with the "nucleation model" of condensation proposed by Eucken (1937) and confirmed by many authors (Graham and Griffith (1973), Rose and Glicksman (1973), Tanaka (1975b), etc..).
By collecting the drops in their path, the moving drops grow and sweep diverging tracks causing lower region on the sample to be swept more frequently: this ensures that only drops near the top of the surface can reach the size at which the effect of the shear stress exceed the net surface tension restraining force. In the case of Figure 4.29 the measured critical diameter d_c is around 0.6-0.9mm with a vapour velocity of 12 m s^{-1}. This value is substantially less than the capillary length:

$$k^{-1} = \sqrt{\frac{\sigma_{LV}}{\rho_L \cdot g}} \tag{4.30}$$

where is σ_{LV} the water surface tension, ρ_L is the condensate density and g is the acceleration term due to the gravity. The calculated value of the capillary length for water at 1.43 bars is equal to 2.45

mm. Since gravitational removal only affects drops with a diameter comparable to the capillary length, in the present study, the effect of the gravity is negligible.
Figure 4.30 reports the heat flux measured during this test: as it can be seen, the experimental values are in good agreement with the value predicted by the correlation of Rose (1998) reported below (Eq. 4.31).

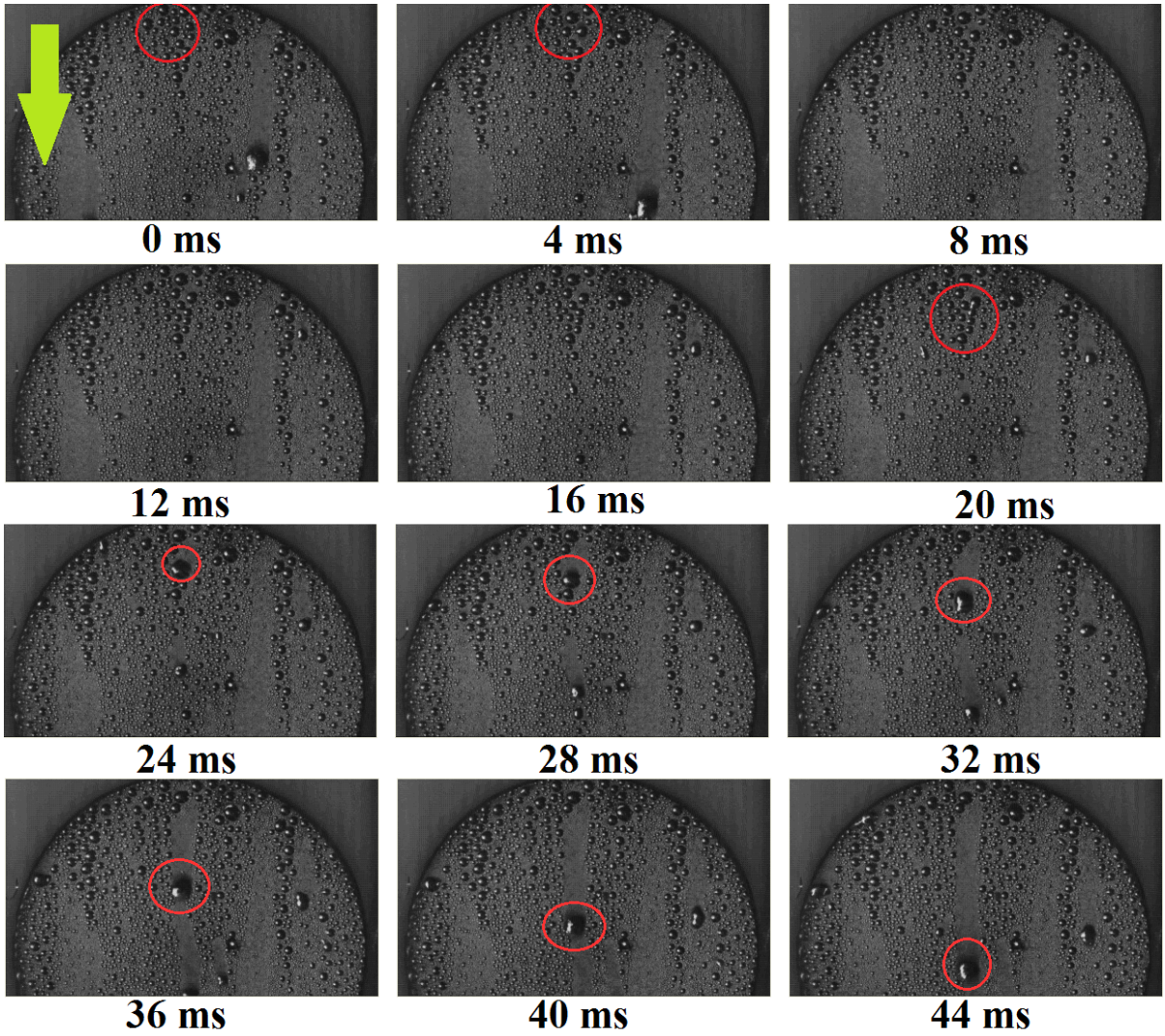

Figure 4.29. Droplet cycle on a polished copper sample at G=10 kg m^{-2} s^{-1} at 2 K *of surface subcooling. The arrow indicates the vapour flow direction.*

$$q = t^{0.8} \cdot \left(5 \cdot \frac{\Delta T}{K} + 0.3 \cdot \frac{\Delta T^2}{K^2} \right) \qquad (4.31)$$

where t is the saturation temperature in Celsius, ΔT is the difference between the saturation and the wall temperature, and K is a constant which value is 0.728.
A mist mode of condensation, where FWC was happening in the central part of the sample while a lot of drops were forming in the external part was observed on a copper sample after one day of test. (see Figure 4.28, Right). The mechanism of the condensation was the same just described in the area where the dropwise mode was effective even if, due to the oxidation process, drops were

bigger and less mobile on the surface. The difference was that as soon as they reached the critical radius, they moved very fast towards the center of the surface, where the filmwise mode was taking place. The decreasing performance of such a situation with respect to the pure DWC mode is represented in Figure 4.30: at the same conditions, saturation temperature and vapour velocity, the heat transfer coefficients in the mist mode are less by 50% than the ones measured during DWC. It can be noticed that the heat flux is increasing until ΔT=5 K and then decreasing, with a clear trend towards the curve reported for the pure filmwise mode. This could be explained by the fact than 75% of the surface was covered by a condensate film at 5 K of subcooling, while for ΔT=2 K the film area was 45% of the total.

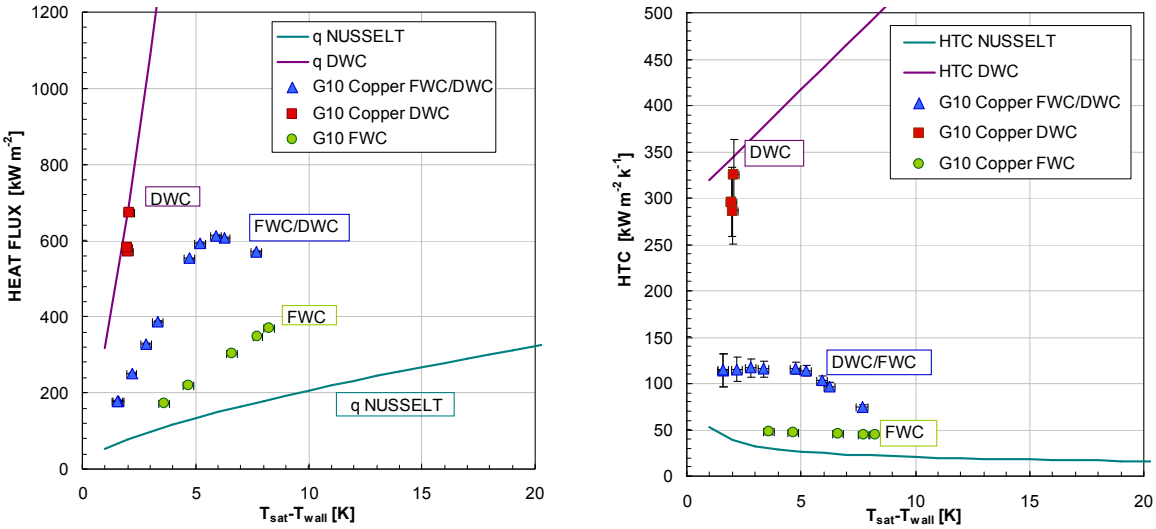

Figure 4.30. Heat flux(Left) and Heat transfer coefficient (Right) during FWC, DWC/FWC and DWC mode on a copper sample at G=10 kg m^{-2} s^{-1}

For comparison, Figure 4.30 also reports the values measured with a naturally oxidized copper sample in which a film of condensate was covering the entire surface. In this case the heat flux is one order of magnitude less than the values measured during the dropwise tests. This is due thermal resistance of the condensate which is responsible for the decreasing performance of the process. This result becomes more clear by observing the measure temperature profiles during there tests with the same vapour conditions: while the different between the first and last wall thermocouple is 20 K for the DWC test, it is 8 and 3 K for the mist and pure FWC mode respectively.

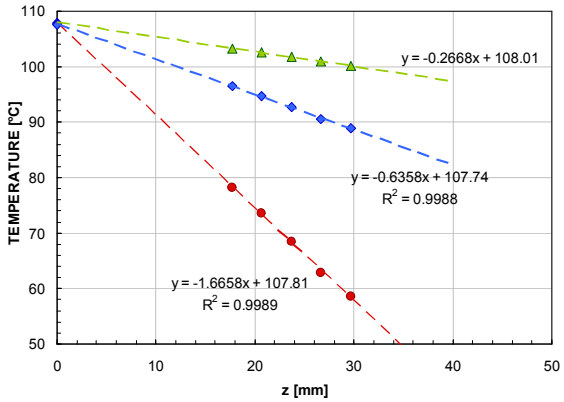

Figure 4.31. Wall temperature profiles during DWC, mist DWC/FWC and FWC condensation on a copper sample at G=10 kg m^{-2} s^{-1}

4.9.3 Corrosion effects on a polished copper sample during steam condensation

A study of the corrosion effects on a polished copper sample is presented in this paragraph. Tests were performed for three consecutive days in order to investigate the effect of the corrosion in the heat transfer performance. In the present setup, the combination of the vapour velocity and the high temperature constitutes a favorable condition for the corrosion process of copper. Tests were started with a polished copper sample which was ultrasonically cleaned in water and ethanol before the experiments. After just one day of test, the surface of the sample turned from the pink color of the polished sample to a darker color.

Every day of test two different mass velocities have been investigated: Figure 4.32 reports the heat transfer coefficient and the heat flux measured at the G=10 kg m^{-2} s^{-1}, which corresponds to 12 m s^{-1} for the vapour velocity, while Figure 4.36 reports results obtained at G=15 kg m^{-2} s^{-1} (v=18 m s^{-1}). Dropwise condensation was observed for the first there days of tests, while it turned to FWC the fourth day. In Figure 4.32 and Figure 4.33 it could be clearly seen the corrosion effect on the heat transfer performance: for both the mass flux, the heat flux decreases by 15% at the same ΔT.

In each test the heat flux increases with the wall subcooling due to the higher condensation of vapor. Also the heat transfer coefficient shows in most of the cases an increasing trend with the wall subcooling as expected for the DWC mode of condensation. This is more evident at higher mass velocities (G=15 kg m^{-2} s^{-1}) while at G=10 kg m^{-2} s^{-1} is clearly visible in the test recorded the last two days. Very interesting is the trend reported for the heat transfer coefficient at a vapour velocity of 12 m s^{-1} measured the second day: as in can be seen in Figure 4.34 it first increases at low ΔT and then reaches a constant value. Also the heat flux shows a linear increasing trend at low subcooling, while for ΔT >3.5 K it sill increases but with a different slope. At higher vapour velocity (18 m s^{-1}) the trend is different: heat transfer coefficient and heat flux increase linearly with the wall subcooling in the entire range investigated. The same behavior is found during the tests in the third day, with no effect of the velocity at low ΔT, while increasing the subcooling grade, higher vapour velocities are responsible for higher heat flux. Nevertheless the heat performance increase is about 5% with an increase of vapour velocity by 50%.

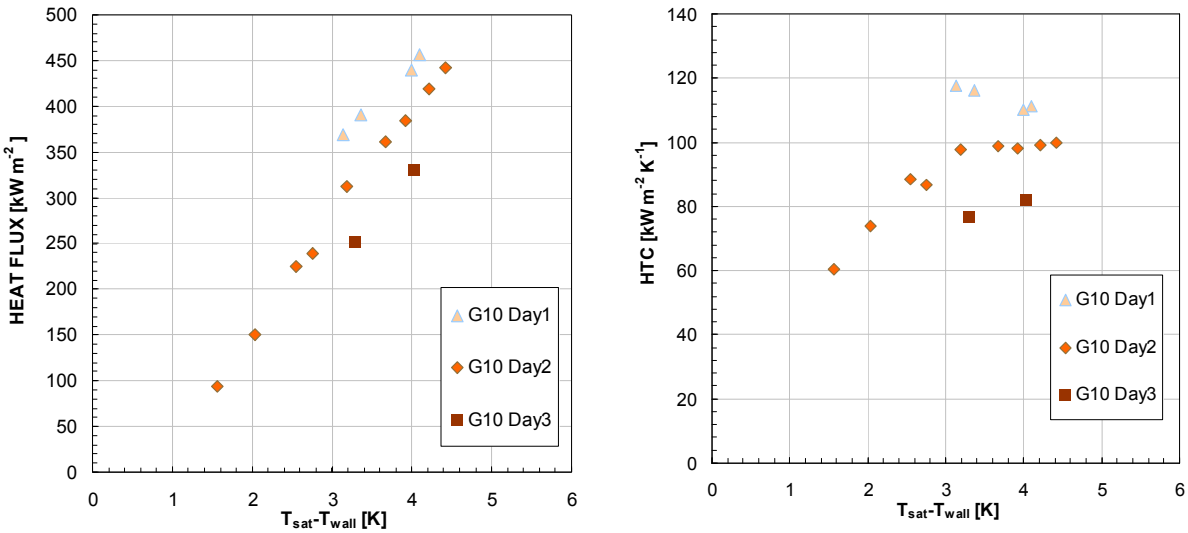

Figure 4.32. Heat flux and Heat transfer coefficient as a function of the wall subcooling during DWC of steam at G=10 kg m^{-2} s^{-1} measured for three consecutive days.

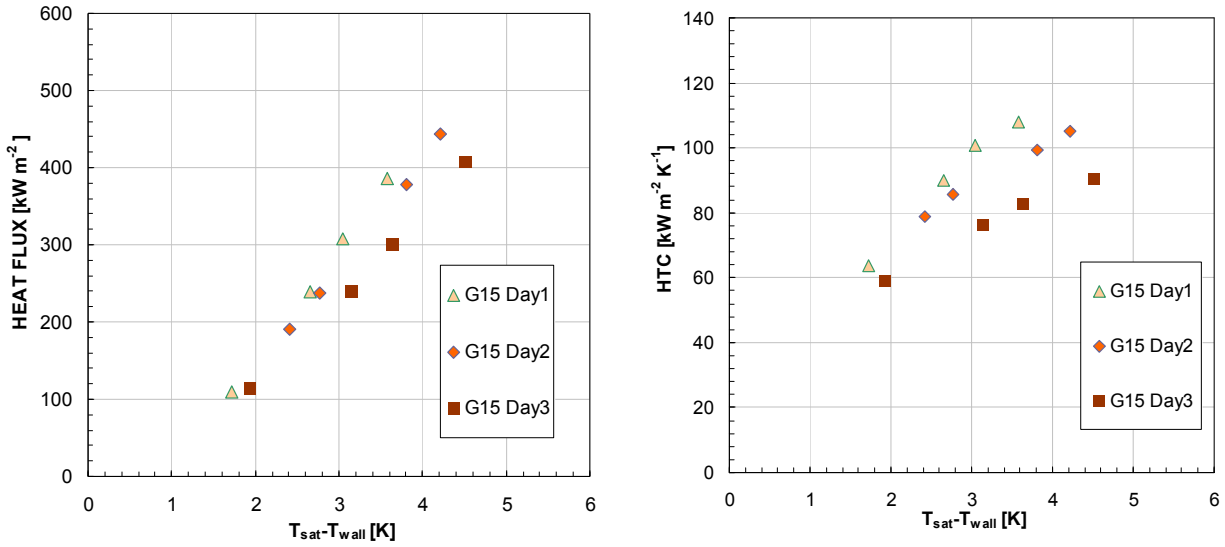

Figure 4.33. Heat flux and Heat transfer coefficient as a function of the wall subcooling during DWC of steam at G=15 kg m^{-2} s^{-1} measured for three consecutive days

Figure 4.35 reports two images comparing the condensation mode at different shear rate. As it can be seen, higher is the vapour velocity, smaller are the droplets covering the surface. Consequently, also the departing diameter is smaller: for example, in the case reported in Figure 4.35, with a wall subcooling of 2 K, the departing diameter with a vapour mass flux of G=10 kg m^{-2} s^{-1} is 0.9 mm, while at G=15 kg m^{-2} s^{-1} is 0.7 mm. On the contrary, the frequency at which droplets depart the surface is higher in the case of high velocity. This is expected due to an increase on the flow drag on the condensate droplet with increase in the vapor velocity. Nevertheless, as reported in Figure 4.34, no sensible improvements are observed in term of heat flux and heat transfer coefficient.
Analysis on the departure diameter of the droplets gives an insight into the heat transfer coefficient trend. In fact, from the visual observation, in the case of Figure 4.34 at G=15 kg m^{-2} s^{-1} , increasing the wall subcooling, results in the decreasing of the droplets departing diameter: it goes from 0.6 mm at ΔT=2°C to 0.48 mm at ΔT=4°C which explains the increasing trend in the heat transfer coefficient. On the contrary, for the same subcooling range, in the case of G=10 kg m^{-2} s^{-1} the departing diameter remains almost constant (equal to 0.9 mm), and so does the heat transfer coefficient.

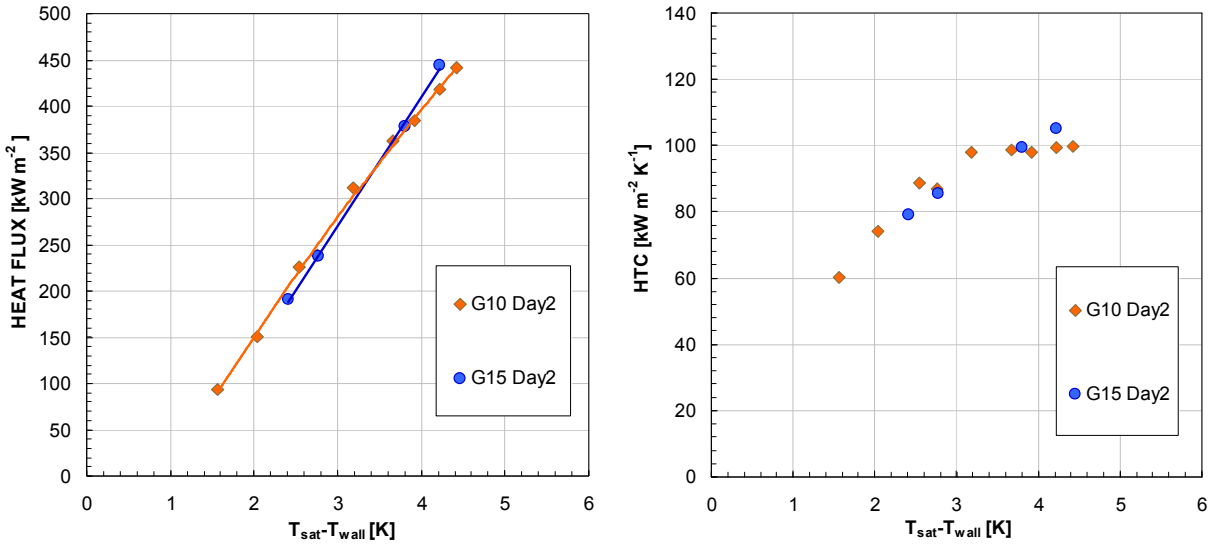

Figure 4.34. Heat flux and Heat transfer coefficient as a function of the wall subcooling during DWC of steam at G=15 kg m^{-2} s^{-1} and G=10 kg m^{-2} s^{-1}measured on the second day of test.

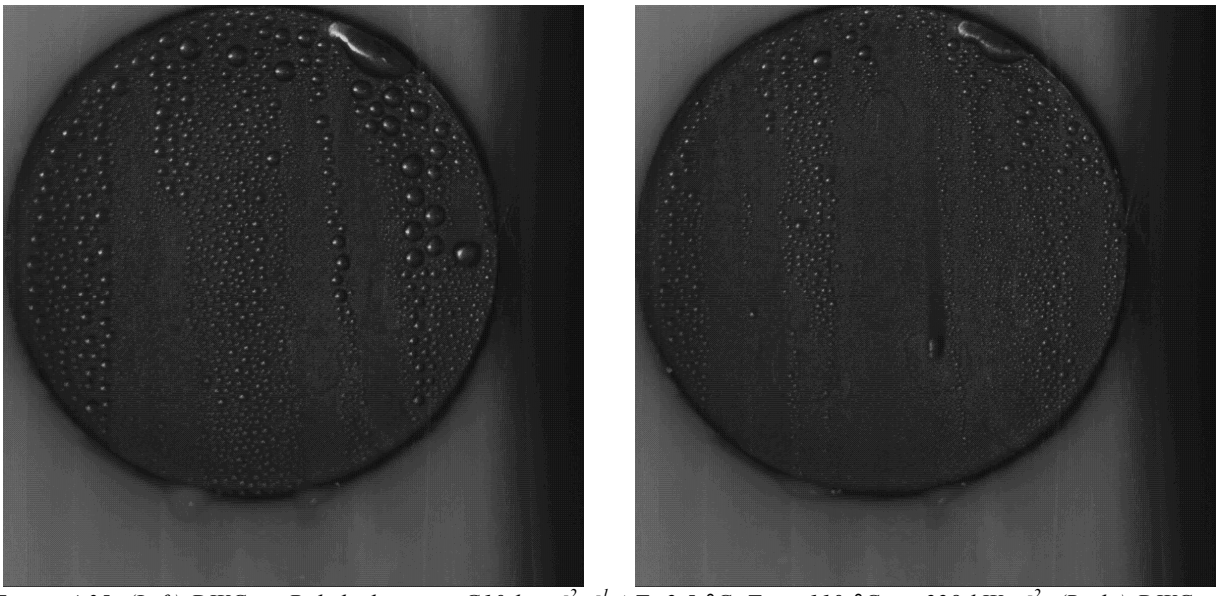

Figure 4.35. (Left) DWC on Polished copper G10 kg m^{-2} s^{-1} ΔT=2.5 °C, Tsat=110 °C, q=228 kW m^{-2}. (Right) DWC, G15 kg m^{-2} s^{-1} ΔT=2.7 °C, Tsat=109.7 °C, q=240 kW m^{-2}

In Figure 4.36 are compared the data measure during FWC at *G* 10 kg m^{-2} s^{-1} and *G* 15 kg m^{-2} s^{-1} with the ones measured during DWC in the second of test for the corrosion investigation. Clearly, while at ΔT <2°C there are no differences, as the subcooling grade increase, the heat flux in the dropwise mode grows much faster than during the filmwise mode: the increase is around 60 % at ΔT =3 K and 90 % at ΔT =4.5 K. Furthermore, while the heat transfer coefficient during FWC mode decreases with the subcooling grade, an opposite trend is observed during DWC.

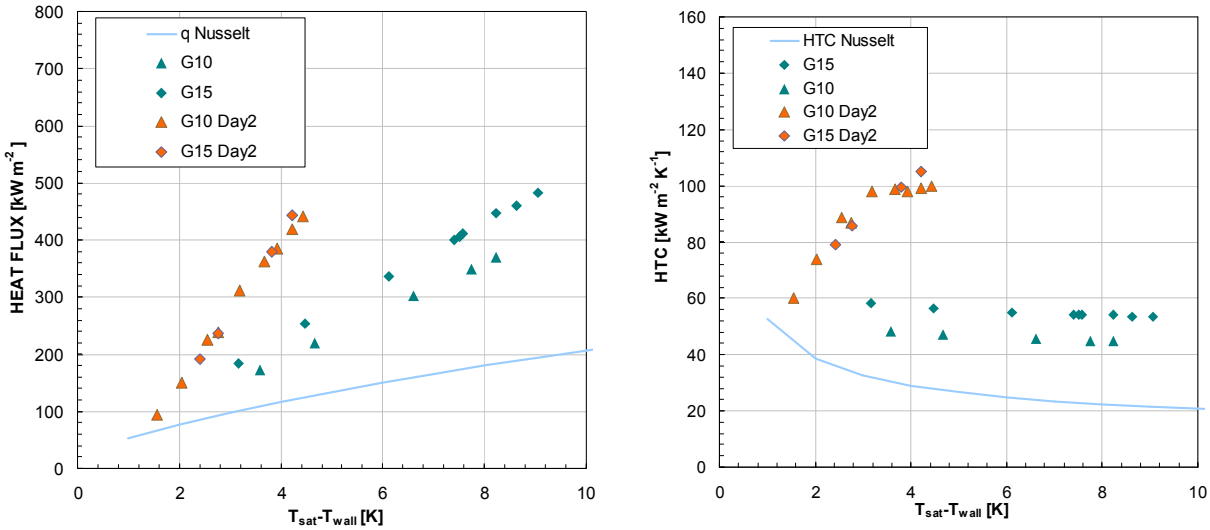

Figure 4.36. Comparison between FWC data reported in Figure 4.27 and DWC data of recorded the second day of Figure 4.28 and Figure 4.29.

4.9.4 Tests on a superhydrophobic copper sample

The superhydrophobic sample prepared as described before in Paragraph 4.5 was testes during steam condensation to investigate the influence of superhydrophobicity during steam condensation. The sample was inserted in the second position inside the channel and then the experimental results could be affected by the disturbance in the hydrodynamic profile due to the condensation in the previous sample. Nevertheless, from the videos recorded with a high speed camera, it could be seen that these effects could have a very small influence: in fact, the condensate of the first sample flows downstream wiping the glass, without influencing the condensation process in the superhydrophobic one.

Figure 4.37, shows the condensation curve obtained with the superhydrophobic sample. As it can be seen there are two distinct regions: the dropwise region at low subcooling (ΔT<6 °C) and the transition region at higher ΔT. In particular, the first region could be further subdivided into three regimes. First, the regime (1) where the heat transfer coefficient and the heat flux grow in function of the subcooling, as already observed in Paragraph 4.9.3. Second, the regime (2) where the heat transfer coefficient remains constant (i.e. the heat flux is proportional to the surface subcooling). Finally, the regime (3) where the heat transfer coefficient decreases but still the heat flux increases until the peak flux 660 kW m^{-2} at ΔT =5 °C. After the regime (3) the mode of condensation is a transition regime: as it can be seen in Figure 4.38 a film of condensate covers almost the entire surface while just in a small part of the surface droplets were still present.

The present trend is in agreement to the experiments of Takeyama and Shimizu (1974) and Tanasawa and Utaka (1983) even if, in the present study, a superhydrophobic surface is used and the transition occurs earlier with a subcooling of 5 K.

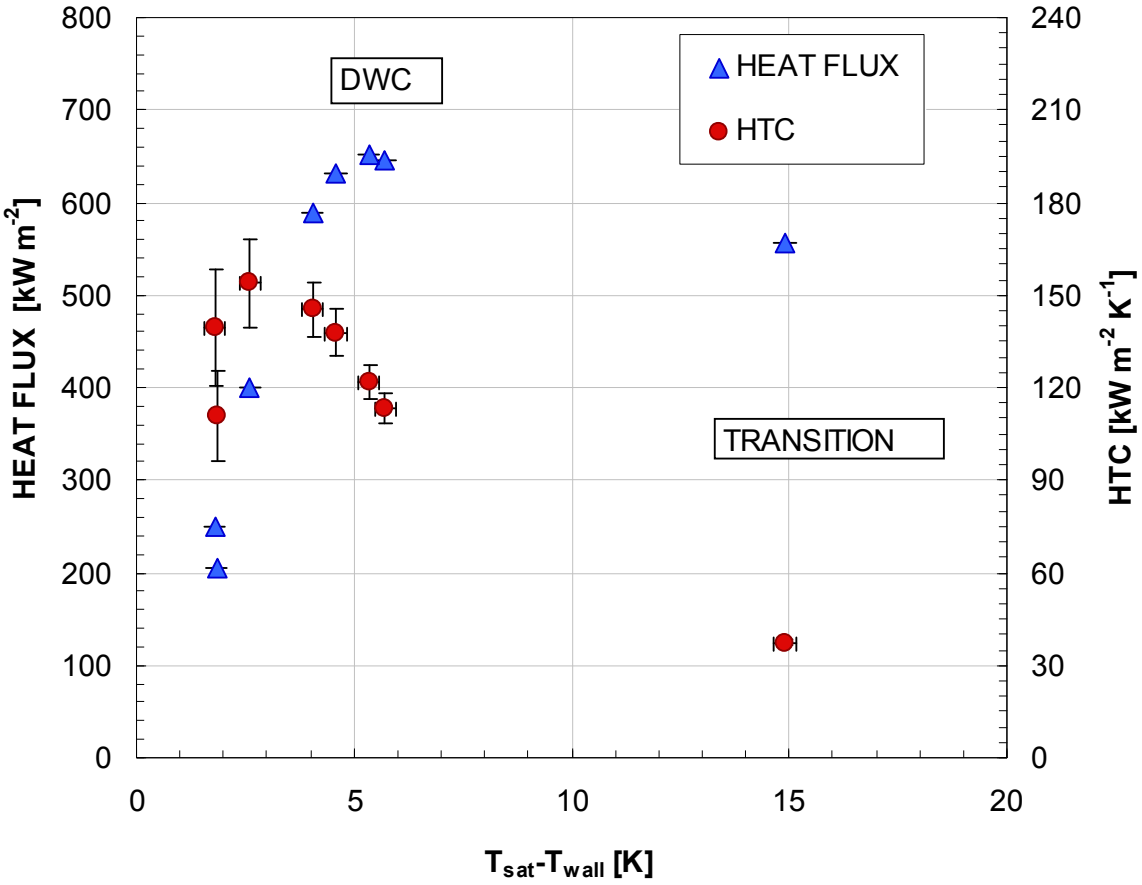

Figure 4.37. Heat flux and Heat transfer coefficient in function of the wall subcooling during steam condensation on the superhydrophobic copper sample

Tests were performed starting with cold water flowing in the cooling system. The first point which has been measured is the one reported in the transition region. The transient characteristics of this regime are confirmed by the high deviation standard of the wall thermocouples: ± 0.2 °C compared to a maximum value of ± 0.1 °C during normal dropwise mode. Then, by decreasing further the inlet temperature of the cooling mixture, drops substituted the condensate film and covered the entire surface. This behavior may be explained because decreasing the cooling water inlet temperature implies decreasing also the wall temperature; then the surface tension increases favoring the condensate drops formation. Transition from filmwise to dropwise mode explains the increase in of the heat flux by 16 % and the wall temperature decreasing by 10 K in Figure 4.37.

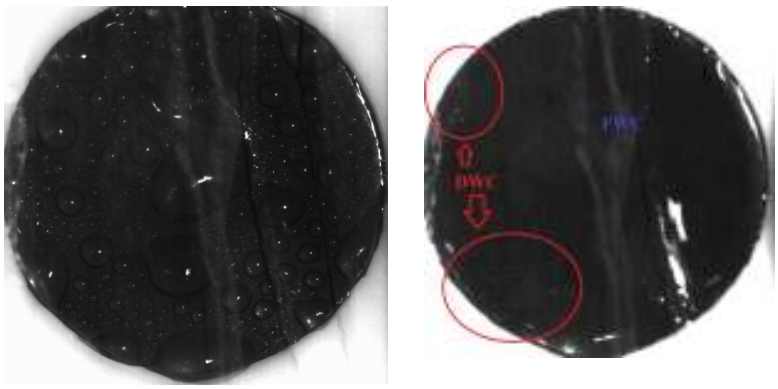

Figure 4.38. Image recorded during prevalent filmwise steam condensation in the superhydrophobic sample at 15 K *subcooling (right) and on dropwise condensation at 6* K *of subcooling (left).*

Video analysis has been performed in order to measure the maximum drops departing diameter in function of the wall subcooling. Measurements have been taken in two different areas of the surface and the mean values are reported in Figure 4.39; in the same graph is also reported the heat transfer coefficient. As it can be seen, the trend of the heat transfer coefficient can be explained by the variation in the departing diameter: in the second regime, while the heat flux increased, the heat transfer coefficient decreases because the drops are growing more before leaving the surface.

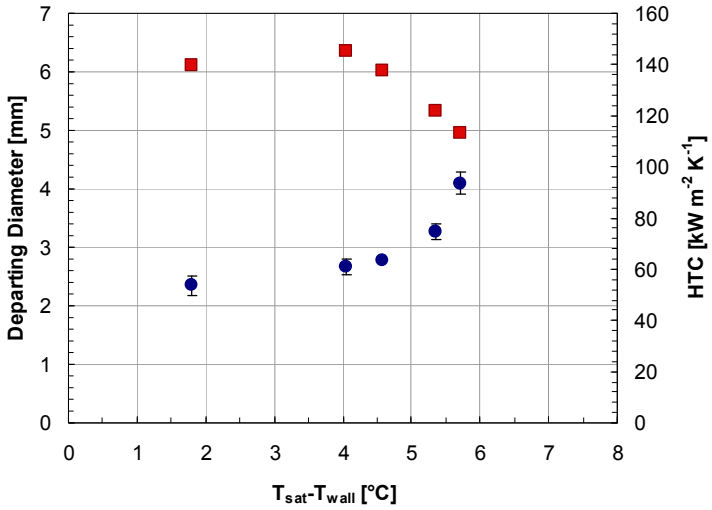

Figure 4.39. Maximum departing diameter as a function of the wall subcooling. The graph reports also the heat transfer coefficient

From the videos which have been recorded, it is possible to see that the mechanism for the drops to form, grow and leave the surface is similar to the one already observed during DWC on a polished copper sample previously reported in Figure 4.29: droplets grow by coalescing with near droplets until they reach the size to be swept away. Nevertheless, several differences could be observed comparing a droplet cycle on a copper polished sample (Figure 4.29) to the one observed on the superhydrophobic sample (Figure 4.40) at the same conditions.
First of all it can be seen that the surface is covered by the drops which are much bigger in size with respect to the polished sample surface. Second the time for a drop to grow and to be swept away is much more than what observed in the polished sample: it is close to 1s while on the polished

sample it is around 50 ms. These two differences penalize the superhydrophobic sample in terms of heat transfer performance with respect to a polished sample.

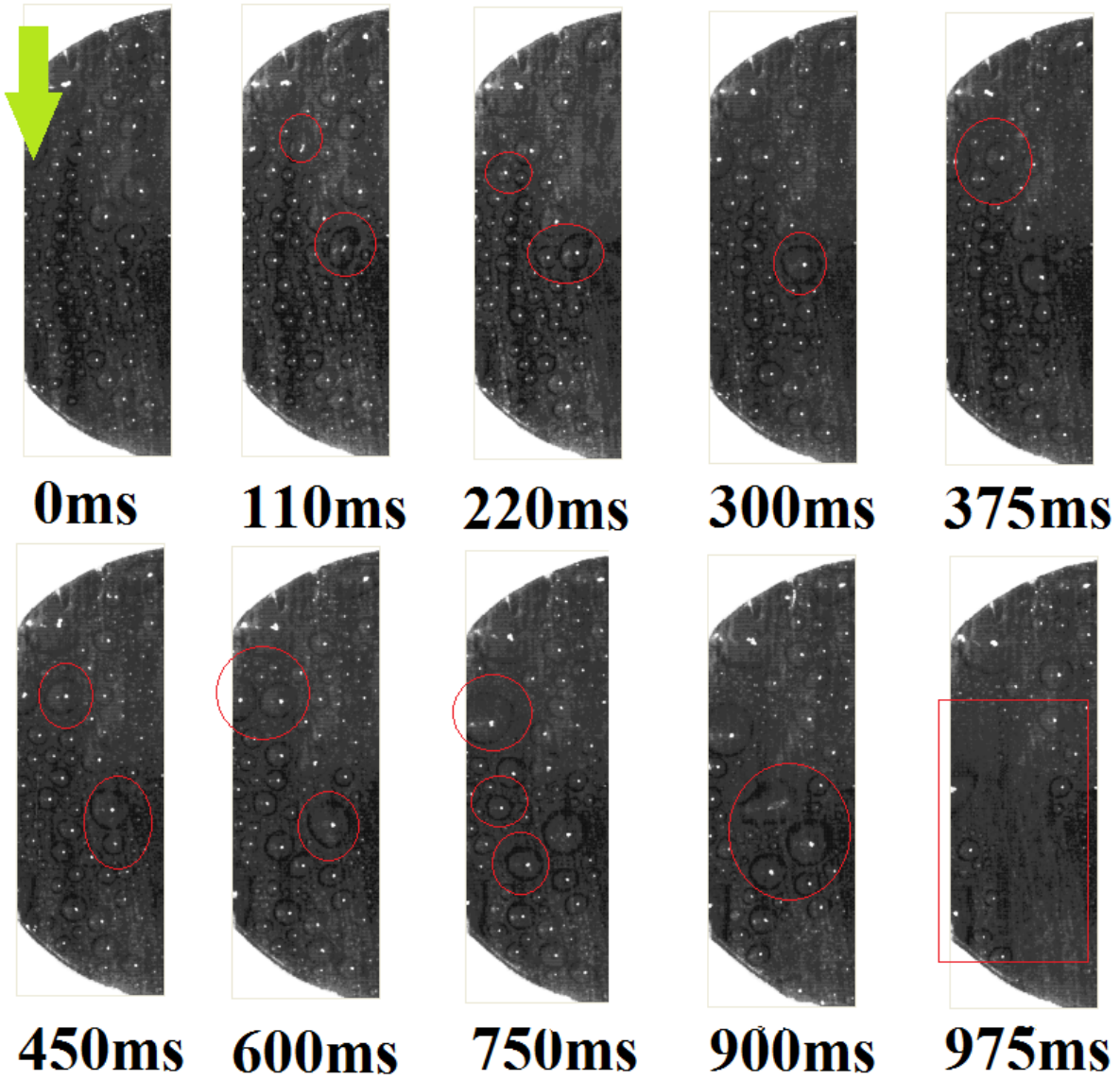

Figure 4.40. Droplet cycle on a superhydrophobic copper sample at G=10 kg m^{-2} s^{-1}ad 2 K of subcooling. The arrow indicates the vapour flow direction.

In Figure 4.41 the heat flux measured during condensation in the superhydrophobic sample are compared to the one measured during DWC, mist DWC/FWC and FWC on a copper in different days. In particular, the DWC was measured on a polished copper sample just inserted in the test section, while mist DWC/FWC was seen in the second day of test on the same sample. Data obtained during FWC on an oxidized copper sample after four day of tests are also reported. Conditions of vapour velocity at the inlet of the test section and saturation temperature are the same for all the tests. As it can be seen, the heat performances of the superhydrophobic sample are in between the ones of a polished sample in which DWC and mist DWC/FWC were observed. It should be pointed out that the performance of the superhydrophobic sample could be affected by its positioning inside the channel.

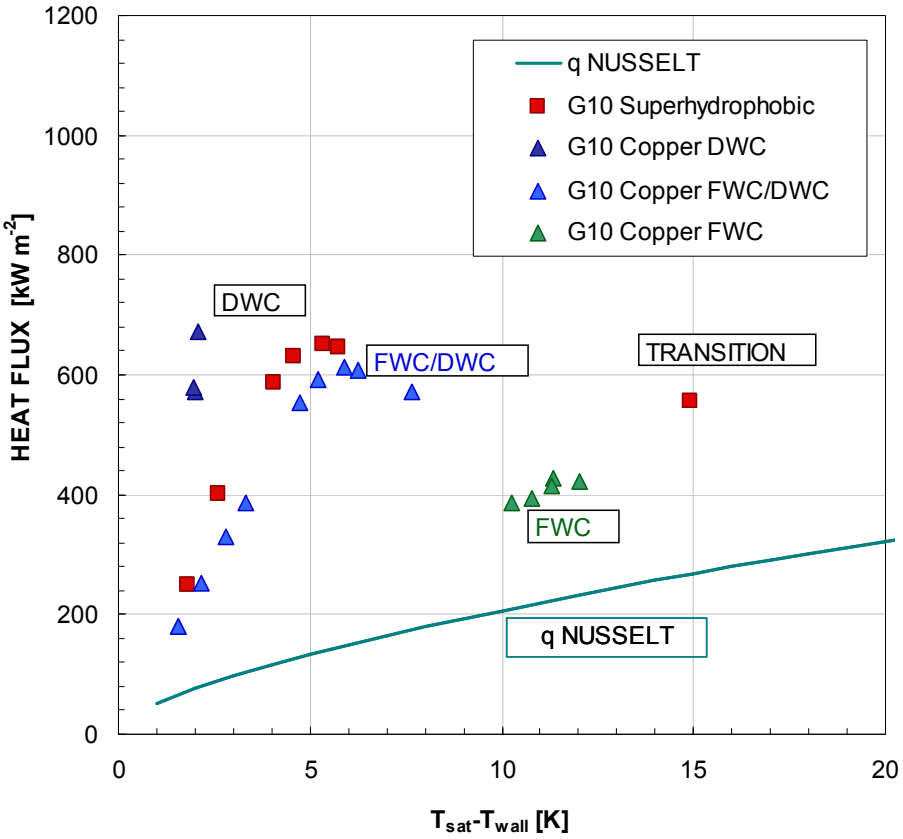

Figure 4.41. Heat flux comparison between the superhydrophobic sample and tests done on a polished copper sample in different day of tests.

Furthermore, in the superhydrophobic sample five days of test were performed before the data reported Figure 4.41, meaning that the effect of corrosion is less important than what reported in Paragraphs 4.9.3 for a simple copper sample. SEM images were taken after five days of tests and as it can be seen in Figure 4.42 the surface texturing results modified with the $CuOH_2$ nanowires that are not well defined in the shape like before starting the experiments.

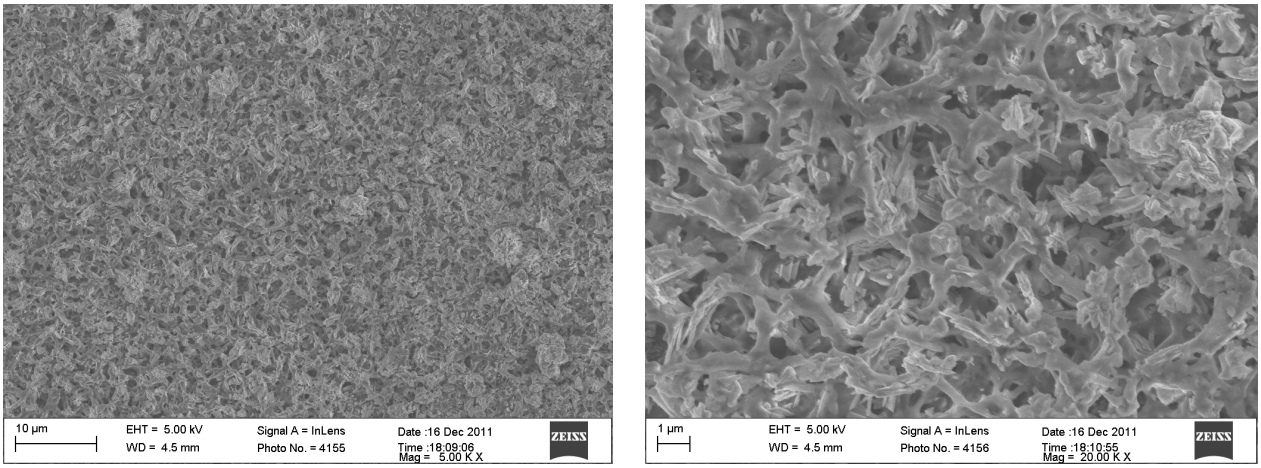

Figure 4.42. SEM images of the sample after five days of experiments.

Recently, Zhong *et al.* (2010) reported that a superhydrophobic surface with nanostructured did not improve the heat transfer performance so much as to be expected for the large apparent contact angle in the air. In particular they prepared self-assembled monolayer coatings of n-octadecyl mercaptan on mirror polished copper (SAM-2) and on a nanostructured surface (SAM-1) obtained thorough an oxidation process. For the SAM-1 the measured contact angle was 165 °, while it was 116° for SAM-2. Their measurements during DWC at atmospheric pressure are reported in Figure 4.43. In the present study the operative pressure is 1.43 bars which mean a lower surface tension by 3.5% with respect to the data of Zhong *et al.* (2010) that affects the promotion of the DWC condensation.

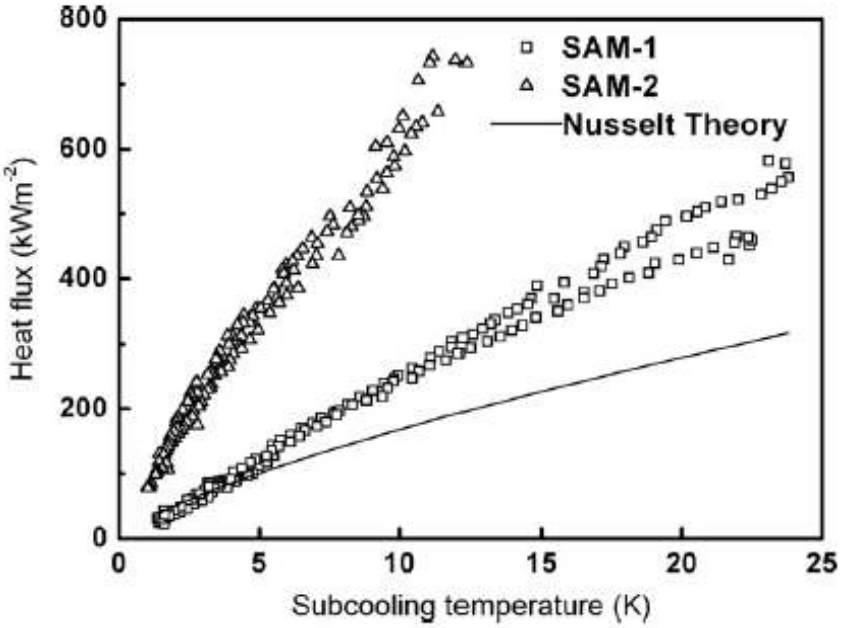

Figure 4.43. Results from Zhong et al. (2010) during dropwise condensation of steam at atmospheric pressure on a superhydrophobic copper surface (SAM-1) and on a hydrophobic surface (SAM-2).

As it can be seen the condensation heat transfer is enhanced by a factor 3 for the SAM-2 surface with respect to the SAM-1. The author explained the decrease in the heat transfer performance of the SAM-1 nanostructured surface by an increase of the droplet departure diameter and a lower departure frequency. This behavior is very similar to what has been observed in the present work comparing the DWC on a polished copper sample and on the superhydrophobic one. A possible explanation could be that during a condensation process, water condenses both between and on the top of the surface features favoring the Wenzel state instead of the Cassie one observed during contact angle measurements in air. That causes an increase in contact angle hysteresis and a decrease in macroscopic water drop mobility. Nevertheless, at the same ΔT, the heat transfer coefficient measured in the present work with a superhydrophobic sample is higher to the one measured by Zhong *et al.* (2010) with a very similar surface: this could be due to effect of the vapour velocity which helps in the droplets removal. This is also probably be the cause of the different trend in the heat transfer coefficient which is an increasing function of the wall subcooling but only for low ΔT. In fact, as it reaches a maximum value, it starts to decrease due to a transition in the mode of condensation. As earlier proposed by O'Bara *et al.* (1967) the vapor velocity across the condensing surface has a significant effect on the heat transfer coefficient. It seems like that the effect of the vapour shear is to increase the heat transfer at low ΔT, when the droplets are very

small. As the surface temperature decreases, drops become bigger, and the vapour velocity effect seems to induce an earlier transition from the dropwise to the filmwise mode with a consequent decreasing in the heat transfer performance. In the case of the superhydrophobic sample this transition is observed thanks to the big drops of condensate. On the previous study in Paragraph 4.9.3 probably this transition is not observed because droplets are small and very large subcoolings are necessary for the transition to occur.

CONCLUSIONS

In this Thesis film condensation, flow boiling and adiabatic two-phase flow in minichannels have been investigated. Also an experimental study on dropwise condensation on plane surfaces in a small diameter channel has been presented. Two were the main goals of this work: the investigation of environmentally friendly refrigerants and the enhancement of the condensation heat transfer.

Condensation tests of R1234yf and R134a inside a single circular and square minichannel

Heat transfer coefficients measured during two phase flow of R1234yf within a single circular 0.96 mm diameter and a square 1.18 mm side length minichannel have been presented. This experimental work has been carried out in a unique test apparatus which allows determining the local heat flux extracted from the condensing fluid from the temperature profile of the coolant. For this purpose, the temperatures of the coolant and of the wall are measured along the test section. Condensation tests have been done at 40 °C saturation temperature with mass fluxes ranging between 200 and 1000 kg m^{-2} s^{-1} in the circular section and between 100 and 800 kg m^{-2} s^{-1} in the square one. For the entire mass flux range, with the exception of the low velocity (G=100 kg m^{-2} s^{-1}) in the square minichannel, the heat transfer coefficient does not show dependence on the saturation to wall temperature difference, while it increases with vapour quality and mass velocity. Heat transfer coefficients in the circular minichannel have shown a good agreement with the model by Cavallini *et al*. (2006), which was developed for condensation inside conventional tubes. A good prediction capability of the heat transfer coefficients measured in the square minichannel (for mass fluxes higher than 200 kg m^{-2} s^{-1}) has been found in the model of Cavallini *et al.* (2005), which was developed for condensation heat transfer coefficient prediction during condensation of refrigerants inside minichannels. Experimental results have been compared to the ones previously measured in the same set up (Matkovic *et al.* (2009) and Del Col *et al.* (2011)) with R134a: at the same conditions, the heat transfer coefficients measured with R1234yf are lower by 15-30%. This may be explained by the fact that, at 40 °C saturation temperature, the liquid thermal conductivity of R1234yf is lower by 21% as compared to the one of R134a.

Vaporization tests of R1234yf and R134a inside a single circular and square minichannel

A comparison between the heat transfer coefficients measured with R1234yf and R134a during convective boiling in a 0.96 mm diameter circular minichannel has also been reported, showing no significant differences between the flow boiling heat transfer performances of R1234yf and R134a. During flow boiling tests, the heat is provided to the boiling fluid by using hot water as a secondary fluid. Therefore the heat flux is not imposed but instead it is the result of the inlet temperatures of the two fluids and the thermal resistances on the two sides. Flow boiling tests have been carried out at 31°C saturation temperature and mass fluxes ranging between 200 and 600 kg m^{-2} s^{-1}. The heat transfer coefficient shows to be highly dependent on the heat flux while the mass velocity has been found to have no effect. With regard to vapour quality, the heat transfer coefficient decreases when vapour quality increases, at least up to 0.4 vapour quality where this effect has been analysed. The same trend has been found during R1234yf flow boiling in the square minichannel. Thanks to the high number of thermocouples installed in the wall, it has been easier to determinate the onset of dryout where the standard deviation of the wall thermocouples starts to fluctuate, as described in Del Col *et al.* (2008) and Cavallini *et al.* (2007). Tests have been performed at 31°C saturation temperature and mass fluxes ranging between 200 and 500 kg m^{-2} s^{-1}.

Single phase and two phase pressure drop during adiabatic flow inside minichannels

An ad-hoc section has been used for the validation of a technique for determining the hydraulic diameter of ducts from pressure drop measurement in laminar flow. This method has been applied for the determination of the geometrical parameters of the square minichannel used for two-phase heat transfer measurements. Furthermore, two new circular minichannels, with 0.96 and 2 mm inner diameter, and a new presection have been designed and realized specifically for single phase and two phase pressure drop measurements. Tests performed during liquid and vapour single phase flow of R134a have been reported. A good agreement between the Hagen-Poiseulle law and the Blasius models in the laminar and turbulent regimes has been found, confirming the validity of the classical theory in the miniscale.
Since the saturation temperature drop directly affects the heat transfer rate, the pressure drop during adiabatic two-phase flow of R1234yf in the circular and square minichannel has been measured and compared to R134a. From this point of view R1234yf performs better than R134a: pressure drop is lower by 10-12% and this may be explained by the reduced pressure of R1234yf, which is greater by 20% than that of R134a at 40 °C saturation temperature. A good capacity of prediction has been found also in some two phase pressure drop models like the Cavallini *et al.* (2009) and Friedel (1979).

Dropwise condensation on nanoengineered copper surfaces

In this Thesis, a study of the dropwise condensation on nanoengineered copper surfaces has also been presented. A wet-chemical fabrication process has been used to modify the wettability of a copper surface which allows preparing a superhydrophobic copper sample in less than two hours, at ambient conditions, and without requiring any special technique. A new experimental apparatus and a new test section have been designed for the measurement of the heat transfer coefficient during steam condensation and the visualization of the droplets movements. The small hydraulic diameter of the test section (d_h=3.6 mm) allows investigating the effect of the vapour velocity. Heat transfer performances of a polished copper sample and of the superhydrophobic sample have been investigated during steam condensation at 110 °C saturation temperature. Experimental data have shown that the superhydrophobic sample promotes the DWC but does not improve the heat transfer performance as expected from the higher contact angle (165°) with respect to a polished copper sample (80°), but promote the DWC for longer time while the polished sample turns to the filmwise mode after few days. The effect of the vapour velocity during DWC has been found to be negligible in terms of heat transfer enhancements at very low subcooling degree, even if increasing the shear rate the departing droplets diameter has been observed to decrease. When the wall temperature decreases, the velocity effect has been found to enhance the heat transfer coefficient and to further reduce the drops departing diameter. Nevertheless, it has been observed that during DWC on the superhydrophobic sample, probably due to the high drops diameter, vapour velocity promotes an early transition from the DWC to the FWC. Surfaces with a combination of hydrophobic and hydrophilic areas could be the further development for improving the heat transfer performance during steam condensation.

REFERENCES

Akers, W.W., Deans, H.A., Crosser, O.K., 1959, Condensing heat transfer within horizontal tubes, Chem. Eng.Prog. Symp. Series, vol. 55, pp. 171-176.

Baehr, H., D., Stephan, K., 2004, Waerme- und Stoffuebertragung, Springer- Verlag, Berlin.

Berndt, V., Zunft, S., Muller, H., 2008, Theoretical and experimental study on dropwise condensation in plate heat exchangers. Proc. 5th. European Thermal-Sciences Conference, The Nederlands.

Bertsch S. S., Groll E. A., Garimella S. V., 2009, A composite heat transfer correlation for saturated flow boiling in small channels, Int. J. of Heat and Mass Transfer, vol. 52, pp., 2110-2118.

Bhatti, M., S., Shah ,R., K., 1987 Turbulent and transition flow convective heat transfer in ducts, In: Kakac S., Shah R. K., and Aung W. (eds.), Handbook of Single-Phase Convective Heat Transfer, Chapter 4, Wiley, New York.

Bico, J., Thiele, U., Quéré, D., 2002, Wetting of textured surfaces, Colloids Surfaces A 206, pp.41–46.

Bonner, R.W., 2010, Dropwise condensation life testing of self assembled monolayers, Proc. 14th Int. Heat Transfer Conf., Washington, DC, USA.

Boreyko, J., B., Chen, C., H., 2009, Self-propelled dropwise condensate on superhydrophobic surfaces, Physical Review Letters, 103, 184501.

Brown, S.F., Zilio, C., Cavallini, A., 2009. Estimations of the thermodynamic and transport properties of R-1234yf using a cubic equation of state and group contribution. In: Proceedings of the 3rd IIR Conference on Thermophysical Properties and Transport Processes of Refrigerants, Boulder, CO, USA.

Bucci, A., Celata, G. P., Cumo, M., Serra, E., and Zummo, G., 2004, Water single-phase fluid flow and heat transfer in capillary tubes, Paper No. ICMM2004-2406, Second International Conference on Microchannels and Minichannels, Rochester, NY USA, June 17–19, 221–228, International Conference on Microchannels and Minichannels. Paper 1037, ASME, 319–326.

Cavallini A., Censi G., Del Col D., Doretti L., Longo G.A., Rossetto L., Zilio C., 2003, Condensation inside and outside smooth and enhanced tubes- a review of recent research, Int. J. of Refrigeration, vol 26, pp. 373-392.

Cavallini A., Del Col D., Doretti L., Matkovic M., Rossetto L., Zilio C., 2005, A model for condensation inside minichannels, Proc. of HT05 National Heat Transfer Conf., ASME, San Francisco, paper HT2005-72528.

Cavallini, A., Censi, G., Del Col, D., Doretti L., Matkovic M., Rossetto L. and Zilio C., 2006, Condensation in Horizontal Smooth Tubes, A New Heat Transfer Model for Heat Exchanger Design. Heat Transfer Engineering 27(8), 31-38.

Cavallini, A., Bortolin, S., Del Col, D., Matkovic, M., Rossetto, L., 2007, Experiments on Dry-Out During Flow Boiling in a Round Minichannel. Microgravity Science and Technology, vol. XIX-3/4, Z-Tec Publishing, Bremen.

Cavallini, A., Del Col, D., Matkovic, M., Rossetto, L., 2009. Frictional pressured drop during vapour-liquid flow in minichannels: Modelling and experimental evaluation. Int. J. Heat and Fluid Flow, 30(1), 131-139.

Celata, G. P., Cumo, M., Guglielmi, M., and Zummo, G., 2002, Experimental investigation of hydraulic and single phase heat transfer in 0.130mm capillary tube, Microscale Thermophys. Eng., **6**, 85–97.

Chen, J., C., 1966. A correlation for boiling heat transfer to saturated fluids in convective flow. Ind. Eng. Chem. Proc. DD. 5 (3), 322-329.

Chen, I., Y., Yang, K., S., Chang, Y., J., Wang, C., C., 2001, Two-phase pressure drop of air-water and R-410A in small horizontal tubes, Int. J. of Multiphase Flow, vol. 27, pp. 1293-1299.

Chen, J., C., 2001, Surface Contact-its significance for multiphase heat transfer: diverse examples, J. Heat Transfer, vol. 125 (4), Max Jacob memorial award lecture.

Chen, C., H., Cai, Q., J., Tsai, C., Chen, L., 2007, Dropwise condensation on superhydrophobic surfaces with two-tier roughness, Appl. Phys. Lett. 90, 173108.

Chen, X., Kong, L., Dong, D., Yang, G., Yu, L., Chen, J., Zhang, P., 2009, Synthesis and characterization of superhydrophobic functionalized Cu(O))2 nanotube arrays on copper foil, Appl. Surf. Sci, 255, pp. 4015-4019.

Churchill S. W., 1977, Friction-factor equation spans all fluid-flow regimes, Chem. Eng., vol. 45, pp. 91-92.

Consolini, L., Thome, J., R., 2009, Micro-channel flow boiling heat transfer of R-134a, R-236fa, and R-245fa, Microfluid Nanofluid, vol. 6, pp. 731-746.

Cornwell K., Kew P.A., 1992, Boiling in small parallel channels. Proceedings of CEC Conference on Energy Efficiency in Process Technology, Athens, October 1992, Paper 22, Elsevier Applied Sciences, 624-638.

Dang C., Saitoh S., Nakamura Y., Li M., Hihara E., 2010, Boiling heat transfer of HFO-1234yf flowing in smooth small-diameter horizontal tube. International Symposium on 200
Next-generation Air Conditioning and Refrigeration Technology, 17-19 February 2010, Tokyo, Japan.

Del Col, D., Cavallini, A., Bortolin, S., Matkovic, M., Rossetto, L., 2008, Dryout during flow boiling in a single circular minichannel: experimentation and modelling. In: Proceedings of ASME Heat Transfer Conference, Jacksonville, FL, USA.

Del Col, D., Bortolin, S., Cavallini, A., Matkovic, M., 2011, Effect of cross sectional shape during condensation in a single square minichannel, Int. J. Heat and Masss Transfer, vol. 54 (17–18), pp 3909–3920.

Depew, C., A., Reisbig, R., L., 1964, Vapor condensation on a horizontal tube using teflon to promote dropwise condensation, I&EC Process Des. Develop. 3 (4), pp. 365–369.

Dietz, C., Rykaczewski, K., Fedorov, A., G., Joshi, Y., 2010, Visualization of droplet departure on a superhydrophobic surface and implications to the heat transfer enhancement during dropwise condensation, Appl. Phys. Lett. 97, 033104.

Directive 2006/40/EC of The European Parliament and of the Council of 17 May 2006 relating to emissions from air-conditioning systems in motor vehicles and amending Council Directive 70/156/EC, Official Journal of the European Union.

Dorrer, C., Ruhe, J., 2007, Condensation and wetting transition on microstuctured ultrahydrophobic surfaces, Langmuir, 23, pp. 3820-3824.

Eucken, A., 1937, Naturwissenschaften, 25, p. 209.

Fedele, L., Bobbo, S., Groppo, F., Brown, J.S., Zilio, C., 2011, Saturated Pressure Measurements of 2,3,3,3-Tetrafluoroprop-1-ene (R1234yf) for Reduced Temperatures Ranging from 0.68 to 0.93. J. of Chemical & Engineering Data 56, 2608-2612.

Friedel, L., 1979, Improved Friction Pressure Drop Correlations for Horizontal and Vertical Two Phase Pipe Flow. European Two Phase Flow Group Meeting, Ispra, Italy, paper E2.

Garimella, S, Agarwal, A., Killon, J., D., 2004, Condensation pressure drops in circular minichannels, 2nd Int. Conf. on Microchannels and Minichannels, Rochester, pp. 649-656.

Gao, L, McCarthy, T., J., 2007, How Wenzel and Cassie were wrong. Langmuir 23:3762–3765.

Gnielinski, V., 1993, Heat transfer in pipe flow. VDI-Heat Atlas, VDI-Verlag GmbH, Düsseldorf, Gb 1-Gb 8.

Gnielinski, V., 2002, Wärmeübertragung bei der Strömung durch Rohre. VDI-Wärmeatlas, 9. Auflage, Springer-Verlag Berlin Heidelberg, Ga 1-Ga 9.

Graham, C., Griffith, P., 1973, Drop Size Distribution and Heat Transfer in Dropwise Condensation, Int. J. Heat Mass Transf., 16, pp. 337–346.

Harirchian, T., Garimella, S., V., 2008, Microchannel size effect on local flow boiling heat transfer to a dielectric fluid, Int. Journal of Heat and Mass transfer, vol. 51, pp. 3724- 3735.

Harirchian, T., Garimella, S., V., 2009, Effects of channel dimension, heat flux, and mass flux on flow boiling regimes in microchannels. International Journal of Multiphase Flow 35, 349-362.

Harirchian, T., Garimella, S., V., 2010, A comprehensive flow regime map for microchannel flow boiling with quantitative transition criteria. International Journal of Heat and Mass Transfer 53, 2694-2702.

Huang, Z., B., Zhu, Y., Zhang, J., H., Yin, G., F., 2007, Stable biomemetic superhydrophobicity and magnetization film with Cu-Ferrite nanorods, J. Phys. Chem., 111, pp. 6821–6825.

Idelchik, I., E., 1996, Handbook of hydroulic resistance, 3rd edition, Begell House Inc., ISBN: 1-56700-074-6.

ISO, 1995. Guide to the expression of uncertainty in measurement.

Johnson, R., E., Dettre, R., H., 1964, Contact angle hysteresis, I study of an idealized rough surface, Advances in Chemistry series, 1964, 43, 112-35

Judy, J., Maynes, D., Webb, B., W., 2002, Characterization of frictional pressure drop for liquid flows through microchannels, Int. J. Heat Mass Trans, **45**, 3477–3489.

Kandlikar, S., G., Grande, W., J., 2003, Evolution of microchannel flow passages, thermodynamic performance and fabrication technology. Heat Transfer Engineering 24, 3-17.

Kandlikar, S., G., 2004, Heat Transfer Mechanisms during flow boiling in microchannels, J. of Heat Transfer, vol. 126, pp. 8-16.

Kandlikar, S., G., Garimella, S., Li, D., Colin, S., King, M., R., 2006, Heat transfer and fluid flow in minichannels and mocrochannels, Elsevier Ltd., ISBN: 0-0804-4527-6.

Kasza, K.E., Didascalou, T., Wambsganss, M.,W., 1997, Microscale flow visualization of nucleate boiling in small channels: mechanisms influencing heat transfer. Proceedings of International Conference on Compact Heat Exchanges for the Process Industries, 343-352.

Kew, P., A., Cornwell, K., 1997, Correlations for the prediction of boiling heat transfer in small-diameter channels. Applied Thermal Engineering, vol. 17, 705-715.

Kim, S., Kim, K., J., 2011, Dropwise Condensation Modeling Suitable for Superhydrophobic Surfaces, ASME: Journal of Heat Transfer, Vol. 133, pp. 081502.

Koch, G., Zhang, D. C., Leipertz, A., 1997, Condensation of steam on the surface of hard coated copper discs, W&me- und Stofftibertragung ,32, 1499156.

Koyama, S., Kuwara, K., Nakashita, K., 2003, Condensation of refrigerant in a multi-port channel, 1st Int. Conf. on Microchannels and Minichannels, Rochester, pp. 193-205.

Kyoto Protocol, 1997, Kyoto Protocol to the United Nations Framework Convention on Climate Change. United Nations (UN), New York.

Lan, Z., Ma, X., Wang, S.,Wang, M., Li, X., 2010, Effects of surface free energy and nanostructures on dropwise condensation, Chemical Eng. Journal, 156, pp 546-552.

Lazarek, G., M., Black, S., H., 1982, Evaporative heat transfer, pressure drop and critical heat flux in a small diameter vertical tube with R-113. International Journal of Heat and Mass Transfer 25, 945-960.

Lee, J., Mudawar, I., 2005, Two phase flow in high-heat-flux micro-channel heat sink for refrigeration cooling applications: Part I-pressure drop characteristics, Part II-heat transfer characteristics, Int. Journal of Heat and Mass transfer, vol. 48, pp. 928-955.

Li, Z. X., Du, D. X., and Guo, Z. Y., 2000, Experimental study on flow characteristics of liquid in circular microtubes, Proceeding of the International Conference on Heat Transfer and Transport Phenomena in Microscale, Banff, Canada, October 15–20, 162–167.

Lockhart, R., W., Martinelli, R., C., 1949, Proposed correlation of data for isothermal two-phase, two-component flow in pipes, Chem. Eng. Prog., 39-45.

Ma, X., Wang, S., Lan, Z., Wang, A., Peng, B., 2010, Dropwise condensation heat transfer on superhydrophobic surface in the presence of non-condensable gas, Proc. 14th Int. Heat Transfer Conf., Washington, DC, USA.

Matkovic M., 2006, Experimental condensation inside minichannles, PhD tesi, University of Padova, Italy.

Matkovic, M., Cavallini, A., Del Col, D., Rossetto, L., 2009, Experimental study on condensation heat transfer inside a single circular minichannel. Int. J. Heat and Mass Transfer. 52(9-10), 2311-2323.

Mishima K., Hibiki T., 1996, Some characteristics of air-water two-phase flow in small diameter vertical tubes, Int. J. of Multiphase Flow, vol. 22, pp. 703-712.

Moser, K., W., Webb, R., L., Na, B., 1998, A new equivalent Reynolds number model for condensation in smooth tubes, J. of Heat Transfer, vol. 120, pp. 410-417.

Müller-Steinhagen, H., Keck, K., 1986, A simple friction pressure drop correlation for two-phase flow in pipes, Chemical Engineering Progress, vol. 20, pp. 297-308.

Narhe, R. D., Beyesen, D. A., 2004, Nucleation and growth on a superhydrophobic grooved surface, Phys Rev Lett, 93, 76103

Neinhuis, C., Barthlott, W., 1997, Characterization and distribution of water-repellent, self cleaning plant surfaces, Ann. Bot. 79, pp. 667-77

Neumann, A., W., Abdelmessih, A., H., Hameed, A., 1978, The role of contact angles and contact angle hysteresis in dropwise condensation heat transfer, Int. J. Heat Mass Transfer. 21 (7), pp. 947–953.

Nielsen, O.J., Javadi, M.S., Sulback Andersen, M.P., Hurley, M.D., Wallington, T.J., Singh, R., 2007. Atmospheric chemistry of $CF_3CF=CH_2$: kinetics and mechanisms of gas-phase reactions with Cl atoms, OH radicals, and O_3. Chem. Phys. Lett. 439, 18-22.

Niklas, M. and Favre-Marinet, M., 2003, Pressure losses in a network of triangular minichannels, ASME, Paper No. ICMM2003-1039, First International Conference on Microchannels and Minichannels, April 24–25, 335–350.

NIST, National Institute of Standard and Technology, Refprop Version 9.0 (2010), Boulder, Colorado

Nukiyama, S., 1966, The maximum and minimum values of the heat q transmitted from a metal to boiling water under atmospheric pressure, Int. J. Heat and Mass Transfer, 9, pp. 1419-1433.

Nusselt, W., 1916, Die Oberflaechenkondensation des Wasserdampfes, Zeitschrift VDI 60 (27) 541–546, and 569–575.

O'Bara, J., T., Killian, E., S., Roblee, L., H., S., 1967, Dropwise condensation of steam at atmospheric and above atmospheric pressures, Chemical Engineering Science, 1967, Vol. 22, pp. 1305-1314.

Paliwoda A., 1992. Generalized method of pressure drop calculation across pipe components containing two-phase flow of refrigerants. International Journal of Refrigeration 15, 119-125.

Park, K.J., Jung, D., 2010. Nucleate boiling heat transfer coefficients of R1234yf on plain and low fin surfaces. Int. J. Refrigeration, 33(3), 553-557, doi: 10.1016/j.ijrefrig.2009.12.020.

Park, K.J, Kang, D.G, Jung, D., 2011. Condensation heat transfer coefficients of R1234yf on plain, low fin, and Turbo-C tubes. Int. J. Refrigeration 34, 317-321.
Patankar, N., A., 2010, Supernucleating surfaces for nucleate boiling and dropwise condensation heat transfer. Soft Matter, 6, pp. 1613-1620.

Ponter, A., B., 1992, Contact angles on metal and polymer surfaces in mass transfer environments, Adv.Colloid Interface Sci., 39, pp. 383–395.

Press, W., H., Flannery, B., P., Teukolsky, S., A., Vetterling, W., T., 2007. Numerical recipes. Cambridge University Press, New York, pp. 773-793.

Quere, D., Lafuma, A., Bico, J., 2003, Slippy and sticky microtextured structures, Nanotechnology, 14, pp. 1109-1112

Quéré, D., 2005, Non sticking drops, Rep. Prog. Phys., 68, pp. 2495-2532.

Quoilin, S., Declaye, S., Tchanche, B.F., Lemort, V., 2011. Thermo-economic optimization of waste heat recovery Organic Rankine Cycles. Applied Thermal Engineering 31, 2885-2893.

Rausch, M. H., Fröba, A. P., Leipertz, A., 2008, Dropwise Condensation Heat Transfer on Ion Implanted Aluminium Surfaces, Int. J. Heat Mass Transf., vol. 8, pp. 1061–1070.

Rausch, M. H., Leipertz, A., and Fröba, A. P., 2010, Mechanism of dropwise condensation on ion implanted metallic surfaces, Proc. 14th Int. Heat Transfer Conf., Washington, DC, USA.

Rawlings, J.O., Pantula, S.G., Dickey, D.A., 1998. Applied regression analysis: a research tool, second ed., Springler.

Regulation (EC) No 842/2006 of The European Parliament and of the Council of 17 May 2006 on certain flourinated greenhouse gases, Official Journal of the European Union.

Revellin, R., Thome, J., R., 2007, Adiabatic two-phase frictional pressure drops in microchannels, Experimental Thermal and Fluid Science, Vol.31 (7), pp. 673–685.

Richter, M., McLinden, M.O., Lemmon, W., 2011. Thermodynamic properties of 2,3,3,3-Tetrefluoroprop-1-ene (R1234yf): vapour pressure and p-ρ-T measurements and an Equation of State. J. of Chemical and Engineering Data 56, 3254-3264.

Rose, J. W., Glicksman, L. R., 1973, Dropwise Condensation—The Distribution of Drop Sizes, Int. J. Heat Mass Transf., 16, pp. 411–425.

Rose, J., W., 1976, Further aspects of dropwise condensation theory, Int. J. Heat Mass Transfer 19, 1363.

Rose, J. W., 1981, Dropwise Condensation Theory, Int. J. Heat Mass Transf., 24, pp-191-194

Rose, J., W., 1998, Condensation Heat Transfer Fundamentals, Trans IChemE, 76, pp. 143-152

Rose, J., W., Laminar film condensation of pure vapors, in: Kandlikar, S., G., Shoji, M., Dhir ,V., K., (Eds.), 1999, Handbook of Phase Change: Boiling and Condensation, Taylor & Francis, Philadelphia, pp. 523–536.

Rose, J.W., 2002, Dropwise condensation theory and experiment: a review, Proc. Inst. Eng. Part A: J. Power Energy. 216, pp 115–128.

Rouhani, Z., Axelsson, E., 1970. Calculation of void volume fraction in the subcooled and quality boiling regions. Int. J. Heat Mass Transfer, 13, 383–393.

SAE CRP1234. 2009, Industry evaluation of low global warning potential refrigerant HFO-1234yf. Presentation retrieved online at: http://www.sae.org/standardsdev/tsb/cooperative/crp1234-3.pdf, November 10, 2009.

Schmidt, E., Schurig, W. and Sellschopp, W., 1930, Versucheueber die Kondensation in Film- und Tropfenform. Tech. Mech. Thermodynamik, l, pp 53–63.

Schmitt, D., J., Kandlikar, S., G., 2005, Effects of repeating microstructures on pressure drop in rectangular minichannels, ASME, Third International Conference on Microchannels and Minichannels, Toronto, Canada, Paper No. ICMM2005-75111.

Shah, R., K. London, A., L., 1978, Laminar flow forced convection in ducts, Academic Press, New York.

Shiferaw, D., Karayiannis, T., G., Kenning, D., B., R., 2009, Flow boiling in a 1.1 mm tube with R134a: Experimental results and comparison with model, Int. J. of Thermal Sciences, vol. 48, pp. 331–341.

Steinke, M., E., Kandlikar, S., G., 2005, Single-phase liquid friction factors in microchannels, Paper No. ICMM2005-75112, ASME, Third International Conference on Microchannels and Minichannels, Toronto, Canada, June 13–15.

Tables of Physical & Chemical Constants, 2008, 2.1.2 Barometry. Kaye & Laby Online. Version 1.1, www.kayelaby.npl.co.uk

Takeyama, T., Shimizu, S., 1974, On the transition of dropwise-filmwise condensation, Proc. Int. Heat Transfer Conf., 5th 3, 274.

Tanaka, H., 1975a, Measurements of drop-size distribution during dropwise condensation, J. Heat Transfer 97, 341.

Tanaka, H., 1975b, A Theoretical Study of Dropwise Condensation, ASME J. Heat Transfer, 97(1), pp. 72–78.

Tanaka, K., Higashi, Y., 2009. Thermodynamic properties of HFO-1234yf (2,3,3,3-Tetrafluoropropene). In: Proceedings of the 3rd IIR Conference on Thermophysical Properties and Transport Processes of Refrigerants, Boulder, CO, USA.

Tanasawa, I., Ochiai, J., Utak, Y., Enya, S., 1976, Experimental study on dropwise condensation (Effect of departing drop size on heat-transfer coefficient), Trans. JSME 42, 2846.

Tanasawa, I., Utaka, Y., 1983, Measurements of condensation curves for dropwise condensation of steam at atmospheric pressure. J. Heat Transfer 105, 633.

Tanner, D.,W., Potter, C., J., Pope, D., West, D., 1965, Heat transfer in dropwise condensation—Part I The effects of heat flux, steam velocity and non-condensable gas concentration, Int. Journal of Heat and Mass Transfer, vol 8 (3), pp. 419–420.

Thome J.R., Dupont V., Jacobi A.M., 2004. Heat transfer model for evaporation in microchannels. Part I: presentation of the model. International Journal of Heat and Mass Transfer 47, 3375-3385.

Thome J. R., 2004b, Boiling in microchannels: a review of experiment and theory, Int. J. ofHeat and Fluid Flow, vol. 25, pp. 128-139.

Thome J. R., 2006, State-of-the-art overview of boiling and two-phase flows inmicrochannels, Heat Transfer Engineering, vol. 27(9), pp. 4-19.

Thome J.R., Consolini L., 2010. Mechanisms of boiling in micro-channels: critical assessment. Heat Transfer Engineering 31, 288-297.

Tran, T., N., Wambsganss, M., W., France, D., M., 1996. Small circular- and rectangular-channel boiling with two refrigerants. International Journal of Multiphase Flow 22, 485-498.

Tuckerman, D. B. and Pease, R. F. W., 1981, High performance heat sink for VLSI, IEEE Electron Dev. Lett., EDL-2, (5), 126–129.

Umur, A., and Griffth, P., 1965, Mechanism of Dropwise Condensation, ASME J. Heat Transfer, 87, pp. 275-282.

Varanasi, K., K., Hsu, M., Bathe, N., Yang, W., S., Deng, T., 2009, Spatial control in the heterogeneous nucleation of water, Appl. Phys. Lett., 95, 094101, 2009.

Wang W.W., Radcliff T.D., Christensen R.N., 2002, A condensation heat transfer correlation for millimetre-scale tubing with flow regime transition, Experimental Thermal and Fluid Science, vol. 26, pp. 473-485.

Wambsganss M.W., France D.M., Jendrzejczyk J.A., Tran T. N., 1993. Boiling heat transfer in a small diameter tube. ASME Journal of Heat Transfer 115, 963-972.

Wier, K., A., McCarthy, T., J., 2006, Condensation on ultrahydrophobic surfaces and its effect on droplet mobility: ultrahydrophobic surfaces are not always water repellant, Langmuir, 22 (6), pp. 2433-2436

Xi, W., J., Qiao, Z., M., Zhu, C., L., Jia, A., Li, M., 2009, The preparation of lotus-like super-hydrophobic copper surfaces by electroplating, Appl. Surf. Sci., 255, 4836–4839.

Xi, J., Feng, L., Jiang, L., 2008, A general approach for fabrication of superhydrophobic and superamphiphobic surfaces, Appl. Phys. Lett., 92, 053102.

Yan Y.Y., Lin T.F., 1999, Condensation heat transfer and pressure drop of refrigerant R134a in a small pipe, Int. J. Heat Mass Transfer, vol. 42, pp. 697-708.

Zhang M., Webb R.L., 2001, Correlation of two-phase friction for refrigerants in small-diameter tubes, Experimental Thermal and Fluid Science, vol. 25, pp. 131-139.

Zhang, W., Hibiki, T., Mishima, K., 2004. Correlation for flow boiling heat transfer in mini-channels. *International Journal of Heat and Mass Transfer 47*, 5749-5763.

Zhang, Y., F., Yu, X., Q., Zhou, Q., H., Chen, F., Li, K., N., 2010, Fabrication of superhydrophobic copper surface with ultra-low water roll angle, Appl.Surf. Sci., 256, 1883–1887.

Zhao, QI., Zhang D., Lin J., 1991, Surface materials with dropwise condensation made by ion implantation technology, Int. J. Heat Mass Transfer, vol 34, iussue 11, pp. 2833-2835.

Zilio, C., Brown, J.S., Schiochet, G., Cavallini, A., 2011. The refrigerant R1234yf in air conditioning systems. Energy, doi:10.1016/j.energy.2011.08.002

PUBLICATIONS

D. Del Col, D. Torresin, A. Cavallini 2010, Heat transfer coefficient and pressure drop during condensation of the low GWP refrigerant R-1234yf. Proc. Workshop on refrigerant charge reduction in refrigerating systems, 2rd /IIR, Stockholm.

D. Del Col, D. Torresin, A. Cavallini 2010, Heat transfer and pressure drop during condensation of the low GWP refrigerant R-1234yf. Int. J. Refrigeration, 33-7, pp. 1307-1318.

D. Del Col, S. Bortolin, D. Torresin, A. Cavallini 2011, Flow boiling of R-1234yf in a 1 mm diameter channel. Proc. International Congress of Refrigeration, 23rd /IIR, Prague.

D. Del Col, S. Bortolin, D. Torresin, A. Cavallini 2011, Flow boiling of R1234yf in single 1mm diameter channel. Suibmitted to Int. J. Refrigeration.

NOMENCLATURE

c_p	specific heat [J kg^{-1} K^{-1}]
D,d	diameter [m]
f	friction factor [-]
g	gravity acceleration [m s^{-2}]
G	mass velocity [kg m^{-2} s^{-1}]
$grad$	temperature gradient [°C m^{-1}]
H,h	enthalpy [J kg^{-1} k^{-1}]
h_{LG}	latent heat [J kg^{-1}]
h_{SL}	specific enthalpy of saturated liquid [J kg^{-1}]
h_{sub}	specific enthalpy of subcooled liquid [J kg^{-1}]
HTC	heat transfer coefficient [W m^{-2} K^{-1}]
k	coverage factor [-]
k^{-1}	capillary length [m]
l,L	length [m]
MS	measuring sector
$\dot{m}$	mass flow rate [kg s^{-1}]
p	pressure [Pa]
p_i	perimeter [m]
PS	pre-sector
p_{RED}	reduced pressure [-]
Ra	arithmetical mean deviation of the profile (according to ISO 4287:1997) [µm]
Re	Reynolds number=$G\,D/\,\mu$ [-]
q'	heat flux [W m^{-2}]
Q,q	heat flow rate [W]
s	standard deviation
$t,\ T$	temperature [°C]
$\overline{T}$	mean temperature [°C]
TS	test section
T'	temperature gradient [°C m^{-1}]
v	velocity [m s^{-1}]
u	uncertainty
u_c	combined uncertainty
U_M, u_M	expanded uncertainty
x	vapor quality
z	axial position [m]
$\bar{z}$	mean axial position [m]

Greeks

α	heat transfer coefficient [W m^{-2} K^{-1}]
γ	interfacial free energy per unit of area [J m^{-2}]
ΔT	temperature difference [K]
Δp	pressure difference [Pa]
$\Delta\theta$	contact angle hysteresis [°]

Θ	frictional multiplier
θ	contact angle
λ	thermal conductivity [W m^{-1} K^{-1}]
ρ	density [kg m^{-3}]
σ	surface tension [N m^{-1}]
μ	dynamic viscosity [Pa s]
ζ	coefficient of fluid resistance
τ	shear stress

Subscripts

A	*air*
Adv	advancing
amb	ambient
cont	contraction
diss	dissipated
exp	expansion
h	hydraulic diameter
i	internal
IN, in	inlet
inox	stainless steel capillary, adiabatic sector
l,L	liquid
loc	local
mean	mean value
out	outlet
r,ref	refrigerant
Rec	receding
S	solid
sat	saturation
ss	stainless steel
sub,*SUB*	subcooled
tot	total
v,V	vapor
w	water
wall	wall

ACKNOWLEDGEMENTS

This study concerning condensation and vaporization of refrigerants inside minichannels has been carried out at the Dipartimento di Fisica Tecnica, Università degli Studi di Padova, under the supervision of Prof. Davide Del Col.
The study concerning the dropwise condensation of steam on nanoengineered copper surfaces has been done at ETH Zurich under the supervision of Prof. Dimos Poulikakos and Dr. Manish K. Tiwari.
Many thanks to Prof. Del Col for his precious and constant support in the entire course of my Ph.D.
Many thanks to Prof. Dimos Poulikakos for giving me the opportunity to join his lab at ETH for the last year of my Ph.D. and to Dr. Manish K. Tiwari for his precious advise during this period.
Special thanks to Dr. Stefano Bortolin, Post Doc. at the Dipartimento di Fisica Tecnica, for his endless availability during my entire Ph.D., the perfect partner for fruitful discussion and crazy brainstorms.
Dr. Marko Matkovic, is acknowledged for his important work in the design and realization of the minichannels experimental test apparatus.
I want also to remember two special colleagues at ETH, Dany and Simo, for their scientific and moral support.